Growth and Process-Induced Deep Levels in Wide Bandgap Semiconductor GaN and SiC

2022

Kazutaka KANEGAE

Electronic Science and Engineering
Kyoto University

Abstract

In this thesis, deep levels in gallium nitride (GaN) and silicon carbide (SiC) are studied to unleash the full potential of GaN and SiC vertical power devices. Through the vigorous research and development for a long time, the performance of silicon (Si) power devices, which have been commonly used, is approaching the theoretical limit determined from the material properties of Si and it is difficult to dramatically improve the device performance. Wide bandgap semiconductor GaN and SiC have excellent physical properties as power devices such as high critical electric field and are promising candidates as a beyond-Si material for high-performance power devices which have high blocking voltage with low energy loss.

On the other hand, compared with Si, GaN and SiC are immature in crystal growth technology and device process technology, and contain various kinds of point defects which act as deep levels in the bandgap. Deep levels in semiconductors, which are localized electronic states, have impacts on the device performance. To unleash the full potential of GaN and SiC power devices, deep levels in GaN and SiC have to be precisely controlled as in Si devices. To deepen the understanding of deep levels, it is important to accurately quantify densities of deep levels and to elucidate physical properties of deep levels.

Lightly Si-doped n-type GaN layers on n^+-type GaN substrates which are used as drift layers have been generally grown by the metalorganic-vapor-phase epitaxy (MOVPE) method. In MOVPE-grown GaN homoepitaxial layers, the carbon impurity from the Ga source [$(CH_3)_3Ga$] substitutes at the nitrogen site (C_N). C_N acts as a deep acceptor and compensates the Si donor. The donor compensation makes it difficult to control a net donor density in the case of the incorporated carbon concentration ([C]) close to the Si donor one. Such a strong compensation also causes the decrease of the electron mobility due to the impurity scattering. Therefore, reduction and control of [C] in MOVPE-grown GaN layers is one of the most important issues for GaN vertical power device development.

To fabricate high-performance devices, control of point defects induced during device processes which form deep levels is also important. The point defects have density distribution in the depth direction. Depth profiles of density make it difficult to characterize process-induced deep levels.

In this thesis, the author proposes methods based on the capacitance transient spectroscopy technology for accurately quantify densities of a dominant deep level $C_N(0/-)$

introduced during crystal growth in n-type GaN homoepitaxial layers and depth profiles of density of deep levels introduced during device processes in SiC homoepitaxial layers. The $C_N(0/-)$ in n-type GaN layers is detected as the hole trap H1 ($E_V + 0.9$ eV). As process-induced deep levels in SiC layers, the $Z_{1/2}$ center ($E_C - 0.64$ eV) and EH_3 center ($E_C - 0.74$ eV) generated during reactive ion etching (RIE) are investigated. The $Z_{1/2}$ center and EH_3 center originate from carbon vacancy [$V_C(0/2-)$] and interstitial carbon related defect, respectively. The author also discuses the physical properties of the $C_N(0/-)$ in n-type GaN layers and the generation mechanism of contrasting carbon related defects induced during RIE in SiC layers with the proposed methods.

In Chapter 2, the principle of the capacitance transient spectroscopy is explained. In the capacitance transient spectroscopy, deep levels are detected as carrier traps in semiconductor. As the spectroscopy technique, deep-level transient spectroscopy (DLTS) and isothermal capacitance transient spectroscopy (ICTS) are described.

In Chapter 3, the author proposes a method to measure the density of hole trap H1 in n-type GaN with current-injection ICTS for a p^+-n junction diode (PND). The proposed method considers both the depth profile of the injected holes and the quick carrier recombination via the hole traps near the depletion layer edge immediately after a reverse bias is applied. The reverse bias voltage dependence of the current-injection ICTS spectrum indicates that an accurate hole trap density, as well as the hole diffusion length and electron capture cross-section of the hole trap, can be determined.

In Chapter 4, the photoionization cross-section of the hole trap H1 under sub-bandgap-light illumination (390 nm) is investigated. Characterization of the photoionization cross-section enables prediction of the effect of light illumination on the device characteristics and leads to a further understanding of the physical properties of the hole trap H1. There are two photoexcitation processes; (a) photoexcitation of a hole from the conduction band (C.B.) to the hole trap H1 (C_N^- to C_N^0) and (b) photoexcitation of a hole from the hole trap H1 to the valence band (V.B.) (C_N^0 to C_N^-). Here, the ratio of photoionization cross-sections σ_n^o/σ_p^o(390 nm) of 3.0, which enables to calculate hole occupancy ratio f_T at the trap under each measurement condition, is determined with current-injection ICTS and sub-bandgap-light (sub-E_g-light)-excited ICTS for a PND.

In Chapter 5, the author proposes methods to measure the density of hole trap H1 in n-type GaN layers with sub-E_g-light-excited ICTS for a Schottky barrier diode (SBD). In the proposed methods, SBDs, which are fabricated with an easy metal deposition process, can be used. To quantify the density of hole trap H1 in n-type GaN layers, the hole occupancy ratio f_T has to be corrected on the measured density in sub-E_g-light-excited ICTS. The hole occupancy ratio under 390 nm light illumination is determined using the ratio of photoexcitation rates, which is determined in Chapter 4, and the sum of photoexcitation rates. The three ways to extract the sum are described in this chapter. Moreover, the three methods can be combined with the dual-color method, in which the capacitance transient due to not only hole thermal excitation but also photoexcitation from the hole-occupied H1

trap to the V.B. by a long-wavelength light illumination is measured and it makes shortened the measurement time. Easy, accurate, and quick methods to quantify the density of hole trap H1 in n-type GaN layers are demonstrated.

In Chapter 6, nature of the hole trap H1 in n-type GaN layers is investigated. It is important to study the nature of the hole trap H1 as well as to measure the density. In this study, quantitative relationship between carbon concentration and density of hole trap H1, electron capture cross-section of the hole trap H1, and dependence of the photoionization cross-section ratio $\sigma_{\mathrm{n}}^{\mathrm{o}}/\sigma_{\mathrm{p}}^{\mathrm{o}}$ of the hole trap H1 on photon energy ($h\nu$) are investigated. The density of hole trap H1 is investigated in MOVPE-grown n-type GaN homoepitaxial layers with [C] from 10^{15} cm^{-3} to 10^{17} cm^{-3} and in quartz-free hydride-vapor-phase epitaxy (QF-HVPE)-grown n-type GaN homoepitaxial layers with [C] from 10^{14} cm^{-3} to 10^{15} cm^{-3}. In the n-type GaN homoepitaxial layers, the density of hole trap H1 is almost equal to [C] and it is suggested that almost all the incorporated carbon atoms form $\mathrm{C_N}$ defect in n-type GaN layers. The electron capture cross-section of the hole trap H1 $\sigma_{\mathrm{n}} = 3\times10^{-21}$ cm^2 is obtained. The investigated $\sigma_{\mathrm{n}}^{\mathrm{o}}/\sigma_{\mathrm{p}}^{\mathrm{o}}(h\nu)$ in the photon energy range from 2.6 eV to 3.2 eV is reasonably explained from the theoretical model of the photoionization cross-section calculated with reported configuration coordinate diagram of $\mathrm{C_N}(0/-)$.

In Chapter 7, a method to investigate depth profiles of defects is proposed. The method has the high depth resolution and the high resolution in the carrier trap density. Thus, steep depth profiles of defects can be extracted with the method. The depth profiles of the electron traps generated during the RIE process in n-type SiC layers and n-type GaN layers are extracted. As the extracted depth profiles, exponential function is assumed. The author discusses the defect generation mechanism. In RIE-etched SiC, the $\mathrm{Z_{1/2}}$ center and $\mathrm{EH_3}$ center, which originate from $\mathrm{V_C}(0/2-)$ and $\mathrm{C_i}$-related defect, respectively, are generated and are localized near the etched surface (< 1 μm) due to ion bombardment. In the deeper region (~ 3 μm), annihilation of $\mathrm{V_C}$ defects generated during crystal growth and carbon atoms kicked-out from the etched region and/or etched surface is investigated.

In Chapter 8, conclusions of this study and suggestions for future work are described.

Acknowledgements

During my Ph.D. life at Kyoto University, a lot of people supported and encouraged me in so many ways and I would like to thank all of them here.

First of all, I would like to express my most sincere gratitude to Professor Tsunenobu Kimoto for his continuous and attentive supervision, invaluable suggestions, and ceaseless encouragement. Moreover, his generous and graceful personality has deeply inspired me. I am also deeply grateful to Professor Yoichi Kawakami and Associate Professor Yuichiro Ando for their invaluable comments and suggestions through regular discussions and refereeing my Ph.D. thesis. I owe a very important debt to Dr. Giovanni Alfieri in Hitachi Energy for giving fruitiful suggestions and refereeing my Ph.D. thesis.

I am much indebted to Professor Jun Suda in Nagoya University, who had been Associate Professor in Kyoto University until March 2017. He always provided me with many constructive, wonderful advises and stimulating comments as well as continuous encouragement and support on this work. Now I strongly feel that his affectionate and sometimes strict guidance extremely grew me in my Ph.D. life. I am obliged to Associate Professor Masahiro Horita, who had been Assistant Professor in Kyoto University until September 2018. He always kindly gave me constructive comments, supported me in my daily work, and instructed me how to use experimental facilities. Owing to his help, I could conduct my experiments smoothly in Rohm Plaza of Kyoto University and C-TECs of Nagoya University.

I have also greatly benefited from Associate Professor Yusuke Nishi in National Institute of Technology Maizuru College, who had been Assistant Professor in Kyoto University until April 2020, for his meticulous comments and mantenance of equipments.

I would like to express my deep gratitude to Assistant Professor Mitsuaki Kaneko for his constructive comments and support in my daily work. He is indispensable to my Ph.D. study and private life.

I would like to special acknowledge Professor Tetsu Kachi in Nagoya University for providing me with an opportunity of collaborative work with Toyota Central R&D Labs., Inc. and Nagoya University. He gave me a great deal of his invaluable comments and warm encouragements. I would like to express my gratitude to Associate Professor Tetsuo Narita in Nagoya University and Toyota Central R&D Labs., Inc. Through our collaborated work, he always gave me fruitful discussions, stimulating comments and constructive suggestions,

which have grown me well. Owing to his outstanding growth technique of a homoepitaxial GaN layer, I could study on the material defects in GaN layers.

I am very much obliged to Mr. Naoki Sawada and Dr. Takuya Maeda for introducing the research work on ”GaN group”. Without lecture by and energetic discussion with them, I would never write this theses. I also thank Mr. Haruki Fujii for supporting maintenance of equipment and performing experiments.

Dr. Takafumi Okuda gave insightful comments especially for my experiments. I would also appreciate his kindness. I would like to thank Assistant Professor Hajime Tanaka and Assistant Professor Takuma Kobayashi for always giving me appropriate comments and kind supports. Dr. Satoshi Asada gave me constructive comments and warm encouragement.

My special appreciation goes to Mr. Keita Tachiki for having fruitful discussions, cheerful conversations, and sharing pleasant and precious time in our laboratory. I am sure that we will keep the good relationship, as not only a friend but also a rival, after our graduation. I also thank Mr. Satoshi Miyake and Mr. Aogu Yamada for working as teaching assistants in KUEE summer camp with me and making my Ph.D. experience unique. I want to thank Mr. Shin-ichi Kan for fruitful discussions and having energetic online sessions.

My appreciation also goes to all of the members in Kyoto University (Kimoto Laboratory) for their kindness and supports: Dr. Kotaro Kawahara, Dr. Hiroki Niwa, Dr. Ian Booker, Dr. Stefanakis Dionysios, Mr. Akifumi Iijima, Mr. Taro Enokizono, Mr. Zhao Ying Xin, Ms. Kana Hiramatsu, Mr. Takahisa Ono, Mr. Chi Xilun, Mr. Shunsuke Kamata, Mr. Ryosuke Matsui, Mr. Koji Ito, Mr. Naoki Kanegami, Mr. Masashi Nakajima, Mr. Toshiki Miyatani, Mr. Shoma Yamashita, Mr. Masaya Arahata, Mr. Takuya Ohku, Mr. Chansun Ku, Mr. Masahiro Hara, Mr. Toshiya Kobayashi, Mr. Kazutaka Yamada, Mr. Ryoya Ishikawa, Mr. Makoto Imuro, Mr. Mizuki Sato, Mr. Yuto Tsuchiya, Mr. Kenoto Nomoto, Mr. Jin Qimin, Mr. Do Euihyeon, Mr. Noriyuki Maeda, Mr. Taiga Matsuoka, Mr. Kyota Mikami, Mr. Gaku Gouhara, Mr. Katsuya Takahashi, Mr. Akira Inoue, Mr. Takeaki Kitawaki, Mr. Shunya Shibata, Mr. Yuta Murakami, Mr. Shunsei Muraki. I also thanks to all members in Nagoya University (Suda Laboratory): Dr. Hideki Sakurai, Dr. Shinji Yamada, Mr. Keito Aoshima, Mr. Koki Tsurimoto, Mr. Ryosuke Murase, Mr. Keisuke Sakao, Mr. Meguru Endo, Mr. Satomu Furuta, Mr. Shohei Rokuno, Mr. Nam Kyung Pil, Mr. Tomohiro Ueda, Mr. Junya Sawada, Mr. Yuichi Shibata, Mr. Kazufumi Hirukawa, Mr. Daiki Tanaka, Mr. Yuga Tsuda. Through discussions, chats, and sometimes trips with them, I could spend meaningful and enjoyable time in this laboratory.

For very kind supports in my daily work, I also wish to thank Ms. Yoriko Ohnaka in Kimoto laboratory and Ms. Yuki Ishida in Suda Laboratory.

I am strongly indebted to the generous sponsors of part of my work and academic activity, Research Fellowship for Young Scientist, a Grant-in-Aid for Scientific Research (19J23296), WISE Program and, MEXT ”Program for research and development of next-generation semiconductor to realize energy-saving society”.

Finally, I sincerely wish to thank my father, my mother, my yonger sisters, my grand-

mothers, and all of my friends for their understanding, support, and heartfelt encouragement.

February, 2022
Kazutaka KANEGAE

Contents

Abstract i

Acknowledgements v

Contents ix

Chapter 1. Introduction 1

1.1 Background 1
1.2 Wide Bandgap Semiconductors for Power Devices with High Energy Efficiency 3
1.2.1 Wide Bandgap Semiconductors 3
1.2.2 GaN Power Devices 5
1.2.3 SiC Power Devices 6
1.3 Deep Levels in Semiconductors 6
1.3.1 Deep Levels 6
1.3.2 Present Understanding of Deep Levels in GaN and Key Issues 8
1.3.3 Present Understanding of Deep Levels in SiC and Key Issues 9
1.4 Aim of This Study and Outline of This Thesis 10
1.4.1 Aim of This Study 10
1.4.2 Outline 11
References 12

Chapter 2. Detection Methods for Deep Levels in Semiconductors 17

2.1 Introduction 17
2.2 Principles of Capacitance Transient Spectroscopy for Majority Carrier Traps 17
2.2.1 Deep-level Transient Spectroscopy (DLTS) 21
2.2.2 Isothermal Capacitance Transient Spectroscopy (ICTS) 23
2.3 Density of Deep Levels in Capacitance Transient Spectroscopy 27
2.4 Principles of Capacitance Transient Spectroscopy for Minority Carrier Traps 30
References 32

Chapter 3. Measurement Method for Density of Hole Trap H1 in n-Type GaN with p^+-n Junction **35**

3.1 Introduction 35

3.2 Experiments 36

3.3 Current-injection ICTS for p^+-n Junction 36

3.4 Depletion Layer Edge Correction Factor on Measured Density of Hole Trap H1 in Current-injection ICTS 36

3.4.1 Diffusion of Holes into n-Type GaN 40

3.4.2 Quick Carrier Recombination via Hole Trap H1 near Depletion Layer Edge 40

3.4.3 Discussion 42

3.5 Temperature Dependence of Measured Density of Hole Trap H1 in Current-injection ICTS 44

3.6 Summary 47

References 47

Chapter 4. Photoionization Cross-section of Hole Trap H1 under Sub-bandgap-light Illumination **51**

4.1 Introduction 51

4.2 Experiments 53

4.3 Sub-bandgap-light-excited ICTS for p^+-n Junction 53

4.4 Photoionization Cross-section Extracted from Hole Occupancy Ratio of Hole Trap H1 under Sub-bandgap-light Illumination 56

4.4.1 Comparison between Measured Densities of Hole Trap H1 Obtained by Current-injection ICTS and Sub-bandgap-light-excited ICTS 56

4.4.2 Temperature Dependence of Hole Occupancy Ratio 59

4.4.3 Discussion 59

4.5 Summary 59

References 61

Chapter 5. Measurement Methods for Density of Hole Trap H1 in n-Type GaN with Schottky Junction **63**

5.1 Introduction 63

5.2 Experiments 64

5.3 Sub-bandgap-light-excited ICTS for GaN Schottky Junction 67

5.4 Uniform Photoexcitation of Hole Trap H1 in In-plane Direction 67

5.5 Depletion Layer Edge Correction Factor on Measured Density of Hole Trap H1 in Sub-bandgap-light-excited ICTS 73

5.5.1 Electron Capture of Hole Trap H1 near Depletion Layer Edge during Optical Filling Pulse 74

5.5.2 Quick Carrier Recombination via Hole Trap H1 near Depletion Layer Edge . . . 84
5.5.3 Discussion . . . 85
5.6 Quantification of Density of Hole Trap H1 with Schottky Junction . . . 87
5.6.1 Temperature Change Method . . . 87
5.6.2 Optical-Power Change Method . . . 87
5.6.3 Optical-filling-pulse-width Change Method . . . 89
5.6.4 Discussion . . . 93
5.7 Quick and Quantitative Method for Density of Hole Trap H1 with Schottky Junction . . . 98
5.7.1 Dual-color Sub-E_g-light-excited Method . . . 98
5.7.2 Experiments . . . 100
5.7.3 Dual-color sub-E_g-light-excited ICTS for GaN Schottky Junction . . . 100
5.7.4 Condition of Longer-wavelength Light Illumination . . . 103
5.7.5 Depletion Layer Edge Correction in Dual-color Method . . . 105
5.7.6 Quick Quantification of Density of Hole Trap H1 with Dual-color Sub-E_g-light-excited Method . . . 107
5.8 Summary . . . 107
References . . . 111

Chapter 6. Nature of Hole Trap H1 in n-Type GaN 113
6.1 Introduction . . . 113
6.2 Comparison between Density of Hole Trap H1 and Carbon Concentration in n-Type GaN layers . . . 113
6.2.1 Deep Levels in Quartz-free Hydride-vapor-phase Epitaxy Grown n-Type GaN . . . 113
6.2.2 Discussion . . . 120
6.3 Electron Capture Cross-section of Hole Trap H1 . . . 120
6.3.1 Experiments . . . 120
6.3.2 Results and Discussion . . . 128
6.4 Dependence of Photoionization Cross-section of Hole Trap H1 on Photon Energy . . . 128
6.4.1 Experiments . . . 131
6.4.2 Results and Discussion . . . 131
6.5 Summary . . . 136
References . . . 136

Chapter 7. Depth Profiles of Density of Deep Levels Induced by Device Processes in SiC 139
7.1 Introduction . . . 139
7.2 Theoretical and Experimental Approaches . . . 140
7.3 Experiments . . . 142
7.4 Result and Discussion . . . 144
7.4.1 Deep Levels Detected in RIE-etched SiC . . . 144
7.4.2 Condition of Filling Pulse Bias Voltage . . . 147
7.4.3 Depth Profiles of Density of Deep Levels . . . 149
7.4.4 Discussion . . . 153
7.5 Application for RIE-induced defects in n-type GaN . . . 156
7.6 Summary . . . 158
References . . . 158

Chapter 8. Conclusions 161
8.1 Conclusions . . . 161
8.2 Future Work . . . 162
References . . . 163

List of Publications 165

Chapter 1

Introduction

1.1 Background

In these days, electricity has been widely used and efficient use of electricity plays a major role in achieving carbon neutrality. Reduction of energy loss in semiconductor power devices, which are used as switch or rectifier for power conversion in power electronics, is one of the most effective ways for achieving the reduction of energy consumption. Silicon (Si) is the most commonly used semiconductor for semiconductor power devices, which has been extensively investigated and optimized for low-loss and low-cost devices.

Figure 1.1 shows a distribution of electric field for an n-type Schottky barrier diode (SBD) as an example of unipolar device. When the critical electric field E_{cr}, which is defined as the maximum electric field in a semiconductor device at the ideal breakdown, is applied for the junction, the maximum width of depletion layer w_{max} is given by:

$$w_{\mathrm{max}} = \frac{\varepsilon_{\mathrm{s}}\varepsilon_0 E_{\mathrm{cr}}}{eN_{\mathrm{d}}}, \tag{1.1}$$

where ε_{s} is the permittivity of the semiconductor, ε_0 is the vacuum permittivity, e the elementary charge, and N_{d} the donor density of the semiconductor. The breakdown voltage V_{B} is represented as the area of triangle shown in Fig. 1.1, and is described as:

$$\begin{aligned} V_{\mathrm{B}} &= \frac{E_{\mathrm{cr}} w_{\mathrm{max}}}{2} \\ &= \frac{\varepsilon_{\mathrm{s}}\varepsilon_0 E_{\mathrm{cr}}^2}{2eN_{\mathrm{d}}}. \end{aligned} \tag{1.2}$$

The N_{d} and the thickness of drift layer are parameters to adjust V_{B} of unipolar devices. On the other hand, the drift layer behaves as a resistor under forward bias condition. N_{d} directly influences on-resistance of the drift layer, which determines on-state loss. In unipolar devices with a non-punch-through structure, the specific on-resistance of the drift layer $R_{\mathrm{drift_sp}}$ is given as a product of resistivity of the drift layer $\rho_{\mathrm{drift}} = 1/(en\mu)$, where n is free carrier concentration and μ is carrier mobility, and thickness of the drift layer, which

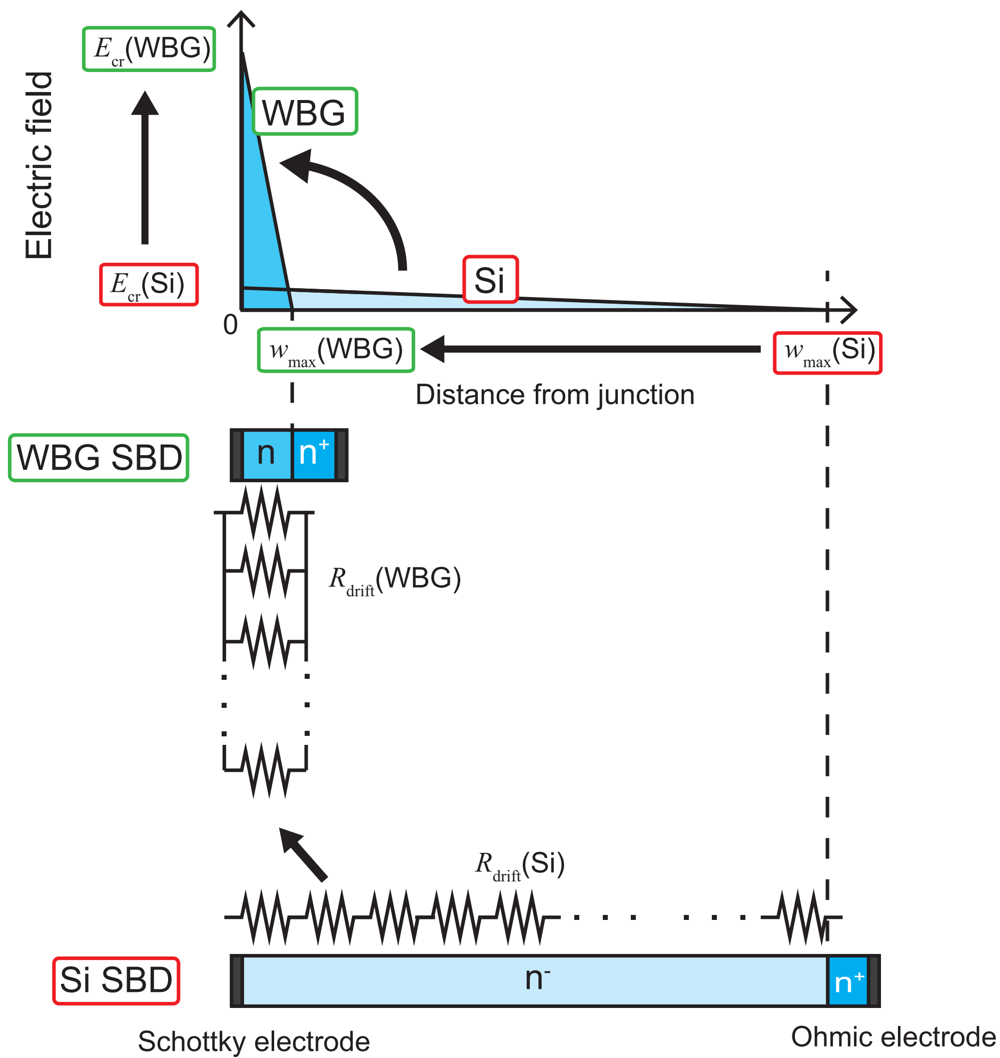

Figure 1.1: Distribution of electric field for Si and wide bandgap semiconductor (WBG) Schottky junction.

is equal to w_{max}. From Eqs. 1.1 and 1.2, the specific on-resistance of the drift layer $R_{\mathrm{drift_sp}}$ can be calculated by the following equation:

$$\begin{aligned} R_{\mathrm{drift_sp}} &= \rho_{\mathrm{drift}} w_{\mathrm{max}} \\ &\simeq \frac{4V_{\mathrm{B}}^2}{\varepsilon_{\mathrm{s}}\varepsilon_0 \mu E_{\mathrm{cr}}^3}. \end{aligned} \tag{1.3}$$

In Eq. 1.3, it is assumed that the donor is completely ionized, i.e., $n = N_{\mathrm{d}}$. When resistance of the drift layer is the dominant component of the on-resistance, i.e., other components such as contact resistance and channel resistance can be negligible, $R_{\mathrm{drift_sp}}$ indicates the unipolar limit, which is the the lower limit of resistance determined from the intrinsic physical properties μ and E_{cr} of a semiconductor material in a unipolar device with a certain breakdown voltage V_{B}. Note that μ and E_{cr} depend on the donor density. Figure 1.2 [1] shows the trade-off relationship between the specific on-resistance of a drift layer $R_{\mathrm{on_sp}}$ and the breakdown voltage V_{B}. The unipolar limit of Si [2] is shown in Fig. 1.2 as the black solid line. Si devices are approaching the unipolar limit of Si through the continuous research and development. Therefore, although Si devices are approaching the unipolar limit of Si, Si unipolar power devices have high on-resistance with high breakdown voltage due to low N_{d} and large w_{max} by comparing with the specific on-resistance required for practical use (e.g., 1 mΩcm^2 for kV-class power devices). To exceed the unipolar limit, bipolar devices such as insulated gate bipolar transistor (IGBT) have been used as Si power devices. On-resistance of bipolar devices can be kept low even in voltage-blocking layers, which corresponds to drift layers in unipolar devices, with low N_{d} thanks to the conductivity modulation. However, bipolar devices have high switching loss and low switching speed.

1.2 Wide Bandgap Semiconductors for Power Devices with High Energy Efficiency

1.2.1 Wide Bandgap Semiconductors

As an approach to dramatically improve the performance of semiconductor power devices, wide bandgap semiconductors has attracted much attention. Wide bandgap semiconductors have a larger bandgap than Si, and have excellent physical properties as semiconductor power device materials such as the high breakdown electric field and low intrinsic carrier density. Among them, gallium nitride (GaN) and silicon carbide (SiC) are promising candidates as semiconductor materials which are superior to Si for use in power devises [2–8]. GaN and SiC, which are wide bandgap semiconductors, have a critical electric field (height of the triangle in Fig. 1.1) about 10 times that of Si [9, 10]. Therefore, as shown in Fig. 1.1, considering a GaN or SiC Schottky barrier diode with a simple non-punch-through structure which has the same breakdown voltage (area of the triangle in Fig. 1.1) as a Si Schottky

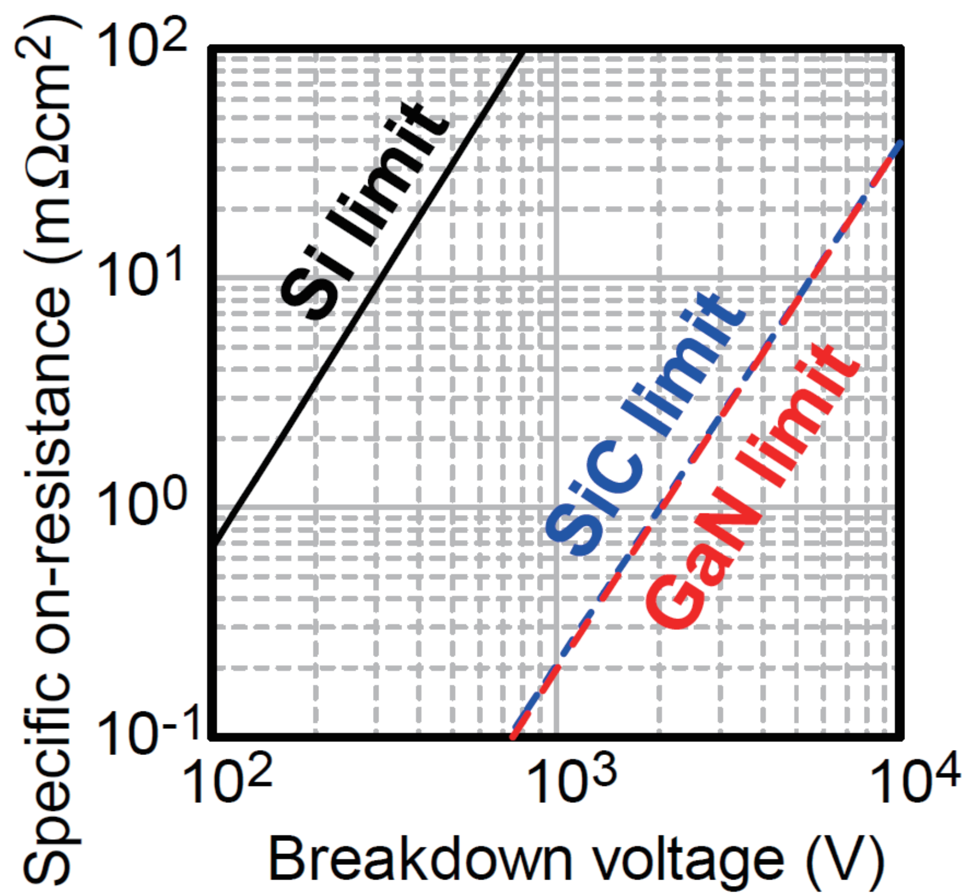

Figure 1.2: Relationship between specific on-resistance and breakdown voltage for Si (black solid line), GaN (red broken line), and SiC (blue broken line) unipolar devices with a non-punch-through structure [1].

barrier diode, the thickness of drift layer (base of the triangle in Fig. 1.1) can be reduced by about 1/10 and the doping density of drift layer (slope of the triangle in Fig. 1.1) can be increased by about 100 times. As a result, the specific on-resistance of the drift layer can be dramatically reduced to a few hundredth. This makes it possible to replace Si bipolar power devices with GaN or SiC unipolar power devices in the high breakdown voltage region [11]. Unipolar devices can operate at higher frequency and with lower switching loss than bipolar devices, enabling high-speed switching operation and miniaturization of peripheral passive components. In addition, since the intrinsic carrier density in GaN and SiC is orders of magnitude smaller than that in Si, GaN or SiC power device can operate even at high temperatures. This makes it possible to simplify the cooling equipment.

1.2.2 GaN Power Devices

GaN, which has a direct bandgap of 3.42 eV, has been widely used as a material for optical devices such as blue, green, or ultraviolet light-emitting diodes (LEDs) and laser diodes (LDs) due to the availability of the alloys and heterostructures of other group-III nitrides, such as indium nitride (InN) and aluminum nitride (AlN) [12–17]. GaN has been also used as a material for electronic devices such as high electron mobility transistors (HEMTs), in which a high-density and high-mobility two-dimensional electron gas (2DEG) induced at an AlGaN/GaN heterostructure is used as the carrier of channel [18–22].In the 1980s, the dawn of research and development of GaN, freestanding substrate was not available. Therefore, these GaN-based devices have been fabricated on foreign substrates such as sapphire, Si and SiC [12–14, 18, 20–24]. As GaN power devices, HEMTs fabricated on Si substrates have been widely used [20, 22].Further, in radio frequency (RF) transistors for communication base stations that are require high-power and high-frequency operation, HEMTs fabricated on SiC substrates have been used [21, 23, 24]. On the other hand, a lot of crystal defects such as threading dislocations (TDs) are induced in heteroepitaxial grown GaN layers, which are grown on foreign substrates. In addition, HEMT has a lateral device structure, in which a current path is in the in-plane direction. In a lateral device structure, an increase of the breakdown voltage is directly linked to the increase in the device area. From the above, HEMT has been used for devices with relatively low breakdown voltage (several hundreds V class).

In recent years, along with research and development aimed LDs with long lifetimes, high quality freestanding GaN substrates have become available [25]. Thus, it has become possible to fabricate devices using homoepitaxial grown GaN layers on GaN substrates. In comparison with heteroepitaxial grown GaN layers on foreign substrates, homoepitaxial grown GaN layers have significantly less crystal defects such as TDs. In addition, in homoepitaxial grown GaN layers on conductive GaN substrates, it has become possible to adopt a vertical device structure having a current path in the film thickness direction. Therefore, the studies on GaN vertical power devices, in which the full potential of GaN

can be unleashed, have been actively reported [3–6, 9, 26, 27].

1.2.3 SiC Power Devices

4H-SiC, which has a indirect bandgap of 3.26 eV, has been studied as a material for semiconductor power devices [2, 7, 8, 28]. Through extensive studies in the last two decades, SiC has basic technologies required for device fabrication, such as growth of large-diameter bulk wafers and high-quality epitaxial layers and wide range doping control of both n- and p-type conductivity via either in situ doping or ion implantation [28–37]. SiC SBDs and metal-oxide-semiconductor field effect transistors (MOSFETs) have been commercially available and put into practical use for kV-class power devices. In recent years, to maximize the potential of SiC power devices, especially for the improvement of MOS channel mobility, research on the reduction and control of the interface state of the MOS interface has been actively studied [11, 38–40]. In addition, SiC has a long carrier lifetime due to its indirect band structure, i.e., has advantage for development of ultrahigh-voltage bipolar power devices [41–44]. Study of SiC bipolar power devices has been carried out as power devices with blocking voltage higher than several kV used in power systems.

1.3 Deep Levels in Semiconductors

1.3.1 Deep Levels

An actual semiconductor crystal contains various kinds of defects such as planar defects (stacking faults), line defects (dislocations), and point defects. In particular, point defects can play an important role in the electrical and optical properties of semiconductor crystals, which are sensitive to the crystal structure of semiconductors. Point defects are classified into three types: intrinsic point defects, impurity atoms, and complexes of these. Intrinsic point defects are composed of disorders of the ordered arrangement of the constituent atoms of a semiconductor crystal, such as vacancies, self-interstitials, and antisite defects. Impurity atoms are atoms other than the constituent atoms of a semiconductor crystal incorporated into the crystal, such as interstitials and substitutional atoms.

A part of point defects disturbs the periodicity of the potential in a semiconductor crystal, resulting in the formation of localized electronic states (energy levels) in the bandgap. Some point defects have multiple energy levels in the bandgap, with the charge state changing depending on the position of the Fermi level in the bandgap of the semiconductor.

A point defect which form "shallow level", whose energy levels is close to the conduction band (C.B.) minimum E_{C} or valence band (V.B.) maximum E_{V} so that the energy levels are sufficiently ionized at a certain temperature [e.g. room temperature (RT)], may be intentionally introduced into semiconductor crystals as a dopant. In various semiconductor materials, shallow levels at RT whose energy position E_{T} is located at several $k_{\mathrm{B}}T$ below E_{C}

or above E_V have been studied to control n-type or p-type conductivity, respectively. On the other hand, energy levels that are not ionized at a certain temperature are called "deep levels" as opposed to "shallow levels". Deep levels have properties as carrier traps, generation / recombination centers, and unintentional donors / acceptors, and can electrically and optically affect the properties of semiconductor crystals and device operation.

In the point of view as a carrie trap, a deep level is classified into an electron trap and a hole trap. When a deep level acts an electron trap, an electron is captured from the C.B. to the deep level in the empty state or thermal excited from the deep level in the electron-occupied state to the C.B. In the same way, when a deep level acts a hole trap, a hole is captured from the V.B. to the deep level in the empty state or thermal excited from the deep level in the hole-occupied state to the V.B. A carrier trap near a junction, which is the active region of device, may lead hysteresis in the device operation due to a change in electrical charge of the carrier trap with the carrier occupancy state.

When a deep level acts as a generation center, electrons and holes are thermally excited from the deep level to the C.B. and V.B, respectively. An increase of generation center density leads to an increase in junction leakage current. When a deep level acts as a recombination center, electrons and holes are captured from the C.B. and V.B. to the deep level, respectively. Recombination canters reduce carrier lifetimes. Thus, in bipolar devices, precise control of recombination center density is required to control a carrier lifetime. For example, in Si, it has been reported that Au ($E_V + 0.56$ eV) and Pt ($E_V + 0.42$ eV), which form levels near the midgap, act as recombination centers [45–47].

Deep levels can acts as unintentional donors and acceptors. A deep level which has negative charge in the electron-occupied state [e.g. $(0/-)$, $(-/2-)$] is called an acceptor-like type. An acceptor-like type deep level in an n-type layer and a p-type layer can act as a compensating acceptor and a residual acceptor, respectively. A deep level which has positive charge in the hole-occupied state [e.g. $(+/0)$, $(2+/+)$] is called a donor-like type. A donor-like type deep level in an n-type layer and a p-type layer can act as a residual donor and a compensating donor, respectively. In drift layers, residual donors and acceptors which are ionized in the depletion layer lead a decrease of blocking voltage. When residual donors and acceptors which are located near shallow levels, conductivity of the semiconductor unintentionally increases. Compensating donors and acceptors lead a unintentional decrease of conductivity of the semiconductor. These unintentional donors and acceptors can also act as scattering centers and reduce a carrier mobility.

Compared with Si, GaN and SiC are immature in crystal growth technology and device process technology, and contain more point defects. To maximize the potential of GaN and SiC power devices, it is necessary to elucidate an origin and generation mechanism of deep levels and precisely control through detailed and systematic studies on deep levels.

1.3.2 Present Understanding of Deep Levels in GaN and Key Issues

One of the most important parts of GaN vertical power devices is the drift layer, which consists a lightly n-type GaN layer. Precise control of doping as well as high electron mobility (low compensation) are needed. Typical net donor density and thickness are 10^{16} cm^{-3} and 5-10 μm for 1200 V-class devices and 10^{15} cm^{-3} and 20-35 μm for 3300 V-class devices [9, 48]. In GaN, the Si atom substituting on the Ga site (Si_{Ga}) acts as a shallow donor [$E_C - (0.02$-$0.03)$ eV] [49–52] and Si-doped GaN layers have been used as n-type layers. As a growth method for drift layers, the metalorganic vapor phase epitaxy method (MOVPE method), which has a proven track record in fabrication of LEDs, has been used [3–6, 9, 12, 26, 27]. In the MOVPE method, carbon atoms are incorporated into the films from the methyl ligand of the trimehylgallium [$(CH_3)_3Ga$] used as a Ga source [48]. From first-principles calculations, it has been reported that the C atom substituting on the N site (C_N) acts as a deep acceptor in the n-type GaN layers [$C_N(0/-)$: $E_V + 0.9$ eV] [53, 54]. Reducing and controlling the density of deep acceptors, which compensate donors, is important.

To optimize growth conditions as well as to modify growth apparatus, it is necessary to know the carbon acceptor density in n-type GaN layers. When the concentration of the carbon impurity is high ($> 10^{16}$ cm^{-3}), it is possible to accurately quantify the carbon concentration by the secondary ion mass spectrometry (SIMS). However, recent vigorous research [48, 55] has reduced the incorporation of carbon and the carbon concentration is approaching to the SIMS detection limit (around 10^{16} cm^{-3}). It is reported that the carbon acceptor is detected as the yellow luminescence (YL) band in hydride-vaper-phase epitaxy (HVPE)-grown GaN layers on sapphire substrates and the carbon acceptor density is estimated by using photoluminescence (PL) [56]. Reshchikov et al. showed that the carbon concentration obtained by SIMS agreed with the carbon acceptor density obtained by PL in GaN sample with the carbon concentration of former half of 10^{15} cm^{-3}. For control of low net donor density in n-type GaN layers, a method for electrically sensitively quantifying the carbon acceptor density rather than the carbon concentration is essential. Considering industrial applications, it is also required to quickly quantify with simple devices.

It has been reported that the carbon acceptor $C_N(0/-)$ in n-type GaN layers can be detected as a hole trap H1 ($E_V + 0.9$ eV) [53, 57–63]. Capacitance transient spectroscopy is widely used to detect carrier traps in semiconductors [64–66]. The details about the capacitive transient spectroscopy are described in Chapter 2, carrier traps are detected by measuring the transient change in the junction capacitance due to the change in the charge state of carrier traps in the depletion layer. To detect hole traps, which are minority carrier traps in an n-type layer, it is necessary to supply holes to the n-type layer and change the state of hole trap from empty to hole-occupied. As methods to detect minority carrier traps, the current-injection method and the above-E_g-light-irradiation method are used. Here, for simplicity, the detection of hole traps in an n-type layer is described as minority

carrier traps. In the current-injection method, by applying a forward bias voltage to a p^+-n junction, holes are injected from the p^+-type layer to the n-type layer and the holes are captured to hole traps. However, in the current-injection method, it is necessary to form a mesa structure to clarify the junction area and grow the p^+-type layer which supplies holes. Thus, it is difficult to fabricate a p^+-n junction mesa diode for the evaluation of hole traps in the n-type layer. In the above-E_g-light-illumination method, a p^+-n junction or a n-type Schottky junction is used. By irradiation light having photon energy higher than the bandgap, electron−hole pairs are generated. The holes diffuse into the depletion layer and captured to hole traps. In the above-E_g-light-illumination method, a Schottky barrier diode which can be easily fabricated with deposition of Schottky electrodes on the surface of n-type layer can be used. However, since GaN has a direct bandgap, the penetration length of above-E_g-light and the diffusion length of holes in n-type layers are short (< 1 μm). Thus, it is difficult to supply holes to hole traps in the depletion layer extending under the electrode, whose diameter is several hundred μm. For this reason, it is difficult to accurately quantify trap densities.

Therefore, in this study, the sub-E_g-light-excited method, in which minority carrier traps can be detected with a Schottky barrier diode, is focused. In the sub-E_g-light-excited method, the junction is illuminated with sub-E_g-light and holes are photoexcited from the C.B. to the hole traps. When the surface of epitaxial layer is illuminated with sub-E_g-light, the sub-E_g-light is hardly absorbed in a GaN epitaxial layer and conductive GaN substrate [67]. Thus, multiple reflections between the surface Schottky electrodes and backside ohmic electrodes occur and hole traps in the depletion layer even under the Schottky electrodes can be photoexcited spatially and uniformly. On the other hand, it is difficult to estimate the hole occupancy ratio of a hole trap, which is the ratio of hole-occupied hole trap to hole trap during light illumination. Thus, reports on application of the sub-E_g-light-excited method have been limited [57]. In this study, methods to measure the density of hole trap H1 in n-type GaN layers by correcting the hole occupancy of the hole trap H1 during sub-E_g light illumination are proposed. The proposed methods are useful technique as a monitoring tool of GaN device process. Using the proposed methods, physical properties of the hole trap H1 (C_N) in n-type GaN layers are successfully elucidated. The methods are useful for measuring the density of not only the hole trap H1 in n-type GaN layers but also other minority carrier traps.

1.3.3 Present Understanding of Deep Levels in SiC and Key Issues

Research and development of SiC as a power device material is more advanced than that of GaN, and the origin and density control method of the dominant deep level introduced during crystal growth have been clarified. In particular, since the $Z_{1/2}$ center is the dominant recombination center, systematic and detailed studies have been conducted on its properties

and density control [28, 68–71].

On the other hand, a deep level induced during device processes is difficult to evaluate due to the wide variety of defect candidates that depend on a device process and its condition. The depth direction of the defect density also makes it difficult to evaluate device process-induced defects. Thus, many of them have not been clarified about the origins and generation mechanisms. To maximize the performance of SiC power devices, it is necessary to control deep levels induced during device processes and it is important to elucidate each origin and generation and annihilation mechanisms, characterize physical properties, and quantify the depth profiles of defect density.

In this study, depth profiles of process-induced defect density are focused. In previous studies, the double-correlation method [72] has been used to measure depth profiles carrier trap densities [73–78]. In the double-correlation method, the narrowed detection area of carrier traps is changed in the depth direction and the average trap density in each narrowed detection area is obtained. The double-correlation method is a useful method when depth profiles of carrier trap density have relatively loose shape. On the other hand, the double-correlation method has a trade-off relationship between the spatial resolution in the depth direction and the resolution in carrier trap density to be detected. Therefore, it is difficult to accurately quantify steep depth profiles of carrier trap density. In this study, the author proposed a measurement method of depth profiles of carrier trap density which overcomes the trade-off relationship in the conventional double-correlation method. Furthermore, depth profiles of carrier trap density of deep levels induced during reactive ion etching (RIE), in which process damage is expected to be localized near the etched surface, was accurately quantified and the generation mechanism of the RIE-induced defects is discussed.

1.4 Aim of This Study and Outline of This Thesis

1.4.1 Aim of This Study

As mentioned in Section 1.3, control of deep levels in GaN and SiC is important to maximize the potential of GaN and SiC power devices. In this thesis, the aims were as follows towards the control of the dominant deep level induced during crystal growth in GaN and the control of the deep levels generated during device processes in SiC.

- Development of accurate, easy and quick quantification methods for the density of hole trap H1 in n-type GaN
- Elucidation of the physical properties of hole trap H1 in n-type GaN
- Development of a quantitative method for the depth profiles of carrier trap density with the high depth resolution and the resolution in the carrier trap density

- Quantification of depth profiles of density and elucidation of generation mechanism of carrier trap induced during reactive ion etching in SiC

1.4.2 Outline

In Chapter 2, methods for characterization of deep levels in semiconductors are explained. In this study, Deep levels in GaN and SiC are investigated with the capacitance transient spectroscopy. In the capacitance transient spectroscopy, deep levels are detected as carrier traps in the depletion layer of junctions.

In Chapter 3, a method for measurement of density of the hole trap H1 in n-type GaN with a p^+-n junction is proposed. Using a GaN mesa p^+-n junction diode, current-injection method, in which holes are injected from p^+-layer to n-layer, is performed to detect the hole trap H1 in n-type GaN. The measured density of hole trap H1 in the current-injection method depends on device structure and measurement conditions due to the effects of injected hole density distribution in n-type layer and the quick carrier recombination via hole-occupied hole traps near the depletion layer edge. In the proposed method, the measured density of hole trap H1 is corrected to the true density by considering the two effects.

In Chapter 4, the photoionization cross-section of the hole trap H1 for sub-E_g-light is investigated. In sub-bandgap (E_g)-light-excited method with Schottky junctions for measurement of the density of hole trap H1 discussed in Chapter 5, correction of the hole occupancy ratio of the hole trap H1 under sub-E_g-light illumination is needed. In Chapter 4, the ratio of photoionization cross-sections of electron to hole for a sub-E_g-light, which enables calculation of the hole occupancy ratio under arbitrary measurement conditions, is extracted.

In Chapter 5, methods for measurement of the density of hole trap H1 in n-type GaN with the Schottky junction are demonstrated. In the proposed methods, measurement conditions (temperature, optical power, or optical pulse width) are modulated and the true density of hole trap H1 is extracted from the measured density of that. Then, the hole occupancy ratio of the hole trap H1 under sub-E_g-light illumination is calculated by using the ratio of photoionization cross-sections determined in Chapter 4. Furthermore, the dual-color sub-E_g-light-excited method, in which capacitance transients with quick photoexcitation of holes from hole traps to the valence band by longer-wavelength light illumination are measured, is proposed and it makes measurement time shortened.

In Chapter 6, nature of the hole trap H1 in n-type GaN is investigated. Deep levels in MOVPE-grown n-type GaN layers and quartz-free (QF) HVPE-grown n-type GaN layers are investigated. Then, the densities of hole trap H1 in the n-type GaN layers are measured with the proposed methods in Chapter 5, and the quantitative comparison between the carbon concentration and density of hole trap H1 in the MOVPE-grown GaN layers and QF-HVPE-grown GaN layers is obtained. The electron capture cross-section of the hole trap

H1 is extracted. The dependence of the ratio of photoionization cross-sections on photon energy is investigated.

In Chapter 7, a method for measurement of depth profiles of process-induced defects is proposed. Compering with the double-correlation method, the trade-off relationship between the depth resolution and resolution in the carrier trap density is overcame in the proposed method. Using the method, depth profiles of defects generated during reactive ion etching (RIE) in SiC are investigated. From the analysis of the depth profiles, the generation mechanism of RIE-induced defects is described.

In Chapter 8, conclusions of this study and suggestions for future work are described.

References

[1] T. Maeda, Doctor Thesis (2020).

[2] B. J. Baliga, Fundamentals of Power Semiconductor Devices.

[3] T. Kachi, Jpn. J. Appl. Phys. **53**, 100210 (2014).

[4] H. Nie, Q. Diduck, B. Alvarez, A. P. Edwards, B. M. Kayes, M. Zhang, G. Ye, T. Prunty, D. Bour, and I. C. Kizilyalli, IEEE Electron Device Lett. **35**, 939 (2014).

[5] T. Oka, Y. Ueno, T. Ina, and K. Hasegawa, Appl. Phys. Express **7**, 021002 (2014).

[6] I. C. Kizilyalli, A. P. Edwards, O. Aktas, T. Prunty, and D. Bour, IEEE Transactions on Electron Devices **62**, 414 (2015).

[7] J. A. Cooper and A. Agarwal, Proceedings of the Institute of Electrical and Electronics Engineers **90**, 956 (2002).

[8] T. Kimoto, Jpn. J. Appl. Phys. **58**, 018002 (2018).

[9] T. Maeda, T. Narita, S. Yamada, T. Kachi, T. Kimoto, M. Horita, and J. Suda, J. Appl. Phys. **129**, 185702 (2021).

[10] H. Niwa, J. Suda, and T. Kimoto, IEEE Trans. Electron Devices **62**, 3326 (2015).

[11] T. Kimoto and H. Watanabe, Appl. Phys. Express **13**, 120101 (2020).

[12] H. Amano, N. Sawaki, I. Akasaki, and Y. Toyoda, Appl. Phys. Lett. **48**, 353 (1986).

[13] H. Amano, M. Kito, K. Hiramatsu, and I. Akasaki, Jpn. J. Appl. Phys. **28**, L2112 (1989).

[14] S. Nakamura, T. Mukai, and M. Senoh, Appl. Phys. Lett. **64**, 1687 (1994).

[15] S. Nakamura, M. Senoh, N. Iwasa, and S. Nagahama, Jpn. J. Appl. Phys. **34**, L797 (1995).

[16] S. Nakamura, M. Senoh, S. Nagahama, N. Iwasa, T. Yamada, T. Matsushita, H. Kiyoku, and Y. Sugimoto, Jpn. J. Appl. Phys. **35**, L74 (1996).

[17] S. Nagahama, N. Iwasa, M. Senoh, T. Matsushita, Y. Sugimoto, H. Kiyoku, T. Kozaki, M. Sano, H. Matsumura, H. Umemoto, K. Chocho, and T. Mukai, Jpn. J. Appl. Phys. **39**, L647 (2000).

[18] M. A. Khan, J. N. Kuznia, J. M. V. Hove, N. Pan, and J. Carter, Appl. Phys. Lett. **60**, 3027 (1992).

[19] U. Mishra, P. Parikh, and Y.-F. Wu, Proceedings of the IEEE **90**, 1022 (2002).

[20] M. Ishida, T. Ueda, T. Tanaka, and D. Ueda, IEEE Trans. Electron Devices **60**, 10 (2013).

[21] Y. Dora, A. Chakraborty, L. McCarthy, S. Keller, S. P. DenBaars, and U. K. Mishra, IEEE Trans. Electron Devices **60**, 10 (2013).

[22] M. Kuzuhara, J. T. Asubar, and H. Tokuda, Jpn. J. Appl. Phys. **55**, 070101 (2016).

[23] Y.-F. Wu, A. Saxler, M. Moore, R. Smith, S. Sheppard, P. Chavarkar, T. Wisleder, U. Mishra, and P. Parikh, IEEE Electron Device Lett. **25**, 117 (2004).

[24] R. S. Pengelly, S. M. Wood, J. W. Milligan, S. T. Sheppard, and W. L. Pribble, IEEE Trans. on Microwave Theory and Techniques **60**, 1764 (2012).

[25] H. Fujikura, T. Konno, T. Suzuki, T. Kitamura, T. Fujimoto, and T. Yoshida, Jpn. J. Appl. Phys. **57**, 065502 (2018).

[26] J. Suda, K. Yamaji, Y. Hayashi, T. Kimoto, K. Shimoyama, H. Namita, and S. Nagao, Appl. Phys. Express **3**, 101003 (2010).

[27] T. Maeda, M. Okada, M. Ueno, Y. Yamamoto, M. Horita, and J. Suda, Appl. Phys. Express **9**, 109201 (2016).

[28] T. Kimoto and J. A. Cooper, Fundamentals of Silicon Carbide Technology.

[29] T. Kimoto, A. Itoh, and H. Matsunami, Phys. Stat. Sol. (B) **202**, 247 (1997).

[30] H. Matsunami, Jpn. J. Appl. Phys. **43**, 6835 (2004).

[31] T. Kimoto, Progress in Crystal Growth and Characterization of Materials **62**, 329 (2016).

[32] A. Itoh, H. Akita, T. Kimoto, and H. Matsunami, Appl. Phys. Lett. **65**, 1400 (1994).

[33] H. Tsuchida, M. Ito, I. Kamata, and M. Nagano, Phys. Status Solidi B **246**, 1553 (2009).

[34] S. Nishino, H. Suhara, H. Ono, and H. Matsunami, J. Appl. Phys. **61**, 4889 (1987).

[35] T. Troffer, M. Schadt, T. Frank, H. Itho, G. Pensl, J. Heindl, H. P. Strunk, and M. Maier, Phys. St. Solidi A **162**, 277 (1997).

[36] T. Kimoto, N. Inoue, and H. Matsunami, Phys. St. Sol. A **162**, 263 (1997).

[37] T. Kimoto, A. Itoh, H. Matsunami, T. Nakata, and M. Watanabe, J. Electronic Materials **25**, 879 (1996).

[38] H. Watanabea, T. Kirinoa, Y. Uenishia, A. Chanthaphana, A. Yoshigoeb, Y. Teraokab, S. Mitanic, Y. Nakanoc, T. Nakamurac, T. Hosoia, and T. Shimuraa, ECS Transactions **35**, 265 (2011).

[39] J. A. C. Jr., Phys. St. Solidi A **162**, 305 (1997).

[40] M. Noborio, J. Suda, S. Beljakowa, M. Krieger, and T. Kimoto, Phys. St. Solidi A **206**, 2374 (2009).

[41] T. Kimoto and Y. Yonezawa, Mater. Sci. in Semiconductor Processing **78**, 43 (2018).

[42] E. v. Brunt, L. Cheng, M. J. O'Loughlin, J. Richmond, V. Pala, J. Palmour, C. W. Tipton, and C. Scozzie, Mater. Sci. Forum **821-823**, 847 (2015).

[43] N. Kaji, H. Niwa, J. Suda, and T. Kimoto, IEEE Trans. Electron Devices **62**, 374 (2015).

[44] K. Nakayama, A. Tanaka, M. Nishimura, K. Asano, T. Miyazawa, M. Ito, and H. Tsuchida, Mater. Sci. Forum **821-823**, 847 (2015).

[45] J. E. Lowther, J. Phys. C: Solid St. Phys. **13**, 3681 (1980).

[46] M. D. Miller, H. Schade, and C. J. Nuese, J. Appl. Phys. **47**, 2569 (1976).

[47] C. B. Collins, R. O. Carlson, and C. J. Gallagher, Phys. Rev. **105**, 1168 (1957).

[48] G. Piao, K. Ikenaga, Y. Yano, H. Tokunaga, A. Mishima, Y. Ban, T. Tabuchi, and K. Matsumoto, J. Crystal Growth **456**, 137 (2016).

[49] D. C. Look, D. C. Reynolds, J. W. Hemsky, J. R. Sizelove, R. L. Jones, and R. J. Molnar, Phys. Rev. Lett. **79**, 2273 (1997).

[50] W. Götza, N. M. Johnson, H. L. C. Chen, C. Kuo, and W. Imler, Appl. Phys. Lett. **68**, 3144 (1996).

[51] N. Sawada, T. Narita, M. Kanechika, T. Uesugi, T. Kachi, M. Horita, T. Kimoto, and J. Suda, Appl. Phys. Express **11**, 041001 (2018).

[52] E. C. H. Kyle, S. W. Kaun, P. G. Burke, F. Wu, Y. R. Wu, and J. S. Speck, J. Appl. Phys. **115**, 193702 (2014).

[53] J. L. Lyons, A. Janotti, and C. G. V. d. Walle, Appl. Phys. Lett. **97**, 152108 (2010).

[54] J. L. Lyons, A. Janotti, and C. G. V. d. Walle, Phys. Rev. B **89**, 035204 (2014).

[55] T. Narita, M. Horita, K. Tomita, T. Kachi, and J. Suda, Jpn. J. Appl. Phys. **59**, 105505 (2020).

[56] M. A. Reshchikov, M. Vorobiov, O. Andrieiev, K. Ding, N. Izyumskaya, V. Avrutin, A. Usikov, H. Helava, and Y. Makarov, Science Reports **10**, 2223 (2020).

[57] Y. Tokuda, ECS Transactions **75**, 39 (2016).

[58] R. Armitage, W. Hong, Q. Yang, H. Feick, J. Gebauer, E. R. Weber, S. Hautakangas, and K. Saarinen, Appl. Phys. Lett. **82**, 3457 (2003).

[59] A. Armstrong, A. R. Arehart, D. Green, U. K. Mishra, J. S. Speck, and S. A. Ringel, J. Appl. Phys. **98**, 053704 (2005).

[60] Y. Tokuda, Y. Yamada, T. Shibata, S. Yamaguchi, H. Ueda, T. Uesugi, and T. Kachi, Phys. St. Solidi C **8**, 2239 (2011).

[61] U. Honda, Y. Yamada, Y. Tokuda, and K. Shiojima, Jpn. J. Appl. Phys. **51**, 04DF04 (2012).

[62] T. Tanaka, N. Kaneda, T. Mishima, Y. Kihara, T. Aoki, and K. Shiojima, Jpn. J. Appl. Phys. **54**, 041002 (2015).

[63] T. Tanaka, K. Shiojima, T. Mishima, and Y. Tokuda, Jpn. J. Appl. Phys. **55**, 061101 (2016).

[64] D. V. Lang, J. Appl. Phys. **45**, 3023 (1974).

[65] H. Okushi1 and Y. Tokumaru, Jpn. J. Appl. Phys. **20**, 261 (1981).

[66] G. L. Miller., D. V. Lang., and L. C. Kimerling, Ann. Rev. Marer. Sci. **7**, 377 (1977).

[67] S. Pimputkar, S. Suihkonen, M. Imade, Y. Mori, J. S. Speck, and S. Nakamura, J. Crystal Growth **432**, 49 (2015).

[68] K. Kawahara, J. Suda, and T. Kimoto, J. Appl. Phys. **111**, 053710 (2012).

[69] T. Kimoto, K. Danno, and J. Suda, Phys. Stat. Sol. B **245**, 1327 (2008).

[70] H. M. Ayedh, V. Bobal, R. Nipoti, A. Hallen, and B. G. Svensson, J. Appl. Phys. **115**, 012005 (2014).

[71] B. Zippelius, J. Suda, and T. Kimoto, J. Appl. Phys. **111**, 033515 (2012).

[72] H. Lefèvre and M. Schulz, Appl. Phys. **12**, 45 (1977).

[73] Y. Zohta and M. O. Watanabe, J. Appl. Phys. **53**, 1809 (1982).

[74] A. Usami, Y. Tokuda, M. Katayama, S. Kaneshima, and T. Wada, J. Phys. D: Appl. Phys. **19**, 1079 (1986).

[75] K. Danno and T. Kimoto, J. Appl. Phys. **100**, 113728 (2006).

[76] L. Storasta, H. Tsuchida, T. Miyazawa, and T. Ohshima, J. Appl. Phys. **103**, 013705 (2008).

[77] K. Kawahara, G. Alfieri, and T. Kimoto, J. Appl. Phys. **106**, 013719 (2009).

[78] K. Kawahara, M. Krieger, J. Suda, and T. Kimoto, J. Appl. Phys. **108**, 023706 (2010).

Chapter 2

Detection Methods for Deep Levels in Semiconductors

2.1 Introduction

In this chapter, measurement methods to characterize deep levels in semiconductors are explained. To characterize deep levels in semiconductors, the capacitance transient spectroscopy technology has been used. In the capacitance transient spectroscopy, deep levels are detected as carrier traps. For simplicity, measurement methods of deep levels in an n-type semiconductor are described in this chapter.

2.2 Principles of Capacitance Transient Spectroscopy for Majority Carrier Traps

In the capacitance transient spectroscopy, the change of charge state of carrier trap (empty or carrier occupied state) is detected as the change of capacitance. Figure 2.1(a) shows the pulse sequence for detection of electron traps in an n-type semiconductor with a Schottky junction. The band diagrams of the Schottky junction applied a measurement bias voltage U_{R}, which is typically a reverse bias voltage, at a certain temperature in the thermal equilibrium state is shown in Fig. 2.1(b). The electron traps in the neutral region are in electron-occupied state at the certain temperature. On the other hand, the electron traps in the depletion layer are empty state. Then, a filling pulse bias voltage U_{P} which is hold $U_{\mathrm{P}} > U_{\mathrm{R}}$ is applied to the junction to reduce the depletion layer width [Fig. 2.1(c)]. The electron traps in the region changed from the depletion layer to the neutral region by applying U_{P} capture electrons and become in an electron-occupied state. After interruption of the filling pulse bias voltage U_{P} and applying the measurement bias voltage U_{R}, the depletion layer is extended [Fig. 2.1(d)]. Then, the electrons captured into the electron traps which change from empty to the electron-occupied state by applying the filling pulse signal

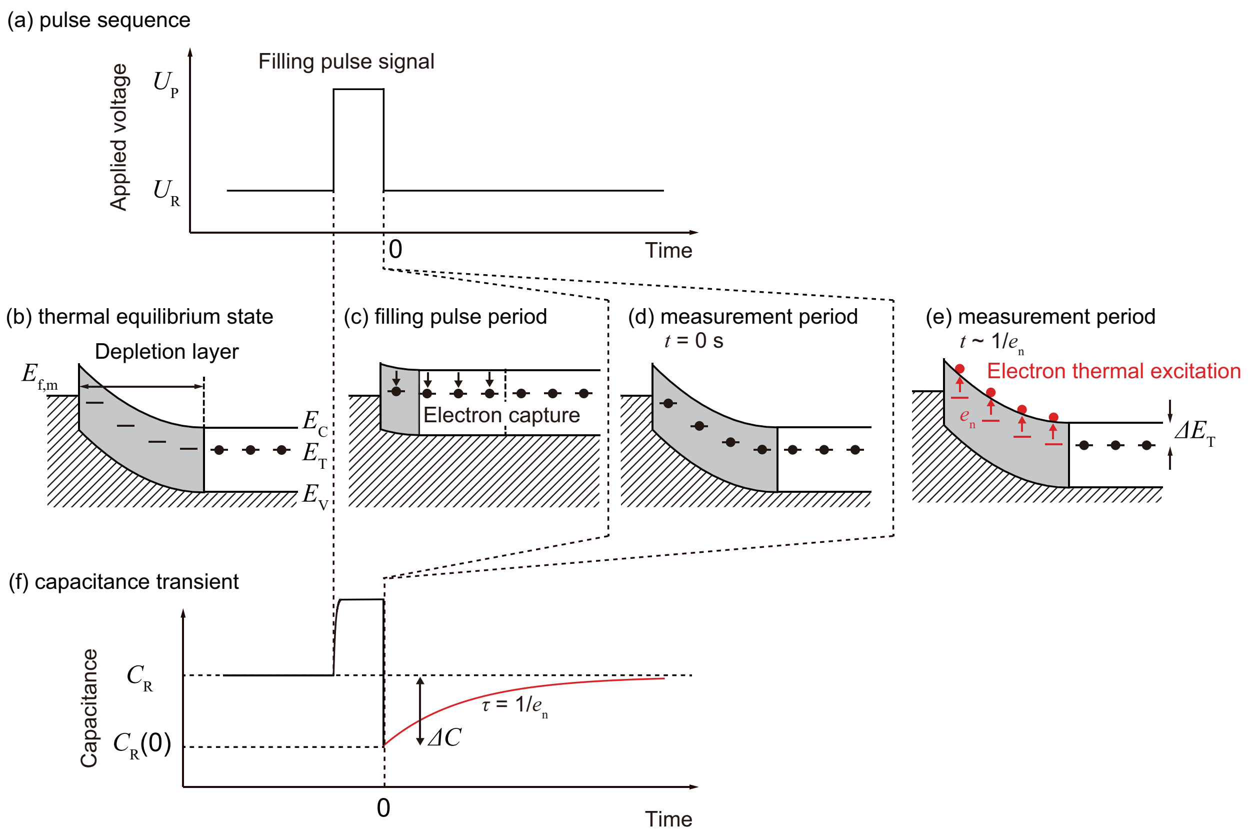

Figure 2.1: Illustration of measurement principle of the capacitance transient spectroscopy for electron traps in n-type material with n-type Schottky barrier diode. (a) pulse sequence. Band diagrams of the Schottky barrier diode (b) during thermal equilibrium state, (c) during filling pulse period, (d) at $t = 0$ s, and (e) during measurement period ($t = 1/e_n$). (f) capacitance transient with the filling pulse signal.

are thermal excited to the C.B. [Fig. 2.1(e)]. For simplicity, here, it is assumed that all electron traps in the depletion layer become the electron-occupied state during the filling pulse period and the captured electron is thermally emitted from each electron trap to the C.B. in the depletion layer. Immediately after the interruption of the filling pulse signal [Fig. 2.1(d)], in the depletion layer, the electron traps are in the electron-occupied state and the net donor density is smaller than that in the thermally equilibrium state at U_{R}. During the measurement period [Fig. 2.1(e)], in the depletion layer, the electron traps return from the electron-occupied state to empty state and the net donor density also return. Here, an acceptor-like type electron trap is assumed. The time evolution of net donor density $N_{\mathrm{d,net}}(t)$, where t is time from application of the measurement bias voltage, is given as:

$$N_{\mathrm{d,net}}(t) = N_{\mathrm{d}} - N_{\mathrm{T}} f_{\mathrm{T}}(t). \tag{2.1}$$

Here, N_{d} is the donor density and N_{T} is the electron trap density. It is assumed that N_{d} and N_{T} have a uniform distribution in the depth direction. $f_{\mathrm{T}}(t)$ is the electron occupancy ratio. Then, the capacitance transient of the junction $C_{\mathrm{R}}(t)$ is given as:

$$\begin{aligned} C_{\mathrm{R}}(t) &= \sqrt{\frac{e\varepsilon_{\mathrm{s}}\varepsilon_0(N_{\mathrm{d}} - N_{\mathrm{T}} f_{\mathrm{T}}(t))}{2(V_{\mathrm{d}} - U_{\mathrm{R}})}} \\ &= C_{\mathrm{R}}\sqrt{1 - \frac{N_{\mathrm{T}} f_{\mathrm{T}}(t)}{N_{\mathrm{d}}}} \\ \text{where,} C_{\mathrm{R}} \equiv C_{\mathrm{R}}(\infty) &= \sqrt{\frac{e\varepsilon_{\mathrm{s}}\varepsilon_0 N_{\mathrm{d}}}{2(V_{\mathrm{d}} - U_{\mathrm{R}})}}. \end{aligned} \tag{2.2}$$

Here, eV_{d} is the diffusion potential. $N_{\mathrm{d}} \gg N_{\mathrm{T}}$ is assumed and an approximation of McLaughlin expansion $\sqrt{1-x} \simeq 1 - x/2$ is applied, Eq. 2.2 can be descried as:

$$C_{\mathrm{R}}(t) \simeq C_{\mathrm{R}}\left(1 - \frac{N_{\mathrm{T}} f_{\mathrm{T}}(t)}{2N_{\mathrm{d}}}\right). \tag{2.3}$$

$C_{\mathrm{R}}(0)$ is smaller than C_{R} because the electron traps in the depletion layer are in the electron-occupied state at $t = 0$ s. As shown in Eq. 2.3, the capacitance transient $C_{\mathrm{R}}(t)$ reflects the time evolution of the electron occupancy ratio. Considering the principle of detailed balance, the processes of electron capture from the C.B. to an electron trap and of electron thermal excitation from the electron trap to the C.B. are not independent of each other. The electron capture rate nC_{n} and electron thermal excitation rate e_{n} satisfy the following differential equation for electron occupancy ratio f_{T}:

$$\frac{\mathrm{d}f_{\mathrm{T}}}{\mathrm{d}t} = -f_{\mathrm{T}} e_{\mathrm{n}} + (1 - f_{\mathrm{T}}) nC_{\mathrm{n}}. \tag{2.4}$$

Here, C_{n} is the electron capture coefficient, which is the product of the thermal velocity of electron $v_{\mathrm{th,n}}$ and the electron capture cross-section σ_{n}. Assuming $f_{\mathrm{T}}(0) = 1$ as the initial condition for the differential equation of Eq. 2.4, i.e., the electron traps in the depletion

layer are in the electron-occupied state at $t = 0$ s, the electron occupancy ratio $f_{\mathrm{T}}(t)$ is given as:

$$f_{\mathrm{T}}(t) = \frac{nC_{\mathrm{n}}}{nC_{\mathrm{n}} + e_{\mathrm{n}}} + \frac{e_{\mathrm{n}}}{nC_{\mathrm{n}} + e_{\mathrm{n}}} \exp\left(-\frac{t}{1/(nC_{\mathrm{n}} + e_{\mathrm{n}})}\right). \tag{2.5}$$

Assuming the electron concentration $n = 0$ cm^{-3} in the depletion layer, Eq. 2.5 can be described as:

$$f_{\mathrm{T}}(t) = \exp\left(-\frac{t}{1/e_{\mathrm{n}}}\right). \tag{2.6}$$

Considering Eqs. 2.3 and 2.6, $C_{\mathrm{R}}(t)$ has the same time constant as the time constant of electron thermal excitation $1/e_{\mathrm{n}}$. In the thermal equilibrium state, i.e., $\mathrm{d}f_{\mathrm{T}}/\mathrm{d}t = 0$ in Eq. 2.4, assuming the Fermi-Dirac distribution function as the electron occupancy ratio f_{T}, e_{n} is given as:

$$e_{\mathrm{n}} = \frac{\sigma_{\mathrm{n}} v_{\mathrm{th,n}} N_{\mathrm{C}}}{g} \exp\left(-\frac{E_{\mathrm{C}} - E_{\mathrm{T}}}{k_{\mathrm{B}} T}\right). \tag{2.7}$$

Here, N_{C} is the effective density of state of C.B, g is the degeneracy, and k_{B} is the Boltzmann constant. When the temperature dependence of the electron capture cross-section σ_{n} can be negligible, the energy level E_{T} and the electron capture cross-section σ_{n} are obtained from the slop and intercept of the Arrhenius plot of e_{n}/T^2, respectively. The energy level E_{T} and the electron capture cross-section σ_{n} are important physical properties of deep levels which act as electron traps. The capacitance change due to electron thermal excitation from electron traps to the C.B. ΔC is given as:

$$\begin{aligned} \Delta C &= C_{\mathrm{R}} - C_{\mathrm{R}}(0) \\ &= \frac{C_{\mathrm{R}} N_{\mathrm{T}}}{2N_{\mathrm{d}}}. \end{aligned} \tag{2.8}$$

Thus, the electron trap density N_{T} is obtained from measurement of ΔC:

$$N_{\mathrm{T}} = 2\frac{\Delta C}{C_{\mathrm{R}}} N_{\mathrm{d}}. \tag{2.9}$$

Note that, in a precise sense, $2\Delta C/C_{\mathrm{R}} \times N_{\mathrm{d}}$ in Eq. 2.9 is not the true electron trap density N_{T} but the averaged electron trap density in the entire depletion layer $\tilde{N}_{\mathrm{T}}$. The details are described in Sec. 2.3. As mentioned above, in the capacitance transient spectroscopy, the energy level E_{T}, the capture cross-section σ, and trap density N_{T} are obtained from measurement of the capacitance transient with application of the filling pulse signal.

Semiconductor materials have some deep levels in the bandgap. To separately detect deep levels in capacitance transients, deep-level transient spectroscopy (DLTS) [1] and isothermal capacitance transient spectroscopy (ICTS) [2] have been widely used. The measurement principle of DLTS and ICTS are explained in Sec. 2.2.1 and Sec. 2.2.2,respectively.

2.2.1 Deep-level Transient Spectroscopy (DLTS)

The principle of deep-level transient spectroscopy (DLTS) [1], which is a very powerful method to separately detect deep levels, is explained in this section.Figure 2.2 shows the illustration of measurement principle of DLTS with a Schottky barrier diode. Here, two deep levels which act electron traps (trap X: $\Delta E_{\mathrm{T,X}} = 0.3$ eV, trap Y: $\Delta E_{\mathrm{T,Y}} = 1$ eV) in an n-type material are assumed. The electron capture cross-sections are set to 1×10^{-16} cm^2 for both trap X and trap Y.

As mentioned in Sec. 2.2, the capacitance transient during measurement period reflects electron thermal excitation from electron traps to the C.B. in the depletion layer. The time constant of electron thermal excitation $1/e_{\mathrm{n}}$ is strongly temperature- and energy-position-dependent as shown in Fig. 2.2(d). In DLTS, capacitance transients in a time window ($T_{\mathrm{w}} = t_{\mathrm{B}} - t_{\mathrm{A}}$) are measured at various temperatures. In Fig. 2.2, the time window T_{w} is set to 200 ms. At temperature where the time constants of electron thermal excitation of trap X and trap Y are sufficiently longer than the time window, i.e., $1/e_{\mathrm{n,X,Y}} \ll t_{\mathrm{B}}$ ($T \sim 150$ K in Fig. 2.2), capacitance is almost constant in the measurement period ($t_{\mathrm{A}} \leqq t < t_{\mathrm{B}}$). Elevating temperature, the time constant of electron thermal excitation $1/e_{\mathrm{n,X,Y}}$ dramatically decreases. At temperature where the time constant of electron thermal excitation of trap Y is sufficiently longer than the time window and that of trap X is almost the same as the time window, i.e., $1/e_{\mathrm{n,Y}} \ll 1/e_{\mathrm{n,X}} \sim t_{\mathrm{B}}$ ($T \sim 300$ K in Fig. 2.2), capacitance transient occurs due to the electron thermal excitation from the trap X to the C.B. At temperature where the time constant of electron thermal excitation of trap Y is sufficiently longer than the time window and that of trap X is sufficiently shorter the time window, i.e., $1/e_{\mathrm{n,Y}} \ll t_{\mathrm{B}} \ll 1/e_{\mathrm{n,X}}$ ($T \sim 400$ K in Fig. 2.2), capacitance is almost constant in the measurement period again. At temperature where the time constant of electron thermal excitation of trap Y is almost the same as the time window, i.e., $1/e_{\mathrm{n,Y}} \sim t_{\mathrm{B}} \ll 1/e_{\mathrm{n,X}}$ ($T \sim 550$ K in Fig. 2.2), capacitance transient occurs due to the electron thermal excitation from the trap Y to the C.B. At temperature where the time constants of electron thermal excitation of trap X and trap Y are sufficiently shorter than the time window, i.e., $t_{\mathrm{B}} \ll 1/e_{\mathrm{n,X,Y}}$ ($T \sim 700$ K in Fig. 2.2), capacitance is almost constant in the measurement period again.

By plotting the temperature on the horizontal axis and the capacitance change ΔC in the time window on the vertical axis, the trap X and trap Y can be represented as separate peaks as shown in Fig. 2.2(c). Each peak intensity is equal to the capacitance change ΔC due to electron thermal excitation from each trap. At a DLTS peak position, which is the temperature where the DLTS signal is equal to the peak intensity, the time window T_{w} reflects the time constant of electron thermal excitation $1/e_{\mathrm{n}}$. Thus, from a DLTS spectrum with a time window, the capacitance change ΔC and time constant of electron thermal excitation at a temperature $1/e_{\mathrm{n}}$ can be obtained for each electron trap.

To extract the electron capture cross-section σ_{n} and trap energy $\Delta E_{\mathrm{T}} = E_{\mathrm{C}} - E_{\mathrm{T}}$ from the electron thermal excitation rate e_{n} in Eq. 2.7, temperature dependence of e_{n} is investigated

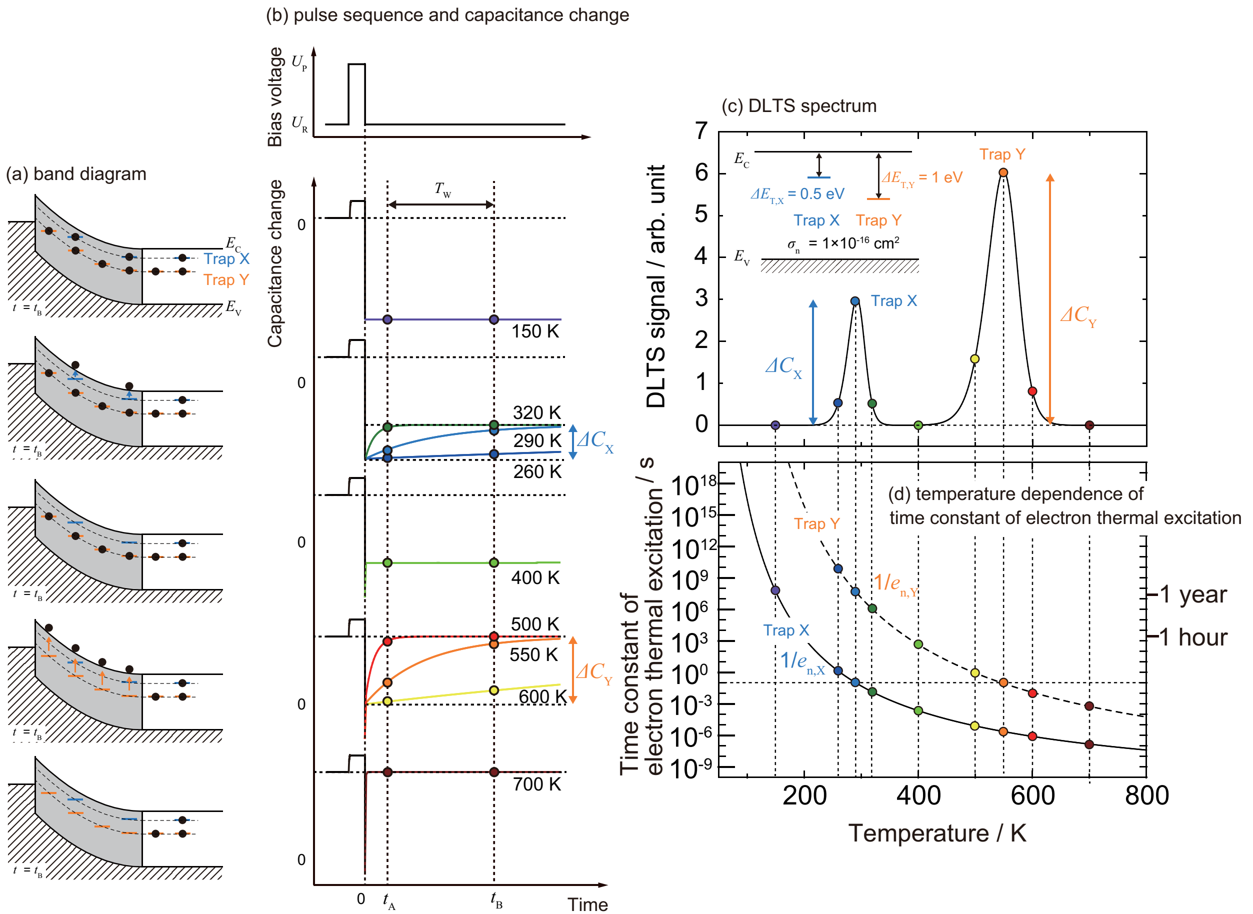

Figure 2.2: Illustration of measurement principle of deep-level transient spectroscopy (DLTS) with n-type Schottky barrier diode. Two electron traps [trap X: $\Delta E_{\mathrm{T,X}} = 0.5$ eV, trap Y: $\Delta E_{\mathrm{T,Y}} = 1$ eV] in n-type material are assumed and how to separately detect the two electron traps is described. The electron capture cross-sections are set to 1×10^{-16} cm^2 for both trap X and trap Y. (a) band diagrams of the Schottky barrier diode under application of measurement bias voltage U_{R} at $t = t_{\mathrm{B}}$. (b) pulse sequence and capacitance change of the Schottky barrier diode with the filling pulse signal. (c) DLTS spectrum for the Schottky barrier diode. (d) temperature dependence of the time constant of electron thermal excitation form electron traps to the C.B.

in DLTS. At a DLTS peak position, the time window reflects the time constant of electron thermal excitation $1/e_{\mathrm{n}}$ and varying the time window, the temperature dependence of e_{n} can be obtained in DLTS. Figure 2.3(a) shows DLTS spectra with the time window T_{w} of 20 ms, 200 ms, and 2 s. From the DLTS peak position, the temperature dependence of $1/e_{\mathrm{n}}$ are obtained as shown in Fig. 2.3(b). Considering Eq. 2.7, the energy level E_{T} and the electron capture cross-section σ_{n} are obtained from the slop and intercept of the Arrhenius plot of e_{n}/T^2, respectively.

2.2.2 Isothermal Capacitance Transient Spectroscopy (ICTS)

Isothermal capacitance transient spectroscopy (ICTS) [2] is the other spectroscopy technology for the capacitance transient. The principles of ICTS is explained in this section. In ICTS measurement, capacitance transients at a certain temperature are measured. Figure 2.4 shows the illustration of measurement principle of ICTS with the Schottky barrier diode as shown in Fig. 2.2. The trap parameters are also the same as assumed for the explanation of the DLTS measurement principle.

At a certain temperature, when the time constants of electron thermal excitation of trap X and trap Y are sufficiently longer than the time window, i.e., $t_{\mathrm{B}} \ll 1/e_{\mathrm{n,X,Y}}$ ($t_{\mathrm{B}} \sim 10^{-4}$ s in Fig. 2.4), capacitance is almost constant in the measurement period ($t_{\mathrm{A}} \leqq t < t_{\mathrm{B}}$). By increasing the width of time window T_{w}, capacitance transients with longer time constant can be measured. When the time constants of electron thermal excitation of trap Y is sufficiently longer than the time window and that of trap X is almost the same as the time window, i.e., $1/e_{\mathrm{n,X}} \sim t_{\mathrm{B}} \ll 1/e_{\mathrm{n,Y}}$ ($t_{\mathrm{B}} \sim 5\times10^{-2}$ s in Fig. 2.4), capacitance transient occurs due to the electron thermal excitation from the trap X to the C.B. When the time constants of electron thermal excitation of trap Y is sufficiently longer than the time window and that of trap X is sufficiently shorter than the time window, i.e., $1/e_{\mathrm{n,X}} \ll t_{\mathrm{B}} \ll 1/e_{\mathrm{n,Y}}$ ($t_{\mathrm{B}} \sim 5$ s in Fig. 2.4), capacitance is almost constant again.

By plotting the time window on the horizontal axis and the capacitance change ΔC in the time window on the vertical axis, the trap X can be represented as a peak as shown in Fig. 2.4(c). Each peak intensity is equal to the capacitance change ΔC due to electron thermal excitation from each trap. At an ICTS peak position, which is the time window T_{w}, reflects the time constant of electron thermal excitation $1/e_{\mathrm{n}}$. Thus, from a ICTS spectrum at a certain temperature, the capacitance change ΔC and time constant of electron thermal excitation at a temperature $1/e_{\mathrm{n}}$ can be obtained for each electron trap.

To extract the electron capture cross-section σ_{n} and trap energy $\Delta E_{\mathrm{T}} = E_{\mathrm{C}} - E_{\mathrm{T}}$ from the electron thermal excitation rate e_{n} in Eq. 2.7, temperature dependence of e_{n} is investigated in ICTS. At a ICTS peak position, the time window reflects the time constant of electron thermal excitation $1/e_{\mathrm{n}}$ and elevating temperature, the temperature dependence of e_{n} can be obtained in ICTS. Figure 2.5(a) shows ICTS spectra at temperature from 250 K to 600 K. From the DLTS peak position, the temperature dependence of $1/e_{\mathrm{n}}$ are obtained

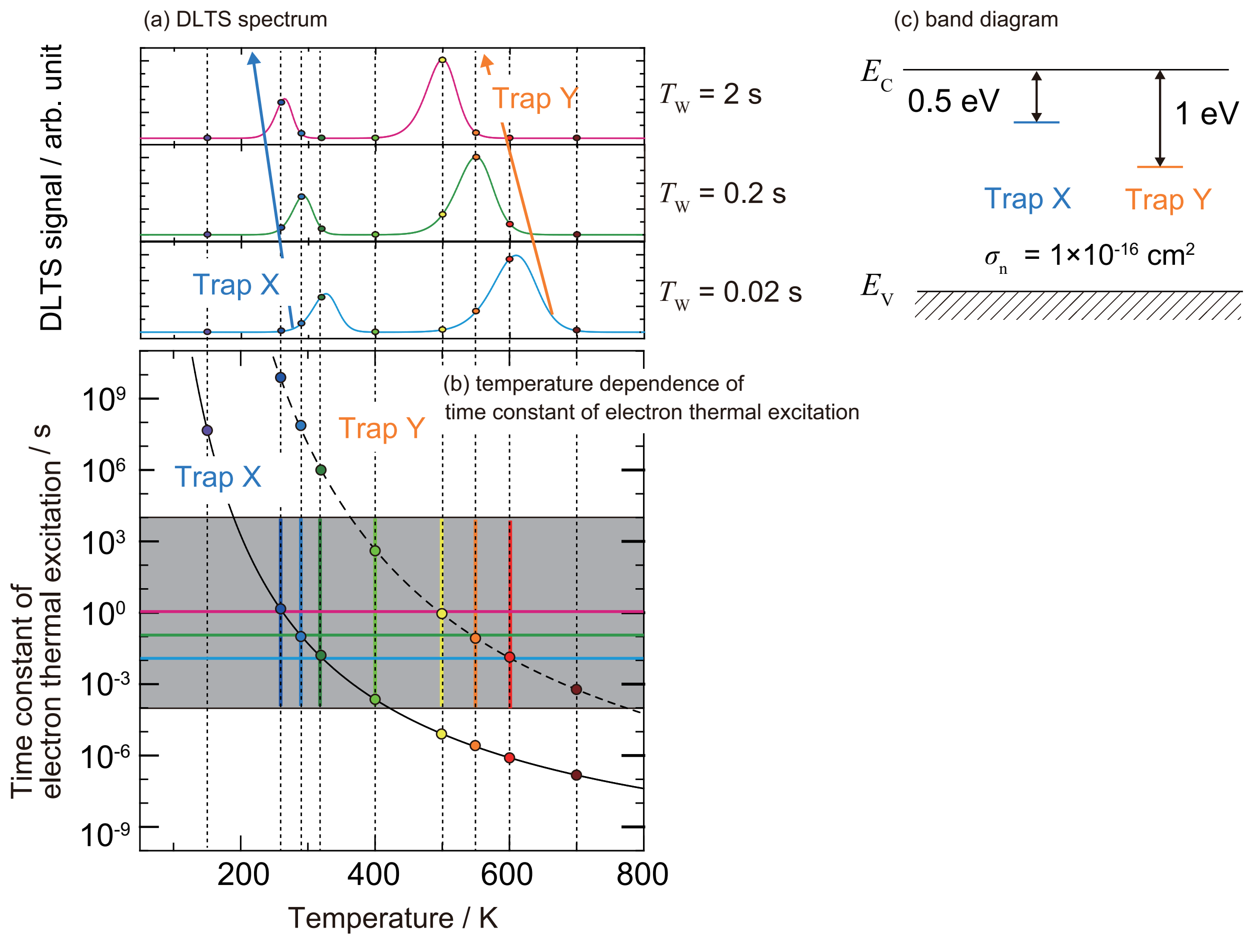

Figure 2.3: Illustration of measurement principle of DLTS with n-type Schottky barrier diode. (a) DLTS spectra for the Schottky barrier diode with the time window of 20 ms, 200 ms, and 2 s. (b) temperature dependence of the time constant of electron thermal excitation form electron traps to the C.B. (c) band diagrams of the assumed two electron traps.

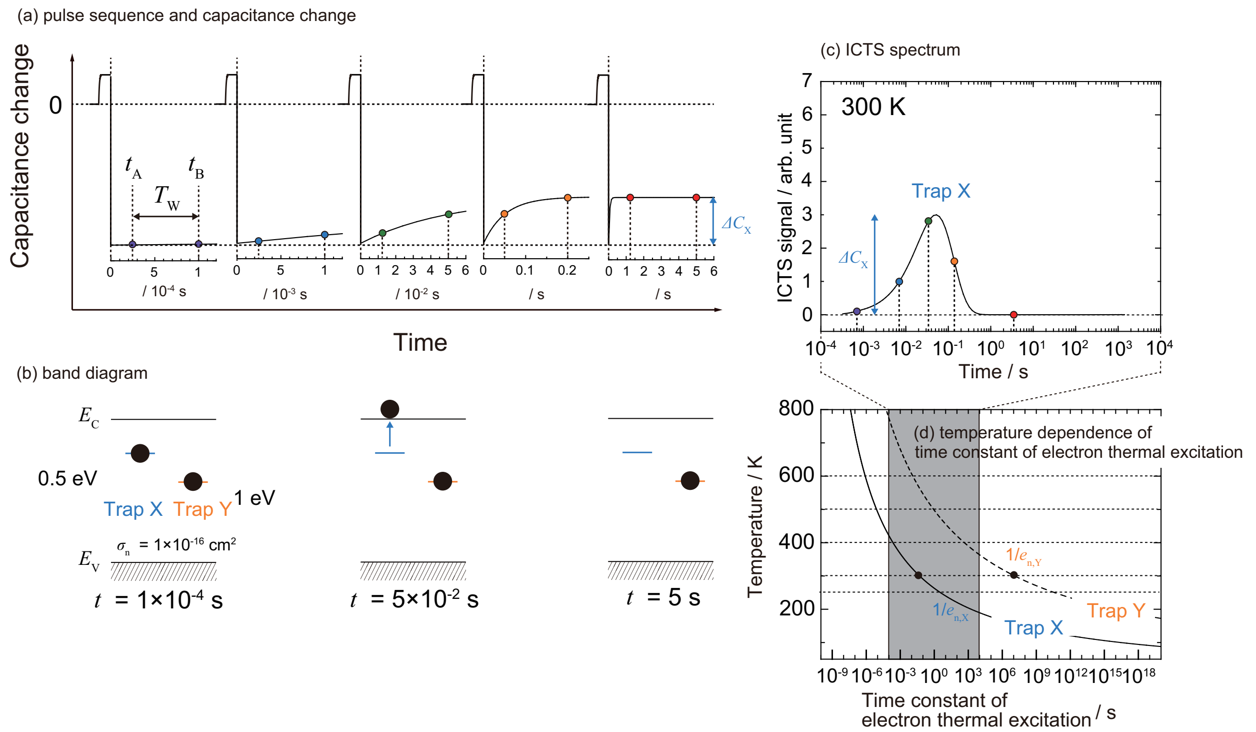

Figure 2.4: Illustration of measurement principle of isothermal capacitance transient spectroscopy (ICTS) with n-type Schottky barrier diode. (a) pulse sequence and capacitance change of the Schottky barrier diode with the filling pulse signal. (b) band diagrams of the assumed two electron traps (c) ICTS spectrum for the Schottky barrier diode. (d) temperature dependence of the time constant of electron thermal excitation form electron traps to the C.B.

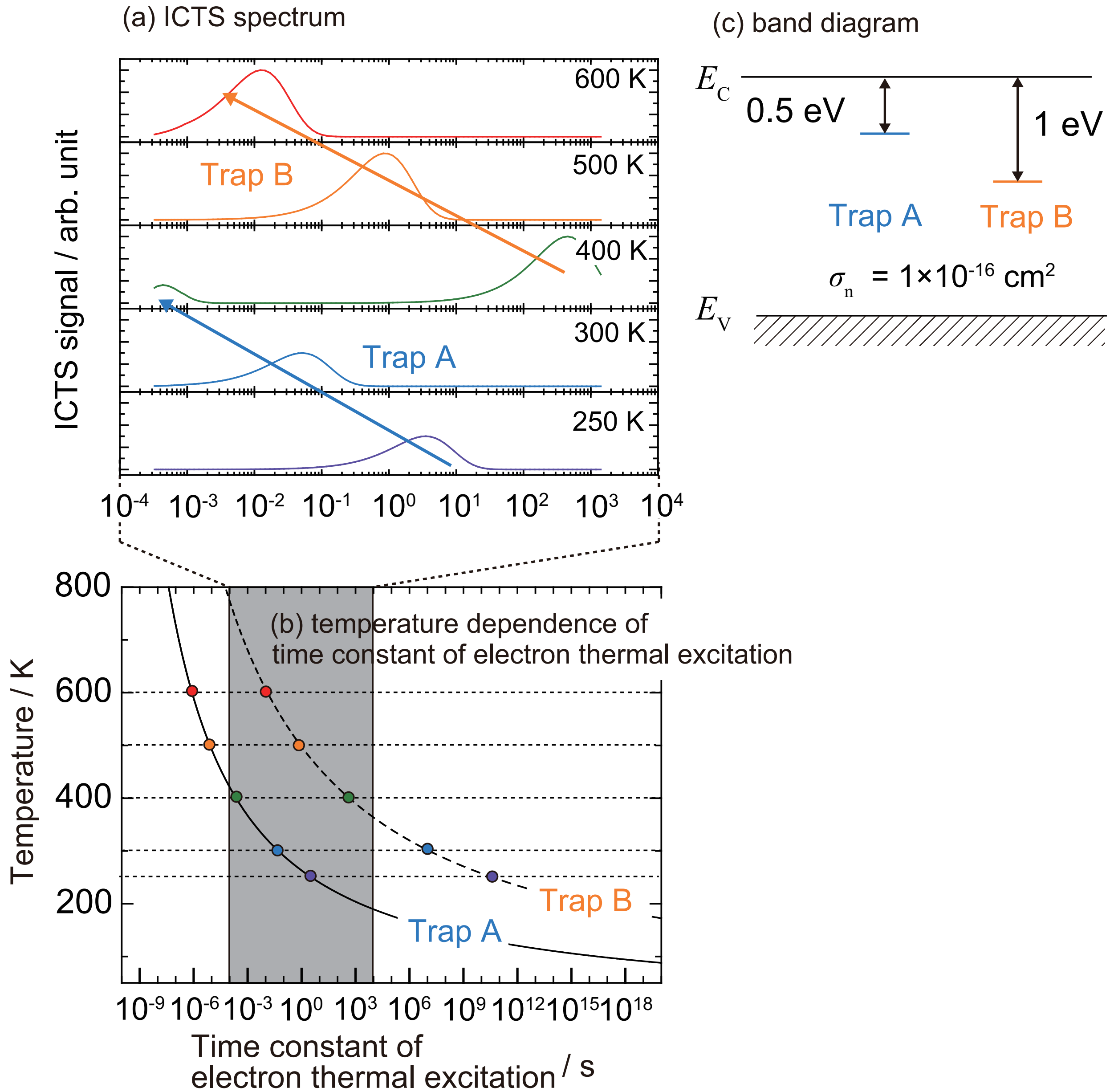

Figure 2.5: Illustration of measurement principle of ICTS with n-type Schottky barrier diode. (a) ICTS spectra for the Schottky barrier diode at temperature from 250 K to 600 K. (b) temperature dependence of the time constant of electron thermal excitation form electron traps to the C.B. (c) band diagrams of the assumed two electron traps.

as shown in Fig. 2.5(b). Considering Eq. 2.7, the energy level E_T and the electron capture cross-section σ_n are obtained from the slop and intercept of the Arrhenius plot of e_n/T^2, respectively.

2.3 Density of Deep Levels in Capacitance Transient Spectroscopy

When an n-type SBD is used to investigate electron traps with DLTS or ICTS measurements, the electron trap density calculated from the DLTS or ICTS peak height ($\tilde{N}_T$) has the following relationship with the depth profile of the actual trap density $N_T(x)$ [3, 4].

$$\begin{aligned}\tilde{N}_{\mathrm{T}} &= 2\frac{\Delta C}{C_{\mathrm{R}}}N_{\mathrm{d,net}} \\ &= \frac{2}{w_{\mathrm{R}}^2}\int_{x_{\mathrm{start}}}^{x_{\mathrm{end}}} xN_{\mathrm{T}}(x)[f(x,0)-f(x,\infty)]\,\mathrm{d}x. \end{aligned} \tag{2.10}$$

$f(x,t)$, where t is time from application of the measurement bias voltage, is the time evolution of the depth profile of the electron occupancy ratio of the electron traps. The electron traps in $x_{\mathrm{start}} < x \leqq x_{\mathrm{end}}$ can be detected. In Eq. 7.1, the following assumptions are typically made: (1) ΔC is small compared with C_R and (2) $N_{\mathrm{d,net}}$ is a function that varies slowly in the range of $x_{\mathrm{start}} < x \leqq x_{\mathrm{end}}$. In this study, the following assumption is also made: (3) each electron trap in $x_{\mathrm{start}} < x \leqq x_{\mathrm{end}}$ emits one electron during the measurement period, which is sufficiently longer than the time constant of electron thermal emission from the electron trap to the conduction band (τ_n), i.e., $f(x,0) = 1$ and $f(x,\infty) = 0$ in $x_{\mathrm{start}} < x \leqq x_{\mathrm{end}}$. $\tilde{N}_T$ obtained from Eq. 7.1 is not equal to the actual trap density N_T and is the averaged trap density in the entire depletion layer when the measurement bias voltage is applied. Considering that electrons in the conduction band are captured by electron traps in the depletion layer under application of the measurement bias voltage, $f(x,t)$ can be approximated as follows [3, 4]:

$$\begin{aligned} f(x,t) &= f(x,0) - \left[f(x,0) - \frac{n(x,w)\sigma_{\mathrm{n}}v_{\mathrm{th,n}}}{e_{\mathrm{n}}+n(x,w)\sigma_{\mathrm{n}}v_{\mathrm{th,n}}}\right]\left(1-\exp\left[-\frac{t}{1/(e_{\mathrm{n}}+n(x,w)\sigma_{\mathrm{n}}v_{\mathrm{th,n}})}\right]\right) \\ &\backsimeq \begin{cases} \exp\left(-\frac{t}{1/e_{\mathrm{n}}}\right) & , x_{\mathrm{start}} < x \leqq w-\lambda \\ 1 & , w-\lambda < x \leqq w. \end{cases} \end{aligned} \tag{2.11}$$

Here, $e_n = 1/\tau_n$ is the thermal emission rate of electrons from the electron traps to the conduction band, w is the depletion layer width, and $v_{\mathrm{th,n}}$ is the electron thermal velocity. $n(x,w)$ is the free carrier concentration, assuming that [4, 5]:

$$n(x) = \begin{cases} N_{\mathrm{d,net}}(w)\exp\left(-\frac{(w-x)^2}{2L_{\mathrm{D}}(w)^2}\right) & , 0 < x \leqq w \\ N_{\mathrm{d,net}}(x) & , w \leqq x. \end{cases} \tag{2.12}$$

Here, $L_{\rm D}(w) = \sqrt{(\varepsilon_{\rm s} k_{\rm B} T)/(n(w,w)e^2)}$ is the Debye length, $\varepsilon_{\rm s}$ is the static permittivity and the static permittivity of 4H-SiC in the direction parallel to the c axis $\varepsilon_{\rm s}^{||} = 10.3\varepsilon_0$, where ε_0 is the vacuum permittivity. $k_{\rm B}$ is the Boltzmann constant. In Eq. 2.12, it is assumed that the donor is completely ionized. In Eq. 6.4, $w - \lambda$ is the depth where the trap energy level crosses the bulk Fermi level, i.e., the trap energy level in the depletion layer of $w - \lambda < x \leqq w$ is below the Fermi level in the neutral region, and $f(w - \lambda, \infty) = 0.5$. λ is given as [5]:

$$\lambda(w) = L_{\rm D}(w)\sqrt{2\ln\left(\frac{N_{\rm d,net}(w)\sigma_{\rm n} v_{\rm th,n}}{e_{\rm n}}\right)}. \tag{2.13}$$

In $w_{\rm R} - \lambda(w_{\rm R}) < x \leqq w_{\rm R}$, the electron traps emit very few electrons because the trap energy level is located below the quasi-Fermi level. This phenomenon is called the lambda effect [4–8]. It is noted that the magnitude of the lambda effect depends on $e_{\rm n}^{\rm t}$ and $\sigma_{\rm n}$ of the electron trap and n, which is assumed to be equal to $N_{\rm d,net}$ in this study. In this study, $\lambda(w_{\rm P})$ and $\lambda(w_{\rm R})$ are considered to be equal [$\lambda = \lambda(w_{\rm P}) = \lambda(w_{\rm R})$]. Considering the lambda effect, Eq. 7.1 can be approximated as:

$$\begin{aligned}\tilde{N}_{\rm T} &= 2\frac{\Delta C}{C_{\rm R}} N_{\rm d,net} \\ &= \frac{2}{w_{\rm R}^2}\int_{x_{\rm start}}^{x_{\rm end}} x N_{\rm T}(x)\,{\rm d}x.\end{aligned} \tag{2.14}$$

In $0 < x \leqq x_{\rm start}$, the electron traps do not capture electrons during the filling pulse period and the electron traps can not be detected during the measurement period. When the lambda effect during the filling pulse period is considered, $x_{\rm start}$ is given as:

$$x_{\rm start} = \begin{cases} 0 & , 0 < w_{\rm P} \leqq \lambda(w_{\rm P}) \\ w_{\rm P} - \lambda(w_{\rm P}) & , \lambda(w_{\rm P}) < w_{\rm P}. \end{cases} \tag{2.15}$$

When the depth profile of an electron trap density has a constant distribution, i.e., $N_{\rm T}(x) = N_{\rm T}$, the dependence of the averaged trap density on the depletion layer width $\tilde{N}_{\rm T}(w_{\rm R})$ is influenced by the lambda effect. $\tilde{N}_{\rm T}(w_{\rm R})$ calculated from Eq. 2.14 using $N_{\rm T}(x) = N_{\rm T}$ is shown in Fig. 2.6(a). Here, the two depletion layer widths, the small depletion layer $w_{\rm R1}$ and the large depletion layer $w_{\rm R2}$, are considered to explain the lambda effect on $\tilde{N}_{\rm T}(w_{\rm R})$. Figure 2.6(b) and Fig. 2.6(c) show band diagrams of an SBD with an assumed depth profile of trap density during the filling pulse period (upper side) and the measurement period (lower side) with $U_{\rm R}$ of $U_{\rm R1}$ and $U_{\rm R2}$ ($U_{\rm P} > U_{\rm R1} > U_{\rm R2}$), respectively. The depletion layer widths during the measurement period with $U_{\rm R1}$ and $U_{\rm R2}$ are set to $w_{\rm R1}$ and $w_{\rm R2}$, respectively. For simplicity, $x_{\rm start}$ is set to $w_{\rm P} - \lambda$ in Fig. 2.6. Figure 2.6(b) shows that when the depletion layer width is small, the width of the no-electron-capture region and the width of the no-electron-emission region, where the electron traps can not be detected by capacitance transient spectroscopy, can not be negligible with respect to the width of the detection region. Therefore, the averaged trap density $\tilde{N}_{\rm T}$ is strongly underestimated compared to the true trap density $N_{\rm T}$. On the other hand, as shown in Fig. 2.6(c), when the

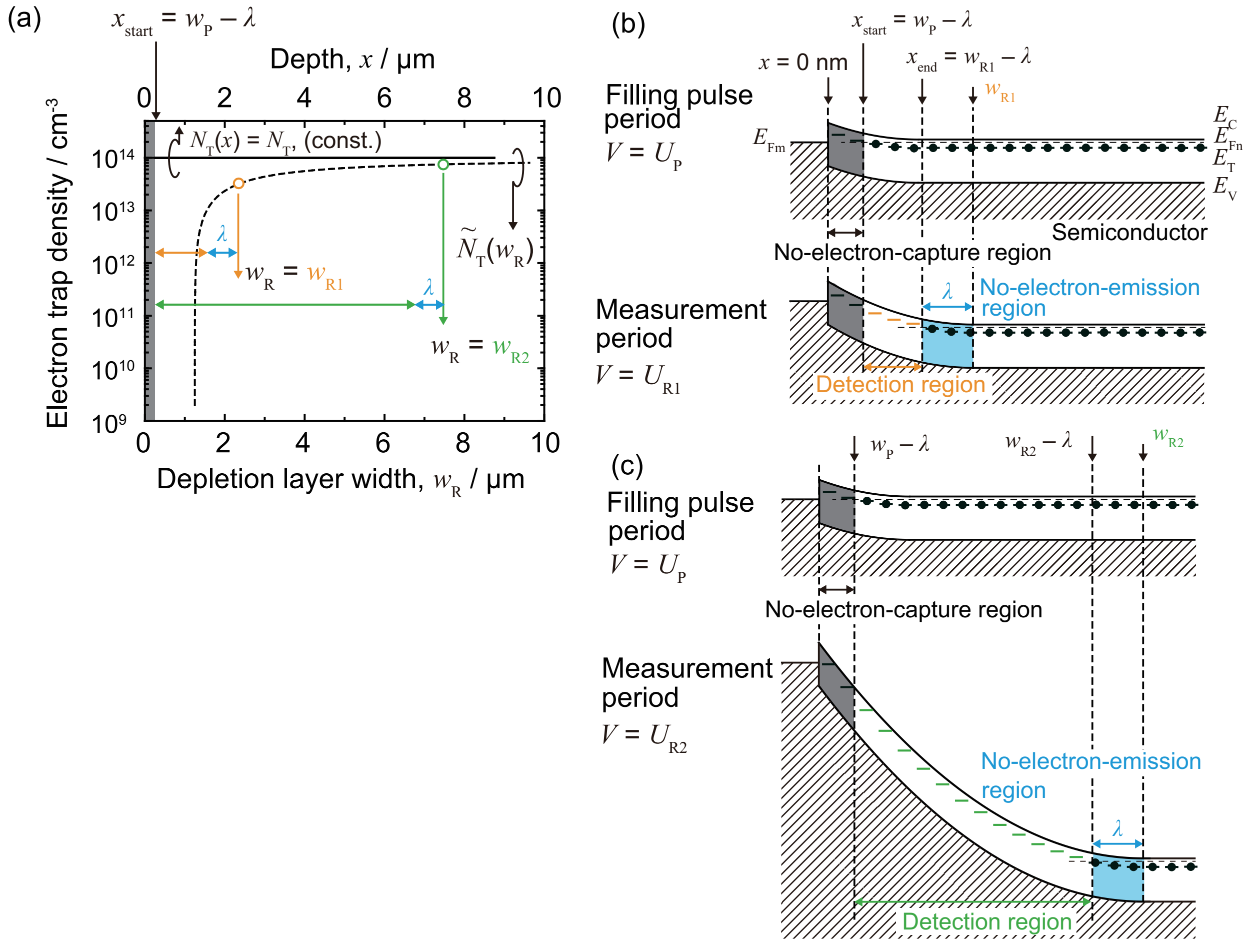

Figure 2.6: Representative example for the lambda effect. (a) Constant depth profile of an electron trap density [$N_\mathrm{T}(x) = N_\mathrm{T}$; black solid line] and the dependence of the averaged trap density on the depletion layer width calculated from Eq. 2.14 [$\tilde{N}_\mathrm{T}(w_\mathrm{R})$; black broken line].

depletion layer width is large, the width of the no-electron-capture region and the width of the no-electron-emission region can be negligible with respect to the width of the detection region. Therefore, the lambda effect can be negligible in the averaged trap density $\tilde{N}_{\rm T}$. $\tilde{N}_{\rm T}(w_{\rm R})$, where the trap density is constant in the depth direction, increases with increasing $w_{\rm R}$ and $\tilde{N}_{\rm T}(w_{\rm R})$ is asymptotic to $N_{\rm T}$ as shown in Fig. 2.6(a).

It is typically assumed that carrier traps are uniformly distributed in as-grown materials [6, 9] or that the carrier trap density is constant in the detection region ($w_{\rm P}-\lambda < x \leqq w_{\rm R}-\lambda$) in the case of carrier traps generated during device processes or electron irradiation [10–14].

2.4 Principles of Capacitance Transient Spectroscopy for Minority Carrier Traps

In Sec. 2.2, detection methods for majority carrier traps are explained. In the capacitance transient spectroscopy, to detect carrier traps, the state of the carrier traps should change from empty state to carrier-occupied state by application of filling pulse signal In the methods DLTS and ICTS for detection of majority carrier traps, electrical pulse, which makes the depletion layer width small, is used as the filling pulse signal.

On the other hand, for detection of minority carrier trap, it is necessary minority carriers which have extremely low concentration in a semiconductor material in thermal equilibrium to occupy minority carrier traps. As methods for detection of minority carrier traps, current-injection method [1, 4, 15–18], above-$E_{\rm g}$-light-illumination method [18–22], and sub-$E_{\rm g}$-light-excited method [4, 22–25] have been used. For simplicity, measurement methods of hole traps in an n-type semiconductor are described. Figure 2.7 shows schematic cross-sections of devices in MCTS: (a) current-injection method, (b) above-$E_{\rm g}$-light-illumination method, and (c) sub-$E_{\rm g}$-light-excited method.

- **current-injection method:** In current-injection method, a p$^+$-n junction is used and a current pulse is used as the filling pulse signal. By applying a forward bias voltage to the p$^+$-n junction, holes are injected from the p$^+$-type layer to the n-type layer. The injected holes are captured in hole traps in n-type layer and the hole traps become in the hole-occupied state.

- **above-$E_{\rm g}$-light-illumination method:** In above-$E_{\rm g}$-light-illumination method, a p$^+$-n junction or n-type Schottky junction is used and an above-$E_{\rm g}$-light pulse is used as the filling pulse signal. By illumination of above-$E_{\rm g}$-light to the device surface, electron-hole pairs are generated near the surface around the junction. The generated holes drift into the depletion layer and are captured in hole traps in n-type layer.

- **sub-$E_{\rm g}$-light-excited method:**] In sub-$E_{\rm g}$-light-excited method, a p$^+$-n junction or n-type Schottky junction is used and a sub-$E_{\rm g}$-light pulse is used as the filling pulse signal. When sub-$E_{\rm g}$-light is illuminated to the device surface, holes are photoexcited

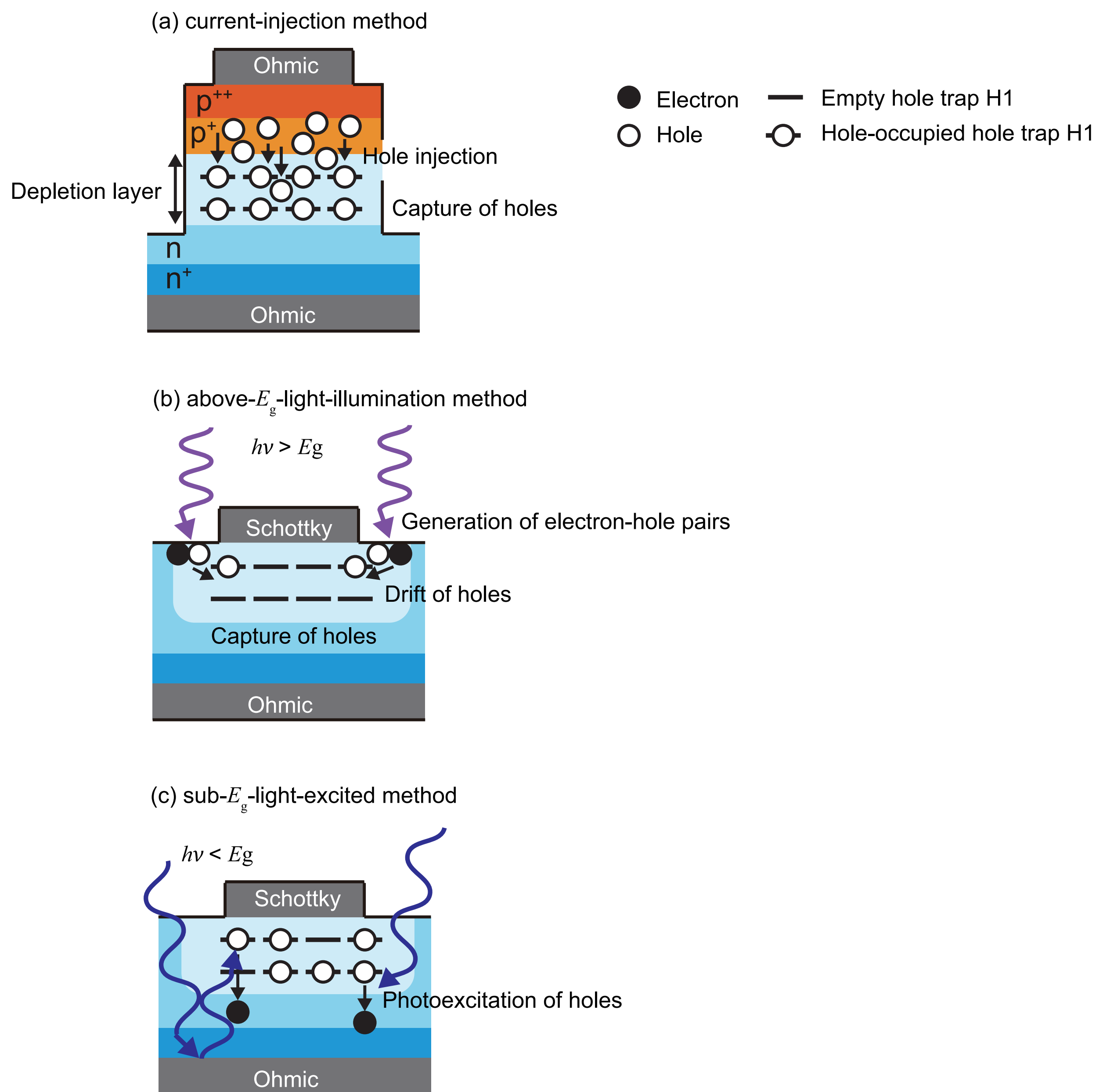

Figure 2.7: Schematic cross-sections of devices in (a) current-injection method, (b) above-E_g-light-illumination method, and (c) sub-E_g-light-excited method for an n-type semiconductor.

from the C.B. to hole traps due to the light which penetrates into the n-type layer. Then, the hole traps become in the hole-occupied state.

These methods are collectively called minority carrier transient spectroscopy (MCTS). The way to separately detection of minority carrier traps are the same in that of majority carrier traps, i.e., temperature scan (DLTS) or time scan (ICTS). The minority carrier occupancy ratio of minority carrier traps is strongly temperature-dependent (Chapter 5). Thus, ICTS is more suitable than DLTS for characterization of minority carrier traps.

References

[1] D. V. Lang, J. Appl. Phys. **45**, 3023 (1974).

[2] H. Okushi1 and Y. Tokumaru, Jpn. J. Appl. Phys. **20**, 261 (1981).

[3] D. Pons and S. Makram-Ebeid, J. de Physique **40**, 1161 (1979).

[4] G. M. Martin, A. Mitonneau, D. Pons, A. Mircea, and D. W. Woodard, J. Phys. C: Solid St. Physics **13**, 3855 (1980).

[5] S. D. Brotherton, Solid-State Electronics **26**, 987 (1983).

[6] R. R. Senechal and J. Basinski, J. Appl. Phys. **39**, 4581 (1968).

[7] Y. Zohta and M. O. Watanabe, J. Appl. Phys. **53**, 1809 (1982).

[8] C. T. Sah and V. G. K. Reddi, IEEE Trans. Electron Device **11**, 345 (1964).

[9] K. Kanegae, M. Horita, T. Kimoto, and J. Suda, Appl. Phys. Express **11**, 071002 (2018).

[10] K. Kawahara, G. Alfieri, and T. Kimoto, J. Appl. Phys. **106**, 013719 (2009).

[11] A. Usami, Y. Tokuda, M. Katayama, S. Kaneshima, and T. Wada, J. Phys. D: Appl. Phys. **19**, 1079 (1986).

[12] K. Danno and T. Kimoto, J. Appl. Phys. **100**, 113728 (2006).

[13] L. Storasta, H. Tsuchida, T. Miyazawa, and T. Ohshima, J. Appl. Phys. **103**, 013705 (2008).

[14] K. Kawahara, M. Krieger, J. Suda, and T. Kimoto, J. Appl. Phys. **108**, 023706 (2010).

[15] K. L. Wang and A. O. Evwaraye, J. Appl. Phys. **47**, 4574 (1976).

[16] D. L. Partin, J. W. Chen, A. G. Milnes, and L. F. Vassamillet, J. Appl. Phys. **50**, 6845 (1979).

[17] D. V. Lang, R. L. Hartman, and N. E. Schumaker, J. Appl. Phys. **47**, 4986 (1976).

[18] T. Tanaka, K. Shiojima, T. Mishima, and Y. Tokuda, Jpn. J. Appl. Phys. **55**, 061101 (2016).

[19] I. D. Henning and H. Thomas, J. Electronie Materials **10**, 361 (1980).

[20] C. Hurtes, M. Boulou, A. Mitonneau, and D. Bois, Appl. Phys. Lett. **32**, 821 (1978).

[21] T. Okuda, G. Alfieri, T. Kimoto, and J. Suda, Appl. Phys. Express **8**, 111301 (2015).

[22] Y. Tokuda, ECS Transactions **75**, 39 (2016).

[23] B. Balland, G. Vincent, and D. Bois, J. Appl. Phys. **34**, 108 (1979).

[24] A. Mitonneau, A. Mircea, G. M. Martin, and D. Pons, Revue de Physique Appliquée, Société française de physique / EDP **14**, 853 (1979).

[25] M. Takikawa and T. Ikoma, Jpn. J. Appl. Phys. **19**, L436 (1980).

Chapter 3

Measurement Method for Density of Hole Trap H1 in n-Type GaN with p^+-n Junction

3.1 Introduction

In this chapter, the author proposes a method to accurate qualify densities of the hole trap H1 in n-type GaN layers with p^+-n junction. In current-injection ICTS, a forward bias voltage is applied to the p^+-n junction as a filling pulse. Hole traps in n-type GaN layers capture the injected holes, and then a measurement bias voltage (reverse bias voltage) is applied to measure the capacitance transient due to the hole thermal excitation from the traps to the V.B.

The spatial distribution of the injected hole concentration corresponds to the exponential decay with diffusion length (L_{diff}) [1]. Only a limited region of the hole traps becomes in hole-occupied state; thus, a small reverse bias voltage is typically utilized as the measurement bias voltage to keep the depletion layer width within the occupied region. Previous studies on hole trap H1 in n-type GaN have typically used such a measurement condition; however, systematic data have not been discussed. In this study, the reverse bias voltage dependence of the current-injected ICTS spectra is presented and the limited occupation region is clearly shown.

The author also considers another effect: the quick carrier recombination via hole traps near the depletion layer edge immediately after the application of a reverse bias. As a result of the quick recombination, hole traps near the depletion layer edge are already empty and do not contribute to the peak in the current-injection ICTS spectrum; thus, the density of hole traps calculated from ICTS peak intensities $\tilde{N}_{\mathrm{T}}$ can be underestimated. This effect is significant when the hole thermal excitation from a hole trap is slow.

The dependence of the measured density of hole trap H1 $\tilde{N}_{\mathrm{T}}$ on the depletion layer width w_{R} is investigated. Considering the effects of distribution of injected hole concentration in

n-type GaN layers (effect A) and the quick carrier recombination via hole traps near the depletion layer edge immediately after the application of a reverse bias (effect B) on $\tilde{N}_{\mathrm{T}}(w_{\mathrm{R}})$, the true density of hole trap H1 N_{T} is extracted.

3.2 Experiments

The sample used in this study was a GaN on GaN mesa p^+-n diode (PND). The PND comprised a MOVPE-grown 0.1-μm-thick p^{++}-GaN/0.5-μm-thick p^+-GaN/5-μm-thick n-GaN structure on an HVPE-grown n^+-type GaN substrate. The Mg concentrations of the p^{++}- and p^+-type GaN were obtained via secondary ion mass spectrometry (SIMS) as 1×10^{20} cm^{-3} and 5×10^{19} cm^{-3}, respectively. The Si and C concentrations of the n-type GaN were obtained via SIMS as 3×10^{16} cm^{-3} and 3×10^{15} cm^{-3}, respectively. The net donor density was obtained via capacitance-voltage ($C-V$) measurement as $N_{\mathrm{d,net}} = 2.3\times10^{16}$ cm^{-3}. The author also confirmed the uniform distribution of $N_{\mathrm{d,net}}$ via $C-V$ depth profiling. The mesa structure was formed via inductively coupled plasma reactive ion etching. The height and diameter of the mesa were 1 and 520 μm, respectively. The anode and cathode electrodes were formed via deposition of Ni/Au on the top and Ti/Al/Ni on the back side, respectively. Current-injection ICTS was performed at temperatures ranging from 300 K to 370 K. The forward bias voltage and the pulse width of the filling pulse were fixed to $U_{\mathrm{P}} = 3.5$ V and $t_{\mathrm{P}} = 100$ ms, respectively. U_{R} was varied from 1 V to -50 V.

3.3 Current-injection ICTS for p^+-n Junction

Figure 3.1 shows the current-injection ICTS spectrum with $U_{\mathrm{R}} = -5$ V at 300 K. One positive peak and one negative peak correspond to a majority carrier trap (electron trap) and a minority carrier trap (hole trap), respectively. The electron trap E3 ($E_{\mathrm{T}} = E_{\mathrm{C}} - 0.62$ eV, $\sigma_{\mathrm{n}} = 3\times10^{-14}$ cm^2) and hole trap H1 ($E_{\mathrm{T}} = E_{\mathrm{V}} + 0.85$ eV, $\sigma_{\mathrm{p}} = 5\times10^{-15}$ cm^2) in the n-type GaN layer are observed. The energy levels E_{T} and capture cross-sections σ indicated by the Arrhenius plot of $\ln(\tau T^2)$ versus reciprocal temperature shown in Fig. 3.2 agree well with the reported values for the electron trap E3 and hole trap H1 [2].

3.4 Depletion Layer Edge Correction Factor on Measured Density of Hole Trap H1 in Current-injection ICTS

Current-injection ICTS with various reverse bias voltages was performed. According to the peak intensities of the electron trap E3 and hole trap H1 in the ICTS spectra obtained with different U_{R} values ranging from 1 V to -50 V at 300 K, the values of the averaged density

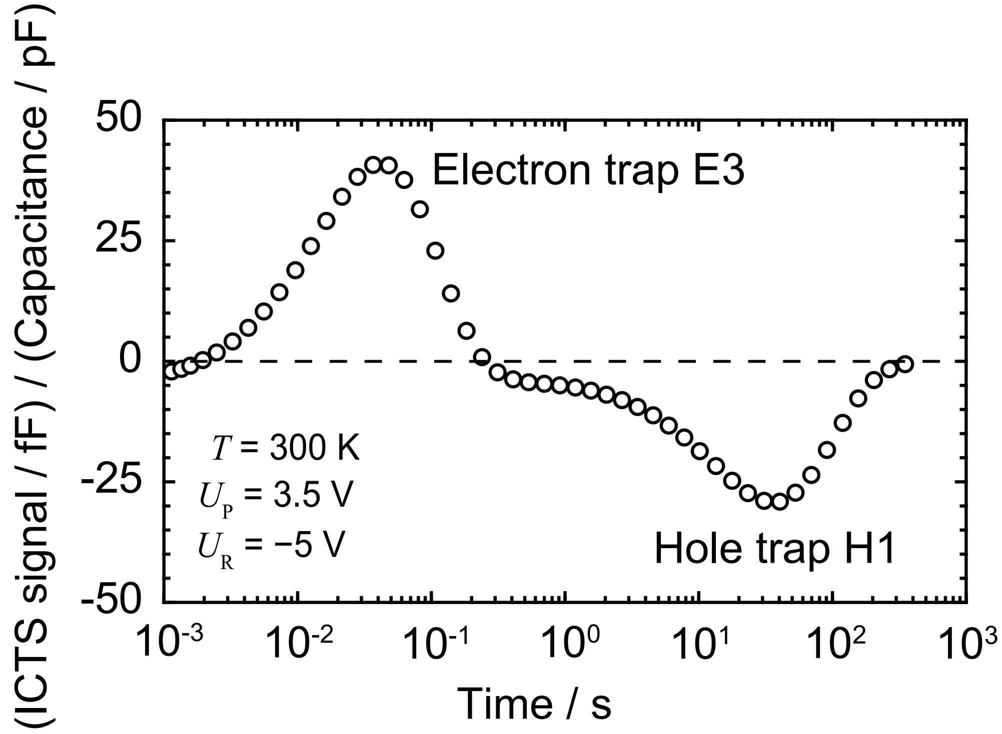

Figure 3.1: Current injection ICTS spectrum for GaN PND at 300 K. The forward bias voltage and pulse width of the filling pulse were $U_{\mathrm{P}} = 3.5$ V and $t_{\mathrm{P}} = 100$ ms, respectively. The measurement bias voltage was $U_{\mathrm{R}} = -5$ V. The electron trap E3 (positive peak) and hole trap H1 (negative peak) are investigated.

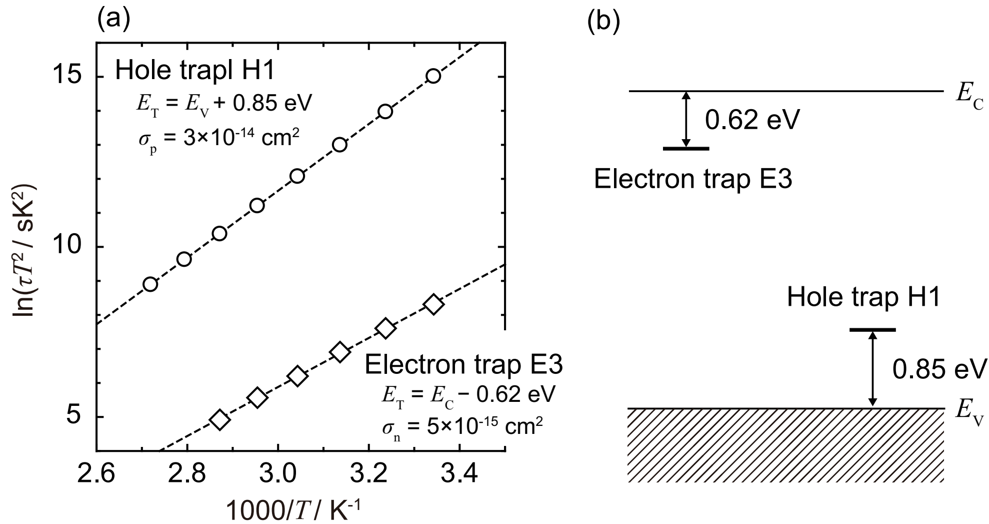

Figure 3.2: Arrhenius plots of $\ln(\tau T^2)$ versus reciprocal temperature obtained from current-injection ICTS with various temperature for the electron trap E3 (open diamonds) and hole trap H1 (open circles).

of trap $\tilde{N}_\mathrm{T}$ were determined as:

$$\tilde{N}_\mathrm{T} = 2\frac{\Delta C}{C_\mathrm{R}}N_\mathrm{d,net}, \tag{3.1}$$

The author confirmed that $\tilde{N}_\mathrm{T}/N_\mathrm{d,net}$ was small enough for applying Eq. (3.1). The results are shown in Fig. 3.3(a) and Fig. 3.3(b), where the horizontal axis indicates the steady-state depletion width at each U_R.

Although the n-type GaN layer was uniformly doped, $\tilde{N}_T$ of the electron trap E3 increased with the depletion width (w), as shown in Fig. 3.3(a). The dependence of $\tilde{N}_T$ on the depletion width is explained by the lambda effect. The lambda effect can be corrected as follows [3]. When U_R is applied, the electron trap E3 near the edge of the depletion layer do not emit electrons. The width of the non-emission region (λ) is determined as the width where the energy level is below the Fermi level in the neutral region of the depletion layer:

$$\begin{aligned} \lambda &= \sqrt{\frac{2\varepsilon_\mathrm{s}\left(E_\mathrm{F}-E_\mathrm{T}\right)}{e^2N_\mathrm{d,net}}} \\ &= L_\mathrm{D}\sqrt{2\ln\left(\frac{N_\mathrm{d,net}C_\mathrm{n}}{e_\mathrm{n}}\right)}. \end{aligned} \tag{3.2}$$

Here, ε_s is the dielectric constant of GaN ($\varepsilon_\mathrm{s} = 10.4\varepsilon_0$ [4], where ε_0 is the vacuum dielectric constant), E_F is the Fermi level, e is an elementary charge, $L_\mathrm{D} = \sqrt{\varepsilon_\mathrm{s}k_\mathrm{B}T/ne^2}$ (where k_B is the Boltzmann constant, T is the temperature, and n is the free carrier concentration, assuming that $n = N_\mathrm{d,net}$) is the Debye length, e_n is the thermal emission rate of electrons from electron traps to the conduction band, and C_n is the capture coefficient of electrons. C_n is given by the product of the electron thermal velocity ($v_\mathrm{th,n}$) and the electron capture cross section (σ_n): $C_\mathrm{n} = v_\mathrm{th,n}\sigma_\mathrm{n}$. Considering the lambda length, $\tilde{N}_\mathrm{T}$ of the electron trap E3 is given as:

$$\tilde{N}_\mathrm{T} = N_\mathrm{T}\left(1-\frac{\lambda}{w}\right)^2. \tag{3.3}$$

Here, N_T is the true density of the electron trap E3. The curve obtained by fitting Eq. (3.3) to the experimental results indicated by the dashed line in Fig. 3.3(a). According to the fitting curve, $\lambda = 207$ nm and $N_\mathrm{T} = 4.3\times\ 10^{15}$ cm^{-3} were obtained for the electron trap E3 in the n-type GaN layer. From the energy level of the electron trap E3, λ was calculated to be 173 nm. The good agreement indicates the uniform distribution of the electron trap E3 in the n-type GaN epitaxial layer.

Next, the hole trap H1 is discussed. Figure 3.3(b) shows the w dependence of the averaged density of hole trap H1 ($\tilde{N}_\mathrm{T}$) at 300 K. As shown, with the increasing depletion layer width, $\tilde{N}_\mathrm{T}$ increases up to a width of 700 nm and decreases thereafter.

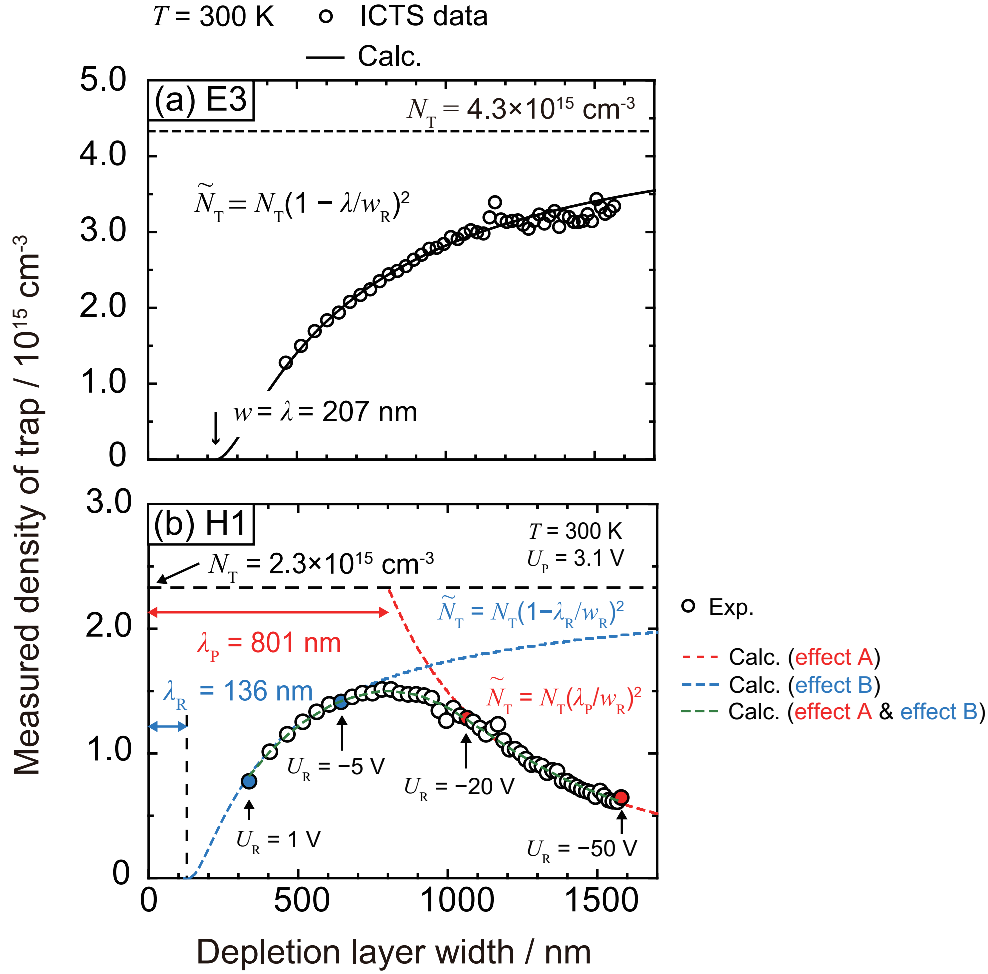

Figure 3.3: (a) Dependence of the measured density of electron trap E3 on the depletion layer width, which is varied by changing the measurement bias voltage. The black solid line indicates the fitting curve obtained using Eq. (3.3). (b) Dependence of the measured density of hole trap H1 on the depletion layer width, which is varied by changing the measurement bias voltage. The green broken lien denotes the fitting curve under a concentration of the true hole occupancy ratio at $t = 1/e^{t}$ shown in Fig. 3.5(d). The red and blue broken lines indicate the calculation curves obtained using Eqs. (3.6) and (3.10), respectively.

3.4.1 Diffusion of Holes into n-Type GaN

The decrease of $\tilde{N}_\mathrm{T}$ for large w (> 700 nm) is explained by the spatial distribution of the hole occupancy ratio during the filling period. Here, x is defined as the distance from the p$^+$-n junction. Figure 3.4(a) shows the calculated spatial distributions of the electron concentration [$n(x)$] and hole concentration [$p(x)$] when the filling pulse is applied at 300 K. A bias voltage of 3.1 V was used in this calculation, as the applied voltage (U_P = 3.5 V) was reduced by the series resistance. Figure 3.4(b) shows the spatial distribution of the electron capture rate [$n(x)C_\mathrm{n}$] and that of the hole capture rate [$p(x)C_\mathrm{p}$]. The thermal emission rate of holes from deep levels near the valence band maximum to the valence band (e^t) is also shown in Fig. 3.4(b). As with the electrons, the capture coefficient of holes (C_p) is given by the product of the thermal velocity of the holes ($v_\mathrm{th,p}$) and the capture cross section of the holes (σ_p): $C_\mathrm{p} = \sigma_\mathrm{p} v_\mathrm{th,p}$. The hole occupancy ratio of deep levels near the valence band maximum [$f_\mathrm{T}(x,t)$] in the steady state of the filling pulse period, i.e., the initial state of the measurement period ($t = 0$ s), is given by:

$$f_\mathrm{T}(x,0) = \frac{p(x)C_\mathrm{p}}{e_p + p(x)C_\mathrm{p} + n(x)C_\mathrm{n}}. \tag{3.4}$$

as plotted in Fig. 3.4(c). The position at which $f_\mathrm{T}(x,0)$ becomes half of the value at the p$^+$-n junction is defined as:

$$\lambda_\mathrm{P} = L_\mathrm{diff} \ln\left(\frac{p_\mathrm{n} C_\mathrm{p}}{e^\mathrm{t} + N_\mathrm{d,net} C_\mathrm{n}}\right) + w_\mathrm{n,P}. \tag{3.5}$$

Here, $w_\mathrm{n,P}$ is the depletion layer width during the filling period, and p_n is the hole concentration at $x = w_\mathrm{n,P}$. When w is small, all deep levels near the valence band maximum in the depletion region are initially occupied, and the constant $\tilde{N}_\mathrm{T}$ is obtained. When $w > \lambda_\mathrm{P}$, deep levels near the valence band maximum in the depletion layer located at $x > \lambda_\mathrm{P}$ are empty, and a smaller $\tilde{N}_\mathrm{T}$ is obtained. Considering $f_\mathrm{T}(x,0)$, $\tilde{N}_\mathrm{T}$ is given as:

$$\tilde{N}_\mathrm{T} = \begin{cases} N_\mathrm{T} & , w \leq \lambda_\mathrm{P} \\ N_\mathrm{T}\left(\frac{\lambda_\mathrm{P}}{w}\right)^2 & , w > \lambda_\mathrm{P}, \end{cases} \tag{3.6}$$

where N_T is the true density of hole trap H1. When the applied measurement bias is small enough ($w \leq \lambda_\mathrm{P}$), $\tilde{N}_\mathrm{T} = N_\mathrm{T}$. The red dashed line in Fig. 3.3(b) represents the curve calculated using Eq. (3.6). From the curve fitting, $N_\mathrm{T}\lambda_\mathrm{P}^2 = 1.5$ nm^{-1} was obtained. N_T and λ_P could not be extracted separately.

3.4.2 Quick Carrier Recombination via Hole Trap H1 near Depletion Layer Edge

As shown in Fig. 3.3(b), even in the case of a small w (<700 nm), i.e., a small reverse bias voltage, $\tilde{N}_\mathrm{T}$ exhibits strong dependence on w. This dependence is explained by the quick

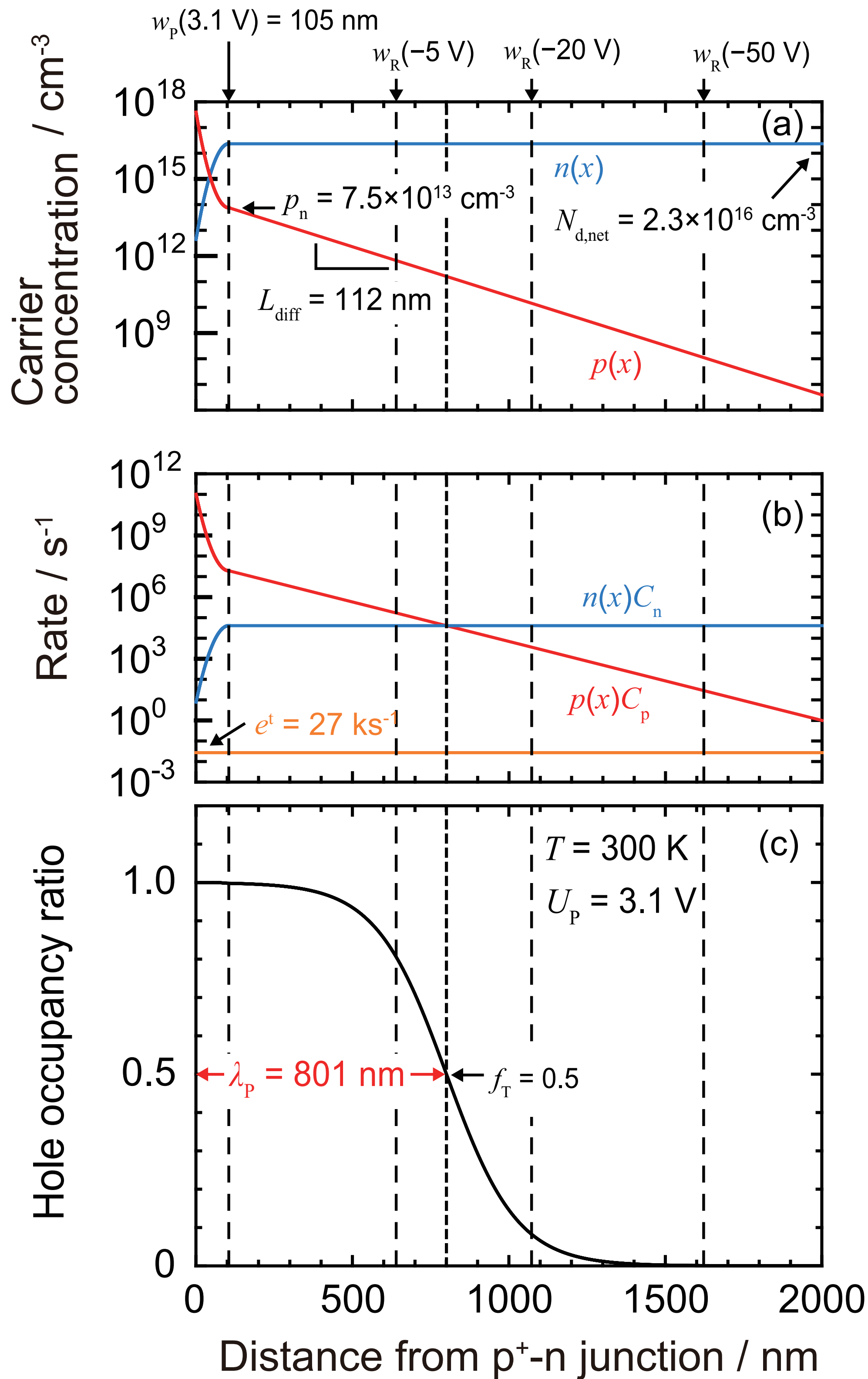

Figure 3.4: Spatial distributions of (a) the concentrations of electrons $[n(x)]$ and holes $[p(x)]$; (b) the capture rates of electrons $[n(x)C_{\mathrm{n}}]$ and holes $[p(x)C_{\mathrm{p}}]$ and the hole thermal excitation rate (e^{t}); and (c) the hole occupancy ratio of the hole trap H1 $[f_{\mathrm{T}}(x,0)]$ during the steady state of the filling pulse period (forward bias is 3 V).

carrier recombination via the deep levels near the valence band maximum near the depletion layer edge immediately after the application of the reverse bias. Figure 3.5(a) shows $n(x)$, and Fig. 3.5(b) shows $n(x)C_\mathrm{n}$ and e^t with the reverse bias voltage of -5 V. The trailing off of the electron concentration near the depletion layer edge results in carrier recombination via the hole traps; i.e., the filled hole traps become unoccupied with the following time constant (τ):

$$\tau(x) = \frac{1}{e^\mathrm{t} + n(x)C_\mathrm{n}}. \tag{3.7}$$

Owing to the spatial distribution of $n(x)$, τ also has a spatial distribution [$\tau(x)$], which is plotted in Fig. 3.5(c). The temporal evolution of the hole occupancy ratio [$f_\mathrm{T}(x,t)$] is given as:

$$f_\mathrm{T} = f_\mathrm{T}(x,0)\exp\left(-\frac{t}{\tau(x)}\right). \tag{3.8}$$

Figure 3.5(d) shows $f_\mathrm{T}(x,t)$ calculated using Eq. (3.8). When the position at which $f_\mathrm{T}(x,1/e^\mathrm{t})$ is half of the value at the p$^+$-n junction is defined as $x = w - \lambda_\mathrm{R}$, λ_R is given as:

$$\lambda_\mathrm{R} = L_\mathrm{D}\sqrt{2\ln\left(\frac{N_\mathrm{d,net}C_\mathrm{n}}{e^\mathrm{t}\ln 2}\right)}. \tag{3.9}$$

Deep levels in the region of $w - \lambda_\mathrm{R} < x \leq w$ do not contribute to the peak in the current-injection ICTS spectrum determined from the thermal emission. Considering $f_\mathrm{T}(x,t)$, $\tilde{N}_\mathrm{T}$ at small w ($w < \lambda_\mathrm{P}$) is given as:

$$N_\mathrm{T} = N_\mathrm{T}\left(1 - \frac{\lambda_\mathrm{R}}{w}\right)^2. \tag{3.10}$$

Therefore, $\tilde{N}_\mathrm{T}$ is underestimated with the small w. The blue dashed line in Fig. 3.3(b) represents the curve calculated using Eq. (3.10). From the curve fitting, $\lambda_\mathrm{R} = 136$ nm and $N_\mathrm{T} = 2.3 \times 10^{15}$ cm^{-3} were obtained. Using the true density of trap, the aforementioned λ_P can be extracted from the product $N_\mathrm{T}\lambda_\mathrm{P}^2$, and $\lambda_\mathrm{P} = 801$ nm was obtained.

3.4.3 Discussion

These results demonstrate that the analysis of $\tilde{N}_\mathrm{T}$ must consider the effects of both the spatial distribution of the hole occupancy ratio during a filling period in the case of a large w and the quick carrier recombination via the deep levels near the depletion layer edge immediately after the application of a reverse bias in the case of a small w. For this analysis method, it is necessary that λ_P is large enough to measure the apparent density of deep level characterized by only the quick carrier recombination [Eq. (3.10)], as in the case of this study. According to previous reports, it is possible that the hole trap H1 is associated with $\mathrm{V_{Ga}}$-related and/or C-related ($\mathrm{C_N}$) defects, which act as a compensation

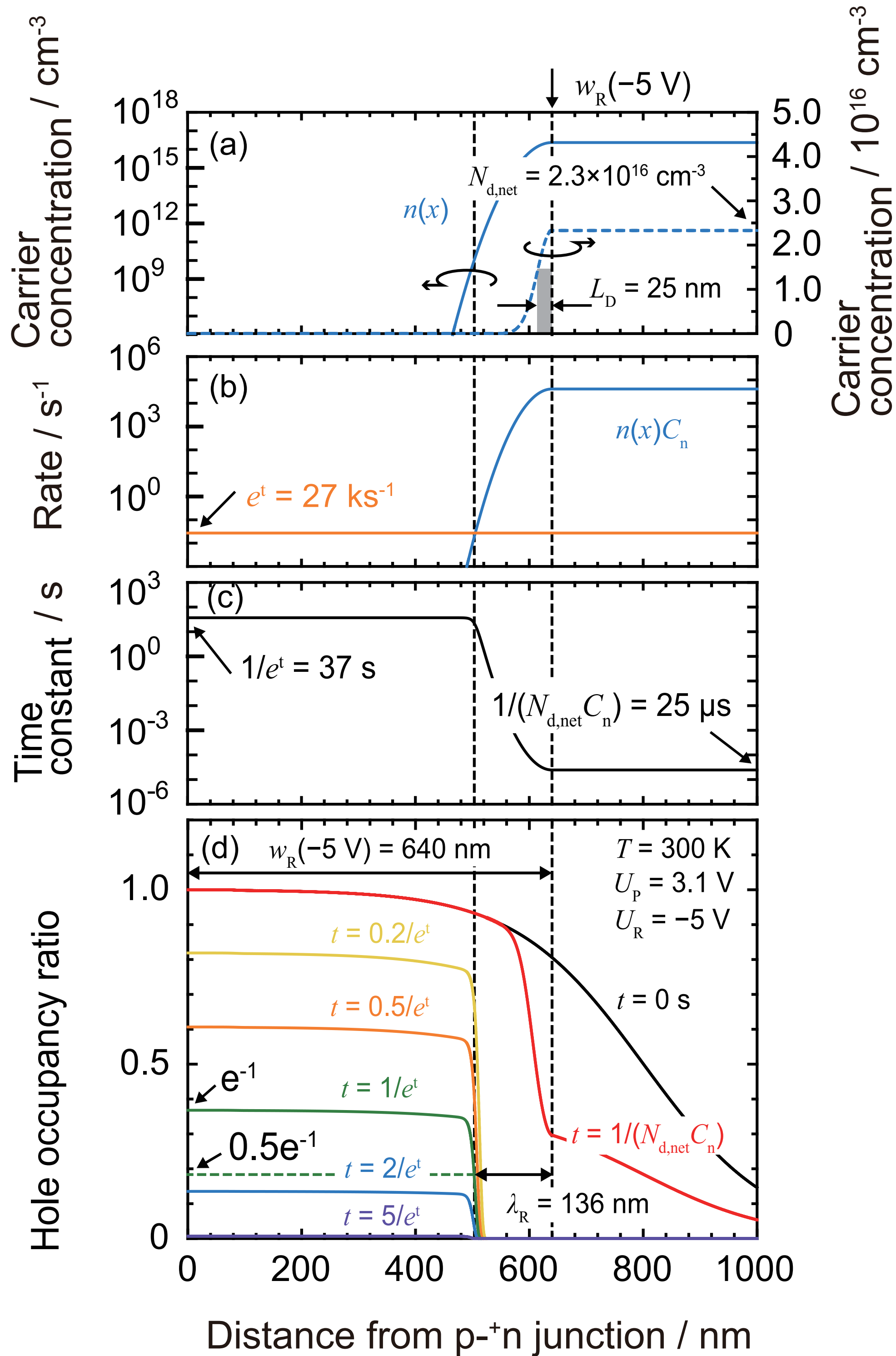

Figure 3.5: Spatial distributions of (a) the concentrations of electrons $[n(x)]$; (b) the capture rates of electrons $[n(x)C_\mathrm{n}]$ and the hole thermal excitation rate (e^t); (c) the time constant; and (d) the temporal evolution of the hole occupancy ratio $[f_\mathrm{T}(x,t)]$ of the hole trap H1 under the measurement bias of -5V.

acceptor [2, 5–14]. The N_T obtained in this study via our proposed analysis method shows excellent agreement with the C concentration of [C]$= 3 \times 10^{15}$ cm^{-3} in the n-type layer obtained via SIMS. This result suggests that the hole trap H1 is mainly associated with C_N defects in our epitaxial layer. Our group discovered that the electron trap E3 acts as compensation acceptors via a combination of Hall-effect and DLTS measurements [28]. In the present study, the difference between the Si concentration ([Si]$= 3 \times 10^{16}$ cm^{-3}) and $N_\mathrm{d,net} = 2.3 \times 10^{16}$ cm^{-3} (7×10^{15} cm^{-3}) agrees well with the sum of the densities of electron trap E3 ($N_\mathrm{T} = 4.3 \times 10^{15}$ cm^{-3}) and hole trap H1 ($N_\mathrm{T} = 2.3 \times 10^{15}$ cm^{-3}). Finally, other properties obtained from λ_R and λ_P are discussed. Using the obtained λ_R, the electron capture cross section of the hole trap H1 was determined as $\sigma_\mathrm{n} = 7 \times 10^{-20}$ cm^2 via Eq. (3.9). Polyakov et al. obtained $\sigma_\mathrm{n} = 1.4 \times 10^{-22}$ cm^2 via direct observation of the recombination process at the hole trap H1 at a low temperature ($T = 85$ K) [15]. Furthermore, using the λ_P and σ_n obtained in this study, $L_\mathrm{diff} = 112$ nm was obtained from Eq. (3.5).

3.5 Temperature Dependence of Measured Density of Hole Trap H1 in Current-injection ICTS

Figure 3.6 shows the current-injection ICTS spectra in the temperature range from 300 K to 370 K at $U_\mathrm{R} = -5$ V. The thermal excitation rate of carrier from traps increases with elevating temperature, the peak positions of electron trap E3 and hole trap H1 are shifted to the left. The peak intensity of electron trap E3 does not depend on temperature. On the other hand, the peak intensity of hole trap H1 increases with elevating temperature. This result suggests that the measured density of hole trap H1 depends on measurement temperature in current-injection method. In this section, the dependence of the measured density of hole trap H1 on temperature is investigated.

The dependences of the measured density of hole trap H1 $\tilde{N}_\mathrm{T}$ on depletion layer width at 300 K (blue open circles), 340 K (green open circles), 370 K (red open circles) are shown in Fig. 3.7. The circle symbols denote the experimental data. The measured densities of hole trap H1 at the same U_R increase with elevating temperature. Curve fitting was performed for the experimental data at $T = 340$ K and 370 K as the same way shown in Fig. 3.3(b). The black solid lines denote the fitting curves under the consideration of the true hole occupancy ratio at $t = 1/e^\mathrm{t}$ shown in Fig. 3.5(d). In the curve fitting, λ_R and λ_P at each temperature were used as the fitting parameters. The density of hole trap H1 is set to 2.3×10^{15} cm^{-3} obtained from the analysis at 300 K [Fig. 3.3(b)]. The calculation results are also shown in Fig. 3.7 as the color solid lines (effect A) and the color broken lines (effect B).

λ_R decreases with elevating temperature and the magnitude of underestimation in $\tilde{N}_\mathrm{R}$ by effect B decreases. Figure 3.8 shows the depth profiles of hole thermal excitation rate e^t (orange solid line) and electron capture rate nC_n (blue solid line) at (a) 300 K, (b) 340 K,

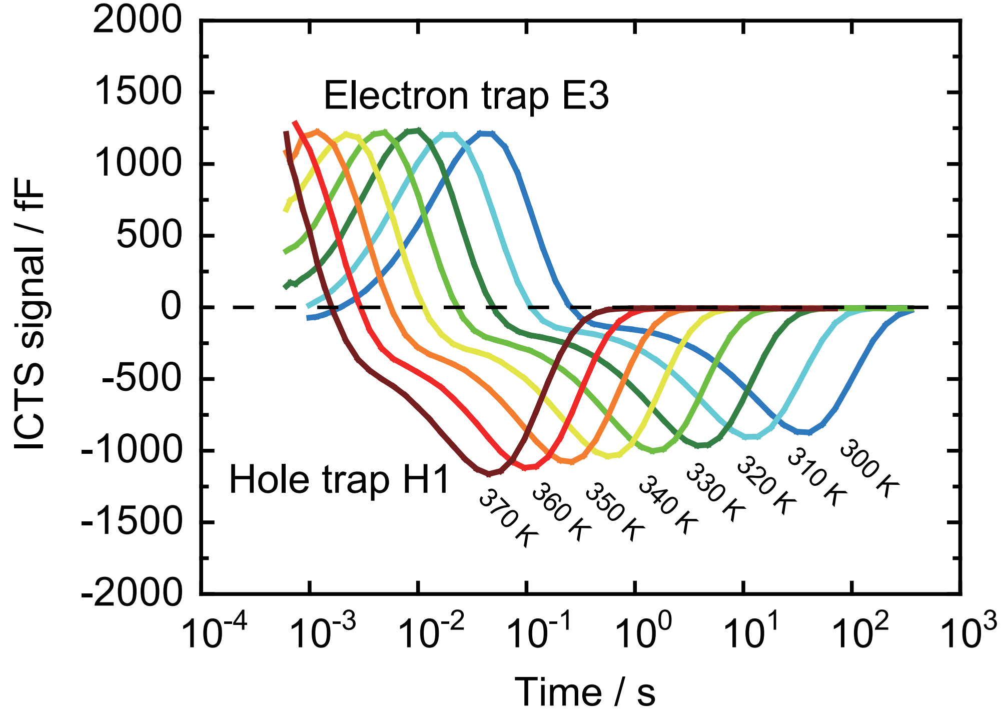

Figure 3.6: Current injection ICTS spectra for GaN PND at 300 K to 370 K. The forward bias voltage and pulse width of the filling pulse were $U_{\mathrm{P}} = 3.5$ V and $t_{\mathrm{P}} = 100$ ms, respectively. The measurement bias voltage was $U_{\mathrm{R}} = -5$ V. The electron trap E3 (positive peak) and hole trap H1 (negative peak) are investigated.

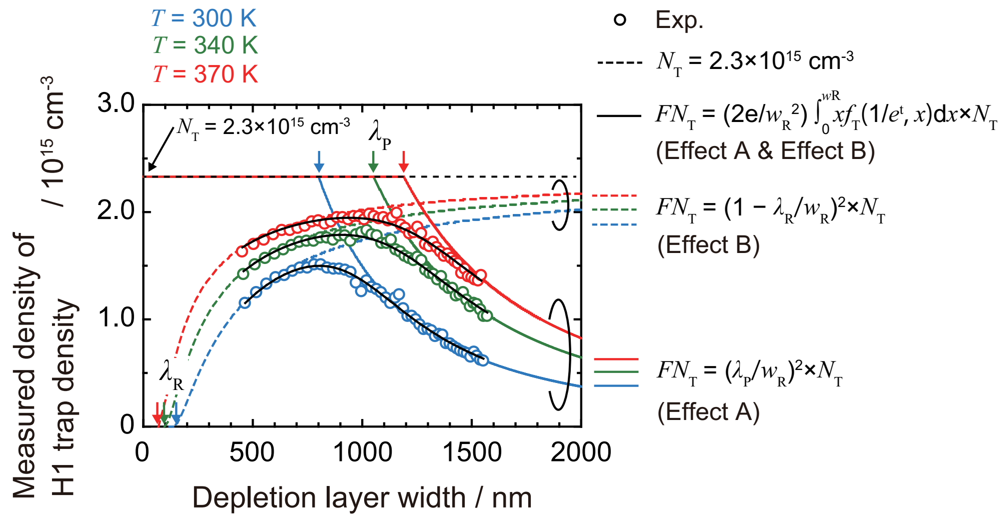

Figure 3.7: Dependence of the measured density of hole trap H1 on the depletion layer width, which is varied by changing the measurement bias voltage at 300 K (blue), 340 K (green), and 370 K (red). The black solid lines denote the fitting curve under a concentration of the true hole occupancy ratio at $t = 1/e^{\mathrm{t}}$. The color solid and color broken lines indicate the calculation curves obtained using Eqs. (3.6) and (3.10), respectively.

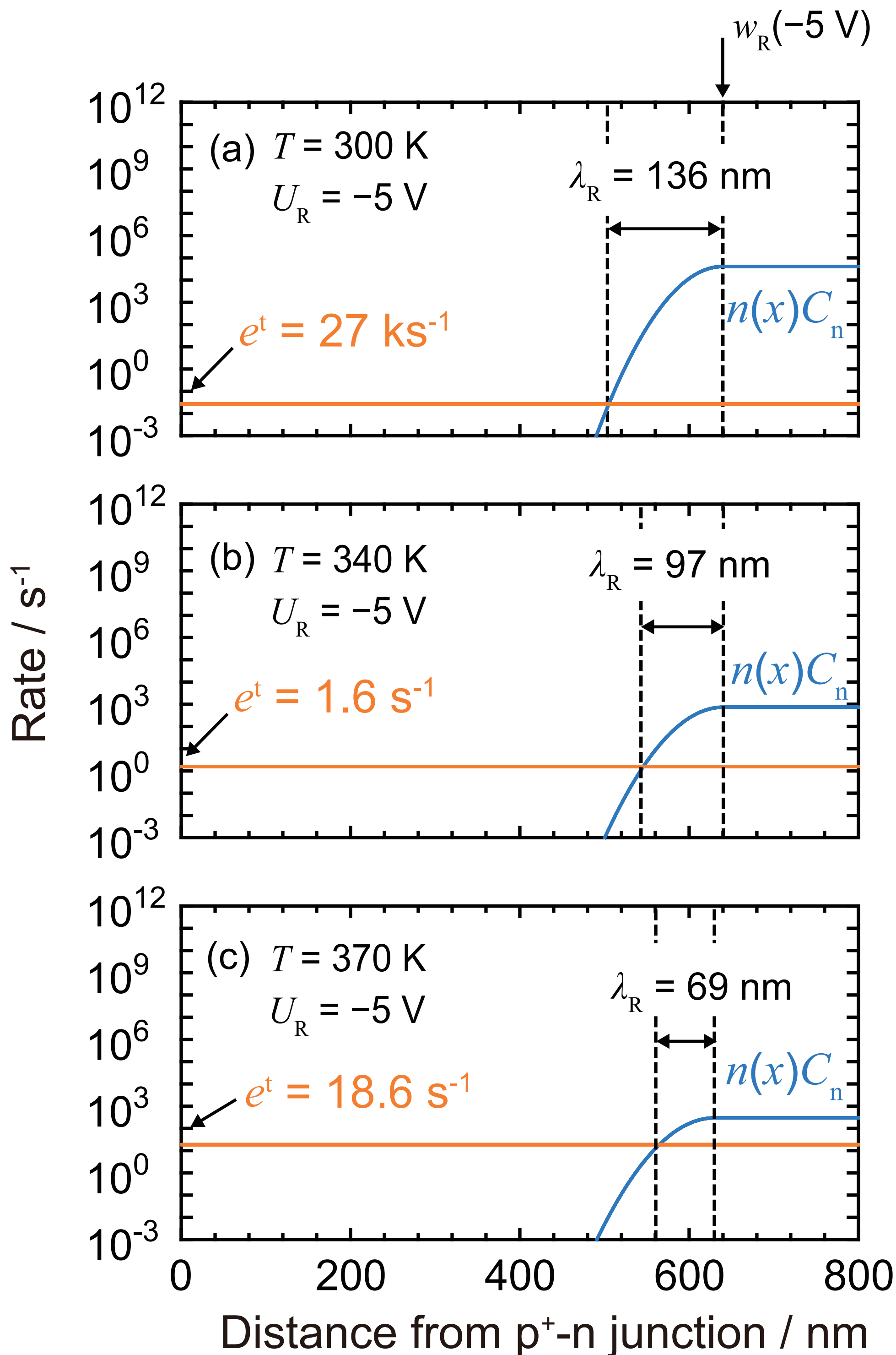

Figure 3.8: Depth profiles of the capture rates of electrons $n(x)C_{\mathrm{n}}$ (blue) and the hole thermal excitation rate e^{t} (orange) of the hole trap H1 under the measurement bias of −5V at (a) 300 K, (b) 340 K, and (c) 370 K.

and (c) 370 K under U_R of -5 V. e^t increases and nC_n decreases with elevating temperature. Thus, λ_R, which is determined tha balance between e^t and $n(x)C_\mathrm{n}$ near the depletion layer edge, decreases with elevating temperature. The details of dependence of λ_R on temperature is discussed in Sec. 5.5 and Sec. 6.3.

λ_P increases with elevating temperature and the magnitude of underestimation in $\tilde{N}_\mathrm{R}$ by effect A decreases, i.e. hole traps far from the p$^+$-n junction become able to capture the injected holes. Figure 3.9 shows the depth profiles of hole thermal excitation rate e^t (orange solid line) and electron capture rate nC_n (blue solid line) and hole capture rate pC_P (red solid line) at (a) 300 K, (b) 340 K, and (c) 370 K under a forward bias voltage of 3.5 V. $pC_\mathrm{p}(w_\mathrm{n,P})$ decreases with elevating temperature. On the other hand, L_diff increases with elevating temperature as shown in Fig. 3.10. Temperature decrease of L_diff is discussed later. Temperature dependence of pC_p in the neutral region is suppressed due to a decrease of $pC_\mathrm{p}(w_\mathrm{n,P})$ and increase of L_diff in the measurement conditions. λ_P increases with elevating temperature mainly due to a decrease of nC_n.

Temperature dependence of L_diff is given as [16, 17]:

$$L_\mathrm{diff} = \sqrt{\frac{k_\mathrm{B}T}{e}\mu\tau} \sim L_0\sqrt{\exp\left(-\frac{E_\mathrm{a}}{k_\mathrm{B}T}\right)}. \tag{3.11}$$

Here, τ is a life time, L_0 is a scaring factor. In this model, it is assumed that the temperature dependence of L_diff mainly reflects the temperature dependence of carrier mobility μ. In the case of GaN, the polar optical phonon scattering acts as a dominant scattering mechanism [18] at 300 K to 370 K, and E_a corresponds to an energy of transverse optical (TO) phonon in GaN. From the curve fitting base on Eq. 3.11, L_0 of 481 nm and E_a of 74 meV are obtained. Considering the TO phonon energies of E_1 mode (69 meV) and A_1 mode (66 meV) in GaN [19], the temperature dependence of L_diff is reasonably explained.

3.6 Summary

An analysis method for the accurate estimation of density of the hole trap H1 (E_V+0.85 eV) in n-type GaN via current-injection ICTS is proposed. The proposed method considers both the hole occupation during a filling (current injection) period and the quick carrier recombination via the deep levels near the depletion layer edge immediately after a reverse bias is applied. The reverse bias voltage dependence of the current-injection ICTS spectrum indicates that an accurate density of hole trap, as well as the hole diffusion length and electron capture cross-section of the hole traps, can be determined.

References

[1] N. Fourches, J. Appl. Phys. **70**, 209 (1991).

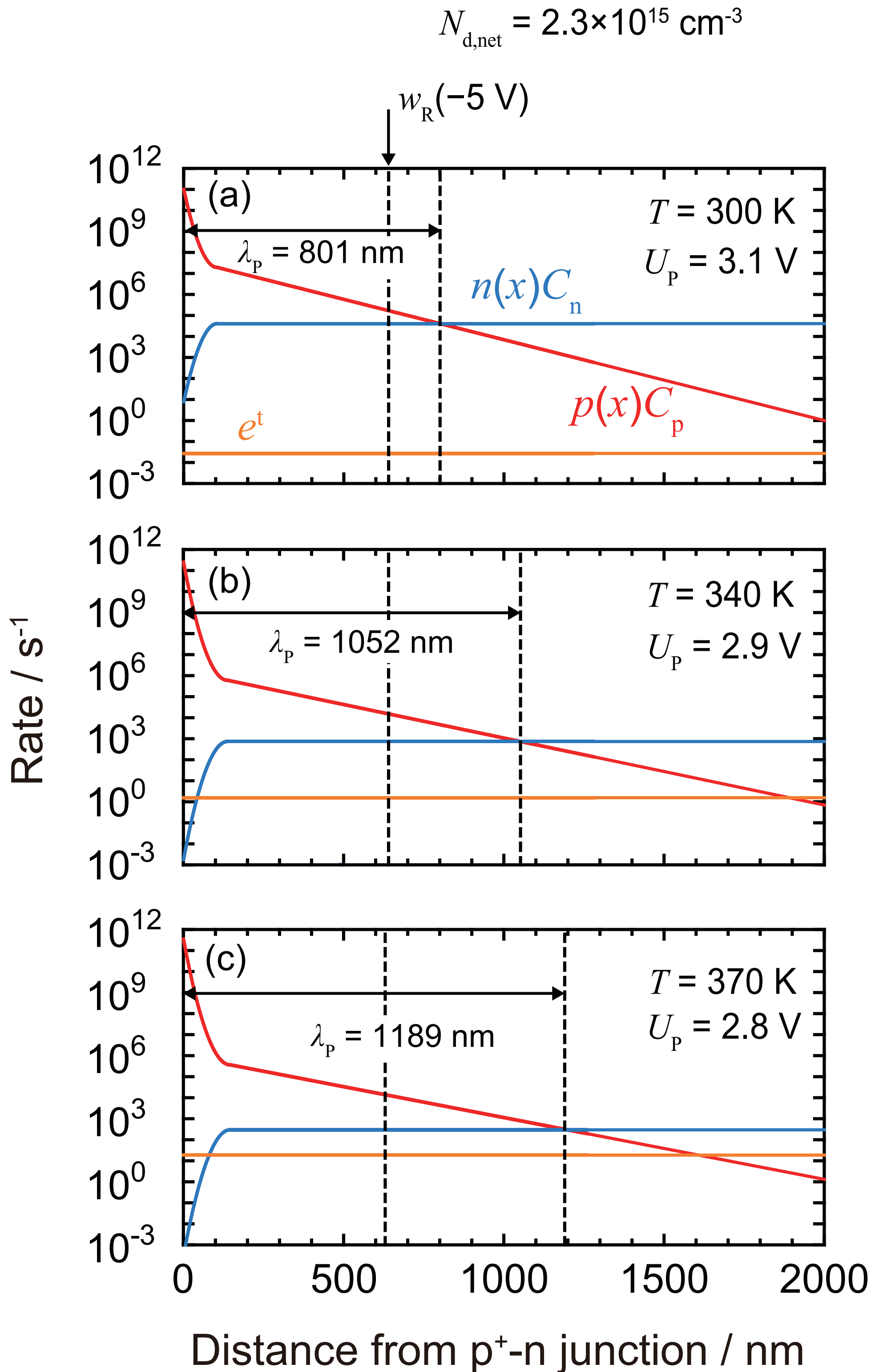

Figure 3.9: Depth profiles of the capture rates of electrons $n(x)C_\mathrm{n}$ (blue) and holes $p(x)C_\mathrm{p}$ (red) and the hole thermal excitation rate e^t (orange) of the hole trap H1 at (a) 300 K, (b) 340 K, and (c) 370 K during the steady state of the filling pulse period (forward bias is 3.5 V).

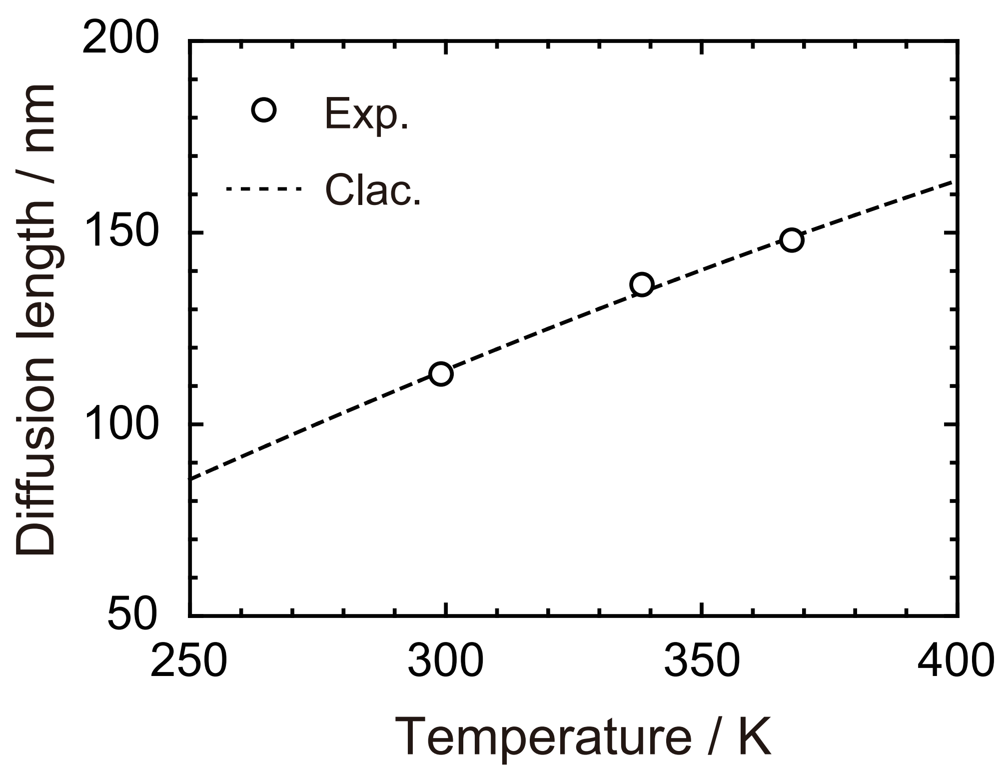

Figure 3.10: Temperature dependence of the diffusion length. The open circles and broken line denote the experimental data and calculation curve.

[2] Y. Tokuda, ECS Trans. **75**, 39 (2016).

[3] Y. Zohta and M. O. Watanabe, J. Appl. Phys. **53**, 1809 (1982).

[4] M. J. Kane, M. J. Uren, D. J. Wallis, P. J. Wright, D. E. J. Soley, A. J. Simons, and T. Martin, Sci. Technol. **26**, 085006 (2011).

[5] T. Tanaka, N. Kaneda, T. Mishima, Y. Kihara, T. Aoki, and K. Shiojima, Jpn. J. Appl. Phys. **54**, 041002 (2015).

[6] T. Tanaka, K. Shiojima, T. Mishima, and Y. Tokuda, Jpn. J. Appl. Phys. **55**, 061101 (2016).

[7] A. Hierro, D. Kwon, S. A. Ringel, M. Hansen, J. S. Speck, U. K. Mishra, and S. P. DenBaaers, Appl. Phys. Lett. **76**, 3064 (2000).

[8] R. Armitage, W. Hong, Q. Yang, H. Feick, J. Gebauer, E. R. Weber, S. Hautakangas, and K. Saarinen, Appl. Phys. Lett. **82**, 3457 (2003).

[9] A. Armstrong, A. R. Arehart, D. Green, U. K. Mishra, J. S. Speck, and S. A. Ringel, J. Appl. Phys. **98**, 053704 (2005).

[10] J. L. Lyons, A. Janotti, and C. G. V. d. Walle, Appl. Phys. Lett. **97**, 152108 (2010).

[11] Y. Tokuda, Y. Yamada, T. Shibata, S. Yamaguchi, H. Ueda, T. Uesugi, and T. Kachi, Phys. St. Solidi C **8**, 2239 (2011).

[12] A. Y. Polyakov, I.-H. Lee, N. B. Smirnov, A. V. Govorkov, E. A. Kozhukhova, and S. J. Pearton, J. Appl. Phys. **109**, 123701 (2011).

[13] U. Honda, Y. Yamada, Y. Tokuda, and K. Shiojima, Jpn. J. Appl. Phys. **51**, 04DF04 (2012).

[14] T. Tanaka, K. Shiojima, T. Mishima, and Y. Tokuda, Jpn. J. Appl. Phys. **55**, 061101 (2016).

[15] A. Y. Polyakov, N. B. Smirnov, E. B. Yakimov, S. A. Tarelkin, A. V. Turutin, I. V. Shemerov, S. J. Pearton, K.-B. Bae, and I.-H. Lee, J. Alloys Compd. **686**, 1044 (2016).

[16] R. Mitdank, A. Sturm, and B. Jacobs, Phys. St. Solidi A **117**, 485 (1990).

[17] L. Chernyak, A. Osinsky, and H. Temkina, Appl. Phys. Lett. **69**, 2561 (1996).

[18] N. Sawada, T. Narita, M. Kanechika, T. Uesugi, T. Kachi, M. Horita, T. Kimoto, and J. Suda, Appl. Phys. Express **11**, 041001 (2018).

[19] H. Harima, J. Phys.: Condens. Matter **14**, R967 (2002).

Chapter 4

Photoionization Cross-section of Hole Trap H1 under Sub-bandgap-light Illumination

4.1 Introduction

In this chapter, the photoionization of C_N under sub-bandgap-light illumination (390 nm) is investigated with the ICTS technique. Characterization of the photoionization cross-section of a deep level σ^o enables prediction of the effect of light illumination on the device characteristics and leads to a further understanding of the physical properties of the deep level. For example, the ratio of photoionization cross-section of electron to that of hole σ_n^o/σ_p^o of 0.158 for the Cr-level ($E_V + 0.886$ eV), which is shown to correspond to the Cr^{3+} or Cr^{2+} state, in GaAs has been revealed under sub-bandgap-light illumination (1.06 μm) [1]. It makes possible to estimate the hole occupancy ratio for the Cr-level under light illumination. Thus, the density of Cr-level in n-type GaAs layers can be obtained from optical DLTS [1].

It has been reported that the $C_N(0/-)$ is detected as the hole trap H1 in n-type GaN layers [2–9]. First, the density of hole trap H1 (N_T) was accurately determined with the current-injection ICTS for a p^+-n junction diode using a proposed method in Chapter 3. Second, sub-E_g-light ICTS measurements were performed for a p^+-n junction diode to obtain the steady-state hole occupancy ratio (f_T) of the hole trap H1 under illumination. The hole trap H1 is photoexcited in two processes as shown in Fig. 4.1; (a) photoexcitation of an electron at the hole trap H1 to the C.B. (C_N^- to C_N^0), which means that photoexcitation of a hole from the C.B. to the hole trap H1, and (b) photoexcitation of a hole at the hole trap H1 to the V.B. (C_N^0 to C_N^-) f_T is determined under the competition between these two photoexcitation processes and the thermal excitation process. The ratio of the electron photoionization cross-section σ_n^o to the hole photoexcitation cross-section σ_p^o of the hole trap H1 σ_p^o/σ_n^o) was extracted by analysis of the dependence of f_T on temperature T.

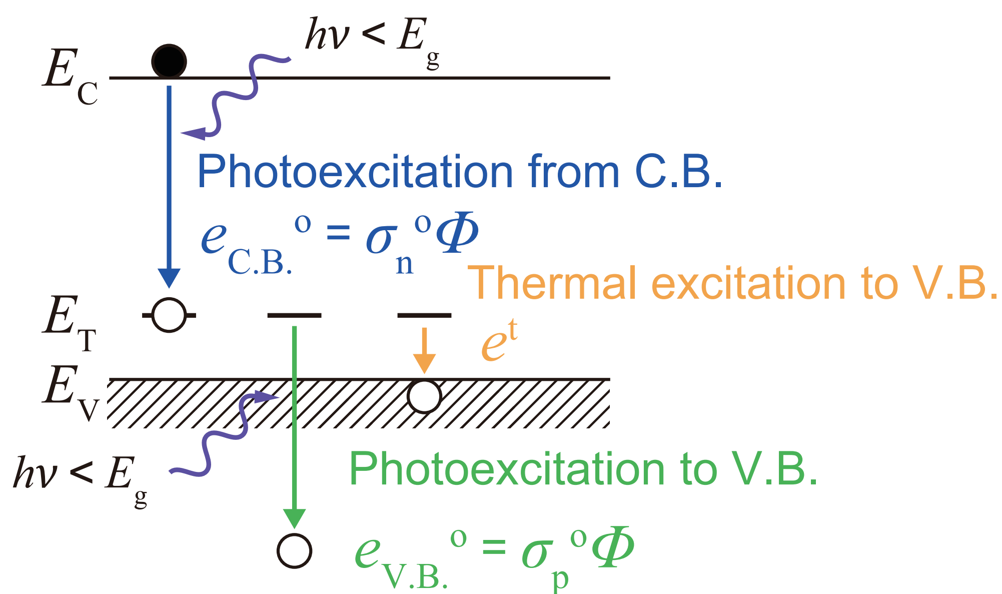

Figure 4.1: Band diagram of the hole trap H1 of n-type GaN under sub-E_g-light illumination.

4.2 Experiments

The GaN p$^+$-n junction diode used in this study was comprised of a MOVPE-grown 0.1-μm-thick p^{++}-type GaN/0.5-μm-thick p$^+$-type GaN/3-μm-thick n-type GaN structure on a hydride vapor phase epitaxy (HVPE)-grown n$^+$-type GaN substrate. The Mg concentrations of the p^{++}- and p$^+$-type GaN were obtained via secondary ion mass spectroscopy (SIMS) to be 1×10^{20} cm^{-3} and 3×10^{19} cm^{-3}, respectively. The depth profiles of dopants and impurities are shown in Fig. 4.2. The Si concentration ([Si]) of the n-type GaN was obtained via SIMS to be 3.0×10^{16} cm^{-3}. A uniform distribution of [Si] was also confirmed from the SIMS depth profiles. The carbon concentration of the n-type GaN was obtained via raster change mode SIMS [10] to be 2×10^{15} cm^{-3}. The p$^+$-n junction was assumed to be a one-side abrupt junction. The net donor density $N_{\mathrm{d,net}}$ of 2.8×10^{16} cm^{-3} obtained from capacitance-voltage measurement is consistent with the SIMS result. The mesa structure was formed via inductively coupled plasma reactive ion etching to define the area of p$^+$-n junction. The height and diameter of the mesa structure are 1 μm and 520 μm, respectively. Anode and cathode electrodes were formed via deposition of Ni/Au on the top and Ti/Al/Ni on the back side, respectively.

4.3 Sub-bandgap-light-excited ICTS for p$^+$-n Junction

The ICTS technique [11] was adopted; current-injection ICTS and sub-E_{g}-light ICTS were performed for the GaN p$^+$-n junction diode in the temperature range from 300 K to 340 K. A U_{P} of 3.5 V and a pulse width of $t_{\mathrm{P}} = 100$ ms were utilized as the filling pulse in current-injection ICTS. U_{R} was varied from 0 V to -15 V. A wavelength of $\lambda = 390$ nm (full width at half maximum of ca. 10 nm) was employed in sub-E_{g}-light ICTS. LEDs were used as the light source with a photon flux density of 10^{20} s^{-1}cm^{-2} at illuminated surface. U_{R} was also varied from 0 V to -15 V for sub-E_{g}-light ICTS measurements. The optical pulse widths of $t_{\mathrm{P}}^{\mathrm{o}} = 1$ s to 10 s used in this study were sufficiently long for the capacitance change during light illumination to be sufficiently saturated. Current-injection ICTS and sub-E_{g}-light ICTS spectra for the same GaN p+-n junction diode are shown in Fig. 4.3. From Arrhenius plots of $\ln(\tau_{\mathrm{p}} T^2)$, where τ_{p} is the time constant of hole thermal excitation, versus the reciprocal temperature, it was confirmed that the hole trap H1 ($E_{\mathrm{T}} = E_{\mathrm{V}} + 0.85$ eV, hole capture cross-section σ_{p} of 3×10^{-14} cm^2) is detected in current-injection ICTS and sub-E_{g}-light ICTS spectra (Fig. 4.3).

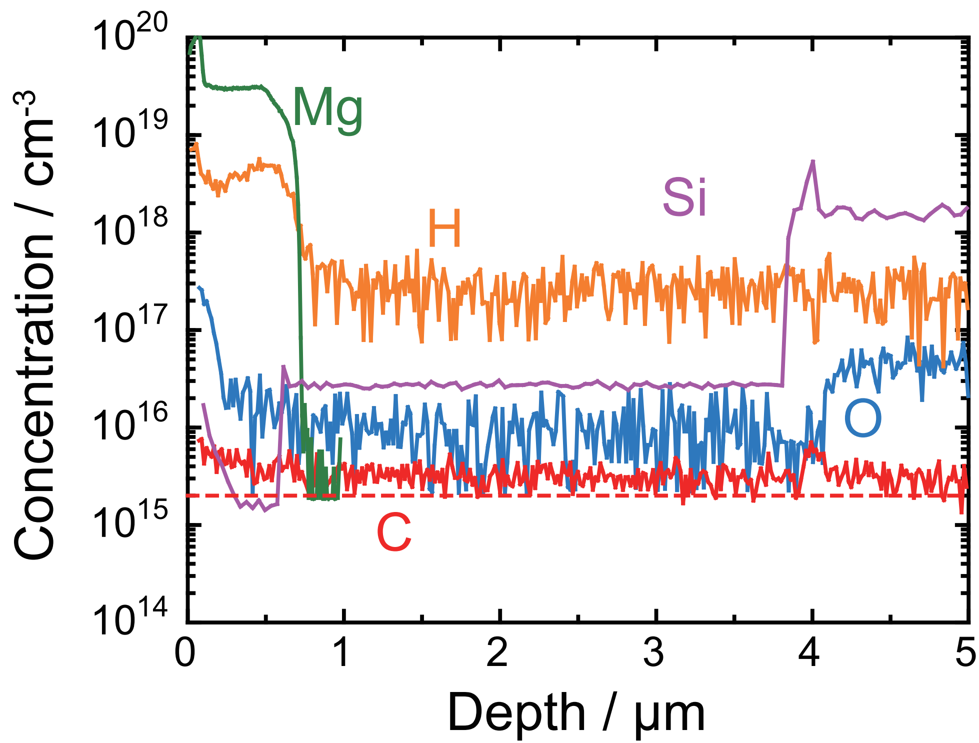

Figure 4.2: The depth profiles of dopants (Mg and Si) and impurities (H, C, and O) in the GaN PND obtained from depth profile mode SIMS. The red broken line denotes the carbon concentration raster change mode SIMS.

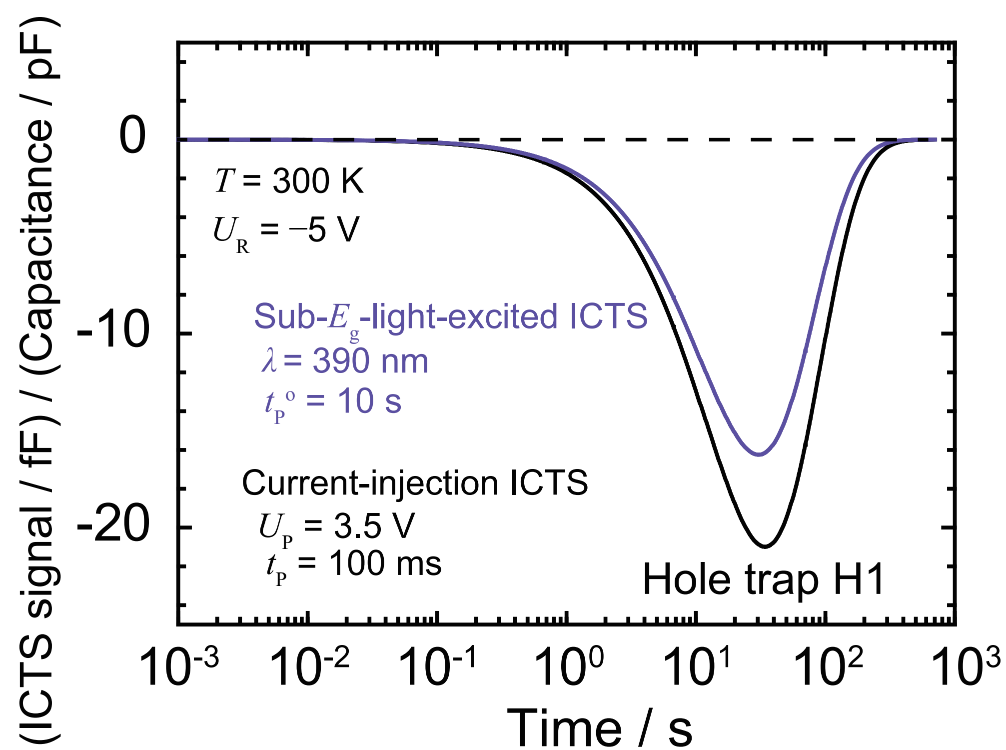

Figure 4.3: ICTS spectra measured with the current-injection (black solid line) and sub-E_g-light-excited (violet solid line) methods with $U_R = -5$ V and $T = 300$ K.

4.4 Photoionization Cross-section Extracted from Hole Occupancy Ratio of Hole Trap H1 under Sub-bandgap-light Illumination

By considering the rate equation under sub-E_g-light illumination for a sufficiently long time, f_T is given as,

$$f_T = \frac{e_n^o}{e_n^o + e_n^o + e^t}. \quad (4.1)$$

Here, e^t is the hole thermal excitation rate from the deep level to the valence band and can be determined from each ICTS spectrum using $e^t = 1/\tau_p$, where τ_p is the time constant of hole thermal excitation form the hole trap H1 to the V.B. e_n^o and e_p^o are the hole photoexcitation rate from the conduction band to a deep level and the hole photoexcitation rate from a deep level to the valence band, respectively. The hole photoexcitation rates are the product of the photoionized cross section σ^o and net photon flux in the material Φ, i.e., $e_n^o = \sigma_n^o\Phi$ and $e_p^o = \sigma_p^o\Phi$. It is difficult to accurately determine Φ for sub-E_g-light due to multiple internal reflections [12]. Therefore, it is also difficult to obtain σ_n^o and σ_p^o, even if e_n^o and e_n^o are extracted from experimental data. On the other hand, the ratio σ_p^o/σ_n^o, which is independent of Φ, is unique physical property value for the deep level and wavelength of illumination light. When e^t is sufficiently smaller than $e_p^o + e_n^o$, then $f_T \cong e_n^o/(e_n^o + e_p^o) = 1/(1 + \sigma_p^o/\sigma_n^o)$ holds and σ_n^o/σ_p^o can be extracted from f_T which is independent of temperature. Martin et al. used this relationship and reported $\sigma_n^o/\sigma_p^o = 0.188$ for the Cr-level ($E_V + 0.886$ eV) in a p-type GaAs layer under excitation from a Nd-YAG laser light (1.06 μm) [1]. They determined f_T by a comparison of N_T and $f_T N_T$ obtained from current-injection DLTS) and sub-E_g-light DLTS for a GaAs p-n$^+$ junction diode. As discussed later, the relationship ($e^t \ll e_n^o + e_p^o$) was determined to be difficult to hold in the case of the hole trap H1 in GaN. f_T is dependent on measurement conditions such as the light illumination and measurement temperature; therefore, e_n^o and e_p^o were extracted from an analysis based on Eq. (4.1) for the dependence of f_T on e^t, i.e., on the temperature.

4.4.1 Comparison between Measured Densities of Hole Trap H1 Obtained by Current-injection ICTS and Sub-bandgap-light-excited ICTS

Figure 4.4 shows the dependence of the measured density of hole trap H1 on the depletion layer width as square symbols and triangle symbols obtained from the current-injection ICTS and the sub-E_g-light ICTS, respectively. When the density of deep level is uniformly distributed in an n-type layer, the measured density of deep level ($\tilde{N}_T$) is given as:

$$\tilde{N}_T = 2\frac{\Delta C}{C_R}N_{d,net}. \quad (4.2)$$

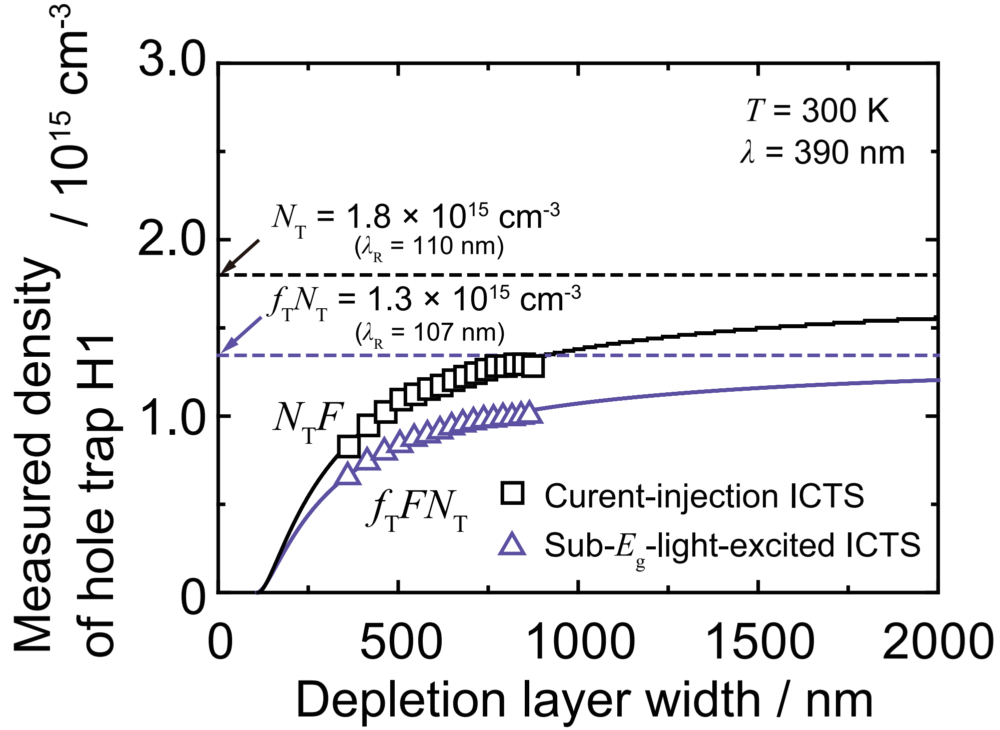

Figure 4.4: Dependence of the measured density of hole trap H1 on the depletion layer width, which is varied by changing the measurement bias in the current-injection (black) and sub-E_g-light-excited (violet) methods. The symbols denote the ICTS data and solid lines show the fitting curves. The black and violet broken lines denote the density of the hole trap H1 extracted with the current-injection method N_T and the hole trap H1 with the sub-E_g-light-excited method $f_T N_T$, respectively. Black and violet solid lines indicate the fitting curves obtained using Eqs. (4.4)–(4.5) and (4.5)–(4.6), respectively.

Here, C_R is the steady-state capacitance of the junction under U_R and ΔC is the peak intensity in the ICTS spectrum. In Fig. 4.4, $\tilde{N}_T$ obtained from the current-injection ICTS and sub-E_g-light ICTS spectra increases with increasing the depletion layer width (w), which reflects the depletion layer edge effect [1, 13]. Near the depletion layer edge, even if a deep level changes to a hole-occupied state under application of an electrical or optical filling pulse, the deep level can return to the unoccupied state immediately after the application of the electrical or optical filling pulse due to quick carrier recombination via the electrons near the depletion layer edge [13]. Therefore, deep levels near the depletion layer edge do not contribute to the ICTS peaks. The width of the region where quick carrier recombination is dominant (λ_R) is determined by the competition between e^t and the electron capture rate (nC_n), which is given as [13]:

$$\lambda_R = L_D \sqrt{2\ln\left(\frac{N_{d,net}C_n}{e_p \ln 2}\right)}. \tag{4.3}$$

λ_R reflects the band bending near the depletion layer edge and is independent of U_R. Considering the depletion layer edge effect, the relationship between $\tilde{N}_T$ and N_T in current-injection ICTS is given as,

$$\begin{aligned}\tilde{N}_T &= 2\frac{\Delta C}{C_R} N_{d,net} \\ &= F N_T.\end{aligned} \tag{4.4}$$

Here, F is the term of the depletion layer edge correction and given as [13]:

$$F = \left(1 - \frac{\lambda_R}{w}\right)^2. \tag{4.5}$$

It was confirmed that the hole trap H1 in the depletion layer were completely filled by holes under application of U_P [13], i.e., the hole trap H1 changes to the hole-occupied state from the p^+-n junction to the deep region (> 1 µm), despite the hole diffusion length in n-type GaN of 10^1 nm to 10^2 nm [14–16] because the electron capture cross section of the hole trap H1 (10^{-22} cm^2 to 10^{-21} cm^2 [13, 17, 18]) is sufficiently smaller than the hole capture cross section (10^{-14} cm^2 to 10^{-13} cm^2 [13, 17, 18]). In sub-E_g-light ICTS, the relationship between $\tilde{N}_T$ and N_T is expressed as:

$$\begin{aligned}\tilde{N}_T &= 2\frac{\Delta C}{C_R} N_{d,net} \\ &= f_T F N_T.\end{aligned} \tag{4.6}$$

Fitting curves of $\tilde{N}_T$ using Eqs. (4.4)-(4.6) to the measured density of hole trap H1 obtained from the current-injection ICTS and sub-E_g-light ICTS are shown as solid lines in Fig. 4.4. λ_R of 110 nm obtained from the current-injection ICTS data is very close to λ_R of 107 nm obtained from the sub-E_g-light ICTS data. This result is reasonable because it is expected that the impact of the depletion layer edge effect in current-injection ICTS is identical to

that in sub-E_g-light ICTS. Considering the depletion layer edge correction for the measured density of hole trap H1 obtained from the current-injection ICTS data, N_T of 1.8×10^{15} cm^{-3} was obtained. This is in agreement with [C] of 2×10^{15} cm^{-3} in the n-type GaN epilayer obtained from SIMS measurement. In the same way, $f_T N_T$ of 1.3×10^{15} cm^{-3} was obtained from the sub-E_g-light ICTS data. By comparing N_T and $f_T N_T$, an f_T(300 K) of 0.75 was obtained. It should be noted that this value is not universal, but is dependent on measurement conditions such as the light intensity and measurement temperature.

4.4.2 Temperature Dependence of Hole Occupancy Ratio

In the same way, f_T was extracted in the temperature range from 300 K to 340 K with the same light intensity. The photoexcitation rates can be assumed to be independent of temperature because of the small temperature range (40 K). Thus, f_T reflects the dependence of e^t on the temperature, which is directly obtained from the ICTS measurement. Figure 4.5 shows the dependence of f_T on e^t as circle symbols. f_T decreases with an increase in e^t, i.e., elevation of the temperature.

4.4.3 Discussion

A fitting curve of Eq. (4.1) using $e_n^o + e_p^o$ and e_n^o/e_p^o as fitting parameters is shown as a black solid line in Fig. 4.5. According to the fitting curve, $e_n^o + e_p^o = 1.3$ s^{-1} and $e_n^o/e_p^o = 3.0$ were extracted for the hole trap H1 under illumination with light of $\lambda = 390$ nm. $e_n^o/e_p^o = \sigma_n^o/\sigma_p^o$ is a physical property value for a trap under illumination light with a wavelength and is independent of Φ. In Fig. 4.5, the calculation curves of Eq. (4.1) for e_n^o/e_p^o of 2, 3, and 4 with $e_n^o + e_p^o = 1.3$ s^{-1} are shown as colored dashed lines. Figure 4.5 shows the measured points are between the curves with e_n^o/e_p^o of 2 and 3, and close to the curve with e_n^o/e_p^o of 3, which suggests that the fitting result of $e_n^o/e_p^o = \sigma_n^o/\sigma_p^o = 3.0$ is reasonable. Under conditions when the hole thermal excitation can be negligible, i.e., at low temperature, the hole occupancy ratio becomes saturated and is determined by σ_n^o/σ_p^o. Under illumination of light with $\lambda = 390$ nm, f_T of the hole trap H1 approaches 0.75 at low temperature. When e^t is equal to $e_n^o + e_p^o$, f_T becomes half the value at low temperature. The validity of the extracted e_n^o/e_p^o of 3.0 and $e_n^o + e_p^o$ of 1.3 s^{-1} can thus be again confirmed from this viewpoint.

4.5 Summary

In this chapter, the $C_N(0/-)$ was detected as the hole trap H1 in n-type GaN with current-injection ICTS and sub-E_g-light ICTS for p$^+$-n junction diode. From comparison of the measured densities of hole trap H11 in the current-injection ICTS and sub-E_g-light ICTS data, the dependence of the hole occupancy ratio under sub-E_g-light illumination (390 nm) on the hole thermal excitation rate e^t. The ratio σ_n^o/σ_p^o of the $C_N(0/-)$ in n-type GaN

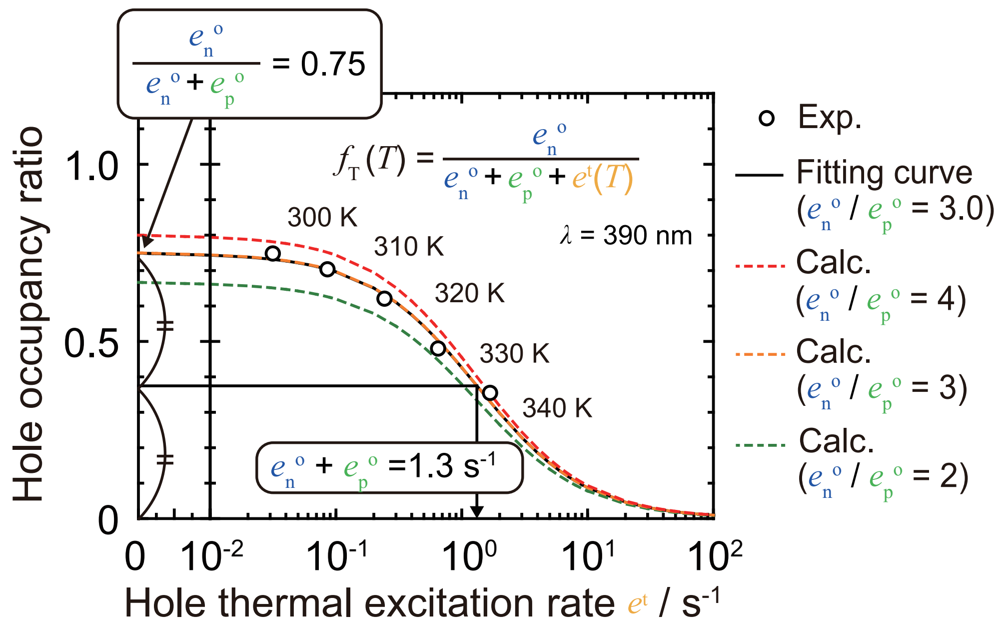

Figure 4.5: Dependence of the hole occupancy ratio on the hole thermal excitation rate. The open circles denote the experimental data. The black solid line shows the fitting curve using Eq. (4.1). The colored broken lines denote the calculation results with the ratio e_n^o/e_p^o of 2 (green), 3 (orange), and 4 (red).

was determined as 3.0 from the analysis of the dependence of $\sigma_\mathrm{n}^\mathrm{o}/\sigma_\mathrm{p}^\mathrm{o}$ on e^t. To understand the electronic state considering the configuration coordination of $C_N(0/-)$, it is important to investigate the dependence of $\sigma_\mathrm{n}^\mathrm{o}/\sigma_\mathrm{p}^\mathrm{o}$ on the photon energy $h\nu$, which is discussed in Chapter 6.

References

[1] G. M. Martin, A. Mitonneau, D. Pons, A. Mircea, and D. W. Woodard, J. Phys. C: Solid St. Physics **13**, 3855 (1980).

[2] J. L. Lyons, A. Janotti, and C. G. V. d. Walle, Appl. Phys. Lett. **97**, 152108 (2010).

[3] Y. Tokuda, ECS Trans. **75**, 39 (2016).

[4] R. Armitage, W. Hong, Q. Yang, H. Feick, J. Gebauer, E. R. Weber, S. Hautakangas, and K. Saarinen, Appl. Phys. Lett. **82**, 3457 (2003).

[5] A. Armstrong, A. R. Arehart, D. Green, U. K. Mishra, J. S. Speck, and S. A. Ringel, J. Appl. Phys. **98**, 053704 (2005).

[6] Y. Tokuda, Y. Yamada, T. Shibata, S. Yamaguchi, H. Ueda, T. Uesugi, and T. Kachi, Phys. St. Solidi C **8**, 2239 (2011).

[7] U. Honda, Y. Yamada, Y. Tokuda, and K. Shiojima, Jpn. J. Appl. Phys. **51**, 04DF04 (2012).

[8] T. Tanaka, N. Kaneda, T. Mishima, Y. Kihara, T. Aoki, and K. Shiojima, Jpn. J. Appl. Phys. **54**, 041002 (2015).

[9] T. Tanaka, K. Shiojima, T. Mishima, and Y. Tokuda, Jpn. J. Appl. Phys. **55**, 061101 (2016).

[10] A. Ishitani, K. Okuno, A. Karen, S. Karen, and F. Soeda, in Proceedings of the International Conference on Materials and Process Characterization for VLSI (ICMPC'88), 124 (1988).

[11] H. Okushi1 and Y. Tokumaru, Jpn. J. Appl. Phys. **20**, 261 (1981).

[12] T. Maeda, M. Okada, M. Ueno, Y. Yamamoto, M. Horita, and J. Suda, Appl. Phys. Express **9**, 109201 (2016).

[13] K. Kanegae, M. Horita, T. Kimoto, and J. Suda, Appl. Phys. Express **11**, 071002 (2018).

[14] S. J. Rosner, E. C. Carr, M. J. Ludowise, G. Girolami, and H. I. Erikson, Appl. Phys. Lett. **70**, 420 (1996).

[15] I.-H. Lee, A. Y. Polyakov, N. B. Smirnov, E. B. Yakimov, S. A. Tarelkin, A. V. Turutin, I. V. Shemerov, and S. J. Pearton, Appl. Phys. Express **9**, 061002 (2016).

[16] S. F. Chichibu, Solid St. Sci. Technol. **9**, 015016 (2020).

[17] A. Y. Polyakov, N. B. Smirnov, E. B. Yakimov, S. A. Tarelkin, A. V. Turutin, I. V. Shemerov, S. J. Pearton, K.-B. Bae, and I.-H. Lee, J. Alloys Compd. **686**, 1044 (2016).

[18] M. Kato, T. Asada, T. Maeda, K. Ito, K. Tomita, T. Narita, and T. Kachi, J. Appl. Phys. **129**, 115701 (2021).

Chapter 5

Measurement Methods for Density of Hole Trap H1 in n-Type GaN with Schottky Junction

5.1 Introduction

To obtain the density of hole trap H1 with sub-E_g-light-excited ICTS, it is necessary to estimate the hole occupancy ratio under sub-E_g-light illumination, which is given as:

$$f_\mathrm{T} = \frac{\sigma_\mathrm{n}^\mathrm{o}\Phi}{[\sigma_\mathrm{n}(h\nu) + \sigma_\mathrm{p}(h\nu)]\Phi + e^\mathrm{t}(T)} \left[1 - \exp\left(-\frac{t_\mathrm{p}^\mathrm{o}}{\tau_\mathrm{p}^\mathrm{o}}\right)\right]. \tag{5.1}$$

Here, t_p^o is the width of the optical filling pulse. $\tau_\mathrm{p}^\mathrm{o} = \{[\sigma_\mathrm{n}(h\nu)+\sigma_\mathrm{p}(h\nu)]\Phi+e^\mathrm{t}(T)\}^{-1}$ is time constant during filling pulse To estimate the hole occupancy ratio, the hole photoexcitation rate from the C.B. to the hole trap H1 $e_\mathrm{n}^\mathrm{o} = \sigma_\mathrm{n}^\mathrm{o}\Phi$, the hole photoexcitation rate from the hole trap H1 to the V.B. $e_\mathrm{p}^\mathrm{o} = \sigma_\mathrm{p}^\mathrm{o}\Phi$, and the hole thermal excitation rate from the hole trap H1 to the V.B. e^t are needed.

In Chapter 4, the ratio of photoexcitation rates from the hole trap H1 to the C.B. to that from the V.B. to the H1 trap ($e_\mathrm{n}^\mathrm{o}/e_\mathrm{p}^\mathrm{o}$) was determined under a sub-E_g-light illumination (390 nm). The hole thermal excitation rate e^t from the V.B. to the H1 trap can be directly obtained from a peak of hole trap H1 in each sub-E_g-light-excited ICTS spectrum. In the methods proposed in this chapter, measurement conditions during the filling pulse period are modulated and the sum of the photoexcitation rates $e_\mathrm{n}^\mathrm{o} + e_\mathrm{p}^\mathrm{o}$ is extracted under each measurement condition. Using the sum $e_\mathrm{n}^\mathrm{o} + e_\mathrm{p}^\mathrm{o}$ and the ratio $e_\mathrm{n}^\mathrm{o}/e_\mathrm{p}^\mathrm{o} = 3.0$ for $\lambda = 390$ nm determined in Chapter 4, the e_n^o and e_p^o are separately determined under each measurement condition. In the first method, temperature is modulated with sufficiently long t_P^o under same light illumination condition (temperature change method). In the second method, optical power is modulated with sufficiently long t_P^o under same temperature (optical-power change method). In the third method, the width of the optical filling pulse is modulated

under same light illumination condition and temperature (optical-filling-pulse-width change method).

5.2 Experiments

A Ni/n-type GaN Schottky barrier diode which comprised a MOVPE-grown 3-μm-thick n-GaN homoepitaxial layer on an HVPE-grown n^+-type GaN substrate was fabricated. The depth profiles of dopant (Si) and impurities (H, C, O) are shown in Fig. 5.1. The Si concentration ([Si]) of the n-type GaN layer was obtained via SIMS as 3.0×10^{16} cm^{-3}. The author also confirmed the uniform distribution of [Si] via SIMS depth profiles. [C] of the n-type GaN layer was obtained via raster change mode SIMS [1] as 2×10^{15} cm^{-3}. The n-type GaN layer has the same growth condition of the n-type GaN layer of the p^+-n junction diode used in Chapter 4. The Schottky and ohmic electrodes were formed via deposition of Ni with thickness of 200 nm on the top and Ti/Al/Ti/Au on the back side, respectively. A typically diameter of Schottky electrodes is 400 μm. From capacitance-voltage measurement for the SBD, the net donor density $N_{d,net}$ of 2.8×10^{16} cm^{-3} was obtained. This value is good agreement with [Si] − [C]. It was confirmed that the distributions of $N_{d,net}$ and [Si] were uniform in the depth direction.

Sub-E_g-light-excited ICTS were performed for the GaN SBD at temperature ranging from 300 K to 370 K in temperature change method (described in Sec. 5.6.1) and at 300 K in optical power change method (described in Sec. 5.6.2) and optical filling pulse width change method (described in Sec. 5.6.3). A wavelength of $\lambda = 390$ nm (full width at half maximum of ca. 10 nm) was employed as excitation light. The light source is 61 LEDs connected in series. The absolute maximum rating for DC forward current of the LEDs is 20 mA. To obtain the depletion layer edge correction factor F, measurement bias voltage U_R was varied from 0 V to −10 V. Figure 5.2 shows the capacitance change of the SBD at measurement bias voltage $U_R = -5$ V and $T = 300$ K with illumination of the light. Other than the optical filling pulse width change method, as shown in Fig. 5.2, optical filling pulse width t_P^o was chosen to be sufficiently long the capacitance change during light illumination to be saturated ($t_P^o \gg \tau_P^o$) as illustrated in Fig. 5.2. In optical power change method, Φ was controlled by the number of LEDs and a drive current of each LED (I_{LED}). Φ was monitored as the photocurrent due to internal photoemission of the SBD at $U_R = 0$ V, which is proportional to Φ. Figure 5.3 shows the relationship between I_{LED} and photocurrent. In optical power change method, the optical power is changed in the range shown in Fig. 5.3. In temperature change method and optical filling pulse width change method, I_{LED} for 61 LEDs was set to 15 mA. Then, irradiated photon flux was 7×10^{20} cm^{-2}s^{-1}. Then, the net photon flux which contributes for the photoexcitation of the H1 trap is defined as Φ_0.

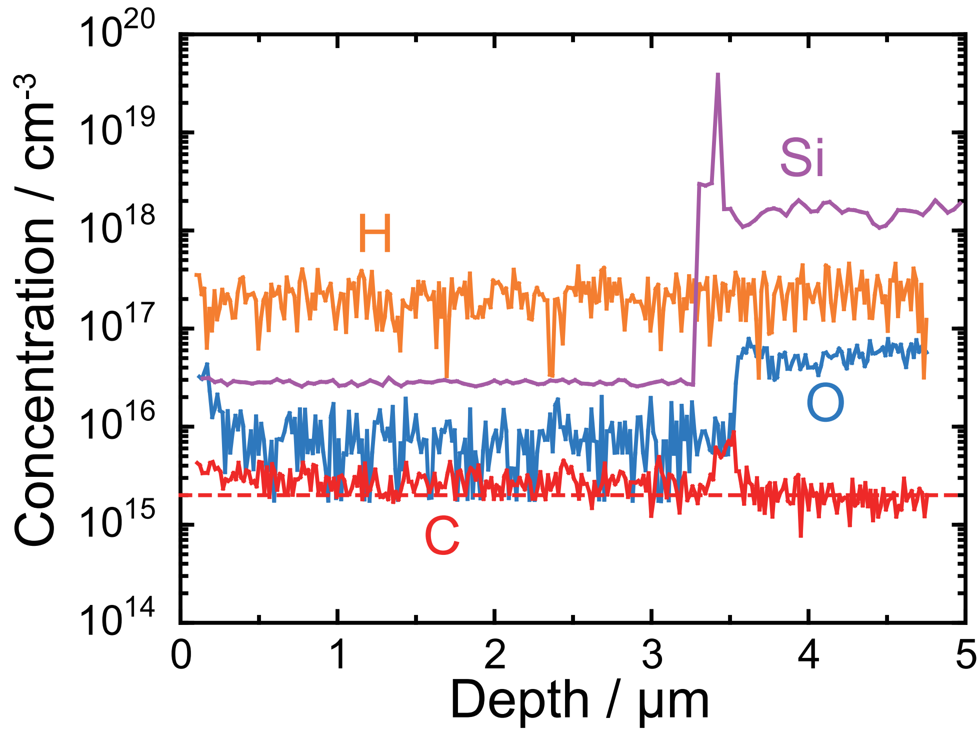

Figure 5.1: The depth profiles of dopant (Si) and impurities (H, C, and O) in the GaN SBD obtained from depth profile mode SIMS. The red broken line denotes the carbon concentration raster change mode SIMS.

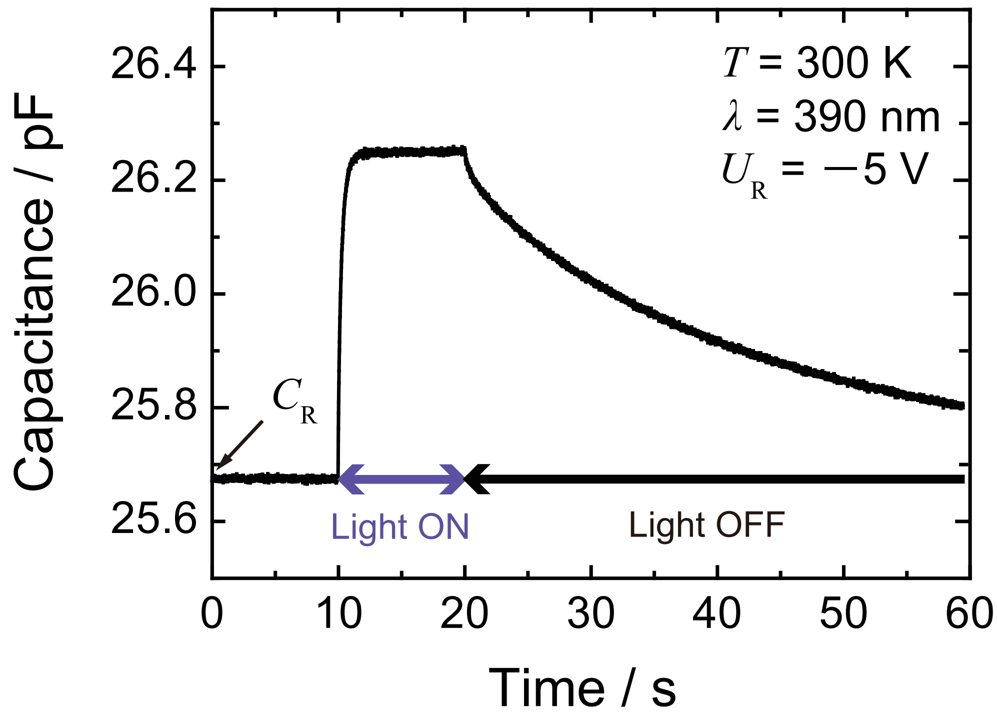

Figure 5.2: Capacitance transient of SBD with sub-E_g-light irradiation at $U_R = -5$ V and $T = 300$ K.

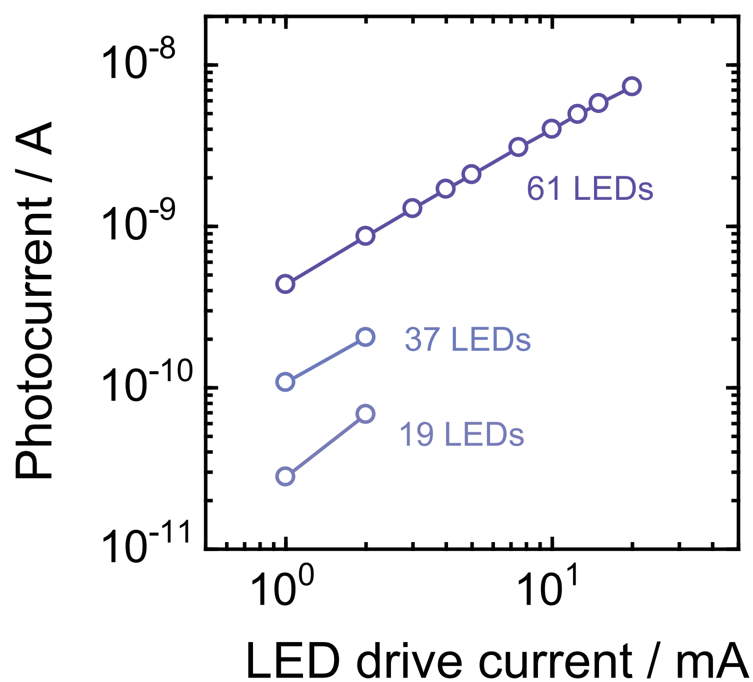

Figure 5.3: Photocurrent of the GaN SBD at zero bias under 390 nm LED light irradiation. To adjust optical power, which is monitored as the photocurrent, the number of LEDs and the drive current of LEDs are changed. When the drive current of 61 LEDs is 15 mA, irradiated photon flux is 7×10^{20} cm^{-2}s^{-1}.

5.3 Sub-bandgap-light-excited ICTS for GaN Schottky Junction

Figure 5.4 shows a sub-E_g-light-excited ICTS spectrum of the GaN SBD under a typical measurement condition (T = 300 K, U_R = −5 V, $\Phi = \Phi_0$) and the insertion shows the Arrhenius plot of $\ln(\tau_p T^2)$ versus the reciprocal temperature with the assumption that the hole capture cross-section (σ_p) is independent of temperature. In Fig. 5.4, the H1 trap ($E_T = E_V + 0.87$ eV, $\sigma_p = 7\times10^{-14}$ cm^2) is detected. These values agree well with the reported values for the H1 trap [2–9].

5.4 Uniform Photoexcitation of Hole Trap H1 in In-plane Direction

Figure 5.5 shows penetration lengths of above-E_g-light and sub-E_g-light in conductivity GaN substrates (open symbols [10, 11]) and semi-insulating (SI)-GaN substrate [12]. A penetration length of sub-E_g-light is several millimeters for a conductivity GaN substrate [11], thus multiple reflects between the Schottky and ohmic electrodes occurs and the depletion layer under the Schottky electrode can be spatially uniformly irradiated by sub-E_g-light even the Schottky electrode is thick. It was reported that internal photoemission current due to sub-E_g-light is independent of Schottky electrode size [13]. The sub-E_g-light-excited ICTS was performed at U_R = −5 V and T = 300 K for several GaN Schottky barrier diodes on the same epilayer with different Schottky electrode diameters. Figure 5.6 shows the dependence of the measured density of hole trap H1 $f_T F N_T$ on the Schottky electrode diameter d in an n-type GaN on n$^+$-type GaN substrate [Fig. 5.7(a)]. Using a peak intensity of sub-E_g-light-excited ICTS spectrum ΔC, the measured density of hole trap H1 $f_T F N_T$ is calculated as:

$$\begin{aligned}\tilde{N}_T &= 2\frac{\Delta C}{C_R} N_{d,net} \\ &= f_T F N_T. \end{aligned} \tag{5.2}$$

It was confirmed that the measured density of hole trap H1 $\tilde{N}_T$ is independent of the Schottky electrode size in the diameter of ranging from 300 μm to 1200 μm. This result suggests that multiple internal reflection occurs between the surface Schottky electrode and the backside ohmic electrode and despite being under the shadow of the Schottky electrode, the depletion layer is spatially uniformly illuminated as shown in Fig. 5.7(a), i.e. the depletion layer and the region where hole traps coincide.

It is noted that the spatially uniform photoexcitation of hole trap does not occur when a Fe-doped SI-GaN substrate is utilized because of the short penetration length of sub-E_g-light [12]. Figure 5.8 shows the dependence of the measured density of hole trap H1 $f_T F N_T$

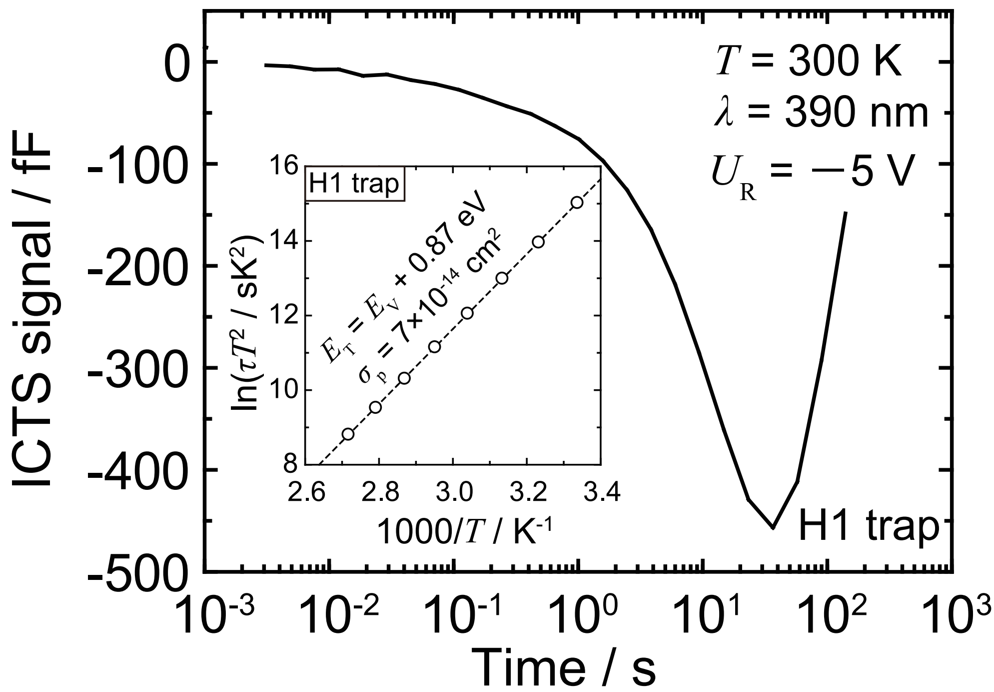

Figure 5.4: Sub-E_g-light-excited ICTS spectrum under a standard measurement condition (T = 300 K, U_R = –5 V, $\Phi = \Phi_0$). The insertion shows the Arrhenius plot of $\ln(\tau_p T^2)$ versus the reciprocal temperature. The H1 trap ($E_T = E_V + 0.87$ eV, $\sigma_p = 7 \times 10^{-14}$ cm^2) is detected.

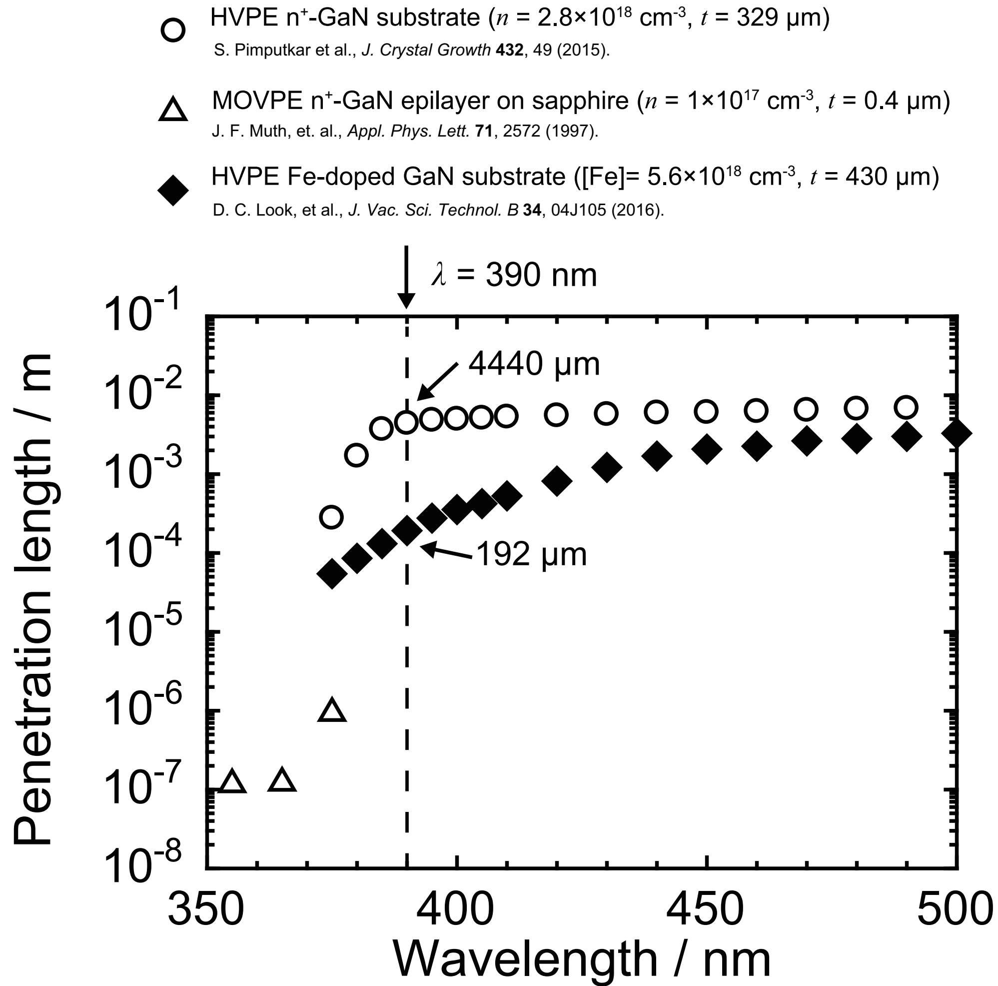

Figure 5.5: Penetration length of above-E_g-light and sub-E_g-light in GaN. The open circles denote penetration length in n^+-type GaN substrate [11]. The open triangles denote penetration length in n^+-type GaN epilayer on sapphire substrate [10]. The closed diamonds denote penetration length in Fe-doped SI-GaN substrate [12].

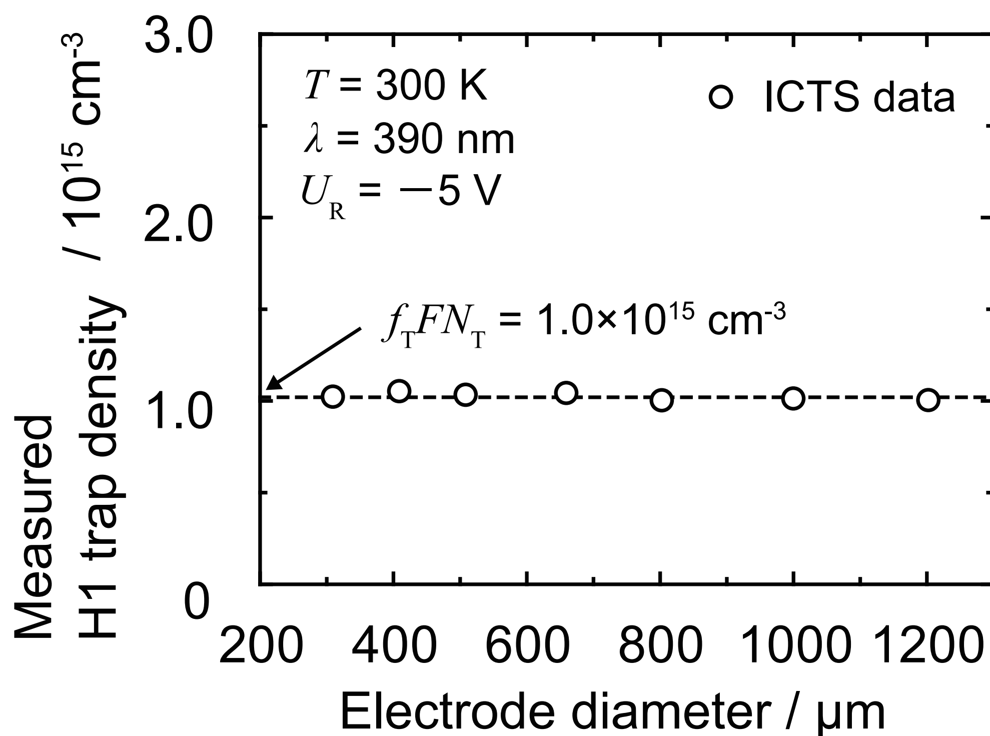

Figure 5.6: Dependence of the measured H1 trap density on the Schottky electrode diameter. The measured H1 trap density of 1.0×10^{15} cm^{-3} under a standard measurement condition is independent of the Schottky electrode diameter in the diameter of ranging from 300 µm to 1200 µm.

(a) n-type GaN layer on n⁺-type GaN sub.

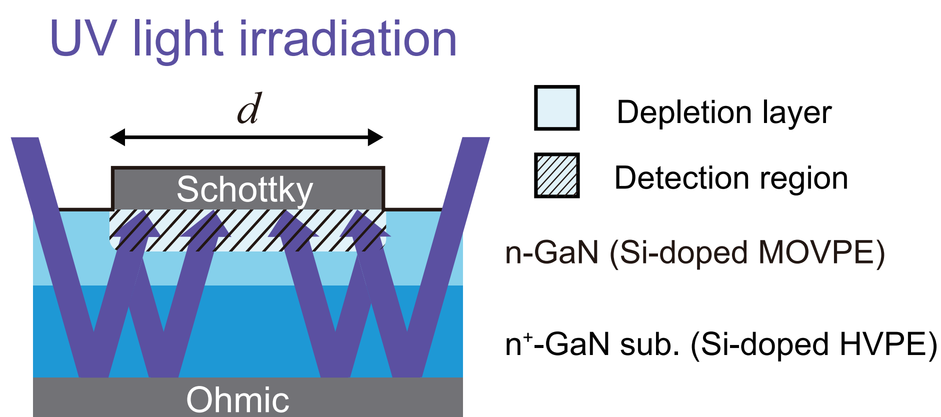

(b) n-type GaN layer on SI-GaN sub.

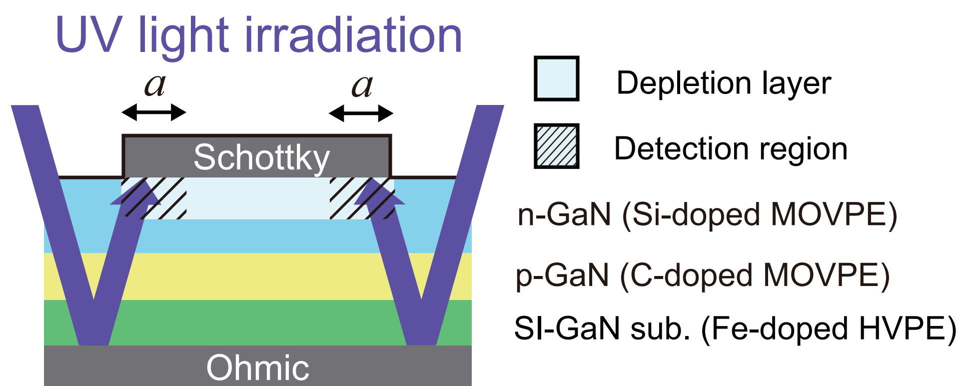

Figure 5.7: Cross views of n-type GaN Schottky barrier diodes fabricated with (a) n-type GaN layer on n^+-type GaN substrate and (b) n-type GaN layer on Fe-doped SI-GaN substrate.

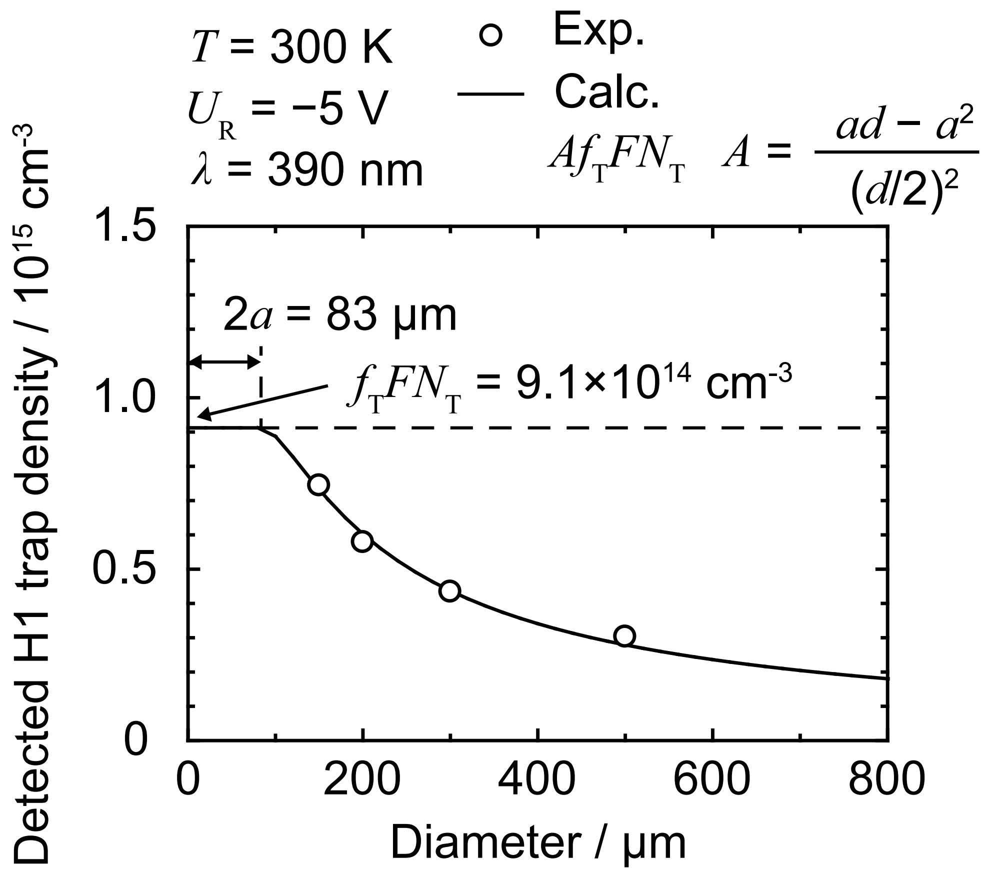

Figure 5.8: Dependence of the measured H1 trap density on the Schottky electrode diameter fabricated with the n-type GaN layer on SI-GaN substrate.

on the Schottky electrode diameter in an n-type GaN on SI-type GaN substrate [Fig. 5.7(b)]. In Fig. 5.8, the measured density of hole trap H1 $f_T F N_T$ decreases with increasing the Schottky electrode diameter. It was confirmed this spatially ununiform photoexcitation of the hole trap H1 in n-type GaN layers on Fe-doped SI GaN substrate. Here, it is assumed that the region where the hole traps are photoexcited is limited to vicinity of the Schottky electrode edge. Then, the measured density of hole trap H1 $\tilde{N}_T$ is given as:

$$\begin{aligned}\tilde{N}_T &= A f_T F N_T \\ &= \frac{ad - a^2}{(d/2)^2}.\end{aligned} \tag{5.3}$$

Here, A is an area correction factor and a is a width of the region where the hole traps are photoexcited near the Schottky electrode edge. Curve fitting with the calculated $\tilde{N}_T(d)$ (black solid line in Fig. 5.8) to the measured $\tilde{N}_T(d)$ (open circles in Fig. 5.8) was performed with the fitting parameters a and $f_T F N_T$ in Eq. 5.3. From the curve fitting, $a = 42$ nm and $f_T F N_T = 9.1 \times 10^{14}$ cm^{-3} were estimated. To accurately quantify $f_T F N_T$ in n-type GaN layers on SI-GaN substrates, it is necessary to measure $f_T F N_T(d)$ with small Schottky diameters ($\sim 2a$).

The photoconductivity of substrate is important for the spatially uniform photoexcitation of deep level using sub-E_g-light unless a Schottky barrier diode is irradiated from backside or a semi-transparent Schottky electrode is utilized. In this study, the Schottky electrode diameter of 400 μm was employed for n-type GaN Schttoky diodes on n$^+$-type GaN substrates.

5.5 Depletion Layer Edge Correction Factor on Measured Density of Hole Trap H1 in Sub-bandgap-light-excited ICTS

Under each measurement condition, sub-E_g-light-excited ICTS with various U_R was performed for the GaN SBD and remove the effect of the depletion layer edge correction factor F on the measured density of hole trap H1. The depletion layer edge correction factor F is given as [7, 14]:

$$F = \left(1 - \frac{\lambda_R}{w}\right)^2. \tag{5.4}$$

Here, w_R is the depletion layer width when measurement vias voltage U_R is applied. λ_R is the width of the region where the quick carrier recombination via the hole trap H1 in the depletion layer near the depletion layer edge is dominant. Under sufficient long filling pulse width and sufficient strong photon flux, λ_R is given as [7]:

$$\lambda_R = L_D \sqrt{2\ln\left(\frac{N_{d,net} C_n}{e_p \ln 2}\right)}. \tag{5.5}$$

Here, $L_D = \sqrt{(\varepsilon_s k_B T)/(ne^2)}$ is the Debye length. $\varepsilon_s = 10.4\varepsilon_0$ is the dielectric constant of GaN [15] where ε_0 is the vacuum dielectric constant, k_B is the Boltzmann constant, n is the free carrier concentration, assuming that $n = N_{d,net}$, and e is an elementary charge. C_n is the electron capture coefficient and is the product of electron capture cross-section σ_n and electron thermal velocity $v_{th,n}$.

In Fig. 5.9, the dependence of the measured density of hole trap H1 $\tilde{N}_T = f_T F N_T$ on the depletion layer width w_R is shown. Curve fitting with the calculated $\tilde{N}_T(w_R)$ (black solid line in Fig. 5.9) to the measured $\tilde{N}_T(w_R)$ (open circles in Fig. 5.9), which is calculated from the ICTS peak intensities of the hole trap H1 using Eq. 5.2, was performed with the fitting parameters $f_T N_T$ and λ_R in Eqs. 5.2 and 5.4. From the curve fitting, $\lambda_R = 110$ nm and the density of hole occupied hole trap H1 during filling pulse period $f_T N_T = 1.8 \times 10^{15}$ cm^{-3} were obtained for the standard measurement condition ($T = 300$ K, $\Phi = \Phi_0$). The same experiments and analyzes as above were performed by changing the measurement temperature, optical power, or optical filling pulse width and λ_R was investigated under each measurement condition. In Fig. 5.10, the dependence of λ_R on (a) hole thermal excitation rate, which means temperature dependence, (b) optical power, and (c) optical filling pulse width are shown as the open circles. As shown in Fig. 5.10, λ_R decreases with elevating temperature but is almost independent of optical power and independent of optical filling pulse width. These results are reasonably explained by considering Eq. 5.5. To obtain accurate density of hole occupied hole trap H1 $f_T N_T$, in temperature change method, λ_R should be measured at each temperature. On the other hand, in optical power change method and optical filling pules width change method, evaluation of λ_R is required a certain condition. In this study, to obtain $f_T N_T$ under each measurement condition, F which was obtained by using λ_R in Fig. 5.10 was used.

5.5.1 Electron Capture of Hole Trap H1 near Depletion Layer Edge during Optical Filling Pulse

When an SBD is used to investigate carrier traps with DLTS or ICTS measurements, the carrier trap density calculated from the DLTS or ICTS peak intensity ($\tilde{N}_T$) has the following relationship with the actual trap density $N_T(x)$ [14, 16]:

$$\begin{aligned}\tilde{N}_T &= 2\frac{\Delta C}{C_R} N_{d,net} \\ &= \frac{2}{w_R^2}\int_{x_{start}}^{x_{end}} x N_T(x)\left[f_T(x,0) - f_T(x,\infty)\right] \mathrm{d}x,\end{aligned} \tag{5.6}$$

$f_T(x,t)$, where x is distance from the junction and t is time from application of the measurement bias voltage, is the time evolution of the depth profile of the carrier occupancy ratio of the deep levels. In the case of sub-E_g-light-excited ICTS to detect deep levels near the valence band maximum on an n-type SBD, $f_T(x,t)$ indicates the time evolution of the depth profile of the hole occupancy ratio of the deep levels. In this study, it is assumed

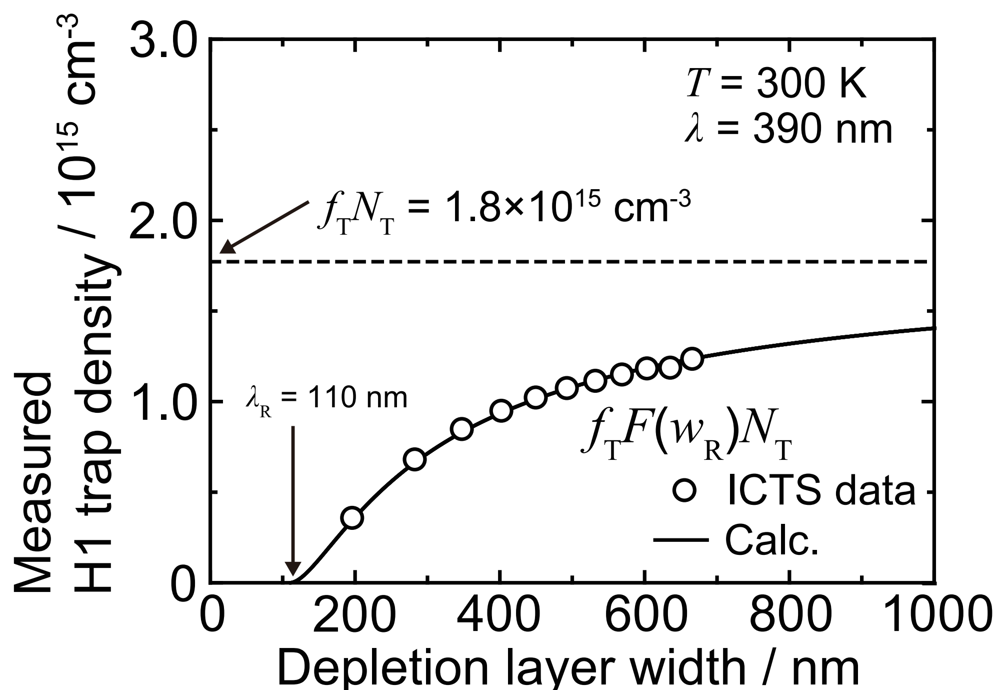

Figure 5.9: Dependence of the measured H1 trap density on the depletion layer width, which is varied by changing the measurement bias voltage U_R in the sub-E_g-light-excited ICTS at $T = 300$ K and $\Phi = \Phi_0$. The open circles denote the ICTS data and black solid line shows the fitting curve. From the curve fitting based on Eqs. 5.2 and 5.4, the hole-occupied H1 trap density of 1.8×10^{15} cm^{-3} (black broken line) and λ_R of 110 nm were obtained at $T = 300$ K and $\Phi = \Phi_0$.

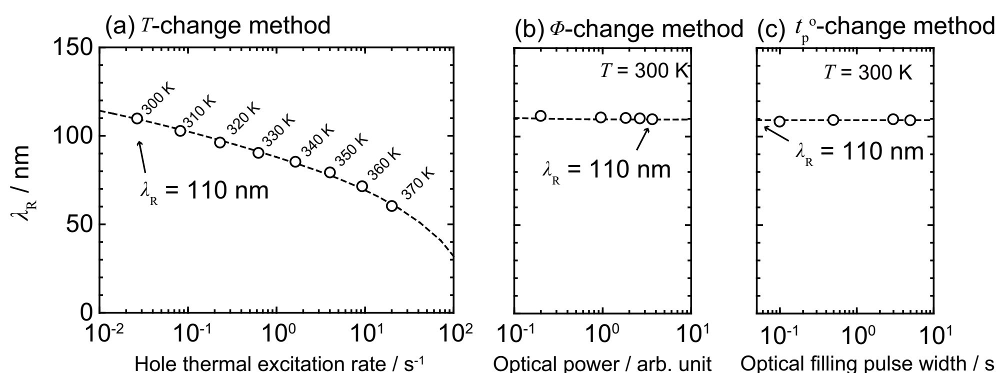

Figure 5.10: Dependence of λ_R on (a) hole thermal excitation rate (temperature), (b) optical power, and (c) optical filling pulse width.

that the net donor density $N_{\mathrm{d,net}}$ and density of deep level have no distribution in the depth direction. In Fig. 5.11, band diagrams of an n-type Schottky barrier diode in sub-E_{g}-light-excited ICTS are shown (a) during optical filling pulse, (b) immediately after optical filling pulse cutoff, and (c) during measurement period. When a bias voltage is applied for the Schottky junction, electrons exist in the conduction band near the depletion layer. The depth profile of electron concentration can be assumed as [14, 17]:

$$n = \begin{cases} N_{\mathrm{d,net}}(w)\exp\left[-\frac{(w-x)^2}{2L_{\mathrm{D}}(w)^2}\right] & ,0\ \mathrm{nm} < x < w \\ N_{\mathrm{d,net}}(x) & ,w \le x, \end{cases} \tag{5.7}$$

Here, w is the depletion layer width. In Eq. (5.7), it is assumed that the donor is completely ionized. Figure 20 shows depth profile of (a) electron concentration, (b) rates, (c) time constant, and (d) hole occupancy ratio in the case of the n-type SBD GaN used in this study at $T = 300$ K and $U_{\mathrm{R}} = -5$ V calculated using the extracted parameters. The trailing off of the electron concentration shown in Fig. 5.12(a) results in the quick carrier recombination via deep levels near the depletion layer edge, i.e., hole occupied deep levels capture electrons in the conduction band during optical filling pulse period [Fig. 5.11(a)] and immediately after optical filling pulse cutoff [Fig. 5.11(b)]. In the depletion layer, whether the quick carrier recombination is dominant or not depends on the relationship between $e_{\mathrm{n}}^{\mathrm{o}}$, $e_{\mathrm{p}}^{\mathrm{o}}$, e^{t}, and $nC_{\mathrm{n}}(C_{\mathrm{n}} = \sigma_{\mathrm{n}} v_{\mathrm{th,n}}$ is the electron capture coefficient, where σ_{n} is the electron capture cross-section and $v_{\mathrm{th,n}}$ is the thermal electron velocity) as shown in Fig. 5.12(b). The hole occupancy ratio which electron capture is taken in account is given as:

$$\begin{aligned} f_{\mathrm{T}}(x,t) &= \frac{e_{\mathrm{n}}^{\mathrm{o}}}{e_{\mathrm{n}}^{\mathrm{o}} + e_{\mathrm{p}}^{\mathrm{o}} + e^{\mathrm{t}} + n(x,w)C_{\mathrm{n}}}\left(1 - \exp\left(-\frac{t_{\mathrm{P}}^{\mathrm{o}}}{\tau_{\mathrm{p}}^{\mathrm{o}}(x,w)}\right)\right)\exp\left(-\frac{t}{\tau_{\mathrm{p}}(x,w)}\right) \\ &= f_{\mathrm{T}}(x,0)\exp\left(\frac{-t}{\tau_{p}(x,w)}\right), \end{aligned} \tag{5.8}$$

where $\tau_{\mathrm{p}}^{\mathrm{o}}(x,w) \equiv 1/(e_{\mathrm{n}}^{\mathrm{o}} + e_{\mathrm{p}}^{\mathrm{o}} + e^{\mathrm{t}} + n(x,w)C_{\mathrm{n}})$ and $\tau_{\mathrm{p}}(x,w) \equiv 1/(e^{\mathrm{t}} + n(x,w)C_{\mathrm{n}})$. Even though spatially uniformly excitation occurs, the hole occupancy ratio has distribution in the depth direction due to the electron capture rate nC_{n} when a measured bias voltage is applied as shown in Fig. 5.12(d). In the depletion layer far from the edge, i.e., $n(x,w) \simeq 0$, Eq. 5.8 can be approximated as Eq. 6.4. In sub-E_{g}-light-excited ICTS spectra, deep levels with $\tau_{\mathrm{p}}(x,w) = 1/e^{\mathrm{t}}$ are detected as ICTS peaks as shown in Fig. 5.4. Thus, to measure a density of deep level near the valence band maximum, it should be considered the depth profile of the hole occupancy ratio during the optical filling pulse period $f_{\mathrm{T}}(x,0)$ and the depth profile of the decay during the measurement period $\exp[-t/\tau_{\mathrm{p}}(x,w)]$. As show in Fig. 5.12(d) by the violet broken line, when the position at which $f_{\mathrm{T}}(x,0) - f_{\mathrm{T}}(w,0)$ is half of the value at the Schottky junction $[f_{\mathrm{T}}(0,0) - f_{\mathrm{T}}(w,0)]$ is defined as $x = w - \lambda_{\mathrm{P}}^{\mathrm{o}}$, $\lambda_{\mathrm{P}}^{\mathrm{o}}$ with sufficiently long $t_{\mathrm{P}}^{\mathrm{o}}$ is given as:

$$\lambda_{\mathrm{P}}^{\mathrm{o}} \simeq L_{\mathrm{D}}\sqrt{2\ln\left(\frac{N_{\mathrm{d,net}}C_{\mathrm{n}}}{e_{\mathrm{n}}^{\mathrm{o}} + e_{\mathrm{p}}^{\mathrm{o}} + e^{\mathrm{t}}}[1 + C]\right)}, \tag{5.9}$$

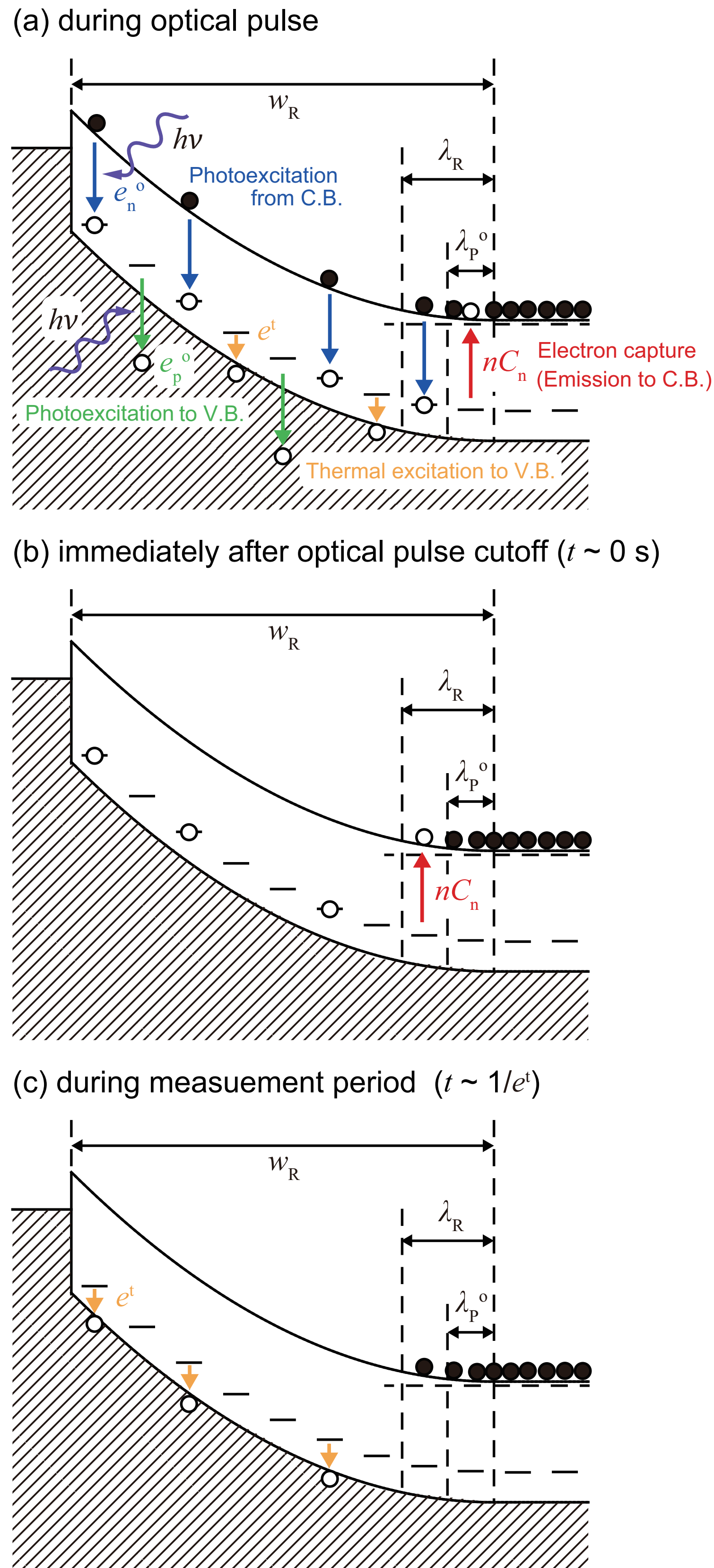

Figure 5.11: Band diagrams of an SBD (a) during optical filling pulse period, (b) immediately after optical pulse cutoff, and (c) during measurement period. In the region near the depletion layer edge, the quick carrier recombination via the H1 trap, i.e., the electron capture, is considered during optical filling pulse period and immediately after optical filling pulse cutoff.

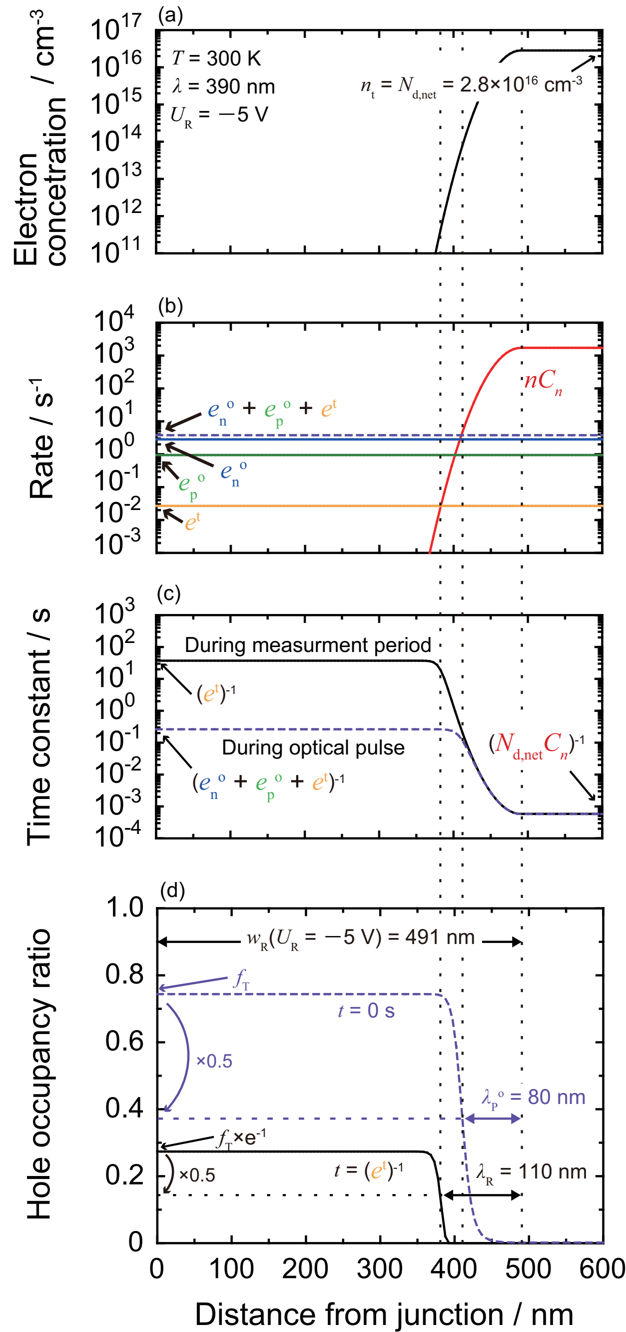

Figure 5.12: Depth profiles from an Schottky barrier junction of (a) electron concentration, (b) rates, (c) time constant, and (d) hole occupancy ratio of the H1 trap when measurement bias voltage of –5 V is applied. In Fig. 5.12(b), the red, orange, green, and blue solid lines denote the depth profiles of the electron capture rate, hole thermal excitation to the V.B. rate, hole photoexcitation to the V.B. rate, and hole photoexcitation from the C.B. rate, respectively. The violet broken line denotes the sum of photoexcitation from the C.B. and photo and thermal excitation to the V.B. rates. In Fig. 5.12(c), the violet broken and black solid lines denote the depth profiles of time constant during the optical filling pulse period and during the measurement period. In Fig. 5.12(d), the violet broken and black solid lines denote the depth profiles of the hole occupancy ratio of the H1 trap during the optical filling pulse period and measurement period, respectively.

where $C \equiv 2(e_n^o + e_p^o + e^t)/(N_{d,net}C_n)$. When $N_{d,net}C_n$ is sufficiently larger than e_n^o, i.e., $f_T(x,0)$ can be considered equal to 0 in the neutral region, the term of C can be negligible. Then, $n(w - \lambda_P^o, w)C_n$ is equal to $e_n^o + e_p^o + e^t$ as shown in Fig. 5.12(b). In this study, λ_P^o under the standard measurement condition (T = 300 K, $\Phi = \Phi_0$, t_P^o = 3 s) of 80 nm was estimated from calculation using the extracted parameters. λ_P^o can not be directly measured in the standard sub-E_g-light-excited ICTS with measurement sequencies such as the sequence shown in Fig. 5.13 because λ_P^o is smaller than λ_R in the measurements.

To conform λ_P^o, sub-E_g-light-excited ICTS with a measurement sequence shown in Fig. 5.14 was performed. In this measurement, during filling pulse period, electrical pulse and optical pulse are applied at the same time. In Fig. 5.15, band diagrams of an n-type Schottky barrier diode in sub-E_g-light-excited ICTS with the filling pulses are shown (a) during filling pulses (electrical pulse and optical pulse), (b) during measurement period. During filling pulse period, the hole traps in 0 nm $< x \leq w_P - \lambda_P^o$ can be photoexcited [Fig. 5.15(a)] and the hole occupied deep levels are detectable during measurement period [Fig. 5.15(b)]. w_P is the depletion layer width during filling pulse period. Figure 5.16 shows the calculation depth profile of the hole occupancy ratio of the hole trap H1 assuming a measurement condition based on the standard one (T = 300 K, $\Phi = \Phi_0$, $U_R = -5$ V) and filling pulse bias voltage $U_P = -1$ V. When $w_P - \lambda_P^o < w_R - \lambda_R$ is held, the quick carrier recombination immediately after light cutoff does not occur because in $0 < x \leq w_P - \lambda_P^o$, existence of electrons in the conduction band can be negligible during the measurement period as shown in Fig. 5.15(b). When $w_R - \lambda_R \leq w_P - \lambda_P^o$ is held, the quick carrier recombination immediately after light cutoff occurs. Thus, the measured density of deep level is given as:

$$\tilde{N}_T = f_T F N_T,$$
$$F = \begin{cases} \left(1 - \frac{\lambda_R}{w_R}\right)^2 & , w_P - \lambda_P^o < w_R - \lambda_R \\ \frac{(w_P - \lambda_P^o)^2}{w_R^2} & , w_R - \lambda_R \leq w_P - \lambda_P^o. \end{cases} \quad (5.10)$$

Fig. 5.17 shows the dependence of measured density of hole trap H1 on the depletion layer width with the filling pulse bias voltage $U_P = -1$ V (violet open circles) and $U_P = 0$ V (blue open circles). The black solid line denotes the dependence of the measured density of hole trap H1 on the depletion layer width considering the quick carrier recombination immediately after light cutoff and $\lambda_R = 110$ nm and $f_T N_T = 1.8 \times 10^{15}$ cm^{-3} were used for calculation. The violet and blue solid lines denote the calculation curves using $\lambda_P^o = 80$ nm and $f_T N_T = 1.8 \times 10^{15}$ cm^{-3} for $U_P = -1$ V and $U_P = 0$ V, respectively. The experimental data is in a good agreement with the calculation curves without curve fitting. It is confirmed that $\lambda_P^o = 80$ nm under the standard measurement condition is reasonable.

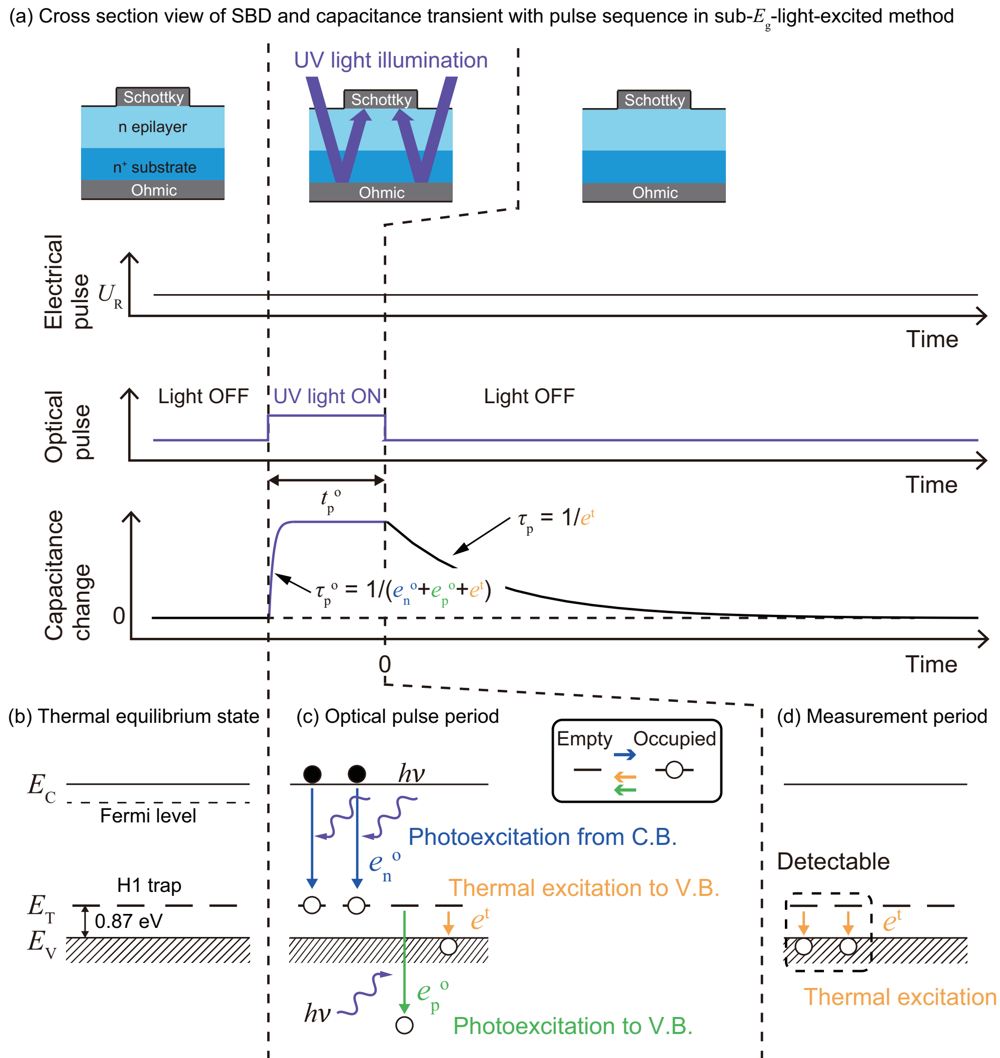

Figure 5.13: (a) Cross-section view of SBD and capacitance transient with UV irradiation. Band diagram of the H1 trap in n-type GaN (b) for steady state, (c) under sub-E_g-light irradiation and (d) after interruption of sub-E_g-light irradiation.

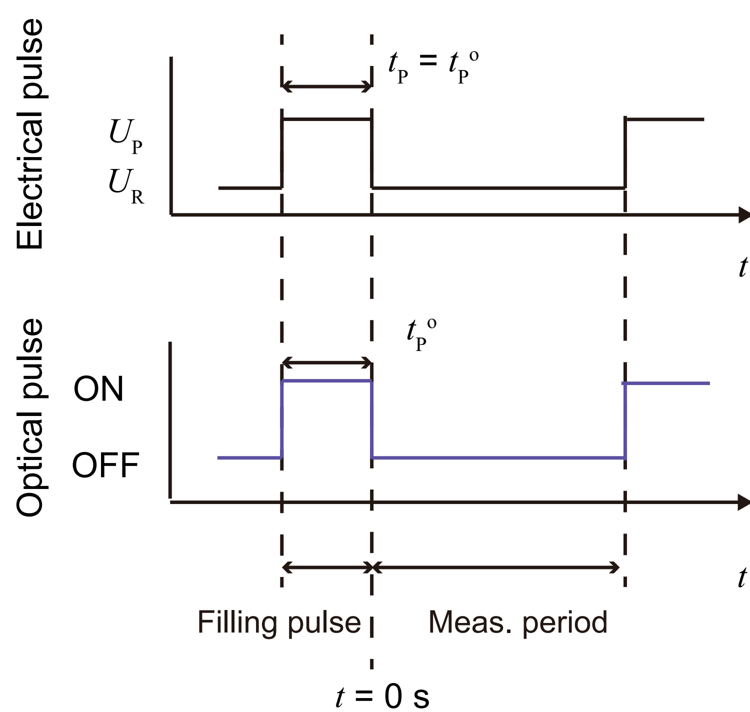

Figure 5.14: Pulse sequence with electrical and optical filling pulses (U_P, $t_P = t_P^o = 3$ s).

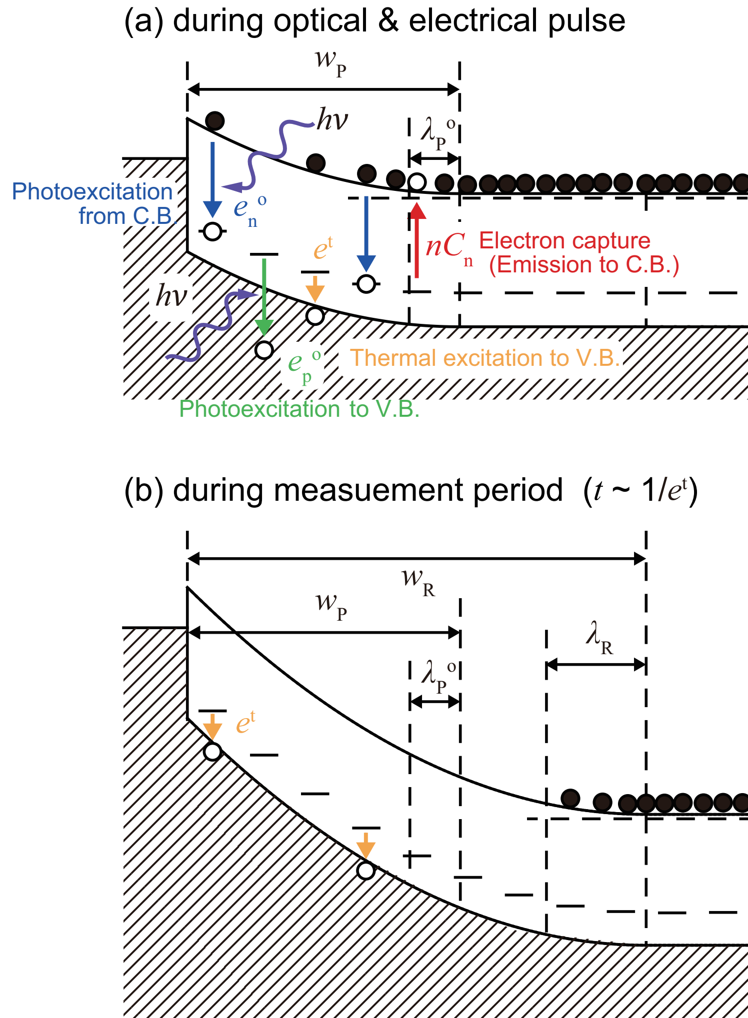

Figure 5.15: Band diagrams of an SBD (a) during electrical and optical filling pulses period and (b) during measurement period. During electrical and optical filling pulses period, electron capture occurs in the region near the depletion layer edge.

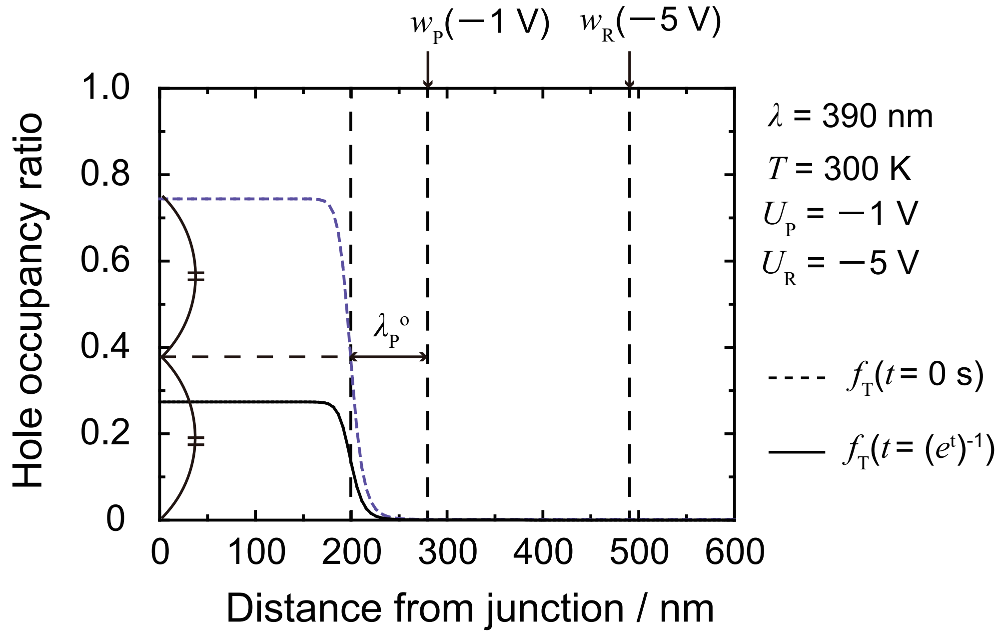

Figure 5.16: Depth profiles of the hole occupancy ratio at $t = 0$ s (violet broken line) and $t = 1/e^t$ when $U_P = -1$ V and $U_R = -5$ V are applied.

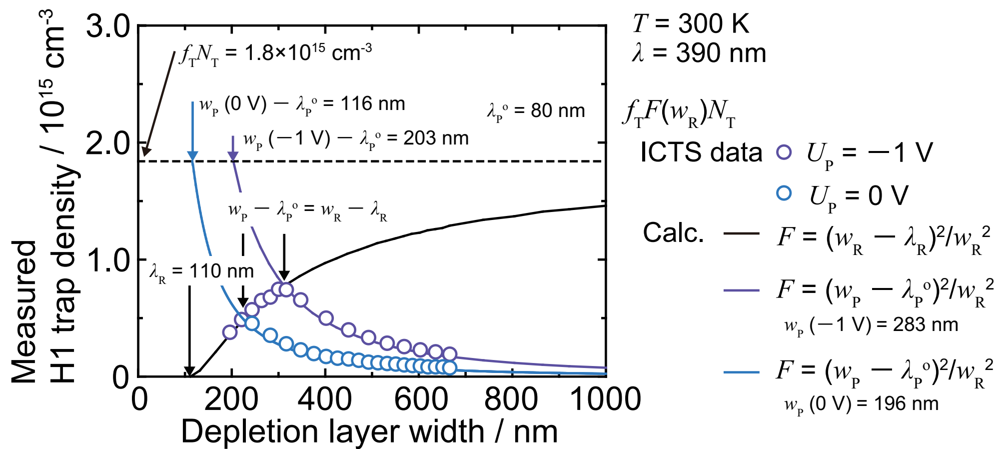

Figure 5.17: Dependence of the measured H1 trap density on the depletion layer width. The violet and blue open circles denote experimental data with $U_P = -1$ V and $U_P = 0$ V, respectively. The violet and blue solid lines are calculated based on Eqs. 5.2 and 5.10 with $U_P = -1$ V and $U_P = 0$ V, respectively. The black solid line denotes calculation result based on Eqs. 5.2 and 5.4.

5.5.2 Quick Carrier Recombination via Hole Trap H1 near Depletion Layer Edge

As show in Fig. 5.12(d) by the black solid line, when the position at which $f_\mathrm{T}(x, 1/e^\mathrm{t})$ is half of the value at the Schottky junction $[f_\mathrm{T}(0, 1/e^\mathrm{t})]$ is defined as $x = w - \lambda_\mathrm{R}$, λ_R is given as:

$$\lambda_\mathrm{R} \simeq L_\mathrm{D}\sqrt{2\ln\left(\frac{N_\mathrm{d,net}C_\mathrm{n}[1 + A - B]}{e^\mathrm{t}\ln 2}\right)}, \tag{5.11}$$

where $A \equiv e^\mathrm{t}/(e^\mathrm{o}_\mathrm{n} + e^\mathrm{o}_\mathrm{p} + e^\mathrm{t})$ and $B \equiv (t^\mathrm{o}_\mathrm{P} e^\mathrm{t})/(\exp((t^\mathrm{o}_\mathrm{P})/(1/(e^\mathrm{o}_\mathrm{n} + e^\mathrm{o}_\mathrm{p} + e^\mathrm{t}))) - 1)$. To obtain Eq. 5.11, an approximation of McLaughlin expansion $\ln(1 + \mathrm{y}) \simeq \mathrm{y}$ is applied and $N_\mathrm{d,net}C_\mathrm{n} \ll e^\mathrm{t}$ is assumed, i.e.,

$$f_\mathrm{T}(x, 1/e^\mathrm{t}) = \begin{cases} f_\mathrm{T}(0, 1/e^\mathrm{t}) & , 0\ \mathrm{nm} < x \leq w_\mathrm{R} - \lambda_\mathrm{R} \\ 0 & , w_\mathrm{R} - \lambda_\mathrm{R} < x. \end{cases} \tag{5.12}$$

As shown in Eq. 5.8, during the measurement period, the hole occupancy ratio which has distribution in the depth direction at $t = 0$ s [violet broken line in Fig. 5.12(d)] decays with the time constant which has distribution in the depth direction [black solid line in Fig. 5.12(c)]. Thus, λ_R depends on not only time constant during measurement period $\tau_p(x, w)$ but also hole occupancy ratio during optical filling pulse period $f_\mathrm{T}(x, 0)$. The term A in Eq. 5.11 indicates the effect of the dependence of $f_\mathrm{T}(x, 0)$ on optical power. When e^o_n and e^o_p is sufficiently larger than e^t, the term A in Eq. 5.11 can be negligible. The term B in Eq. 5.11 indicates the effect of $f_\mathrm{T}(x, 0)$ on optical filling pulse width. When t^o_P is sufficiently long than $1/(e^\mathrm{o}_\mathrm{n} + e^\mathrm{o}_\mathrm{p} + e^\mathrm{t})$, the term B in Eq. 5.11 can be negligible. Therefore, when Φ is sufficiently strong and t^o_P is sufficiently long as in the case of the standard measurement condition, the terms A and B in Eq. 5.11 can be negligible and Eq. 5.11 can be approximated as Eq. 5.5. Then, as shown in Fig. 5.12(b), $n(w - \lambda_\mathrm{R}, w)C_\mathrm{n}$ is equal to $e^\mathrm{t}\ln 2$.

In sub-E_g-light-excited ICTS, deep levels which has time constant of $1/e^\mathrm{t}$ can be contribute to the ICTS peak and can be detectable. Considering the quick carrier recombination via hole traps near the depletion layer edge and assuming $f_\mathrm{T}(x, \infty) = 0$, the depth profile of the hole occupancy ratio can be described as the Eq. 5.6 and the measured density of deep level given as:

$$\begin{aligned} \tilde{N}_\mathrm{T} &= \frac{2}{w_\mathrm{R}^2}\int_{x_\mathrm{start}}^{x_\mathrm{end}} x N_\mathrm{T}\left[f_\mathrm{T}(x, 0) - 0\right]\mathrm{d}x \\ &= f_\mathrm{T} F N_T, \end{aligned} \tag{5.13}$$

where $f_\mathrm{T} \equiv f_\mathrm{T}(0, 0)$. In sub-$E_\mathrm{g}$-light-excited ICTS, it can be assumed that $x_\mathrm{start} = 0$ nm and $x_\mathrm{end} = w_\mathrm{R} - \lambda_\mathrm{R}$. Then, F is given as:

$$F = \left(1 - \frac{\lambda_\mathrm{R}}{w_\mathrm{R}}\right)^2. \tag{5.14}$$

The effect of distribution in the depth direction of hole occupancy ratio due to the quick carrier recombination on the measured density of deep level $\tilde{N}_T$ can be described as the depletion layer edge correction factor F. $\tilde{N}_T$ asymptotes to $f_T N_T$ with increasing the depletion layer width, as shown in Fig. 5.9, and from the experimental data of $\tilde{N}_T(w_R)$, $f_T N_T$ and λ_R can be extracted.

5.5.3 Discussion

Figure 5.18 shows dependences of the depth profile of the hole occupancy ratio at $t = 1/e^t$ on (a) temperature, (b) optical power, and (c) optical filling pulse width. The blue solid lines in Figure 5.18(a)-(c) are calculated using extracted parameters ($e_n^o + e_p^o = 3.8\ s^{-1}$ and $e^t = 2.7 \times 10^{-2}\ s^{-1}$) under the standard measurement condition ($T = 300$ K, $\Phi = \Phi_0$, $t_P^o = 3$ s, $U_R = -5$ V). Based on Eq. 5.11, each dependence of λ_R is calculated and shown in 5.11(a)-7(c) as black broken lines. As shown in Fig. 5.18(a), the hole occupancy ratio $f_T(0, 1/e^t)$ and λ_R decrease with elevating temperature, i.e., increasing hole thermal excitation rate e^t. As shown in Eqs. 5.8, hole occupancy ratio decreases with increasing e^t. Temperature dependence of λ_R is mainly due to e^t. It can be understood from shift of the cross point of $e^t \ln 2$ and nC_n in Fig. 5.12(b).

The dependence of λ_R on the optical power is due to quick carrier recombination via the hole trap near the depletion layer edge during optical filling pulse period and is described as the term A in Eq. 5.11. Under the standard measurement condition, the effect of term A in Eq. 5.11 on λ_R is sufficiently small and can be negligible ($A = 7 \times 10^{-3}$ under the standard measurement condition). When optical power decreases, $e_n^o + e_p^o$ decreases and the cross point of $e_n^o + e_p^o + e^t$ and nC_n becomes close to the cross point of $e^t \ln 2$ and nC_n, i.e., λ_P^o increases and becomes close to λ_R. Under small Φ with sufficiently long t_P^o, the term A in Eq. 5.11 asymptotes to unity (ex. $A = 0.6$ for $e_n^o + e_p^o = 1.9 \times 10^{-3}\ s^{-1}$). However, the dependence of λ_R on optical power is small as shown in Fig. 5.10(b) and Figure 5.18(b). Therefore, λ_R can be considered sufficiently independent of Φ in this study.

The dependence of λ_R on the optical filling pulse width is described as the term B in Eq. 5.11. When the condition shown in Eq. 5.12 is held, the effect of the term B can be negligible. Under our typical measurement condition ($e_n^o + e_p^o = 3.8\ s^{-1}$ and $e^t = 2.7 \times 10^{-2}\ s^{-1}$ at 300 K), the effect of term B on λ_R is extremely small and can be negligible ($B = 9 \times 10^{-7}$ for $t_P^o = 3$ s and $B = 7 \times 10^{-3}$ for $t_P^o = 1$ ms). Thus, in this study, λ_R can be considered independent of t_P^o as shown in Fig. 5.10(c).

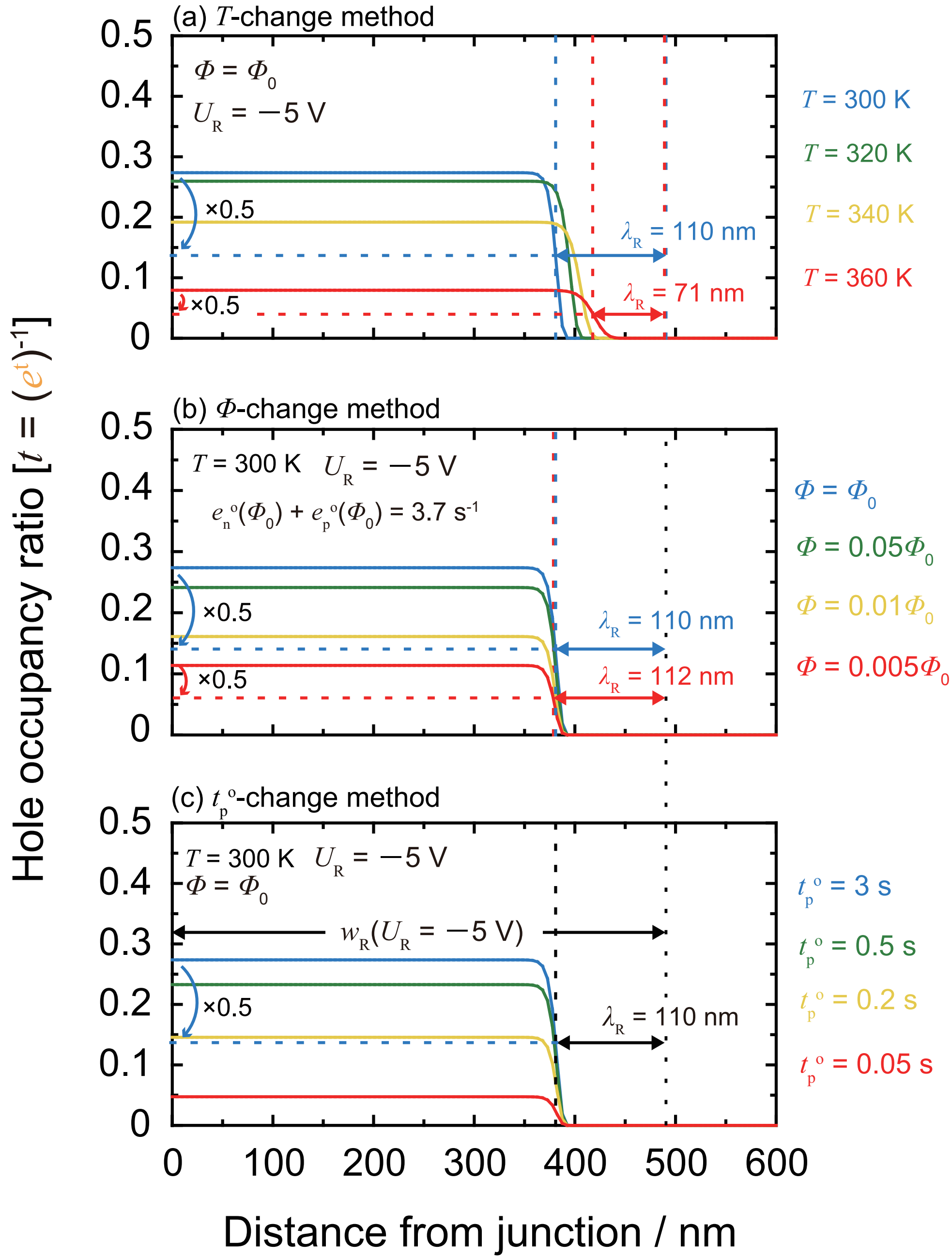

Figure 5.18: Depth profiles of the hole occupancy ratio in (a) temperature change method, (b) optical power change method, and (c) optical filling pulse width change method when measurement bias voltage of –5 V is applied at the time is equal to the reverse of the thermal excitation rate. In Fig. 5.18(a), blue, green, yellow, and red solid lines denote the depth profiles at $T = 300$ K, 320 K, 340 K, and 360 K, respectively. In Fig. 5.18(b), blue, green, yellow, and red solid lines denote the depth profiles at $\varPhi = \varPhi_0$, $0.05\varPhi_0$, $0.01\varPhi_0$, and $0.005\varPhi_0$, respectively. In Fig. 5.18(c), blue, green, yellow, and red solid lines denote the depth profiles at $t_{\mathrm{P}}^{\mathrm{o}} = 3$ s, 0.5 s, 0.2 s, and 0.05 s, respectively.

5.6 Quantification of Density of Hole Trap H1 with Schottky Junction

5.6.1 Temperature Change Method

In the same way for the p$^+$-n junction diode (Chapter 4), it is possible to extract $e_\mathrm{n}^\mathrm{o} + e_\mathrm{p}^\mathrm{o}$ from the analysis of temperature dependence of $f_\mathrm{T}N_\mathrm{T}$. Eq. 6.4 is expressed as a function of T as follows with sufficiently long t_P^o:

$$f_\mathrm{T}(T) = \frac{e_\mathrm{n}^\mathrm{o}}{e_\mathrm{n}^\mathrm{o} + e_\mathrm{p}^\mathrm{o} + e^\mathrm{t}(T)}. \tag{5.15}$$

Sub-E_g-light-excited ICTS with various U_R and T was performed for the GaN SBD. Figure 8 shows the ICTS spectra under $U_\mathrm{R} = -5$ V in the temperature range from 300 K to 370 K. The position of peak of the hole trap H1, which is equal to the time constant of hole thermal excitation $\tau_\mathrm{p}(T) = 1/e^\mathrm{t}(T)$, shifts to left with elevating temperature due to decrease of $\tau_\mathrm{p}(T)$. The intensity of peak of the hole trap H1 decreases with elevating temperature due to the temperature dependence of a product of the depletion layer edge correction factor F and hole occupancy ratio f_T. F was investigated at each temperature from sub-E_g-light-excited ICTS with various U_R and the dependence of the density of hole occupied hole trap H1 $f_\mathrm{T}N_\mathrm{T}$ on the temperature was obtained.

Figure 5.19 shows the dependence of the density of hole occupied hole trap H1 $f_\mathrm{T}N_\mathrm{T}$ on the hole thermal excitation rate e^t obtained sub-E_g-light-excited ICTS as the diamond symbols. $f_\mathrm{T}N_\mathrm{T}$ decreases with elevating temperature reflecting increasing of e^t. Considering Eq. 5.15, when e^t is equal to $e_\mathrm{n}^\mathrm{o}+e_\mathrm{p}^\mathrm{o}$, f_T becomes half the value of f_T in which e^t is negligible. Thus, $e_\mathrm{n}^\mathrm{o}+e_\mathrm{p}^\mathrm{o}$ can be extracted from the dependence of $f_\mathrm{T}N_\mathrm{T}$ on e^t, as shown in Fig. 5.19. In practice, a curve fitting using Eq. 5.15 was performed to improve accuracy. In Fig. 5.19, the fitting result of Eq. 5.15 using $e_\mathrm{n}^\mathrm{o}N_\mathrm{T}$ and $e_\mathrm{n}^\mathrm{o} + e_\mathrm{p}^\mathrm{o}$ as fitting parameters is shown as the black solid line. According to the fitting curve, $e_\mathrm{n}^\mathrm{o}N_\mathrm{T} = 6.5 \times 10^{15}$ s^{-1}cm^{-3} and $e_\mathrm{n}^\mathrm{o} + e_\mathrm{p}^\mathrm{o} = 3.7$ s^{-1} were extracted at $\Phi = \Phi_0$. Using $e_\mathrm{n}^\mathrm{o}/e_\mathrm{p}^\mathrm{o} = 3.0$ obtained from the result of p$^+$-n junction diode [Kanegae-2021] and $e_\mathrm{n}^\mathrm{o} + e_\mathrm{p}^\mathrm{o} = 3.7$ s^{-1}, $e_\mathrm{n}^\mathrm{o} = 2.7$ s^{-1} and $e_\mathrm{p}^\mathrm{o} = 0.9$ s^{-1} were separated. From Eq. 5.15, f_T is calculated at each temperature. By correcting $f_\mathrm{T}, N_\mathrm{T}$ of 2.3×10^{15} cm^{-3} was obtained and is shown as the black broken line in Fig. 5.19. This result is reasonable via compering [C] of 2×10^{15} cm^{-3} in the n-type GaN layer.

5.6.2 Optical-Power Change Method

Eq. 6.4 is expressed as a function of Φ as follows with sufficiently long t_P^o:

$$f_\mathrm{T}(\Phi) = \frac{\sigma_\mathrm{n}^\mathrm{o}\Phi}{(\sigma_\mathrm{n}^\mathrm{o} + \sigma_\mathrm{p}^\mathrm{o})\Phi + e^\mathrm{t}}. \tag{5.16}$$

In Eq. 5.16, when $(\sigma_\mathrm{n}^\mathrm{o}+\sigma_\mathrm{p}^\mathrm{o})\Phi = e_\mathrm{n}^\mathrm{o}+e_\mathrm{p}^\mathrm{o}$ is equal to e^t, $f_\mathrm{T}(\Phi)$ becomes equal to a half value of f_T which is under $e_\mathrm{n}^\mathrm{o}+e_\mathrm{p}^\mathrm{o} \gg e^\mathrm{t}$. Thus, $e_\mathrm{n}^\mathrm{o}+e_\mathrm{p}^\mathrm{o}$ can be also extracted from the dependence of

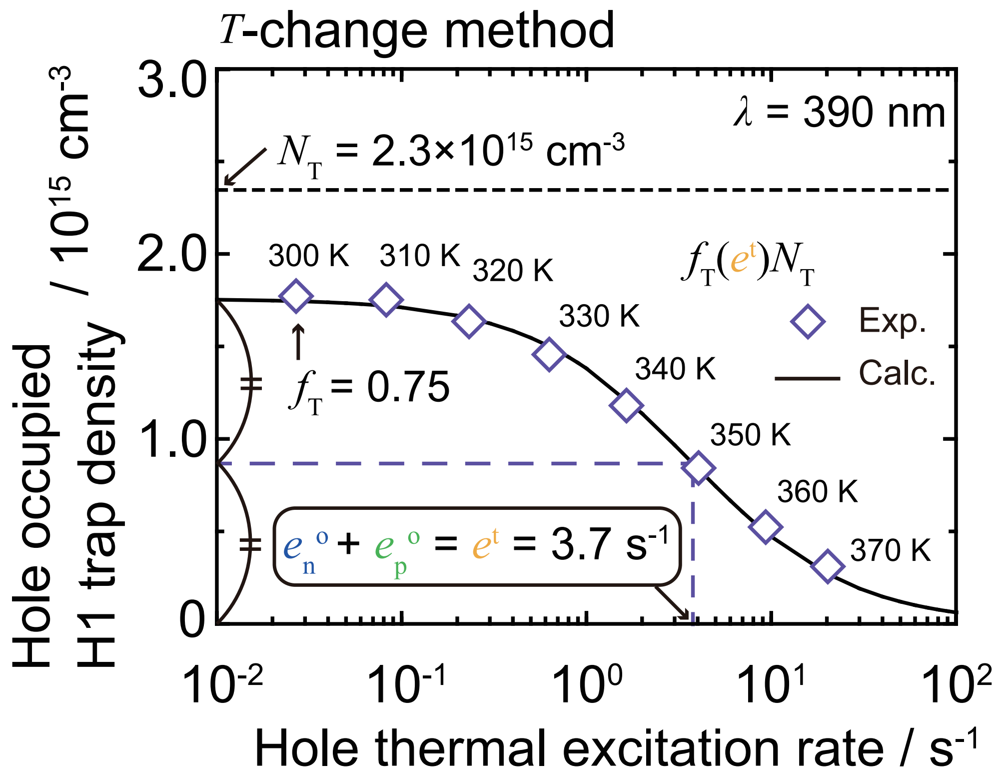

Figure 5.19: Dependence of the hole-occupied H1 trap density on the hole thermal excitation rate. The open diamonds denote the experimental data. The black line shows the fitting curve using Eq. (6). From the curve fitting, the sum of photoexcitation rates of 3.7 s^{-1} and the H1 trap density of 2.3×10^{15} cm^{-3} were extracted.

f_T on Φ. For the Schottky barrier diode, sub-E_g-light-excited ICTS various Φ at $U_R = -5$ V and $T = 300$ K was performed. The sub-E_g-light-excited ICTS spectra with various Φ are shown in Fig. 5.20. Optical power was adjusted by changing I_{LED} and the number of LEDs and monitored as photocurrent in the range shown in Fig. 5.3. In Fig. 5.20, the position of peak of the hole trap H1 is constant and the peak intensity of the hole trap H1 increases with increasing Φ. To obtain the dependence of the density of hole occupied hole trap H1 on Φ, estimation of the depletion layer edge correction factor F is required. λ_R in Eq. (4) depends on Φ (see the Appendix). However, as shown in Fig. 5.10(b), the dependence can be negligible in measurement conditions in this study. In this study, the error when λ_R is regarded as constant is less than 1% on F. Using $\lambda_R = 110$ nm [Fig. 5.10 (b)], the depletion layer edge correction factor F of 0.62 was calculated and the density of hole occupied hole trap H1 $f_T N_T$ was obtained.

The dependence of the density of hole occupied hole trap H1 $f_T N_T$ on Φ was obtained and is shown in Fig. 5.21 as the diamond symbols. $f_T N_T$ increases with increasing Φ. When Φ is sufficiently large, $f_T N_T$ approaches the same value in Fig. 5.19 at 300 K. The black solid line in Fig. 5.21 is a result of curve fitting using Eq. 5.16. Considering Eq. 5.16, when the hole occupancy ratio f_T becomes a half the value of f_T at high optical power, $e_n^o + e_p^o$ is equal to e^t and based on this point, optical power is converted to $e_n^o + e_p^o$ in the horizontal axis in Fig. 5.21. As shown in Fig. 5.21, $e_n^o + e_p^o = e^t = 2.7 \times 10^{-2}$ s^{-1} is extracted when $f_T N_T$ becomes equal to half the value of the saturated value (1.8×10^{15} cm^{-3}). Using $e_n^o / e_p^o = 3.0$, the dependence of f_T on Φ is calculated. By correcting f_T, $N_T = 2.3 \times 10^{15}$ cm^{-3} was obtained and is shown as the black broken line in Fig. 5.21. This value is in a good agreement with that obtained from the above method.

5.6.3 Optical-filling-pulse-width Change Method

Form Eq. 6.4, the hole occupancy ratio during the sub-E_g-light illumination is given as:

$$f_T(t_P^o) = f_T \left(1 - \exp\left(-\frac{t_P^o}{\tau_P^o}\right)\right). \tag{5.17}$$

$e_n^o + e_p^o$ is extracted from the time constant of exponential curve $\tau_P^o = (e_n^o + e_p^o + e^t)^{-1}$ in Eq. 5.17. Sub-E_g-light-excited ICTS with varying t_P^o was performed for the SBD at $T = 300$ K. Figure 5.22(a) shows the measurement sequence to investigate the dependence of the density of hole occupied hole trap H1 $f_T N_T$ on the optical filling pulse width t_P^o. Before the optical filling pulse, a bias filling pulse ($U_P = 0.5$ V, $t_P = 100$ ms) was applied to the Schottky junction to set $f_T = 0$. The effect of parasite ICTS due to the application of U_P was eliminated by comparing ICTS which has the same measurement sequence without only light illumination [Fig. 5.22 (b)]. Figure 5.23 shows the ICTS spectra with the measurement sequences shown in Fig. 5.22(a) and Fig. 5.22(b). In the parasite ICTS spectrum (violet solid line and black solid line in Fig. 5.23), the deep level E3 [6, 18–22], which originates from the substitution of Fe atoms at Ga sites [22], is detected and additional deep levels were not

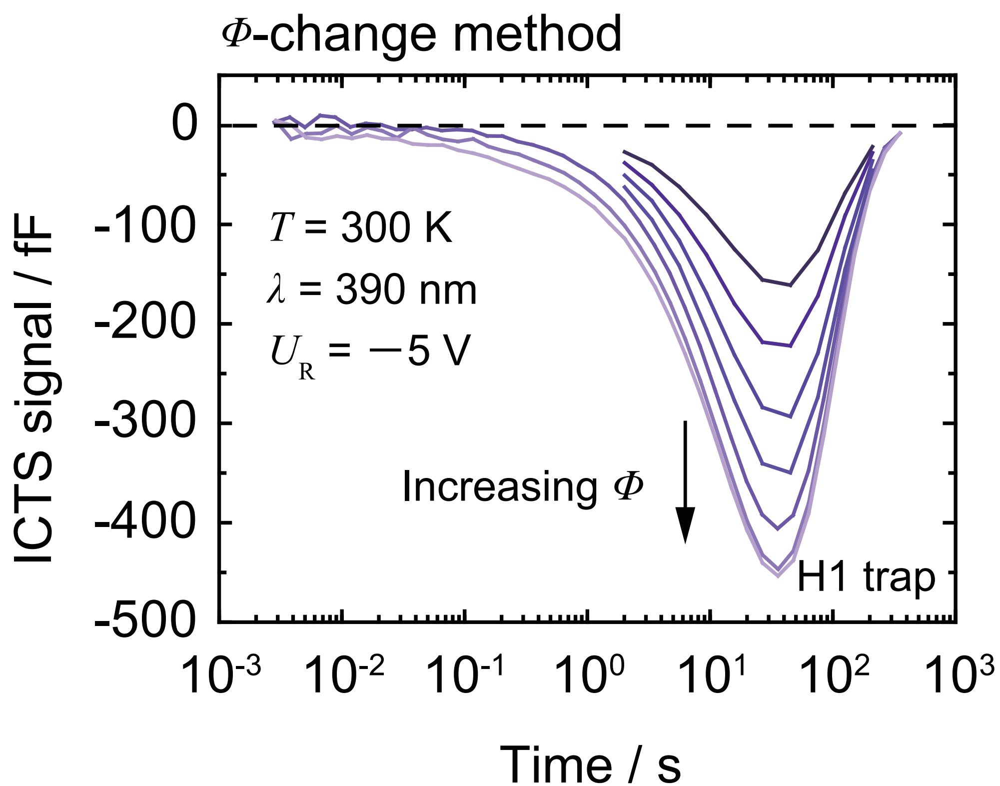

Figure 5.20: Sub-E_g-light-excited ICTS spectra in the optical power change method. The measurement bias voltage and temperature were set to –5 V and 300 K.

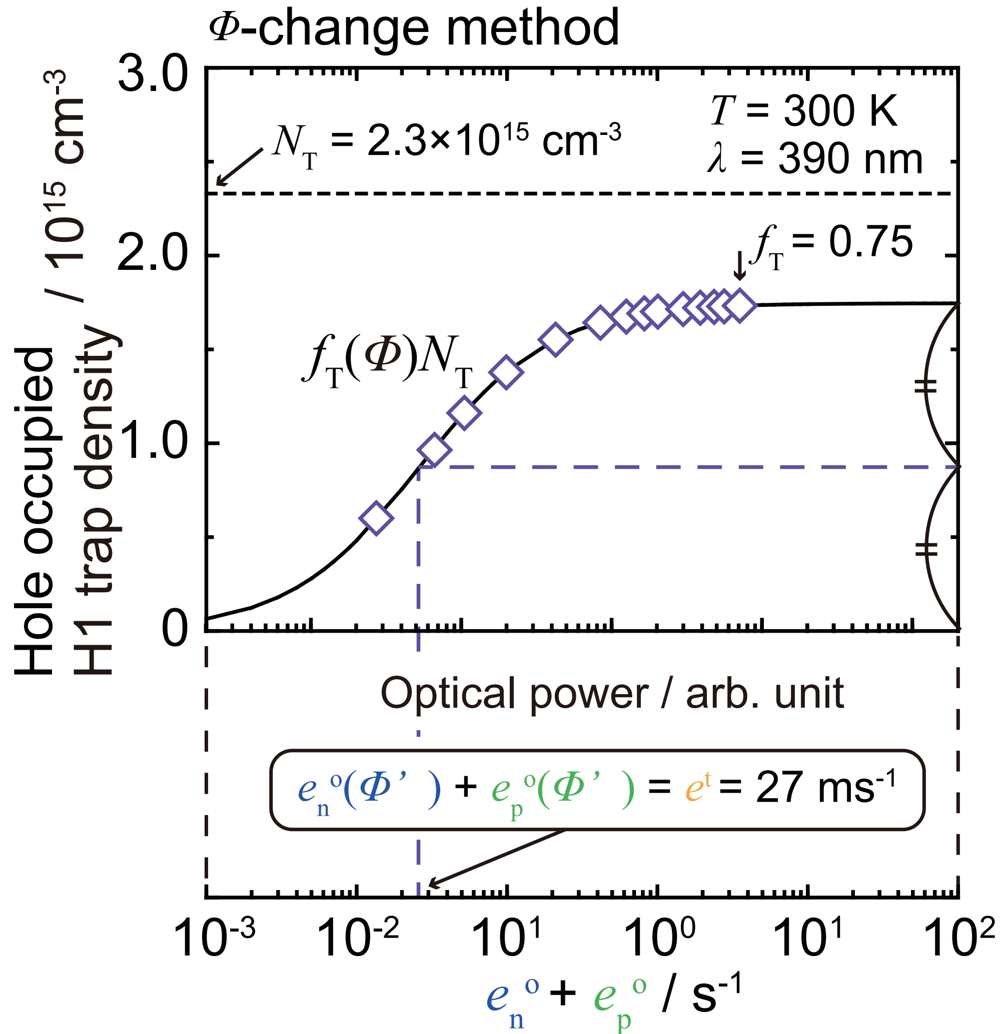

Figure 5.21: Dependence of the hole-occupied H1 trap density on the optical power. The open diamonds denote the experimental data. The black line shows the fitting curve using Eq. 5.16. Considering Eq. 5.16, when the hole occupancy ratio becomes half the value at high optical power, the sum of the photoexcitation rates is equal to the thermal excitation rate and based on this point, optical power is converted to the sum of the photoexcitation rates in the horizontal axis in Fig. 5.21. From the curve fitting, the H1 trap density of 2.3×10^{15} cm^{-3} was extracted.

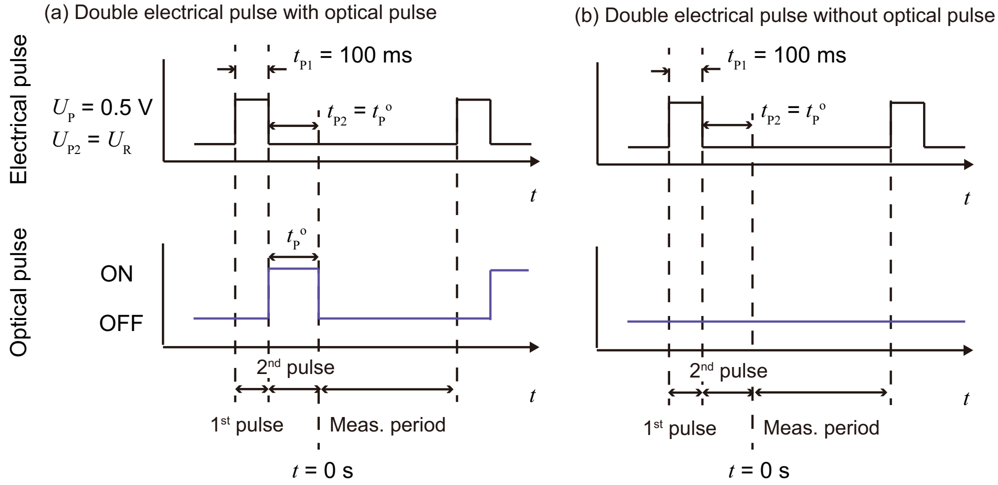

Figure 5.22: Pulse sequence (a) in the double electrical pulse with optical pulse measurement and (b) in the double electrical pulse without optical pulse measurement. In the double electrical pulse with optical pulse measurement, the first pulse is electrical pulse ($U_{P1} = 0.5$ V, $t_{P1} = 100$ ms) and the second pulse is electrical pulse ($U_{P2} = U_R$, $t_{P2} = t_P^o$) and optical pulse. In that without optical pulse measurement, the first pulse is the same as that with optical pulse measurement and the second pulse is only electrical pulse.

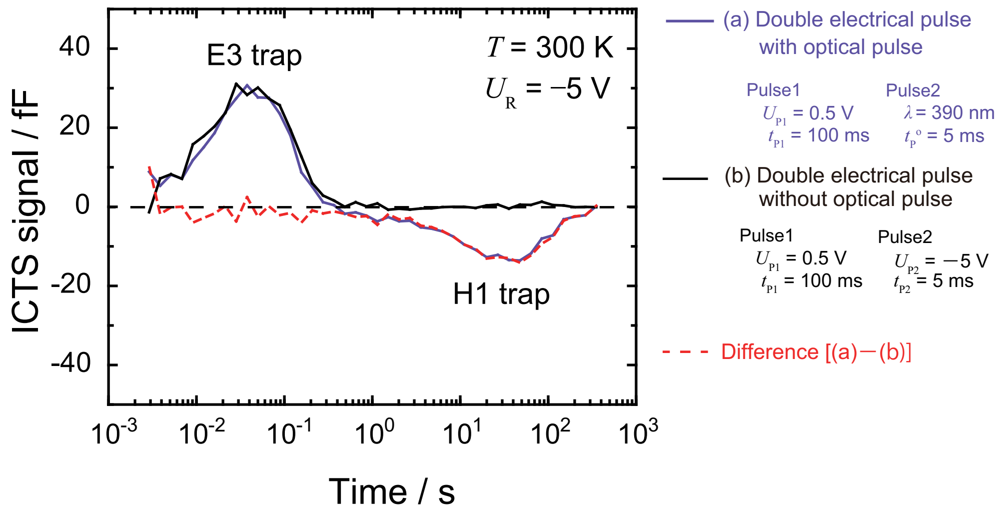

Figure 5.23: Sub-E_g-light-excited ICTS spectra in the double electrical pulse with optical pulse measurement (violet solid line) and without optical pulse measurement (black solid line). The red broken line denotes the difference of the sub-E_g-light-excited ICTS spectra.

detected in the ICTS spectra. The energy position $E_\mathrm{T} = E_\mathrm{C} - 0.61$ eV and electron capture cross-section $\sigma_\mathrm{n} = 4 \times 10^{-15}$ cm^2 was obtained from DLTS measurement (not shown) and the density of deep level E3 of 6.9×10^{13} cm^{-3} was obtained in this epilayer. To analysis $f_\mathrm{T}(t_\mathrm{P}^\mathrm{o})N_\mathrm{T}$ of the hole trap H1, the difference between of ICTS spectra with measurement sequences (a) and (b) were obtained for each t_P^o The difference ICTS spectra with various t_P^o are shown in Fig. 5.24. In Fig. 5.24, the peak position of the hole trap H1 is constant and the peak intensity of the hole trap H1 increases with increasing t_P^o. To obtain the dependence of the density of hole occupied hole trap H1 on t_P^o, estimation of the depletion layer edge correction factor F is required. As shown in Fig. 5.10 (c), λ_R is independent of t_P^o. Thus, using $\lambda_\mathrm{R} = 110$ nm [Fig. 5.10 (c)], the depletion layer edge correction factor F of 0.60 was calculated and the density of hole occupied hole trap H1 $f_\mathrm{T}N_\mathrm{T}$ was obtained.

The dependence of the density of hole occupied hole trap H1 $f_\mathrm{T}N_\mathrm{T}$ on the optical filling pulse width t_P^o is shown in Fig. 5.25 as the diamond symbols. $f_\mathrm{T}(t_\mathrm{P}^\mathrm{o})N_\mathrm{T}$ increases with increasing t_P^o. When t_P^o is sufficiently long, $f_\mathrm{T}(t_\mathrm{P}^\mathrm{o})N_\mathrm{T}$ approaches the same value of $f_\mathrm{T}N_\mathrm{T}$ in Fig. 5.19 at 300 K. Considering Eq. 5.17, when t_P^o is equal to $\tau_\mathrm{P}^\mathrm{o}$, the hole occupancy ratio becomes to be $\{1 - \exp(-1)\} \times f_\mathrm{T}$, where t_P^o is sufficiently long. Therefore, from the exponential curve, $e_\mathrm{n}^\mathrm{o} + e_\mathrm{p}^\mathrm{o}$ can be extracted. To improve accuracy, a curve fitting was performed and the fitting result of Eq. 5.17 using $e_\mathrm{n}^\mathrm{o}N_\mathrm{T}$ and $e_\mathrm{n}^\mathrm{o} + e_\mathrm{p}^\mathrm{o}$ as fitting parameters is shown as the black solid line in Fig. 5.25. According to the fitting curve, $e_\mathrm{n}^\mathrm{o} + e_\mathrm{p}^\mathrm{o} = 4.1$ s^{-1} and $e_\mathrm{n}^\mathrm{o}N_\mathrm{T} = 7.0 \times 10^{15}$ s^{-1}cm^{-3} were extracted. Using $e_\mathrm{n}^\mathrm{o}/e_\mathrm{p}^\mathrm{o} = 3.0$ and $e_\mathrm{n}^\mathrm{o} + e_\mathrm{p}^\mathrm{o} = 4.1$ s^{-1}, $e_\mathrm{n}^\mathrm{o} = 3.1$ s^{-1} and $e_\mathrm{p}^\mathrm{o} = 1.0$ s^{-1} were separated. From Eq. 5.17, $f_\mathrm{T}(t_\mathrm{P}^\mathrm{o})$ is calculated at each t_P^o. By correcting $f_\mathrm{T}(t_\mathrm{P}^\mathrm{o})$, N_T of 2.3×10^{15} cm^{-3} was obtained and is shown as the black broken line in Fig. 5.25. This result is reasonable via compering N_T obtained from the temperature change method and [C] in the n-type GaN layer.

5.6.4 Discussion

Figure 5.26 shows the dependences of f_T (violet solid line), F (black broken line) at U_R = –5 V, and $f_\mathrm{T}F(U_\mathrm{R} = -5$ V) (violet broken line) on the hole thermal excitation rate calculated from the extracted parameters in the measurement conditions. In the temperature range from 300 K to 370 K, e^t is change from 10^{-2} s^{-1} to 10^1 s^{-1}. Thus, in this study, Φ was adjusted so that $e_\mathrm{n}^\mathrm{o} + e_\mathrm{p}^\mathrm{o}$ became 10^0 s^{-1}. The temperature dependence of the measured density of hole trap H1 $f_\mathrm{T}FN_\mathrm{T}$ reflects the temperature dependences of not only f_T but also F due to λ_R [Fig. 5.10(a)]. Thus, in temperature change method, sub-E_g-light-excited ICTS with various U_R at each temperature must be required and coupled with changing the temperature, it leads long measurement time to obtain accurate density of hole trap H1. To reduce the number of measurements for estimating f_T, the following two methods, optical power change method and optical filling pulse width change method, are proposed.

Figure 5.27 shows the dependences of f_T (violet solid line), F (black broken line) at

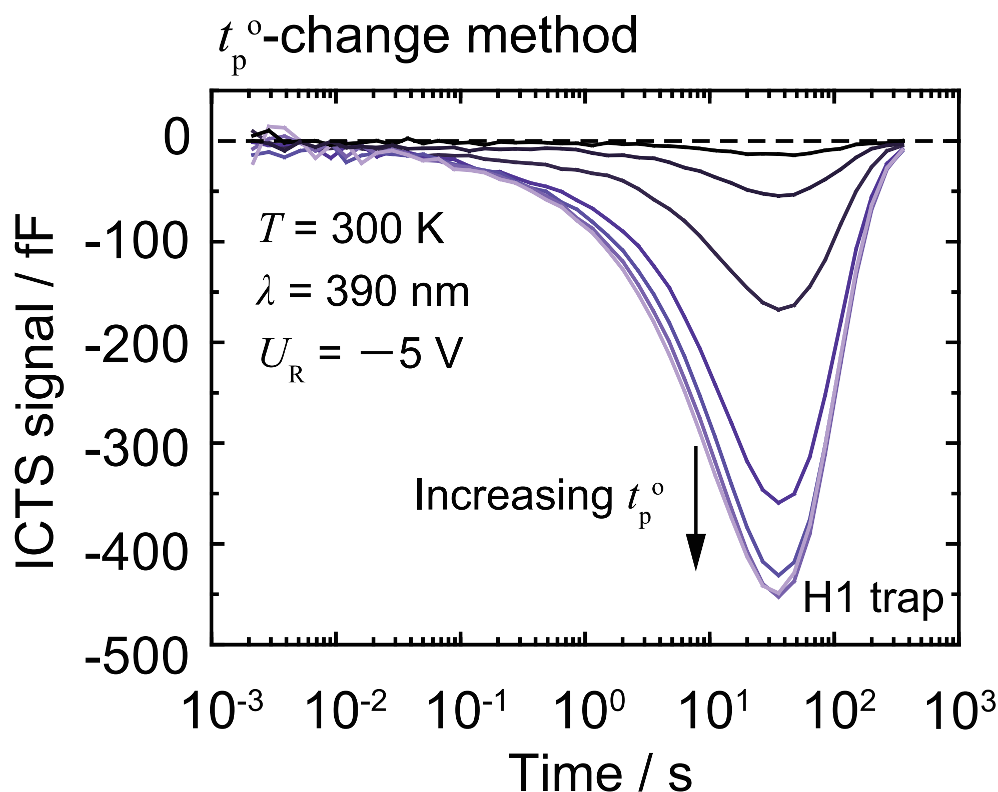

Figure 5.24: Sub-E_g-light-excited ICTS spectra in the optical pulse width change method. The measurement bias voltage and temperature were set to –5 V and 300 K. The illustrated sub-E_g-light-excited ICTS spectra in Fig. 5.24 is the difference of sub-E_g-light-excited ICTS spectra in the double electrical pulse with optical pulse measurement and without optical pulse measurement at each optical pulse width as shown in Fig. 15 ($t_p^o = 5$ ms).

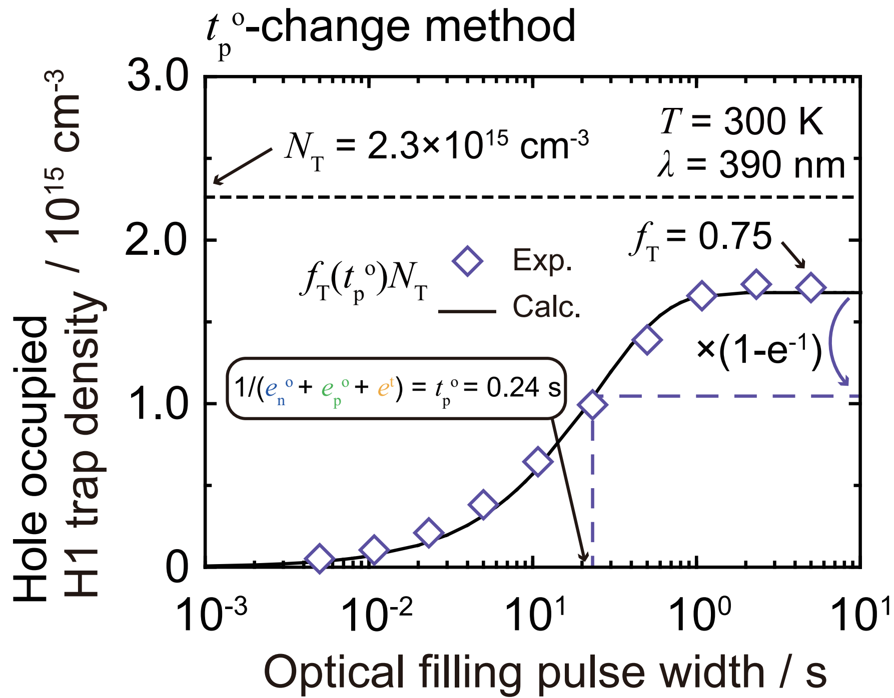

Figure 5.25: Dependence of the hole-occupied H1 trap density on the optical filling pulse width. The open diamonds denote the experimental data. The black line shows the fitting curve using Eq. (8). Considering Eq. (8), when the hole occupancy ratio becomes half the value at long optical filling pulse width, the time constant during optical filling pulse width is equal to the optical pulse width. From the curve fitting, the H1 trap density of 2.3×10^{15} cm^{-3} were extracted.

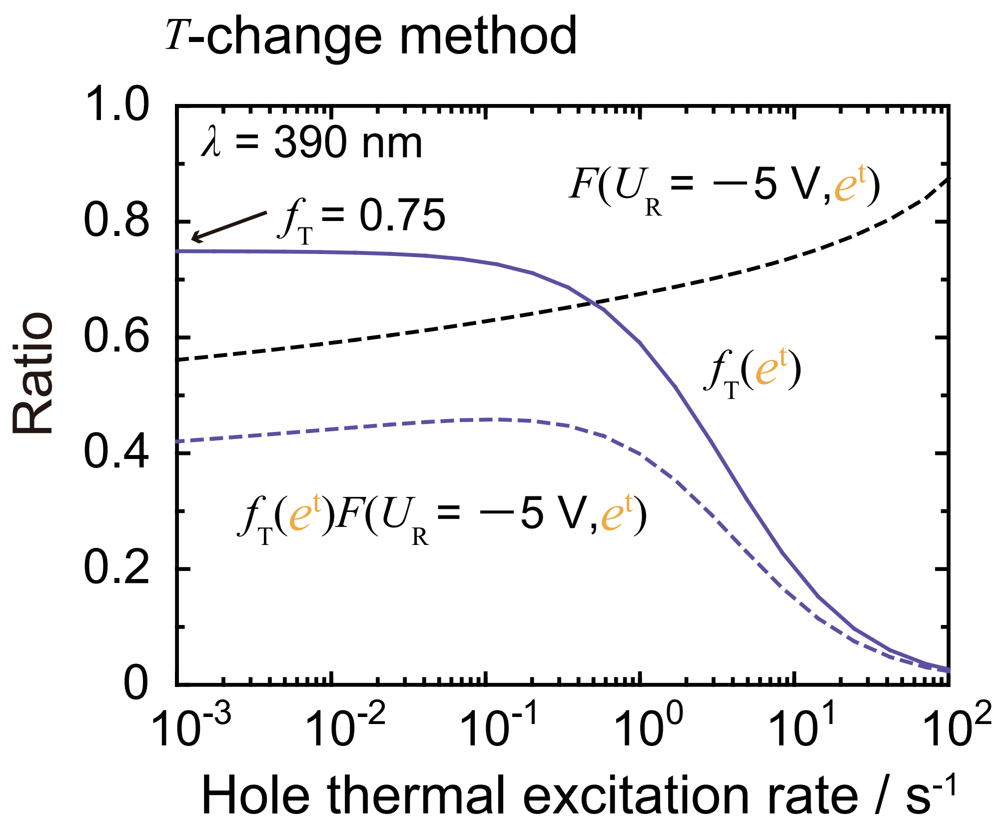

Figure 5.26: Calculation results of dependences of the hole occupancy ratio f_T (violet solid line), the depletion layer edge correction factor F at $U_R = -5$ V (black broken line), and $f_T F(U_R = -5\text{ V})$ (violet broken line) on the hole thermal excitation rate.

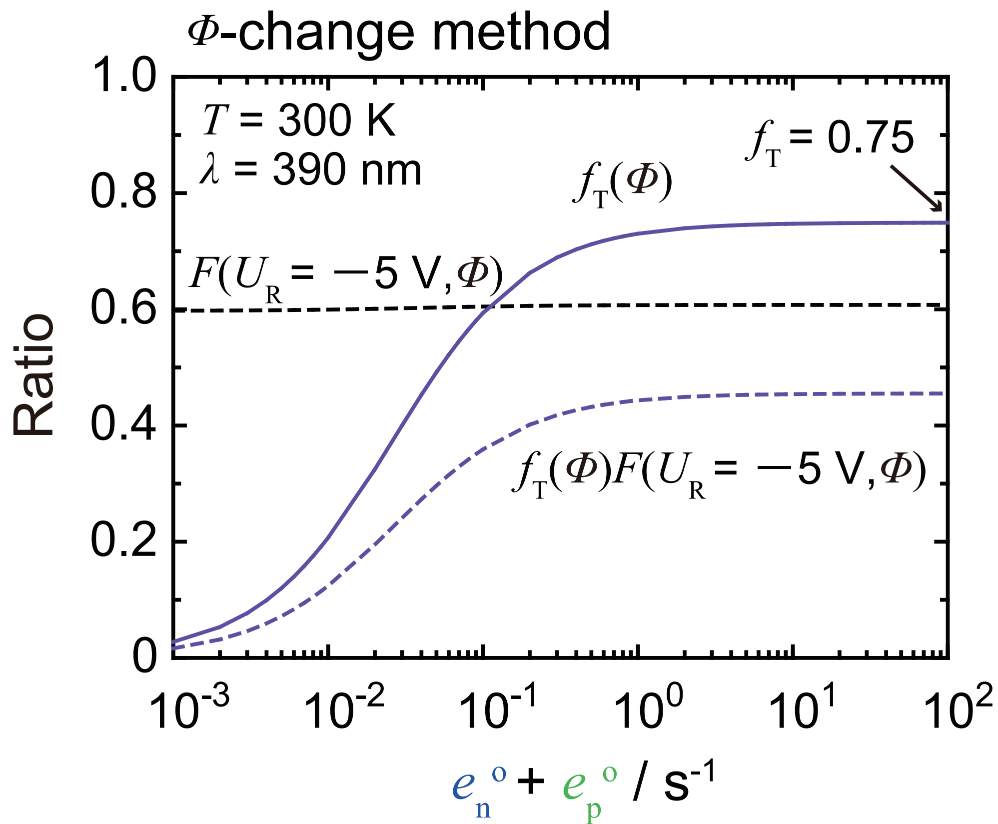

Figure 5.27: Calculation results of dependences of the hole occupancy ratio f_T (violet solid line), the depletion layer edge correction factor F at $U_R = -5$ V (black broken line), and $f_T F(U_R = -5$ V) (violet broken line) on the sum of photoexcitation rates.

$U_R = -5$ V, and $f_T F(U_R = -5$ V) (violet broken line) on the sum of photoexcitation rates, which is proportional to Φ, calculated from the extracted parameters in the measurement conditions. As shown in Fig. 5.27, the depletion layer edge correction factor F is almost independent of Φ. Therefore, in optical power change method, sub-E_g-light-excited ICTS with various U_R is required under one optical power condition and this leads reduction of the number of measurements. It is noted that decrease of Φ leads increase of t_P^o, where the capacitance change during light illumination to be saturated, due to increase of τ_P^o. This means measurement time for one sub-E_g-light-excited ICTS scan becomes longer. However, even if the increase of t_P^o is considered, the total measurement time in optical power change method is shortened compared to that in temperature change method. On the other hands, strong Φ leads to elevating temperature and saturation of $f_T(\Phi)$. In this study, Φ was adjusted to avoid the elevating temperature during filling pulse period and to investigate the change of f_T with respect to Φ, i.e., $e_n^o + e_p^o$ was changed to be close to e^t.

Figure 5.28 shows the dependences of f_T (violet solid line), F (black broken line) at $U_R = -5$ V, and $f_T F(U_R = -5$ V) (violet broken line) on the optical filling pulse width calculated from the extracted parameters in the measurement conditions. As shown in Fig. 5.28, the depletion layer edge correction factor F is almost independent of t_P^o. Therefore, in optical pulse width change method, sub-E_g-light-excited ICTS with various U_R is required under one optical filling pulse width condition and this leads reduction of the number of measurements. Even if the additional ICTS measurement to eliminate the effect of parasite ICTS is considered, the total measurement time in optical filling pulse width change method is shortened compared to that in temperature change method. In the optical filling pulse width change method, strong Φ leads to elevating temperature and weak Φ leads to long τ_P^o, which means long t_P^o is needed for saturation of the hole occupancy ratio, i.e., long measurement time is needed. In this study, Φ was adjusted so that $e_n^o + e_p^o$ became 10^0 s^{-1}, which is sufficiently larger than e^t at 300 K.

5.7 Quick and Quantitative Method for Density of Hole Trap H1 with Schottky Junction

5.7.1 Dual-color Sub-E_g-light-excited Method

Compared with the temperature change method, the optical power change method and optical filling pulse width change method can reduce the number of measurements. In the three methods, the ratio of hole traps to hole-occupied state hole traps under sub-E_g-light illumination (hole occupancy ratio) is obtained by modulating measurement conditions during optical filling pulse period in sub-E_g-light-excited ICTS. In standard sub-E_g-light-excited ICTS, hole traps are detected as the capacitance transient due to hole thermal excitation from the hole traps to the V.B. The hole trap H1 in GaN has long time constant

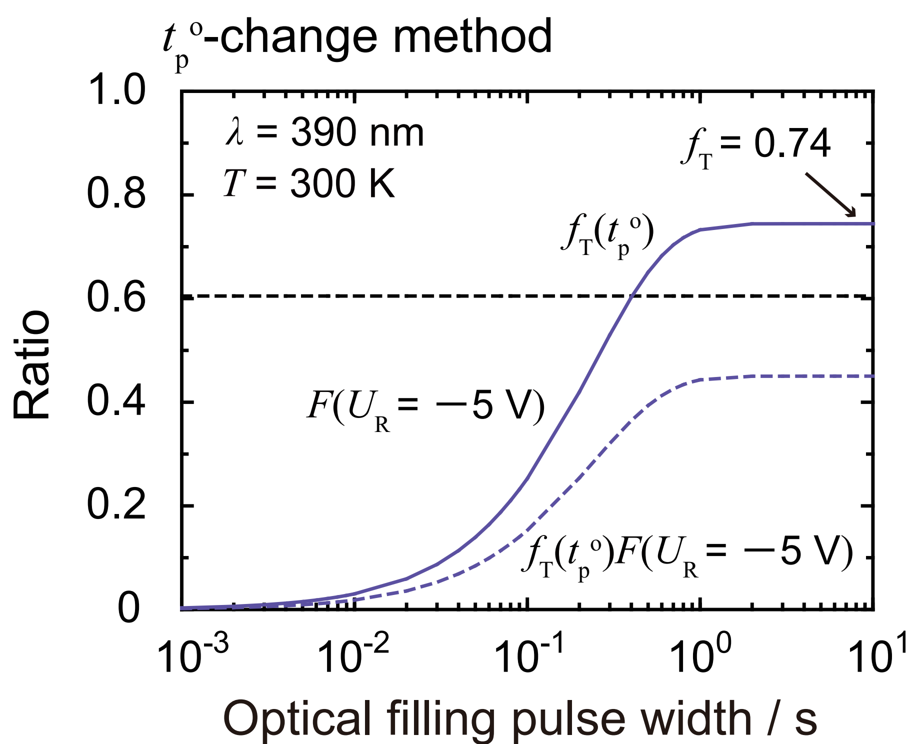

Figure 5.28: Calculation results of dependences of the hole occupancy ratio f_{T} (violet solid line), the depletion layer edge correction factor F at $U_{\mathrm{R}} = -5$ V (black broken line), and $f_{\mathrm{T}}F(U_{\mathrm{R}} = -5\ \mathrm{V})$ (violet broken line) on the optical filling pulse width.

of hole thermal excitation at 300 K ($\tau_p = 1/e^t \sim 30$ s) and it makes lengthen measurement time in one sub-E_g-light-excited ICTS scan.

To be shortened the measurement time, the measurement period was focused, in which the hole is excited from a hole trap to the V.B., and propose a quick method for the measurement of density of hole trap H1 N_T in n-type GaN using dual-color sub-E_T-light-excited ICTS. Figure 5.29(a) shows the pulse sequence in dual-color sub-E_g-light-excited ICTS. In dual-color method, shorter-wavelength light is illuminated as the filling pulse to cause the hole trap H1 to become a hole-occupied state. This is the same as the standard sub-E_T-light-excited method. On the other hand, in dual-color sub-E_g-light-excited ICTS, a longer-wavelength light is illuminated during the measurement period as shown in Fig. 5.29(a). By illumination of the longer-wavelength light, the hole traps which become hole-occupied state during the filling pulse period [Fig. 5.29(c)] are detected as the capacitance transient due to hole thermal excitation and photoexcitation from the hole traps to the V.B [Fig. 5.29(d)]. Compared with thermal excitation, photoexcitation is much faster, which results in a significant reduction of the measurement time.

5.7.2 Experiments

The same n-type Schottky barrier diodes in Sec. 5.6 was used. Dual-color sub-E_g-light-excited ICTS measurements were performed at 300 K. Measurement bias voltage U_R was varied from 0 V to −10 V. As the shorter-wavelength light source, 390 nm LEDs ($h\nu =$ 3.18 eV, which is the same LEDs used in Sec. 5.6, were used. It was shown that no dominant deep levels near the valence band maximum other than the hole trap H1 were detected, and N_T was 2.3×10^{15} cm^{-3} and the hole trap H1 was mainly associated with C_N in the epilayer.

The photon energy of longer-wavelength light should be higher than the minimum hole photoexcitation energy from the C_N^0 to the V.B. [1.02 eV [23]] so that holes can be photoexcited from the hole traps to the V.B as shown in Fig. 5.30. At the same time, the photon energy of longer-wavelength light should be lower than the minimum hole photoexcitation energy from the C.B. to the CN^- [2.60 eV [24]] so that holes can not be photoexcited from the C.B. to the hole traps as shown in Fig. 5.30. In this study, 660 nm LEDs ($h\nu = 1.88$ eV) were used as the longer-wavelength light source. The switching time between the UV light and red light was around 10 µs, which is much shorter than the measurement time. The irradiated photon flux densities of both the UV light and red light were around 10^{20} cm^{-2}s^{-1} at the sample surface.

5.7.3 Dual-color sub-E_g-light-excited ICTS for GaN Schottky Junction

The capacitance transients of standard sub-E_g-light ICTS and dual-color-sub-E_g-light ICTS measurements are illustrated in Fig. 5.29(a). Sub-E_g-light ICTS is performed at constant

Figure 5.29: (a) Capacitance transient of the standard and dual-color method, and band diagrams of the hole trap H1 of n-type GaN for (b) steady state, (c) under sub-E_g-light (shorter wavelength light) irradiation, and (d) after interruption of sub-E_g-light irradiation. The left band diagram in (d) is measured under dark conditions and corresponds to standard sub-E_g-light ICTS. The right band diagram in (d) is measured under sub-E_g-light (longer wavelength light) irradiation and corresponds to dual-color-sub-E_g-light ICTS.

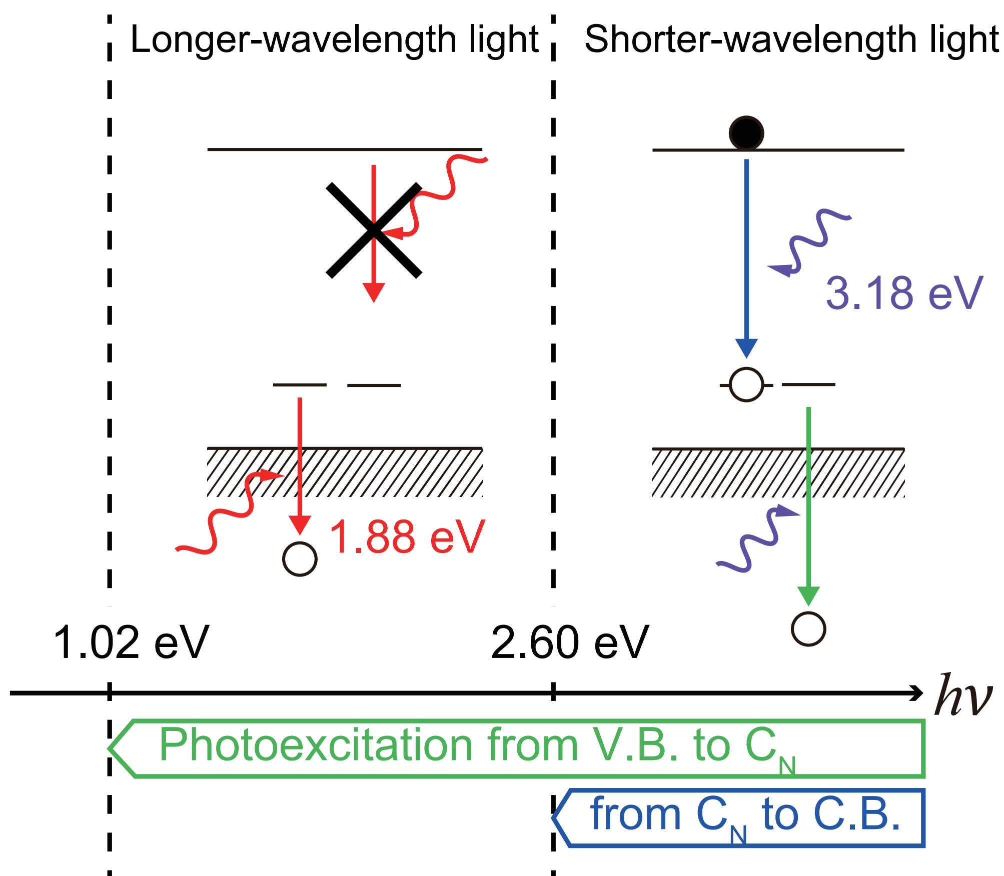

Figure 5.30: Band diagrams of C_N and threshold photon energies to photoexcite holes from the C.B. to the C_N acceptor [24] and to photoexcite holes from the C_N acceptor to the V.B [23].

temperature T and constant reverse bias voltage U_{R}. The filling pulse width is 3−5 s. The hole trap H1 in the depletion layer becomes a hole-occupied state by the shorter-wavelength light illumination, and the junction capacitance increases and is saturated within 1−2 s. The shorter-wavelength light illumination is interrupted, and a hole is then excited from the hole-occupied hole trap H1 to the V.B. at a hole excitation rate (e_{p}), and the capacitance decays at τ_{p} during the measurement period. In the standard method, the hole is only thermally excited at the hole thermal excitation rate e^{t}, and the capacitance transient is shown in Fig. 5.29(a) as the black solid line. On the other hand, in the dual-color method, longer-wavelength light is illuminated during the measurement period. The holes are thermally and optically excited and the capacitance transient is shown as the red solid line in Fig. 5.29(a). In the dual-color method, e_{p} is the sum of e^{t} and the photoexcitation rate ($e_{\mathrm{p}}^{\mathrm{o}}$) and τ_{p} of the dual-color method is shorter than that of the standard method.

The standard sub-E_{g}-light ICTS spectrum and the dual-color-sub-E_{g}-light ICTS spectrum at the standard measurement condition [$T = 300$ K, $U_{\mathrm{R}} = -5$ V, $\Phi(390\mathrm{nm}) = \Phi_0$] are shown as black and red solid lines in Fig. 5.31, respectively. The hole trap H1 ($E_{\mathrm{V}}+0.87$ eV) is detected as a peak with $1/e_{\mathrm{p}} = 1/e^{\mathrm{t}}$ of 37 s by the standard method. In the dual-color method, only the peak with $1/e_{\mathrm{p}} = 1/(e^{\mathrm{t}} + e_{\mathrm{p}}^{\mathrm{o}})$ of 1.0 s is detected and this peak is considered to be that which corresponds to the capacitance transient due to the photo and thermal excitation of holes from the hole trap H1 because the peak intensity in the dual-color method is same as the peak intensity of the hole trap H1 in the standard method, and no additional peak is detected in the dual-color method. In fact, the peak intensity in dual-color method is slightly larger than that in standard method. The reason is discussed in Sec. 5.7.5. Comparing $1/e_{\mathrm{p}}$ in the two peaks reveals that $1/e_{\mathrm{p}}$ in the dual-color method is around 30 times shorter than that in the standard method, and this enables quick detection of the hole trap H1 at 300 K.

5.7.4 Condition of Longer-wavelength Light Illumination

By adjusting light intensity of the longer-wavelength light, the hole photoexcitation rate from the hole trap to the V.B. during the measurement period can be controlled and the time constant of capacitance transient during measurement period can be shortened, i.e., the measurement time in one ICTS scan can be shortened.

The optical power dependence of hole excitation rate is shown in Fig. 5.32. At an optical power of 0, which is a condition in the standard method, an $e_{\mathrm{p}}^{\mathrm{t}}$ of 0.03 s^{-1} is obtained. The photoexcitation rate from the deep level to the valence band is defined as the product of the hole photoionization cross section ($\sigma_{\mathrm{p}}^{\mathrm{o}}$) and the photon flux ($\Phi$). The hole excitation rate in Fig. 5.32 is proportional to an optical power of 1.88 eV light, which indicates that the photoexcitation is dominant. In the dual-color method, the time constant for hole excitation can be controlled by the optical power. A larger optical power gives a shorter measurement time. On the other hand, an increase of temperature during light illumination

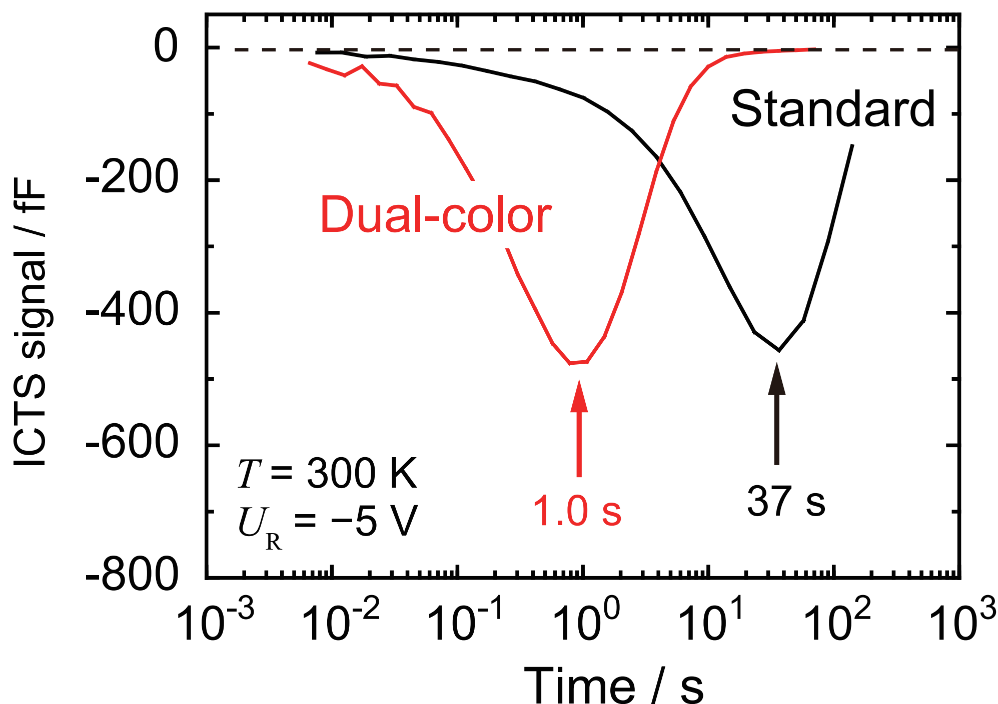

Figure 5.31: Sub-E_g-light ICTS spectra with $U_R = -5$ V and $T = 300$ K. The standard and dual-color methods are shown as black and red solid lines, respectively. The time constants for hole emission from the hole trap H1 are 37 s for the standard method and 1.0 s for the dual-color method.

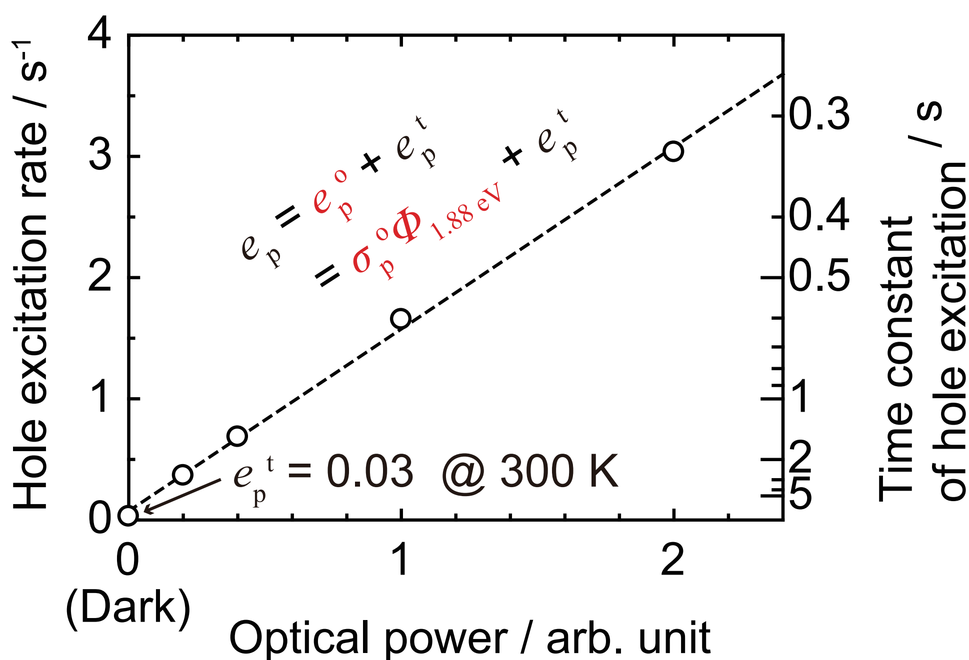

Figure 5.32: Optical power dependence of the hole excitation rate during the measurement period. The photoexcitation rate is proportional to the optical power of 1.88 eV light.

is not negligible in the case of high optical power. In this study, an optical power at a hole excitation rate around 1 s^{-1} was used so that the increase in temperature was negligible.

5.7.5 Depletion Layer Edge Correction in Dual-color Method

In standard sub-E_g-light-excited ICTS, the width of region where the quick carrier recombination via the hole trap H1 in the depletion layer during the measurement period λ_R depends on the electron capture rate nC_n and the thermal hole excitation rate e^t. On the other hand, the width of region where the quick carrier recombination via the hole trap H1 in the depletion layer during the measurement period in dual-color sub-E_g-light-excited ICTS λ_R^o depends on nC_n, e^t, and the hole photoexcitation rate to the V.B. by illumination of longer-wavelength light. Figure 5.33 shows calculated depth profiles from the Schottky barrier junction of (a) rates, (b) time constant, and (c) hole occupancy ratio of the H1 trap during the measurement period in dual-color sub-E_g-light-excited ICTS. In the calculation, the measurement condition of the dual-color sub-E_g-light-excited ICTS spectrum in Fig. 5.31 plotted as the violet solid line was assumed, i.e., T = 300 K, $\Phi(390\text{nm}) = \Phi_0$, $U_R = -5$ V, $\tau_p = 1/[e^t + e_p^o(660\text{nm})] = 1.0$ s. In Fig. 5.33(a), the black, orange, and red solid lines denote the depth profiles of nC_n, e^t, and sum of e^t and $e_p^o(660\text{nm})$, respectively. In Fig. 5.33(b), the black and red solid lines denote the depth profiles of time constant during the measurement period in standard sub-E_g-light-excited ICTS and dual-color sub-E_g-light-excited ICTS, respectively. In Fig. 5.33(c), the black and red solid lines denote the depth profiles of the hole occupancy ratio of the hole trap H1 during the measurement period in standard sub-E_g-light-excited ICTS [$t = 1/e^t$] and dual-color sub-E_g-light-excited ICTS ($t = 1/[e^t + e_p^o(660\text{nm})]$) respectively. In the same way as λ_R, when the position at which $f_T(x, \tau_p)$ is half of the value at the Schottky junction [$f_T(0, \tau_p)$] is defined as $x = w - \lambda_R^o$, λ_R^o is given as: junction [$f_T(0, 1/e^t)$] is defined as $x = w - \lambda_R$, λ_R is given as:

$$\lambda_R^o \simeq L_D \sqrt{2\ln\left(\frac{N_{d,net} C_n [1 + A' - B']}{[e^t + e_p^o(660\text{nm})]\ln 2}\right)}, \tag{5.18}$$

where $A' \equiv [e^t + e_p^o(660\text{nm})]/(e_n^o(390\text{nm}) + e_p^o(390\text{nm}) + e^t)$ and $B' \equiv (t_P^o[e^t + e_p^o(660\text{nm})])/(\exp((t_P^o)/(1/(e_n^o(390\text{nm}) + e_p^o(390\text{nm}) + e^t))) - 1)$. When Φ is sufficiently strong and t_P^o is sufficiently long as in the case of the standard measurement condition, A' and B' in Eq. 5.18 can be negligible and as shown in Fig. 5.33(a), $n(w - \lambda_R^o, w)C_n$ is equal to $[e^t + e_p^o(660\text{nm})]\ln 2$. Compared to the case of sub-E_g-light-excited ICTS, in the case of dual-color sub-E_g-light-excited ICTS, the hole photoexcitation to the V.B. exists and the sum of hole excitation rate to the V.B. increases in the depletion layer. Thus, the width of region where the hole excitation from the hole traps to the V.B. is dominant increases, i.e., $\lambda_R^o < \lambda_R$ holds. As shown in Fig. 5.33, under the standard measurement condition with $\tau_p = 1/[e^t + e_p^o(660\text{nm})] = 1.0$ s, $\lambda_R^o = 92$ nm is estimated and λ_R^o is smaller than $\lambda_R = 106$ nm.

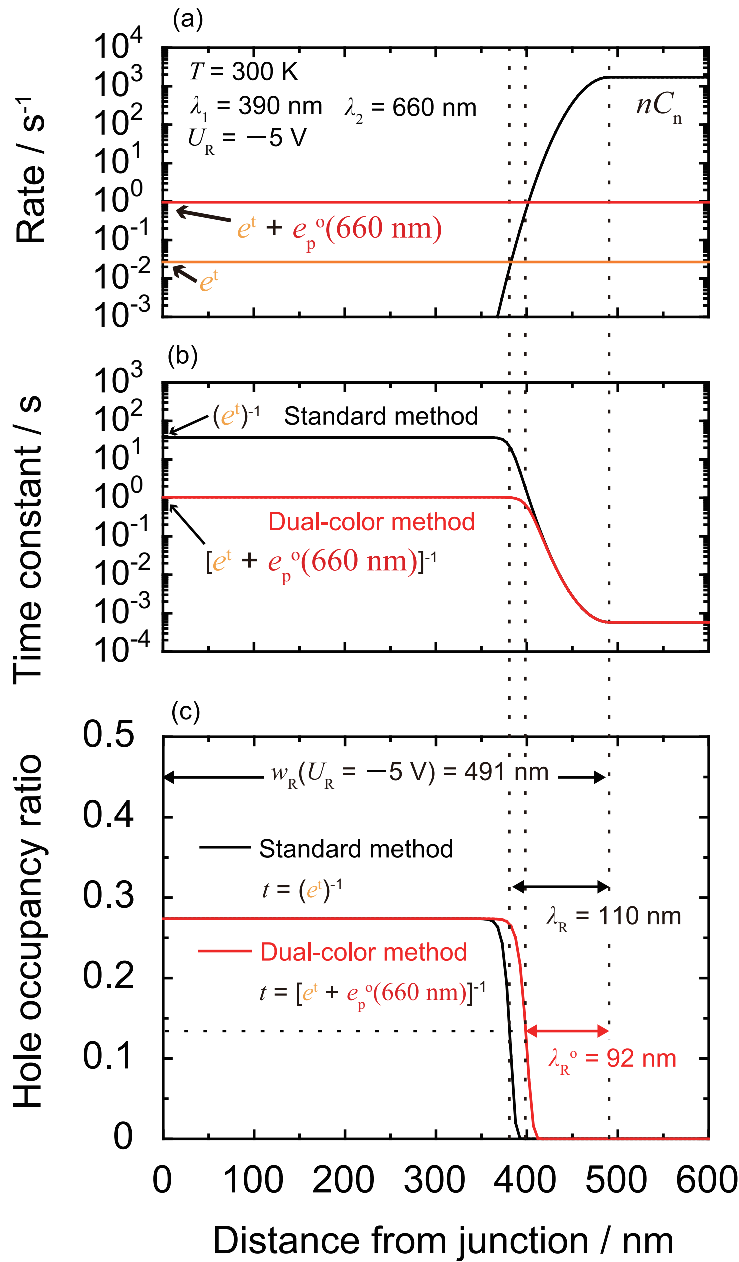

Figure 5.33: Depth profiles from an Schottky barrier junction of (a) rates, (b) time constant, and (c) hole occupancy ratio of the H1 trap when measurement bias voltage of –5 V is applied in dual-color method. In Fig. 5.33(a), the orange and black solid lines denote the depth profiles of the hole thermal excitation rate and the electron capture rate, respectively. The red solid line denotes the sum of photoexcitation rate to the V.B. (660 nm) and thermal excitation rate. In Fig. 5.33(b), the black and red solid lines denote the depth profiles of time constant during the measurement period in standard sub-E_g-light-excited ICTS and dual-color sub-E_g-light-excited ICTS, respectively. In Fig. 5.33(c), the black and red solid lines denote the depth profiles of the hole occupancy ratio of the H1 trap at $t = 1/e^t$ in standard sub-E_g-light-excited ICTS and at $t = 1/[e^t + e_p^o(660\text{nm})]$ dual-color sub-E_g-light-excited ICTS, respectively.

Figure 5.34 shows the dependence of the measured density of hole trap H1 $f_\mathrm{T}FN_\mathrm{T}$ on the depletion layer width under the standard measurement condition with $\tau_\mathrm{p} = 1/[e^\mathrm{t} + e^\mathrm{o}_\mathrm{p}(660nm)] = 1.0$ s. In Fig. 5.34, the open red circles denote the experimental data and the red solid line denotes the fitting curve. From the dependence of $f_\mathrm{T}FN_\mathrm{T}$ on the depletion layer width, $f_\mathrm{T}N_\mathrm{T} = 1.8 \times 10^{15}$ cm^{-3} and $\lambda^\mathrm{o}_\mathrm{R} = 90$ nm were obtained. The density of hole-occupied hole trap H1 $f_\mathrm{T}N_\mathrm{T}$ obtained with dual-color sub-E_g-light-excited ICTS is in a good agreement with that obtained with standard sub-E_g-light-excited ICTS shown in Fig. 5.9 and this result is reasonable because the measurement condition during filling pulse period is same. The extracted $\lambda^\mathrm{o}_\mathrm{R} = 90$ nm is in a good agreement with the calculated $\lambda^\mathrm{o}_\mathrm{R}$ of 92 nm. From the analysis, the depletion layer edge correction factor $F = 0.67$ at $U_\mathrm{R} = -5$ V in dual-color method is obtained.

5.7.6 Quick Quantification of Density of Hole Trap H1 with Dual-color Sub-E_g-light-excited Method

To determine the density of hole trap H1 with the dual-color sub-E_g-light-excited ICTS, the optical power change method (see Sec. 5.6.2) was performed. Dual-color sub-E_g-light-excited ICTS spectra under different optical power of UV light (390 nm) are shown in Fig. 5.35 as the violet broken lines. In the same way as the optical power change method in sub-E_g-light-excited ICTS, the depletion layer edge correction factor F and the hole occupancy ratio under UV light (390 nm) illumination f_T were corrected. From the dependence fo the measured density of hole trap H1 $f_\mathrm{T}TN_\mathrm{T}$ on the depletion layer width w under the standard measurement condition [$T = 300$ K, $\Phi(390\mathrm{nm}) = \Phi_0$] as shown in Fig. 5.34, the depletion layer edge correction factor $F = 0.67$ at $U_\mathrm{R} = -5$ V is obtained. Dual-color sub-E_g-light-excited ICTS measurements were performed with varying optical power ($\Phi(390\mathrm{nm})$) at $T = 300$ K and $U_\mathrm{R} = -5$ V. Using the depletion layer edge correction factor $F = 0.67$, the measured densities of hole trap H1 in dual-color sub-E_g-light-excited ICTS with varying optical power at $U_\mathrm{R} = -5$ V were corrected to the density of hole-occupied hole trap H1. The dependence of the density of hole trap H1 $f_\mathrm{T}N_\mathrm{T}$ on the sum of photoexcitation rates $e^\mathrm{o}_\mathrm{n} + e^\mathrm{o}_\mathrm{p}$ is shown in Fig. 5.36. From the dependence of $f_\mathrm{T}N_\mathrm{T}$ on $e^\mathrm{o}_\mathrm{n} + e^\mathrm{o}_\mathrm{p}$, the hole occupancy ratio under UV light (390 nm) illumination $f_\mathrm{T} = 0.74$ at $T = 300$ K and $\Phi(390\mathrm{nm}) = \Phi_0$ was obtained. By correcting f_T, the density of hole trap H1 $N_\mathrm{T} = 2.3 \times 10^{15}$ cm^{-3} was extracted. This value is in a good agreement with those obtained from the above methods.

5.8 Summary

In this section, three measurement methods of density of the hole trap H1 in n-type GaN layer by sub-E_g-light-excited ICTS with Schottky junction were proposed. In the methods, sum of the photoexcitation ratios $e^\mathrm{o}_\mathrm{n} + e^\mathrm{o}_\mathrm{p}$ is extracted under each measurement condition and using the ratio $e^\mathrm{o}_\mathrm{n}/e^\mathrm{o}_\mathrm{p}(390$ nm), e^o_n and e^o_p are separately obtained. Using measured e^t

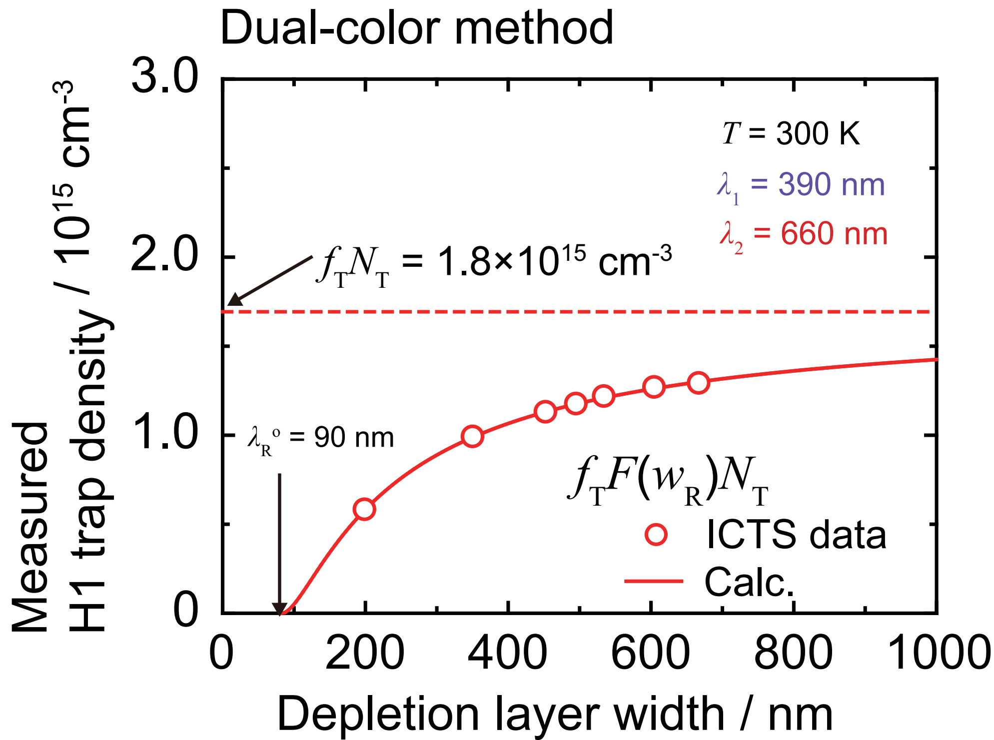

Figure 5.34: Dependence of the measured H1 trap density on the depletion layer width, which is varied by changing the measurement bias voltage U_R in the dual-color sub-E_g-light-excited ICTS at $T = 300$ K and $\Phi(390\text{nm}) = \Phi_0$. The open circles denote the ICTS data and red solid line shows the fitting curve. From the curve fitting based on Eqs. 5.2 and 5.4, the hole-occupied H1 trap density of 1.8×10^{15} cm^{-3} (red broken line) and λ_R^o of 90 nm were obtained at $T = 300$ K and $\Phi = \Phi_0$.

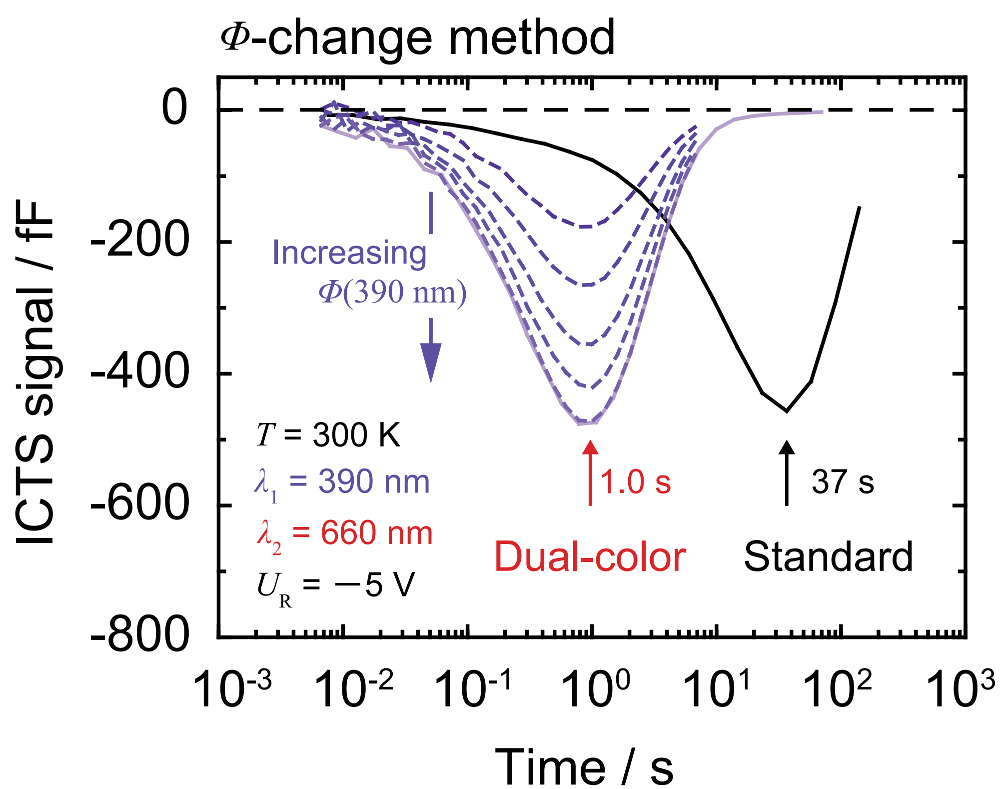

Figure 5.35: Dual-color sub-E_g-light-excited ICTS spectra in the optical power change method. The measurement bias voltage and temperature were set to –5 V and 300 K.

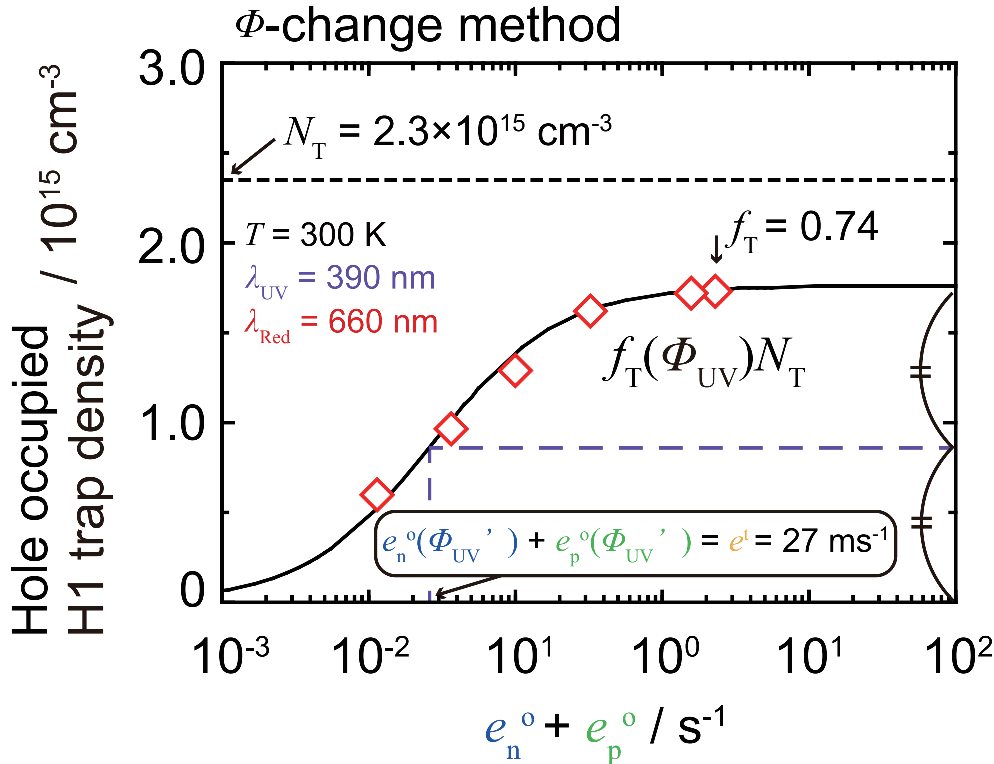

Figure 5.36: Dependence of the hole-occupied H1 trap density on the optical power (Φ(390nm)) in dual-color method. The open diamonds denote the experimental data. The black line shows the fitting curve using Eq. 5.16. Considering Eq. 5.16, when the hole occupancy ratio becomes half the value at high optical power, the sum of the photoexcitation rates is equal to the thermal excitation rate and based on this point, optical power is converted to the sum of the photoexcitation rates in the horizontal axis in Fig. 5.36. From the curve fitting, the H1 trap density of 2.3×10^{15} cm^{-3} was extracted.

and extracted e_n^o and e_p^o, the hole occupancy ratio at the trap under light illumination is calculated and correcting the hole occupancy ratio, it was shown that the accurate density of hole trap H1 can be measured using any of the three proposed methods. In particular, in the optical power and optical filling pulse width change methods, sub-E_g-light-excited ICTS with various U_R may be performed under an optical measurement condition, and it is not necessary to change temperature, so that the measurement time can be reduced as compared with the temperature change method. Moreover, the three methods can be combined with the dual-color method and it makes shortened the measurement time. The proposed methods are useful tool for monitoring the C_N deep acceptor density in n-type GaN epilayers with various growth methods or conditions. Compared with the proposed methods (temperature change, optical-power change, or optical-pulse-width change method), the quick measurement method reduces the measurement time by one order of magnitude in dual-color method.

References

[1] A. Ishitani, K. Okuno, A. Karen, S. Karen, and F. Soeda, in Proceedings of the International Conference on Materials and Process Characterization for VLSI (ICMPC'88), 124 (1988).

[2] A. Armstrong, A. R. Arehart, D. Green, U. K. Mishra, J. S. Speck, and S. A. Ringel, J. Appl. Phys. **98**, 053704 (2005).

[3] Y. Tokuda, Y. Yamada, T. Shibata, S. Yamaguchi, H. Ueda, T. Uesugi, and T. Kachi, Phys. St. Solidi C **8**, 2239 (2011).

[4] U. Honda, Y. Yamada, Y. Tokuda, and K. Shiojima, Jpn. J. Appl. Phys. **51**, 04DF04 (2012).

[5] T. Tanaka, K. Shiojima, T. Mishima, and Y. Tokuda, Jpn. J. Appl. Phys. **55**, 061101 (2016).

[6] Y. Tokuda, ECS Trans. **75**, 39 (2016).

[7] K. Kanegae, M. Horita, T. Kimoto, and J. Suda, Appl. Phys. Express **11**, 071002 (2018).

[8] K. Kanegae, H. Fujikura, Y. Otoki, T. Konno, T. Yoshida, M. Horita, T. Kimoto, and J. Suda, Appl. Phys. Lett. **115**, 012103 (2019).

[9] K. Kanegae, T. Narita, K. Tomita, T. Kachi, M. Horita, T. Kimoto, and J. Suda, Appl. Phys. Express **14**, 091004 (2021).

[10] J. F. Muth, J. H. Lee, I. K. Shmagin, R. M. Kolbas, H. C. C. Jr., B. P. Keller, U. K. Mishra, and S. P. DenBaars, Appl. Phys. Lett. **71**, 2572 (1997).

[11] S. Pimputkar, S. Suihkonen, M. Imade, Y. Mori, J. S. Speck, and S. Nakamura, J. Crystal Growth **432**, 49 (2015).

[12] D. C. look and J. H. Leach, J. Vac. Sci. Technol. B **34**, 04J105 (2016).

[13] T. Maeda, M. Okada, M. Ueno, Y. Yamamoto, M. Horita, and J. Suda, Appl. Phys. Express **9**, 109201 (2016).

[14] G. M. Martin, A. Mitonneau, D. Pons, A. Mircea, and D. W. Woodard, Jpn. Phys. C: Solid St. Physics **13**, 3855 (1980).

[15] M. J. Kane, M. J. Uren, D. J. Wallis, P. J. Wright, D. E. J. Soley, A. J. Simons, and T. Martin, Sci. Technol. **26**, 085006 (2011).

[16] D. Pons and S. Makram-Ebeid, J. de Physique **40**, 1161 (1979).

[17] S. D. Brotherton, Solid-State Electronics **26**, 987 (1983).

[18] P. Hacke, T. Detchprohm, K. Hiramatsu, N. Sawaki, K. Tadatomo, and K. Miyake, J. Appl. Phys. **76**, 304 (1994).

[19] W. Gotz, N. M. Johnson, H. Amano, and I. Akasaki, Appl. Phys. Lett. **65**, 463 (1994).

[20] N. Sawada, T. Narita, M. Kanechika, T. Uesugi, T. Kachi, M. Horita, T. Kimoto, and J. Suda, Appl. Phys. Express **11**, 041001 (2018).

[21] T. Tanaka, K. Shiojima, T. Mishima, and Y. Tokuda, Jpn. J. Appl. Phys. **55**, 061101 (2016).

[22] M. Horita, T. Narita, T. Kachi, and J. Suda, Appl. Phys. Express **13**, 071007 (2020).

[23] D. Wickramaratne, C. E. Dreyer, B. Monserrat, J. X. Shen, J. L. Lyons, A. Alkauskas, and C. G. V. d. Walle, Appl. Phys. Lett. **113**, 192106 (2018).

[24] J. L. Lyons, A. Janotti, and C. G. V. d. Walle, Appl. Phys. Lett. **97**, 152108 (2010).

Chapter 6

Nature of Hole Trap H1 in n-Type GaN

6.1 Introduction

In this Chapter, nature of the hole trap H1 in n-type GaN layers is investigated. It is important to study the nature of the hole trap H1 as well as to measure the density. In this study, quantitative relationship between carbon concentration and density of hole trap H1, electron capture cross-section of the hole trap H1, and dependence of the photoionization cross-section ratio of the hole trap H1 on photon energy are discussed.

6.2 Comparison between Density of Hole Trap H1 and Carbon Concentration in n-Type GaN layers

6.2.1 Deep Levels in Quartz-free Hydride-vapor-phase Epitaxy Grown n-Type GaN

A drift layer, which is applied with a high reverse bias voltage, is important for such power devices. In vertical power devices, a lightly doped thick layer with a low trap density is required for the drift layer and MOVPE-grown GaN layers on GaN freestanding substrates are commonly used for that purpose [1–6]. Such MOVPE-grown GaN layers contain carbon (C) impurities from the gas source (trimethylgallium), and it is known that carbon impurity substitutions at the nitrogen site (C_N) act as a dominant deep acceptor in n-type GaN layers [6–8]. Thus, a low carbon concentration is required in order to obtain lightly doped n-type drift layers. However, in the MOVPE method, low carbon concentration growth conditions result in low growth rates (∼3 μm/h) [6]. When considering power device mass production, this trade-off is a potential obstacle to the application of the MOVPE method.

On the other hand, the hydride-vapor-phase epitaxy (HVPE) method has an extremely

high growth rate of over 100 μm/h and involves the use of carbon-free raw materials [9, 10], which makes it possible to significantly reduce the carbon concentrations in comparison with the MOVPE method. However, the high background donor concentrations originating from residual silicon (Si) and oxygen (O) from a quartz-made reactor have made it difficult to apply the HVPE method to the growth of low-doped drift layers [11, 12].

In the quartz-free-HVPE (QF-HVPE) method, which was recently developed by Fujikura et al. [10], the residual Si and O donor concentrations were significantly reduced to the detection limits of secondary ion mass spectrometry (SIMS) by removing all of the quartz parts from the high-temperature region of the HVPE system. Additionally, lightly doped GaN layers on the order of the net donor density ($N_{\mathrm{d,net}} = N_{\mathrm{d}} - N_{\mathrm{a}}$) of 10^{15} cm^{-3} were realized [10]. Thus, due to its lightly doping control in addition to its high growth rate and low carbon concentration, the QF-HVPE method can be seen as an attractive contender for GaN on GaN epitaxy growth required by vertical power devices. Furthermore, although it is known that deep levels have a negative impact on device performance, there have been no reports regarding deep levels in QF-HVPE-grown GaN layers. Accordingly, in this study, both electron and hole traps in the QF-HVPE-grown homoepitaxial n-type GaN layers were investigated.

In this study, five QF-HVPE-grown n-type GaN layers on HVPE-grown n^{+}-type GaN substrates (Samples A-E) were characterized. These homoepitaxial n-type GaN layers were grown under different conditions. The oxygen concentration ([O]) and [C] were measured by the SIMS raster change mode, which has much lower detection limits compared to conventional SIMS. The Si concentration ([Si]) is controlled on the order of 10^{15} cm^{-3} and was confirmed to be uniformly distributed via the SIMS depth profile mode. As a result of the quartz parts removal, [O] is under 5×10^{14} cm^{-3}, which is the detection limit of [O] when the SIMS raster change mode is used. The SIMS raster change mode provides an accurate way to determine and remove contribution of background atom to the signal because secondary ion intensities and matrix ion intensities can be analyzed at the same location of the sample by changing the primary beam raster size during a profile [13].

By optimizing the growth conditions and the HVPE system, [C] is reduced to 10^{15} cm^{-3} or less. The minimum value of [C] is 3.9×10^{14} cm^{-3}. Since the HVPE-method is essentially carbon-free because of the use of carbon-free raw materials, the detected residual carbon might come from several carbon parts used in our equipment. To characterize the QF-HVPE-grown GaN layers, Schottky and ohmic contacts were formed by Ni depositions on the top and Ti/Al/Ti/Au depositions on the backside, respectively. The author then performed deep-level transient spectroscopy (DLTS) [14] and isothermal capacitance transient spectroscopy (ICTS) [15]. In these scans, the voltage-bias pulse, which is a forward bias voltage (U_{P}) of 0.5V with a pulse width (t_{p}) of 0.1 s, was used for the electron trap measurements. A 390 nm sub-E_{g}-light pulse with a pulse width ($t_{\mathrm{p}}^{\mathrm{o}}$) of 2-5 s was utilized for the hole trap measurements. In this study, DLTS and ICTS spectra of Sample A are shown as representatives.

First, DLTS and ICTS scans were performed to characterize electron traps. In Fig. 6.1(a) and Fig. 6.1(b), the DLTS and ICTS spectra of Sample A are shown, respectively, and three electron traps are detected. In Fig. 6.2(a), the Arrhenius plots of the electron traps are shown. Two of them are E1 ($E_C - 0.22$ eV) and E3 ($E_C - 0.60$ eV) traps, which were detected in the MOVPE-grown homoepitaxial n-type GaN layers [16]. The other trap is EX ($E_C - 0.71$ eV), which was detected in the conventional HVPE-grown GaN layers [17, 18]. In conventional HVPE-grown GaN layers, an additional electron trap ($E_C - 1$ eV) was detected [16]. As shown in Fig. 6.1(b), no other deeper traps are detected. Among the three electron traps, the E3 trap is dominant. However, the E3 trap density ($N_{T,E3}$) is one order of magnitude smaller than $N_{d,net}$. DLTS and ICTS scans were performed for the other samples as well, but no other electron traps were detected. The E1, E3, and EX trap densities ($N_{T,E1}$, $N_{T,E3}$, and $N_{T,EX}$) are shown in Table I.

Second, sub-E_g-light DLTS and sub-E_g-light ICTS scans were performed to characterize hole traps. Figure 6.3(a) and Fig. 6.3(b) show the sub-E_g-light-excited DLTS and ICTS spectra of Sample A, revealing the eight hole traps. In Fig. 6.2(b), the Arrhenius plots of the hole traps are shown. Three of these are H1 ($E_V + 0.87$ eV), H2 ($E_V + 0.38$ eV), and H3 ($E_V + 0.38$ eV) traps, which were also detected in the MOVPE-grown n-type GaN layers [16]. The others are HX ($E_V + 0.44$ eV), HY ($E_V + 0.55$ eV), HZ ($E_V + 0.66$ eV), H5, and H6 traps, which were detected in the conventional HVPE-grown n-type GaN layers [18, 19]. Of these eight hole traps, the H1 trap is detected predominantly. The H1 trap density ($N_{T,H1}$) was determined by the method proposed by our group and is almost equal to [C]. The sub-E_g-light-excited DLTS and ICTS scans were performed for the other samples, but no other hole traps were discovered.

$N_{T,E1}$, $N_{T,E3}$, and $N_{T,H1}$ in Sample A were compared with those in a GaN layer grown by a MOVPE method with a low residual carbon growth condition (LC-MOVPE) in which [C] is 2×10^{15} cm^{-3}. $N_{T,E1}$ and $N_{T,E3}$ values in Sample A were 1.2×10^{13} cm^{-3} and 2.2×10^{14} cm^{-3}, respectively, and comparable with those of the LC-MOVPE-grown GaN layer. On the other hand, $N_{T,H1}$ was 7.7×10^{14} cm^{-3} and much smaller than that of the LC-MOVPE-grown GaN layer (2.3×10^{15} cm^{-3}). This reflects the reduction of [C].

According to the previous reports, the H1 trap has been ascribed to gallium vacancy (V_{Ga}) related defects [16, 19–22] or C related defects [C_N (0/−)] [7, 16, 23–28] which act as deep acceptors. In this study, $N_{T,H1}$ was determined by a method that considers the depletion layer edge correction and the hole occupancy ratio under the sub-E_g-light-excited illumination. [C] was accurately measured by the raster change mode SIMS. Figure 6.4 shows the relationship between [C] and $N_{T,H1}$. In Fig. 6.4, $N_{T,H1}$ is almost equal to [C] over a wide range, which clearly indicates that the H1 trap is associated with C_N (0/−) in our QF-HVPE-grown GaN layers.

The QF-HVPE-grown GaN layers have the low trap densities, among which the H1 trap [C_N (0/−)] is dominant. Thus, the author simply assumed that traps (acceptors) other than the H1 did not contribute to $N_{d,net}$. In Fig. 6.5, the relationship between $N_{d,net}$ obtained

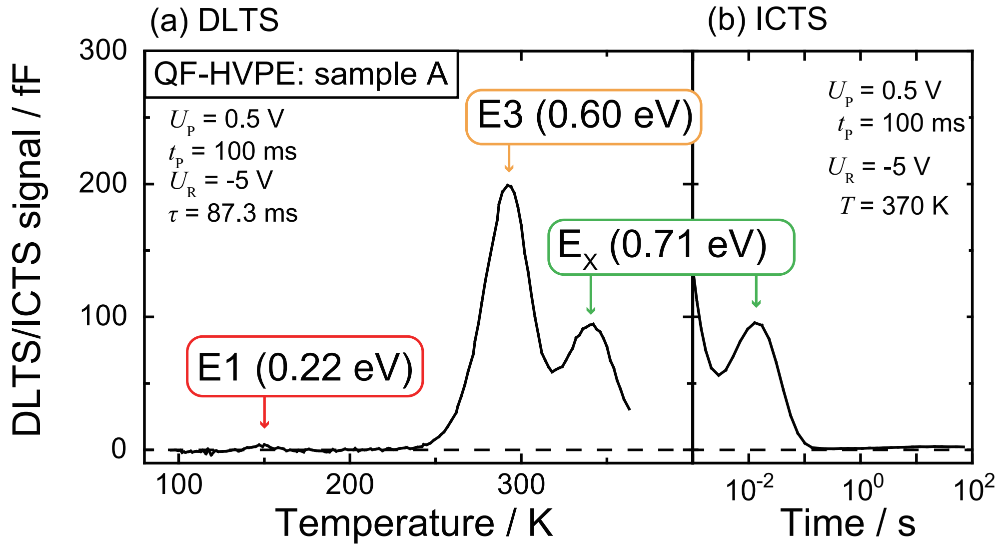

Figure 6.1: (a) DLTS spectrum for the QF-HVPE-grown GaN Schottky barrier diode (SBD) (Sample A). The time window is τ = 87.3 ms. (b) ICTS spectrum for the QF-HVPE-grown GaN SBD (Sample A) at 370 K. The forward bias voltage and pulse width of the filling pulses were U_P = 0.5 V and t_P = 100 ms, respectively, and the measurement bias voltage was U_R = −5 V for both spectra.

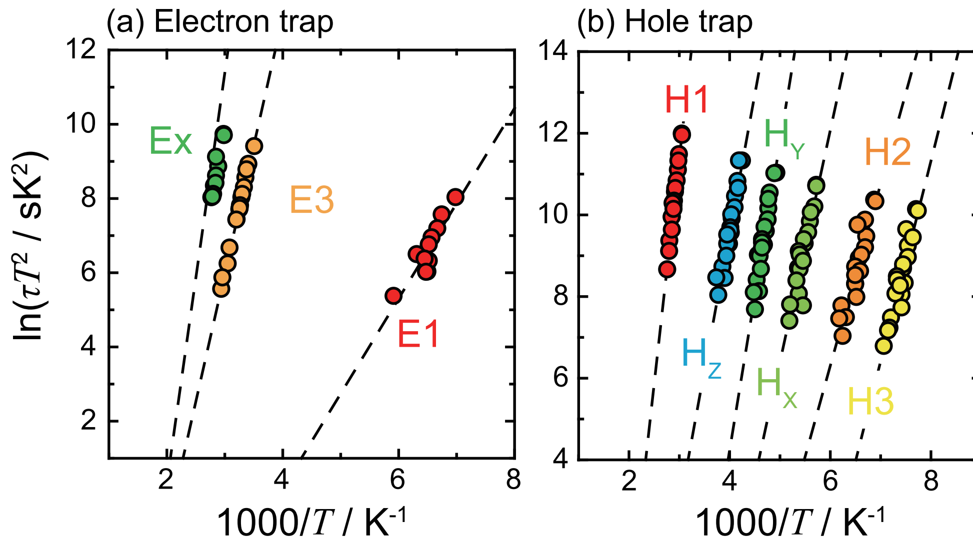

Figure 6.2: Arrhenius plots of (a) electron traps and (b) hole traps in QF-HVPE-grown n-type GaN.

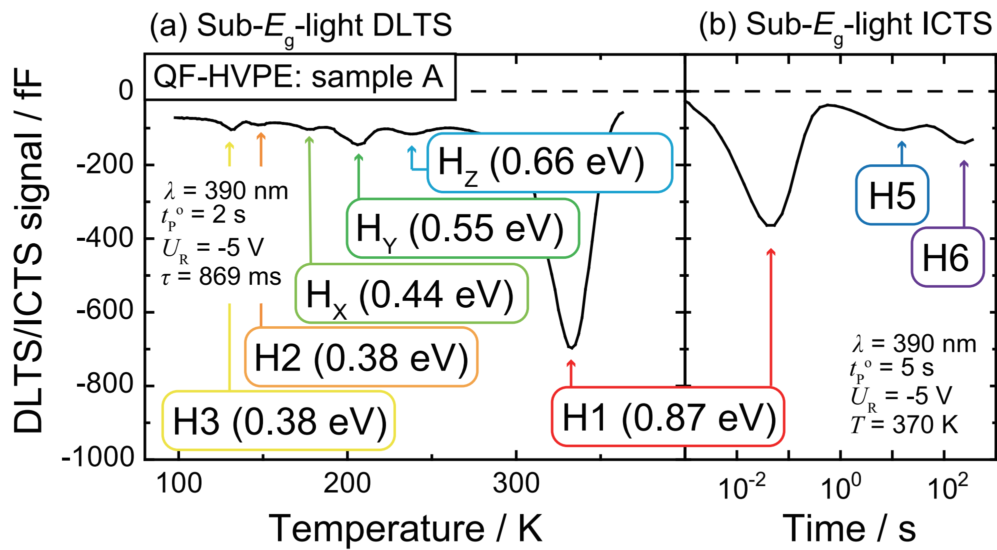

Figure 6.3: (a) Sub-E_g-light DLTS spectrum for the QF-HVPE-grown GaN SBD (Sample A). The time window is $\tau = 869$ ms. (b) Sub-E_g-light ICTS spectrum for the QF-HVPE-grown GaN SBD (Sample A) at 370 K. The wavelength of the filling pulses was $\lambda = 390$ nm for both spectra. The pulse width of the filling pulses was $t_p^o = 2$ s and 5 s for the sub-E_g-light DLTS and the sub-E_g-light ICTS spectra, respectively. The measurement bias voltage was $U_R = -5$ V for both spectra.

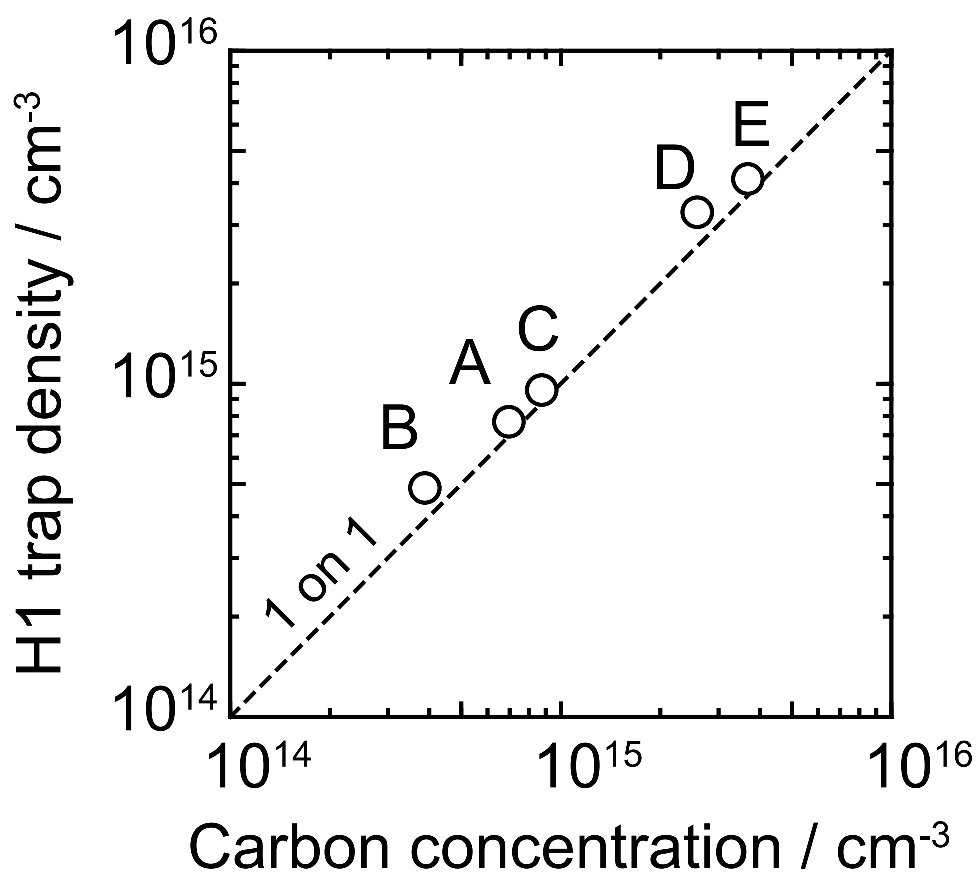

Figure 6.4: Relationship between the carbon concentration and H1 trap density in the QF-HVPE-grown GaN layers.

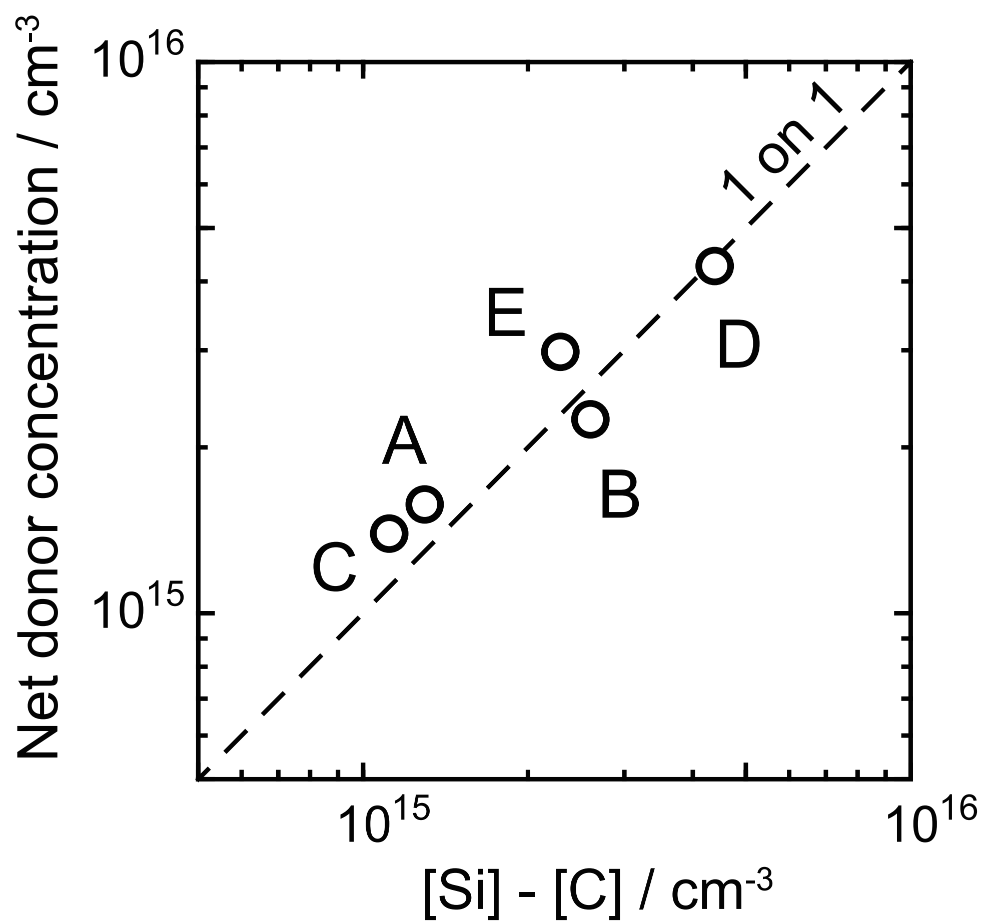

Figure 6.5: Relationship between the Si concentration compensated by the carbon and the net donor concentration in the QF-HVPE-grown GaN layers.

by the $C - V$ measurement and [Si] $-$ [C] is plotted. $N_{\mathrm{d,net}}$ is almost equal to [Si] $-$ [C] over a wide range, which clearly indicates that when $N_{\mathrm{d,net}}$ is in the range of 10^{15} cm^{-3}, the other traps or impurities other than the H1 trap are negligible. In the QF-HVPE-grown GaN layers, the major deep acceptor is considered to be $\mathrm{C_N}$ $(0/-)$. In QF-HVPE-grown GaN, [C] is already much smaller than the smallest [C] in MOVPEgrown GaN layers and it is expected that a further reduction of [C] could be achieved by replacing the HVPE components with those with a higher purity and increasing the purity of the gases. In the QF-HVPE method, $N_{\mathrm{d,net}}$ can be well controlled on the order of 10^{15} cm^{-3} and this allows fabrication of over 3 kV-class GaN on GaN vertical power devices. This shows that the QF-HVPE method is a promising technique for drift layer growth of GaN.

6.2.2 Discussion

For some MOVPE-grown n-type GaN layers with different [C], the optical power change method combined with the dual-color method was performed. Figure 6.6 shows the relationship between the H1 trap density determined from the sub-E_{g}-light-excited ICTS and the carbon concentration determined from SIMS as black open circles. Considering the result in QF-HVPE-grown n-type GaN layers (black closed diamonds) together, the quantitative 1 on 1 relationship between the carbon concentration and the $\mathrm{C_N}$ accentor density is observed in the carbon density range from 10^{14} cm^{-3} to 10^{17} cm^{-3}. This result suggests that the almost all incorporated carbon atoms substitute at the nitrogen site in the n-type GaN layers regardless of the growth methods and growth conditions. Considering the formation energy diagrams of incorporated carbon atoms as shown in Fig. 6.7 [29], it can be seen that an incorporated carbon atom easily form $\mathrm{C_N}$. The result shown in Fig. 6.6 supports the theoretical predictions. Fig. 6.8 shows the relationship between the net donor density ($N_{\mathrm{d,net}} = N_{\mathrm{d}} - N_{\mathrm{a}}$) and the difference between silicon concentration and density of hole trap H1 ([Si] - N_{T}) in the n-type GaN layers. As shown in Fig. 6.8, the net donor density is almost equal to the difference between [Si] and density of hole trap H1 in each n-type GaN layer. This result suggests that the dominant compensation acceptor corresponds to the $\mathrm{C_N}(0/-)$ in the n-type GaN layers used in this study.

6.3 Electron Capture Cross-section of Hole Trap H1

6.3.1 Experiments

In this study, the electron capture cross-section σ_{n} of the hole trap H1 was obtained using sub-E_{g}-light-excited ICTS with a measurement sequence shown in Fig. 6.9. In the sub-E_{g}-light-excited ICTS with the measurement sequence shown in Fig. 6.9, dual filling pulse is applied: the first filling pulse is an optical pulse to photoexcite the hole traps and second filling pulse is an electrical pulse for the hole-occupied hole traps to capture electrons in

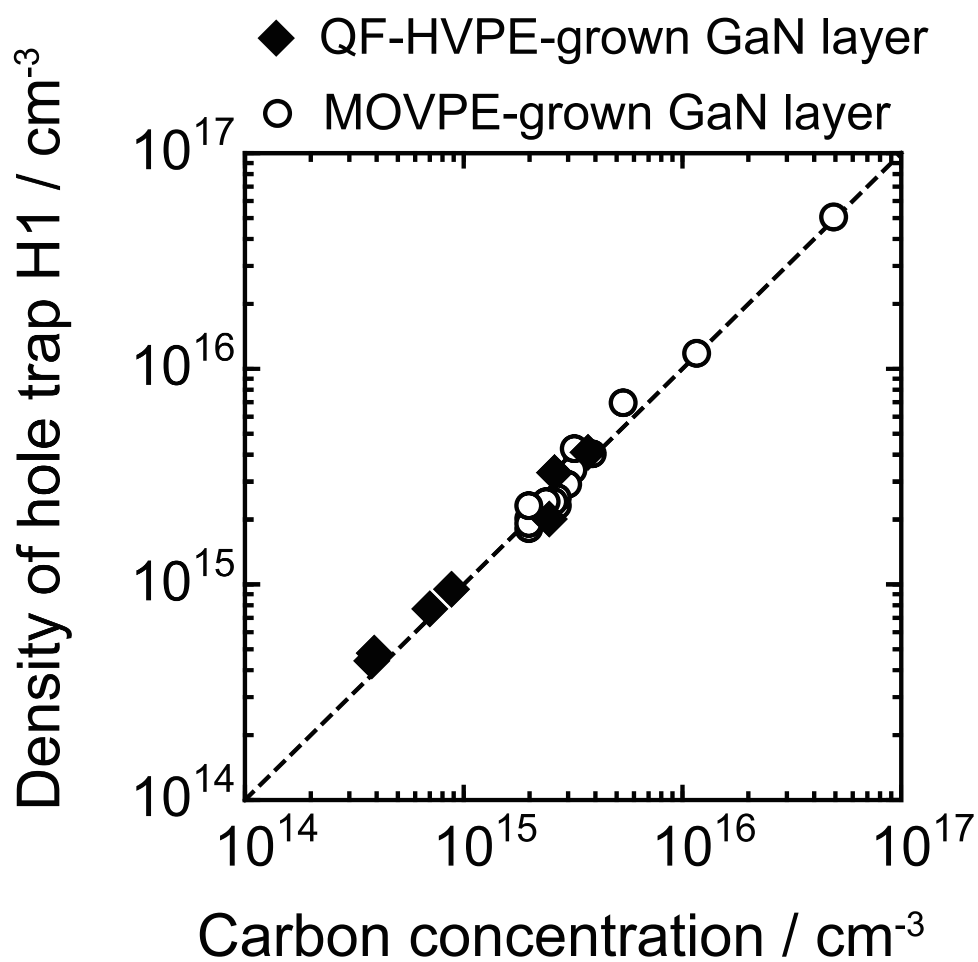

Figure 6.6: Relationship between the carbon concentration and density of hole trap H1 in the n-type GaN layers.

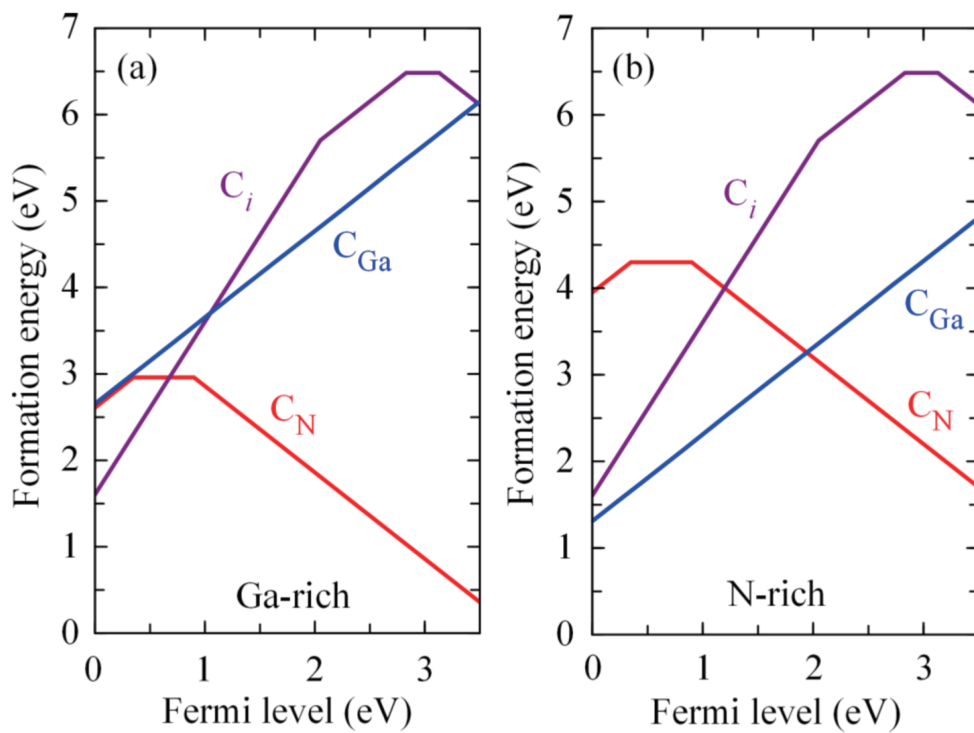

Figure 6.7: Formation energy versus Fermi level for substitutional C_{Ga}, C_N, and interstitial C_i configurations in GaN [29]. (a) Ga-rich conditions. (b) N-rich conditions.

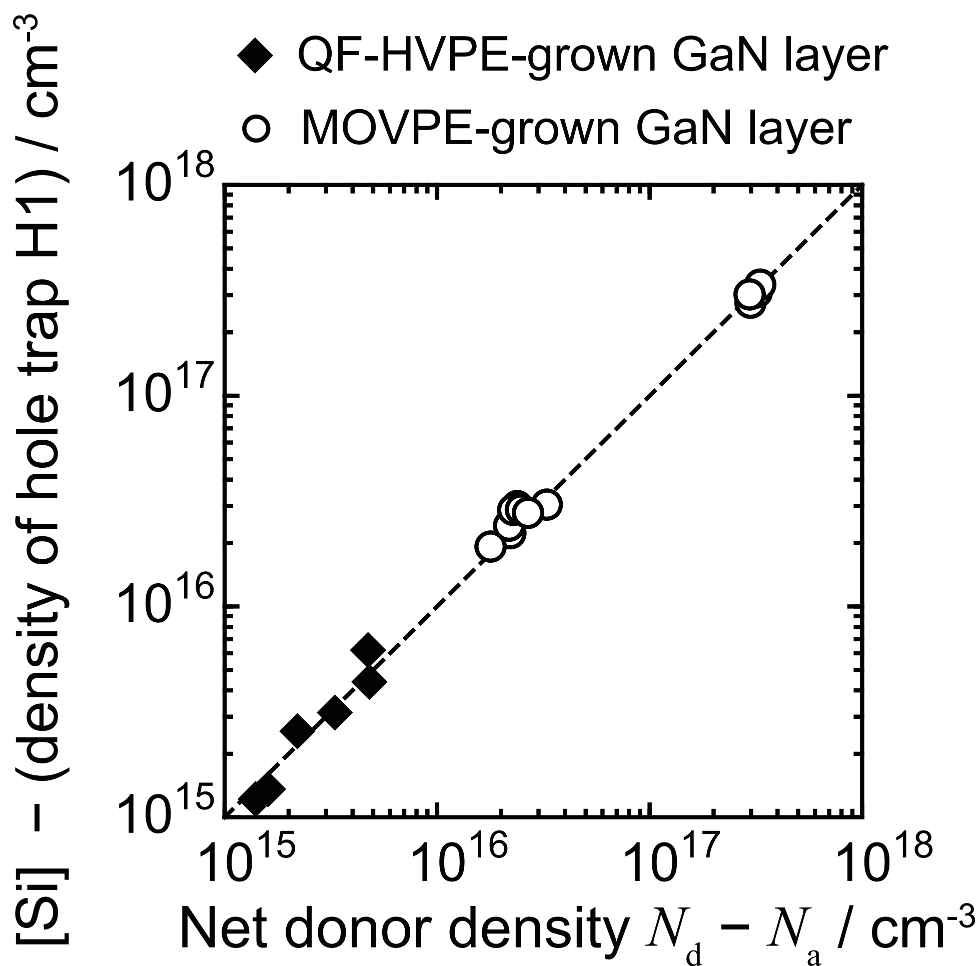

Figure 6.8: Relationship between the net donor density ($N_{\mathrm{d,net}} = N_{\mathrm{d}} - N_{\mathrm{a}}$) and the difference between silicon concentration and density of hole trap H1 ([Si] - N_{T}) in the n-type GaN layers.

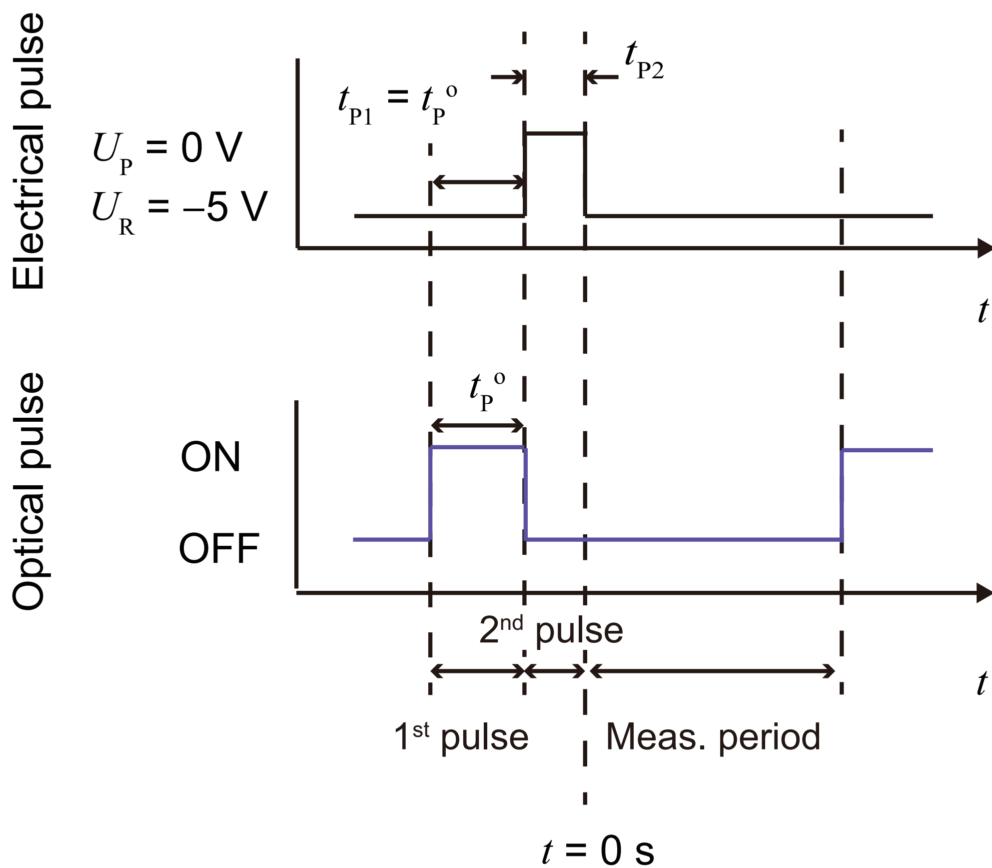

Figure 6.9: Pulse sequence for measurement of electron capture cross section of the H1 trap. In the sequence, the first filling pulse is optical pulse for photoexcitation ($U_{P1} = U_R = -5$ V, $t_{P1} = t_P^o = 3$ s) and the second filling pulse is electrical pulse for electron capture ($U_{P2} = 0$ V, t_{P2}).

the conduction band. In Fig. 6.10, band diagrams of an n-type Schottky barrier diode in sub-E_g-light-excited ICTS with the dual filling pulse are shown (a) during first filling pulse (optical pulse), (b) during second filling pulse (electrical pulse), and (c) during measurement period. Figure 6.11 shows the calculation depth profile of the hole occupancy ratio of the H1 trap assuming a measurement condition based on our standard one ($T = 300$ K, $\Phi = \Phi_0$, $U_\mathrm{R} = -5$ V). The effect of parasite ICTS was also removed in the same way as the optical filling pulse width change method. The first filling pulse width is sufficiently long ($t_\mathrm{P}^\mathrm{o} = 3$ s) and during the first filling pulse period, $U_\mathrm{P1} = -5$ V was applied. Then, hole traps in $0 \text{ nm} < x \leqq w_\mathrm{R} - \lambda_\mathrm{P}^\mathrm{o}$ become the hole-occupied state with the ratio of f_T [Fig. 6.10(a) and violet solid line in Fig. 6.11]. During the second filling pulse period, bias voltage $U_\mathrm{P2} = 0$ V was applied and the light was cut off. Then, the hole-occupied hole taps in $w_\mathrm{P2} - \lambda_\mathrm{P2} < x \leqq w_\mathrm{R} - \lambda_\mathrm{P}^\mathrm{o}$ can capture electrons in the conduction band [Fig. 6.10(b)], i.e., the hole occupancy ratio decreases in $w_\mathrm{P2} - \lambda_\mathrm{P2} < x \leqq w_\mathrm{R} - \lambda_\mathrm{P}^\mathrm{o}$ (black broken line in Fig. 6.11). w_P2 is the depletion layer width when U_P2 is applied and λ_P2 is the width where the electron capture is dominant in the depletion layer edge when U_P2 is applied. Thus, during the measurement period [Fig. 6.10(c) and black solid line in Fig. 6.11], the hole-occupied hole traps in $0 \text{ nm} < x \leqq w_\mathrm{P2} - \lambda_\mathrm{P2}$, which are photoexcited during the first optical filling pulse, and in $w_\mathrm{P2} - \lambda_\mathrm{P2} < x \leqq w_\mathrm{R} - \lambda_\mathrm{P}^\mathrm{o}$, which do not capture the electrons in the conduction band during the second electrical filling pulse, are detectable. The hole occupancy ratio at $t = 0$ s in $w_\mathrm{P2} - \lambda_\mathrm{P2} < x \leqq w_\mathrm{R} - \lambda_\mathrm{P}^\mathrm{o}$ depends on the second filling pulse width t_P2, i.e., by modulating t_P2, the electron capture coefficient C_n can be obtained and σ_n can be extracted. In Fig. 6.11, the depth profile of the hole occupancy ratio with $t_\mathrm{P2} = 1/N_\mathrm{d,net}C_\mathrm{n}$ is shown. As show in Fig. 6.11 by the black broken line, when the position at which $f_\mathrm{T}(x,0) - f_\mathrm{T}(w_\mathrm{P2},0)$ is half of the value at the Schottky junction $[f_\mathrm{T}(0,0) - f_\mathrm{T}(w_\mathrm{P2},0)]$ is defined as $x = w_\mathrm{P2} - \lambda_\mathrm{P2}(t_\mathrm{P2})$, $\lambda_\mathrm{P2}(t_\mathrm{P2})$ is given as:

$$\lambda_\mathrm{P2}(t_\mathrm{P2}) = L_\mathrm{D}\sqrt{2\ln\left(\frac{\frac{t_\mathrm{P2}}{1/(N_\mathrm{d,net}C_\mathrm{n})}}{\ln 2 - \ln\left[\exp\left(-\frac{t_\mathrm{P2}}{1/e^\mathrm{t}}\right) + \exp\left(-\frac{t_\mathrm{P2}}{1/(N_\mathrm{d,net}C_\mathrm{n})}\right)\right] - \frac{t_\mathrm{P2}}{1/e^\mathrm{t}}}\right)}. \tag{6.1}$$

Then, the measured hole trap density is given as:

$$\begin{aligned}
&\tilde{N}_\mathrm{T} = f_\mathrm{T} F N_\mathrm{T},\\
&\text{where, } F \equiv D\exp\left(-\frac{t_\mathrm{P2}}{1/(N_\mathrm{d,net}C_\mathrm{n})}\right) + E\exp\left(-\frac{t_\mathrm{P2}}{1/e^\mathrm{t}}\right),\\
&D \equiv \left(1 - \frac{\lambda_\mathrm{R}}{w_\mathrm{R}}\right)^2 \frac{x_2^2 - x_1^2}{x_2^2},\\
&E \equiv \left(1 - \frac{\lambda_\mathrm{R}}{w_\mathrm{R}}\right)^2 \frac{x_1^2}{x_2^2},\\
&x_1 \equiv w_\mathrm{P2} - \lambda_\mathrm{P2}(1/(N_\mathrm{d,net}C_\mathrm{n})), \text{ and } x_2 \equiv w_\mathrm{R} - \lambda_\mathrm{R}.
\end{aligned} \tag{6.2}$$

In Eq. 6.2, $f_\mathrm{T}DN_\mathrm{T}$ and $f_\mathrm{T}EN_\mathrm{T}$ indicate the hole-occupied hole trap densities in $w_\mathrm{P2} - \lambda_\mathrm{P2} < x \leqq w_\mathrm{R} - \lambda_\mathrm{P}^\mathrm{o}$ and in $0 \text{ nm} < x \leqq w_\mathrm{P2} - \lambda_\mathrm{P2}$, respectively.

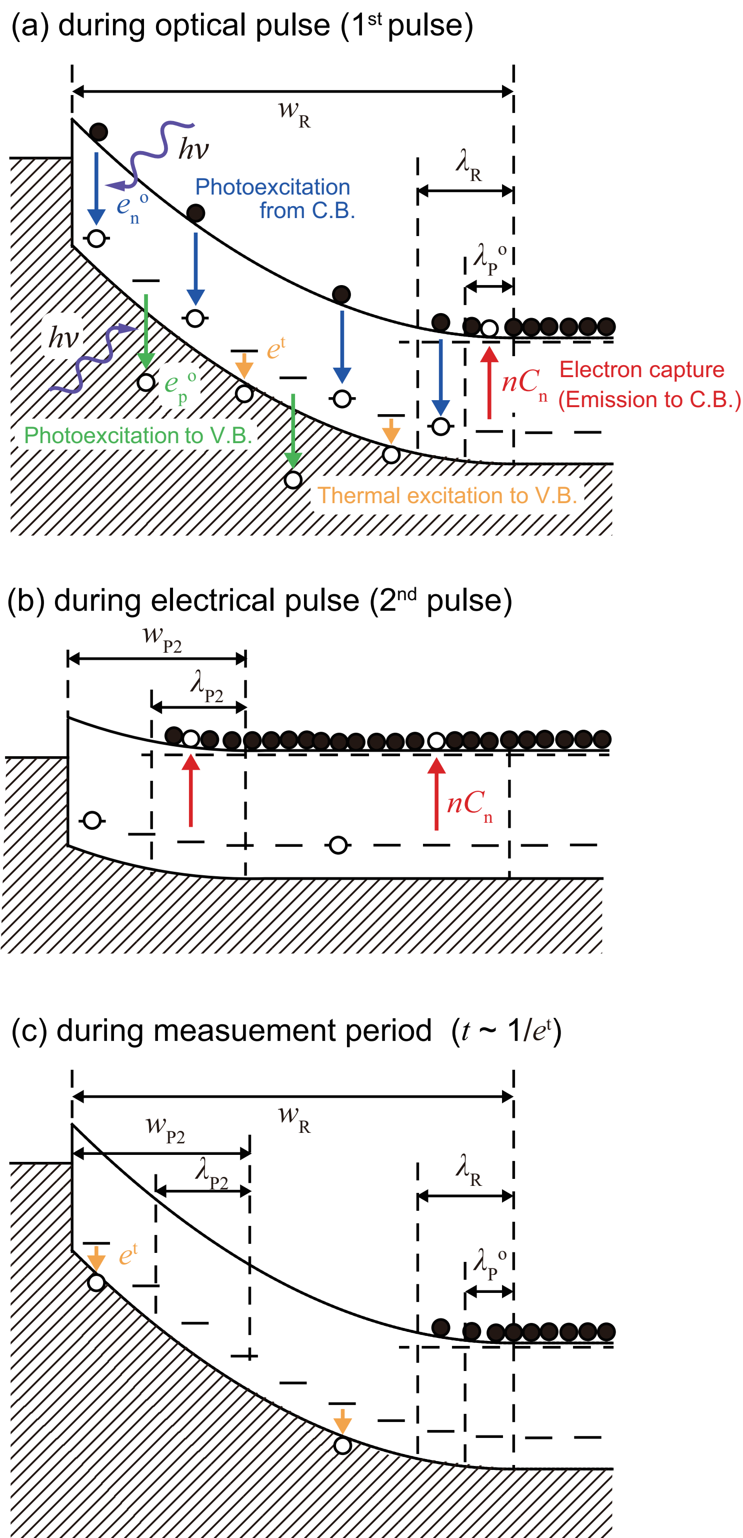

Figure 6.10: Band diagrams of an SBD (a) during first filling pulse period, (b) during second filling pulse period, and (c) during measurement period. During the second filling pulse period, the quick carrier recombination via the H1 trap (electron capture) occurs in the region of the shrunken depletion layer.

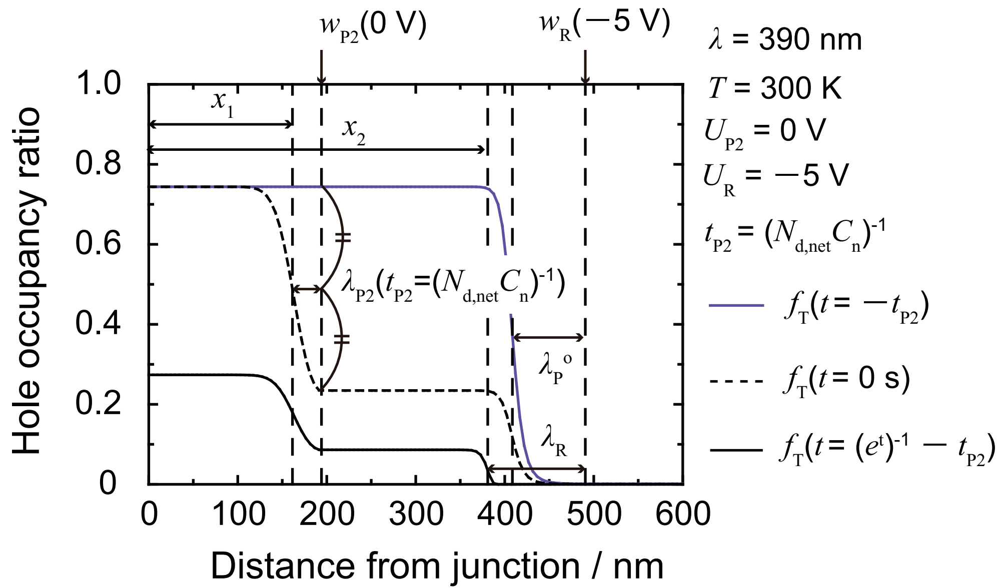

Figure 6.11: Depth profiles of the hole occupancy ratio of the H1 trap at $t = -t_{\mathrm{P2}}$ (violet solid line), 0 s (black broken line), and $1/e^{\mathrm{t}} - t_{\mathrm{P2}}$ (black solid line) when measurement bias voltage of –5 V is applied at $t_{\mathrm{P2}} = 1/N_{\mathrm{d,net}}C_{\mathrm{n}}$.

6.3.2 Results and Discussion

Figure 6.12 shows the dependence of the measured density of hole trap H1 in the sub-E_g-light-excited ICTS with dual filling pulse on the second electrical filling pulse width. In Fig. 6.12, the open circles denote the experimental data. As shown in Fig. 6.12, $\tilde{N}_\mathrm{T}$ is almost equal to $f_\mathrm{T}DN_\mathrm{T}e^{(}-1) + f_\mathrm{T}EN_\mathrm{T}$ at $t_\mathrm{P2} = 1/N_\mathrm{d,net}C_\mathrm{n}$ when $N_\mathrm{d,net}C_\mathrm{n}$ is much larger than e^t, thus from the position at $t_\mathrm{P2} = 1/N_\mathrm{d,net}C_\mathrm{n}$, σ_n can be extracted. To improve accuracy, for the experimental data, a curve fitting was performed based on Eq. 6.2 using $f_\mathrm{T}DN_\mathrm{T} + f_\mathrm{T}EN_\mathrm{T}$ and σ_n as the parameters. The calculation result is shown in Fig. 6.12 as the black solid line. From the curve fitting, $f_\mathrm{T}DN_\mathrm{T} + f_\mathrm{T}EN_\mathrm{T}$ of $1.0{\times}10^{15}$ cm^{-3} and σ_n of $3{\times}10^{-21}$ cm^2 were extracted. This result is reasonable because $f_\mathrm{T}DN_\mathrm{T} + f_\mathrm{T}EN_\mathrm{T} = 1.0 \times 10^{15}$ cm^{-3} indicates $f_\mathrm{T}N_\mathrm{T} = 1.7 \times 10^{15}$ cm^{-3} and this value is almost equal to the hole-occupied H1 trap density of $1.8{\times}10^{15}$ cm^{-3} under the standard measurement condition ($T = 300$ K, $\Phi = \Phi_0$, $t^\mathrm{o}_\mathrm{P} = 3$ s). The electron capture cross-section σ_n can be also extracted from $C_\mathrm{n} = \sigma_\mathrm{n}v_\mathrm{th,n}$ in λ_R. λ_R is given as:

$$\lambda_\mathrm{R} = L_\mathrm{D}\sqrt{2\ln\left(\frac{N_\mathrm{d,net}C_\mathrm{n}}{e_\mathrm{p}\ln 2}\right)}. \tag{6.3}$$

In this study, λ_R of 110 nm was obtained under the standard measurement condition (Chapter 5) and σ_n of $2{\times}10^{-21}$ cm^2 was extracted by using Eq. 6.3 [$C_\mathrm{n} = \sigma_\mathrm{n}v_\mathrm{th,n}$ in Eq. 6.3] and this result is reasonable comparing to σ_n of $3{\times}10^{-21}$ cm^2, which was extracted from Fig. 6.12. These values are in good agreement with the reported value by Polyakov et al. $\sigma_\mathrm{n} = 1.4{\times}10^{-22}$ cm^2 [30], $\sigma_\mathrm{n} = 7{\times}10^{-20}$ cm^2 [31], and by Kato et al. $\sigma_\mathrm{n} = 3{\times}10^{-21}$ cm^2 [32]. In this study, σ_n of $3{\times}10^{-21}$ cm^2 was used to calculate the hole occupancy ratio at 300 K.

Figure 6.13 shows the dependence of electron and hole capture cross-sections of hole trap H1 on temperature. The electron capture cross-section σ_n is extracted from $\lambda_\mathrm{R}(T)$ discussed in Sec. 5.5.3. The hole capture cross-section is extracted from e^t investigated in Sec. 5.6.1 by assuming that the temperature dependence of trap energy can be negligible. The hole capture cross-section σ_p is almost independent of temperature ($\sigma_\mathrm{p} = 7{\times}10^{-16}$ cm^2). On the other hand, the electron capture cross-section decreases with elevating temperature. Similar behavior was observed for the hole capture cross-sections of Cu, Cr, and Fe levels in p-type GaAs [33].

6.4 Dependence of Photoionization Cross-section of Hole Trap H1 on Photon Energy

In metalorganic vapor phase epitaxy (MOVPE)-grown n-type GaN layers, (1) the hole trap H1 ($E_\mathrm{V} + 0.87$ eV) was detected as a dominant minority carrier trap [16] and (2) its origin is most likely the residual carbon from metalorganic source [$(CH_3)_3Ga$] substituting at the nitrogen site [C_N (0/−)] [7, 16, 29]. Understanding the physical properties of hole trap

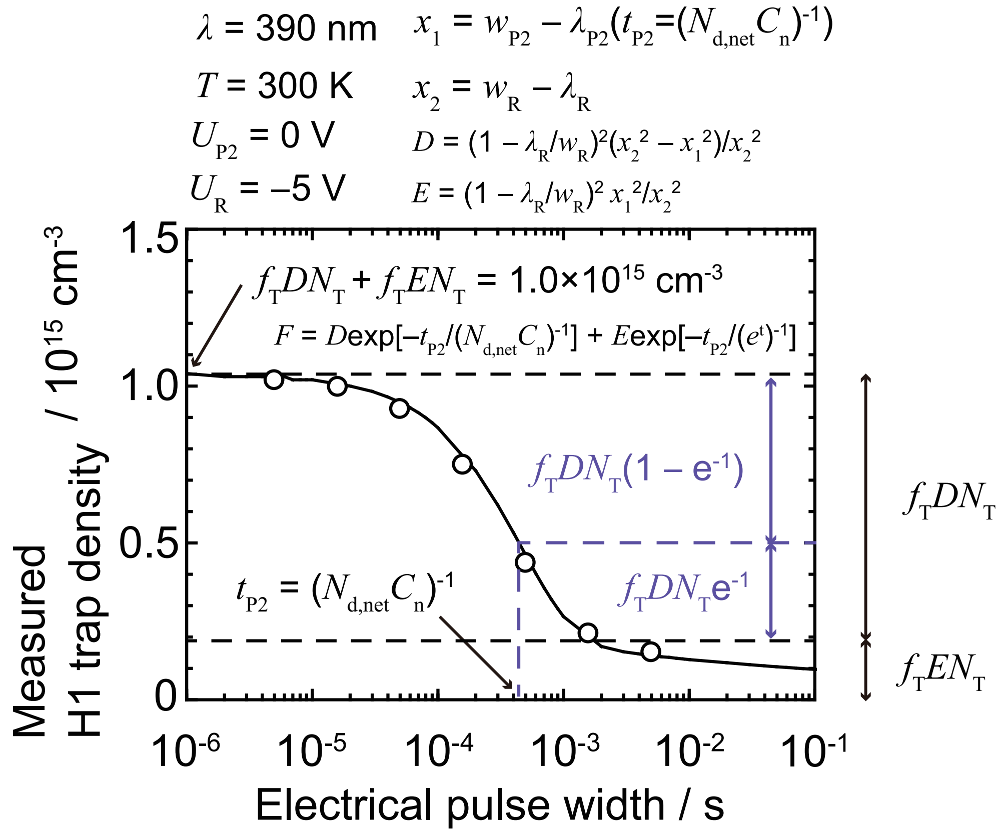

Figure 6.12: Dependence of the measured H1 trap density on the second filling pulse width (electrical pulse width). The open circle denotes the experimental data. The black solid line is calculated based on Eqs. 6.1 and 6.2.

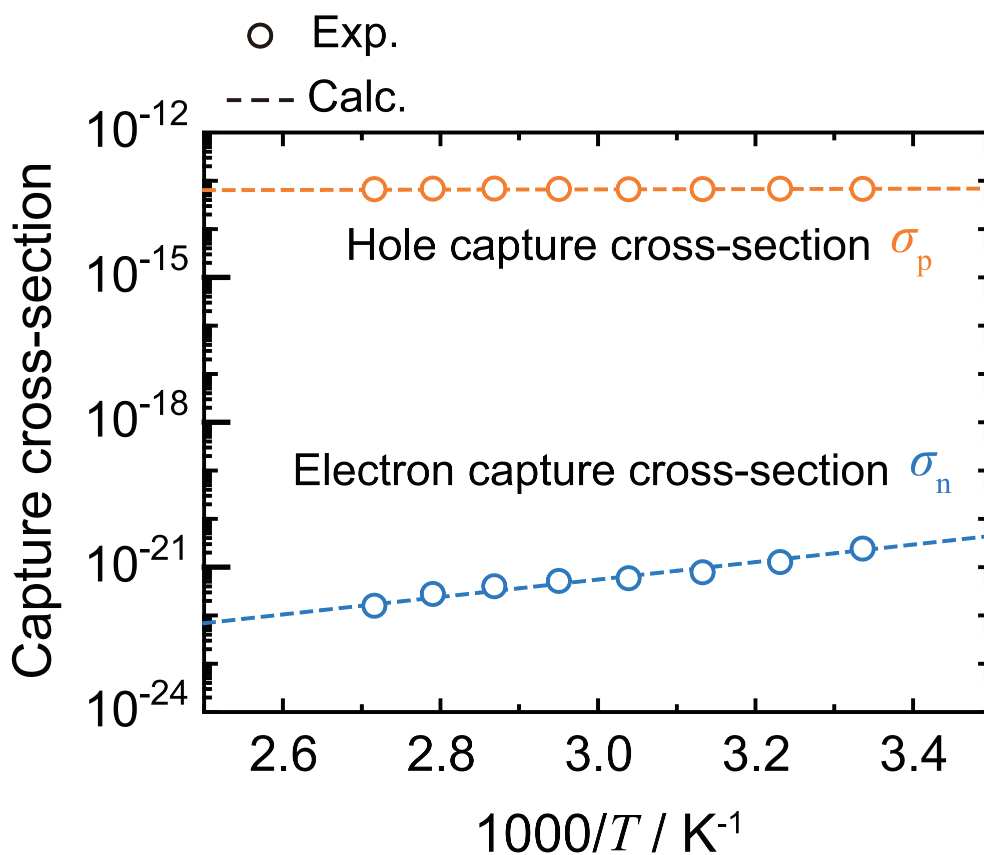

Figure 6.13: Dependence of capture cross-section on temperature. The blue open circles and orange open circles denote the electron and hole capture cross-sections, respectively.

H1 is very important to predict the impact on device characteristics. In this chapter, the author investigate photon energy ($h\nu$) dependence of $\sigma_{\mathrm{n}}^{\mathrm{o}}/\sigma_{\mathrm{p}}^{\mathrm{o}}$. The author found that the obtained dependence can be well explained by using the reported configuration coordinate (CC) diagram for $\mathrm{C_N}$ (based on ab-initio calculation [7, 29, 34]).

6.4.1 Experiments

The Schottky barrier diode comprised a MOVPE-grown 3-μm-thick n-GaN on an HVPE-grown $\mathrm{n^+}$-type GaN substrate. The SBD is the same as that used in Chapter 5. The silicon concentration of the n-type GaN was obtained via depth profile mode SIMS as 3×10^{16} $\mathrm{cm^{-3}}$. The oxygen and carbon concentrations of the n-type GaN were obtained via raster change mode SIMS [13] as $< 3\times10^{14}$ $\mathrm{cm^{-3}}$ (under detection limit) and 2×10^{15} $\mathrm{cm^{-3}}$, respectively. The author also confirmed the uniform distributions of Si concentration via SIMS depth profile. The Schottky and Ohmic electrodes were formed via deposition of Ni on the top and Ti/Al/Ti/Au on the back side, respectively. The diameter of Schottky electrode was 400 μm.

Sub-E_{g}-light-excited ICTS were performed with various $h\nu$ (2.6 eV to 3.2 eV) under temperature ranging from 300 K to 370 K. The light source is LEDs. The optical pulse width (t_{P}) was utilized so that the junction capacitance was saturated as under each measurement condition. Reverse bias voltage (U_{R}) was varied from 0 V to −10 V. The density of hole trap H1 (N_{T}) of 2.3×10^{15} $\mathrm{cm^{-3}}$ was determined in the n-type GaN by sub-E_{g}-light-excited ICTS with the proposed analysis method, showing a good agreement with a C concentration of 2×10^{15} $\mathrm{cm^{-3}}$ by SIMS. Thus, the hole trap H1 is manly associated with $\mathrm{C_N}$ (0/−) in the n-type GaN layer.

6.4.2 Results and Discussion

During sub-E_{g}-light irradiation, the electron photoexcitation (excitation), hole photoionization (quenching), and hole thermal emission occur for hole traps in the depletion layer in n-type semiconductors. A photoionization ratio of the hole trap under sub-E_{g}-light irradiation of the hole trap ($f_{\mathrm{T}} < 1$) is calculated taking account of a competition among the electron photoexcitation rate ($e_{\mathrm{n}}^{\mathrm{o}} = \sigma_{\mathrm{n}}^{\mathrm{o}}\Phi$, Φ: incident photon flux), hole photoionization rate ($e_{\mathrm{p}}^{\mathrm{o}} = \sigma_{\mathrm{p}}^{\mathrm{o}}\Phi$), and hole thermal emission rate (e^{t}) and is given as

$$f_{\mathrm{T}} = \frac{e_{\mathrm{n}}^{\mathrm{o}}}{e_{\mathrm{n}}^{\mathrm{o}} + e_{\mathrm{p}}^{\mathrm{o}} + e^{\mathrm{t}}}. \tag{6.4}$$

The measured H1 trap density is a product of f_{T}, F and N_{T}. F is the depletion layer edge correction factor due to the quick carrier recombination via hole trap near the depletion layer edge and can be extracted from sub-E_{g}-light-excited ICTS with various U_{R}. N_{T} of 2.3×10^{15} $\mathrm{cm^{-3}}$ in the n-type GaN layer was determined in Chapter 5. Thus, f_{T} can be extracted from sub-E_{g}-light-excited ICTS under each irradiation condition. The author

performed sub-E_g-light ICTS with various temperature and the temperature dependence of $e^t = 1/\tau_p^t$ (τ_p^t: time constant of hole thermal emission obtained from sub-E_g-light-excited ICTS peak) and f_T were obtained. The author performed a curve fitting for $f_T(e^t)$ by using Eq. 6.4 and fitting parameters of e_n^o and e_p^o were extracted. Although σ_n^o and σ_p^o can not be obtained because accurate measurement of Φ is difficult, the author experimentally determined $\sigma_n^o/\sigma_p^o (= e_n^o/e_p^o)$ which is a physical property of C_N. The dependence of σ_n^o/σ_p^o on $h\nu$ is shown in Fig. 6.14. σ_n^o/σ_p^o increases with increasing $h\nu$. The photoionization energy (E_n^o) of C_N is 2.95 eV [29]. It can be explained by considering a large magnitude of the Frank-Condon (FC) shift for C_N [7, 29, 34]. For such deep levels, the Lucovsky model of photoionization cross-section in combination with the semiclassical approximation for the FC factor is considered and $\sigma_n^o/\sigma_p^o(h\nu)$ is given as [35]

$$\sigma_n^o/\sigma_p^o(h\nu) = A \times \frac{\int_0^{+\infty} \mathrm{d}x \left[\frac{E_k^{a_n+\frac{1}{2}}}{(E_k+E_n^o-D_n)^{2b_n}} \exp\left(-\frac{(h\nu-E_k-E_n^o)^2}{2D_n\varepsilon\coth\left(\frac{\varepsilon}{2k_B}T\right)} \right) \right]}{\int_0^{+\infty} \mathrm{d}x \left[\frac{E_k^{a_p+\frac{1}{2}}}{(E_k+E_p^o-D_p)^{2b_p}} \exp\left(-\frac{(h\nu-E_k-E_p^o)^2}{2D_p\varepsilon\coth\left(\frac{\varepsilon}{2k_B}T\right)} \right) \right]} \tag{6.5}$$

Here, A is a scaring factor, D is magnitude of FC shift, E^o is photoionization energy, ε is effective (average) phonon energy. a is 0 (for allowed transition) or 1 (for forbidden transition). b is 0 (for Dirac-type potential) or 1 (for Coulomb-type potential). The sub-characters of n and p are correspond to electron and hole photoionization, respectively. In this study, the author used D_n of 400 meV [34], D_p of 550 meV [34], E_n^o of 2.88 eV [34], E_p^o of 1.57 eV [34], and ε of 50 meV [36]. Dirac-type potential ($b = 1$) was assumed for C_N. The configuration coordinate (CC) diagram of $C_N(0/-)$ at $T = 0$ K [34] is shown in Fig. 6.15. The orbital of C_N is p-like [29] and the orbital of near conduction band minimum is s-like. However, the high energy state of conduction band has p-like orbital. Thus, the transition of electron photoexcitation from C_N to the conduction band changes an allowed transition to forbidden transition gradually and a_n also changes from 0 to 1 gradually. In the same way, the valence band maximum has p-like orbital, but the deep energy state of valence band has s-like state and a_p changes from 1 to 0 gradually. It should also be noted that the orbital of the C_N state, which is the localized electrical state, is not a complete p-orbital and contains other orbitals. For simplicity, here, a_n of 0 and a_p of 1 are assumed and the dependence of the photoionization cross-section ratio σ_n^o/σ_p^o on photon energy ($h\nu$) is calculated. Curve fitting was performed for the experimental data $\sigma_n^o/\sigma_p^o(h\nu)$ based on Eq. 6.5. The fitting parameter is only the scaring factor A and the shape of $\sigma_n^o/\sigma_p^o(h\nu)$ is determined from the CC diagram as shown in Fig. 6.15. The calculated result $\sigma_n^o/\sigma_p^o(h\nu)$ is shown in Fig. 6.14 as the black solid line. The calculated result is in good agreement with the experimental one. Form the analysis, photoionization cross-sections $\sigma_n^o(h\nu)$ and $\sigma_p^o(h\nu)$ shown in Fig. 6.16 as the blue solid line and green solid line are successfully extracted, respectively.

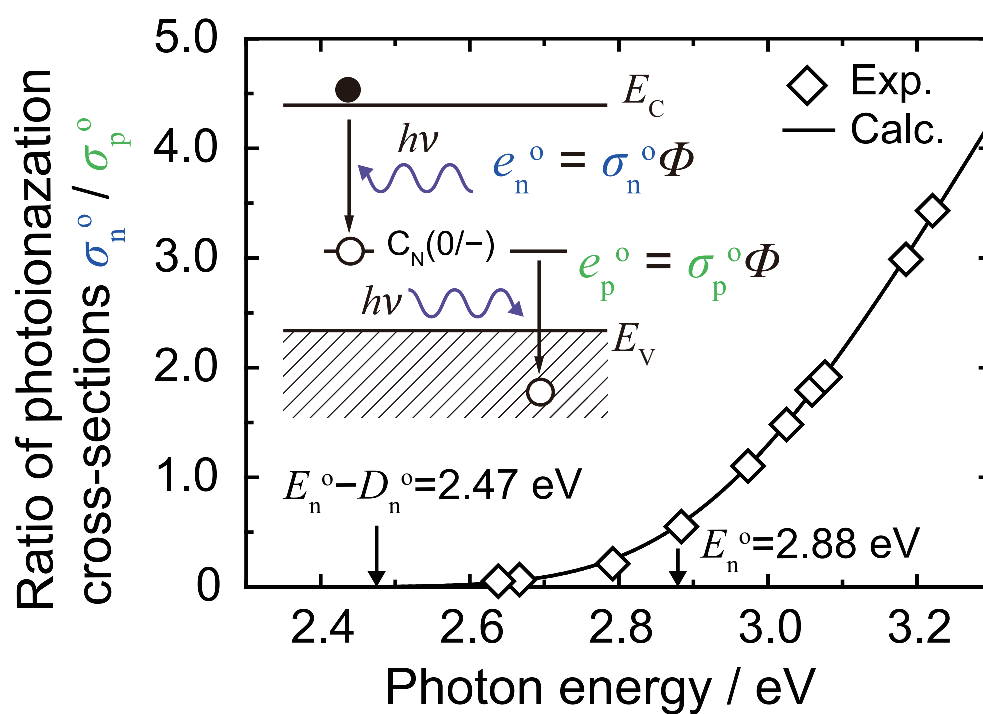

Figure 6.14: Dependence of photoionization cross-section ratio on photon energy.

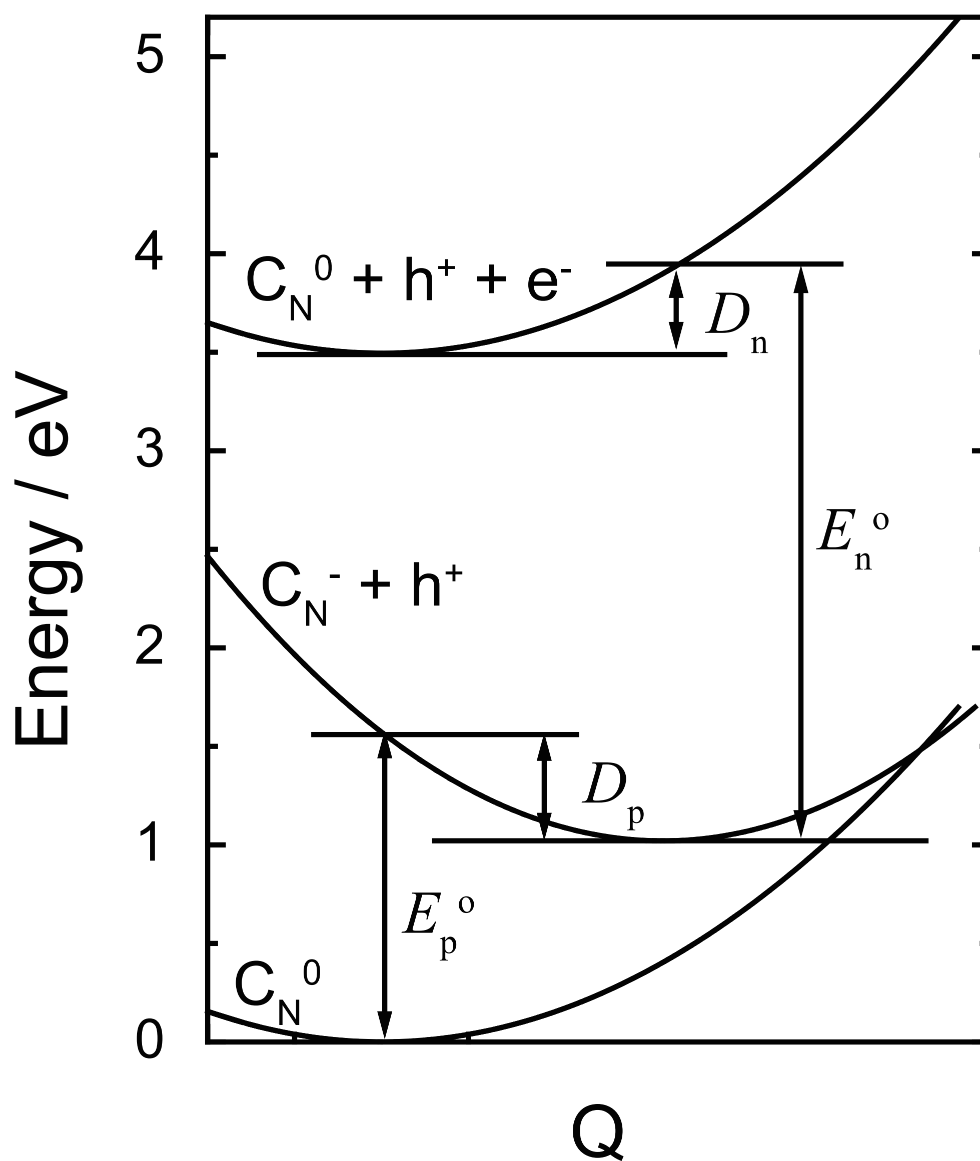

Figure 6.15: Configuration coordinate (CC) diagram of $C_N(0/-)$ at $T = 0$ K. [34].

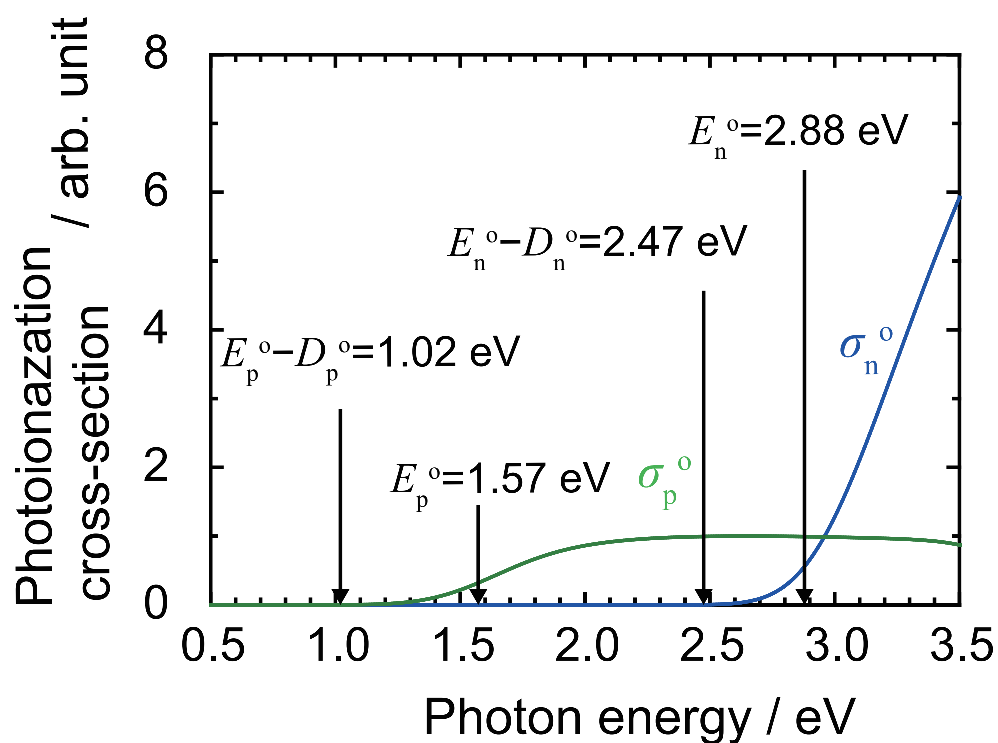

Figure 6.16: Dependence of photoionization cross-section on photon energy. The blue and solid lines denote electron photoionization cross-section σ_n^o and hole photoionization cross-section σ_p^o.

6.5 Summary

Using the proposed method, quantitative 1 on 1 relationship between the carbon concentration and the carbon acceptor density in n-type GaN layer is obtained and the it is shown that the dominant donor compensating acceptor is the carbon acceptor in the donor density range from 10^{15} cm^{-3} to 10^{18} cm^{-3} (carbon density range from 10^{14} cm^{-3} to 10^{17} cm^{-3}). This result suggests that the almost all incorporated carbon atoms substitute at the nitrogen site in the n-type GaN layers regardless of the growth methods and growth conditions. The proposed methods are useful tool for monitoring the C_N deep acceptor density in n-type GaN epilayers with various growth methods or conditions.

The $h\nu$ dependence of σ_n^o/σ_p^o for the H1 trap is experimentally determined. The photoionization of H1 trap with $h\nu$ below can be reasonably explained by the reported CC diagram of $C_N(0/-)$.

References

[1] J. Suda, K. Yamaji, Y. Hayashi, T. Kimoto, K. Shimoyama, H. Namita, and S. Nagao, Appl. Phys. Express **3**, 101003 (2010).

[2] T. Kachi, Jpn. J. Appl. Phys. **53**, 100210 (2014).

[3] H. Nie, Q. Diduck, B. Alvarez, A. P. Edwards, B. M. Kayes, M. Zhang, G. Ye, T. Prunty, D. Bour, and I. C. Kizilyalli, IEEE Electron Device Lett. **35**, 939 (2014).

[4] T. Oka, Y. Ueno, T. Ina, and K. Hasegawa, Appl. Phys. Express **7**, 021002 (2014).

[5] I. C. Kizilyalli, A. P. Edwards, O. Aktas, T. Prunty, and D. Bour, IEEE Trans. Electron Devices **62**, 414 (2015).

[6] G. Piao, K. Ikenaga, Y. Yano, H. Tokunaga, A. Mishima, Y. Ban, T. Tabuchi, and K. Matsumoto, J. Crystal Growth **456**, 137 (2016).

[7] J. L. Lyons, A. Janotti, and C. G. V. d. Walle, Appl. Phys. Lett. **97**, 152108 (2010).

[8] N. Sawada, T. Narita, M. Kanechika, T. Uesugi, T. Kachi, M. Horita, T. Kimoto, and J. Suda, Appl. Phys. Express **11**, 041001 (2018).

[9] T. Yoshida, Y. Oshima, K. Watanabe, T. Tsuchiya, and T. Mishima, Phys. St. Solidi C **8**, 2110 (2011).

[10] H. Fujikura, T. Konno, T. Yoshida, and F. Horikiri, Jpn. J. Appl. Phys. **56**, 085503 (2017).

[11] Y. Oshima, T. Yoshida, T. Eri, M. Shibata, and T. Mishima, Jpn. J. Appl. Phys. **45**, 7685 (2006).

[12] K. Fujito, S. Kubo, H. Nagaoka, T. Mochizuki, H. Namita, and S. Nagao, J. Crystal Growth **311**, 3011 (2009).

[13] A. Ishitani, K. Okuno, A. Karen, S. Karen, and F. Soeda, in Proceedings of the International Conference on Materials and Process Characterization for VLSI (ICMPC'88), 124 (1988).

[14] D. V. Lang, J. Appl. Phys. **45**, 3023 (1974).

[15] H. Okushi1 and Y. Tokumaru, Jpn. J. Appl. Phys. **20**, 261 (1981).

[16] Y. Tokuda, ECS Trans. **75**, 39 (2016).

[17] D. Look, Z.-Q. Fanga, and B. Claflina, J. Crystal Growth **281**, 143 (2005).

[18] I.-H. Lee, A. Y. Polyakov, N. B. Smirnov, A. V. Govorkov, E. A. Kozhukhova, V. M. Zaletin, I. M. Gazizov, N. G. Kolin, and S. J. Pearton, J. Vac. Sci. Technol. B **30**, 021205 (2012).

[19] A. Y. Polyakov, N. B. Smirnov, A. V. Govorkov, H. Cox, A. S. Usikov, H. Helava, Y. N. Makarov, E. B. Yakimov, and I. H. Lee, American J. Appl. Sciences **11**, 1714 (2014).

[20] E. Calleja, F. J. Sánchez, D. Basak, M. A. S 叩 nchez-García, E. M. noz, I. Izpura, F. Calle, J. M. G. Tijero, J. L. Sánchez-Rojas, B. Beaumont, P. Lorenzini, and P. Gibart, Phys. Rev. B **55**, 4689 (1997).

[21] J. Neugebauer and C. G. V. d. Walle, Appl. Phys. Lett. **69**, 503 (1996).

[22] A. Y. Polyakov, I.-H. Lee, N. B. Smirnov, A. V. Govorkov, E. A. Kozhukhova, and S. J. Pearton, J. Appl. Phys. **109**, 123701 (2011).

[23] R. Armitage, W. Hong, Q. Yang, H. Feick, J. Gebauer, E. R. Weber, S. Hautakangas, and K. Saarinen, Appl. Phys. Lett. **82**, 3457 (2003).

[24] A. Armstrong, A. R. Arehart, D. Green, U. K. Mishra, J. S. Speck, and S. A. Ringel, J. Appl. Phys. **98**, 053704 (2005).

[25] Y. Tokuda, Y. Yamada, T. Shibata, S. Yamaguchi, H. Ueda, T. Uesugi, and T. Kachi, Phys. St. Solidi C **8**, 2239 (2011).

[26] U. Honda, Y. Yamada, Y. Tokuda, and K. Shiojima, Jpn. J. Appl. Phys. **51**, 04DF04 (2012).

[27] T. Tanaka, N. Kaneda, T. Mishima, Y. Kihara, T. Aoki, and K. Shiojima, Jpn. J. Appl. Phys. **54**, 041002 (2015).

[28] T. Tanaka, K. Shiojima, T. Mishima, and Y. Tokuda, Jpn. J. Appl. Phys. **55**, 061101 (2016).

[29] J. L. Lyons, A. Janotti, and C. G. V. d. Walle, Phys. Rev. B **89**, 035204 (2014).

[30] A. Y. Polyakov, N. B. Smirnov, E. B. Yakimov, S. A. Tarelkin, A. V. Turutin, I. V. Shemerov, S. J. Pearton, K.-B. Bae, and I.-H. Lee, J. Alloys Compd. **686**, 1044 (2016).

[31] K. Kanegae, M. Horita, T. Kimoto, and J. Suda, Appl. Phys. Express **11**, 071002 (2018).

[32] M. Kato, T. Asada, T. Maeda, K. Ito, K. Tomita, T. Narita, and T. Kachi, J. Appl. Phys. **129**, 115701 (2021).

[33] D. V. Lang and R. A. Logan, J. Electronic Materials **4**, 1053 (1975).

[34] D. Wickramaratne, C. E. Dreyer, B. Monserrat, J. X. Shen, J. L. Lyons, A. Alkauskas, and C. G. V. d. Walle, Appl. Phys. Lett. **113**, 192106 (2018).

[35] A. Chantre, G. Vincent, and D. Bois, Phys. Rev. B **23**, 5335 (1981).

[36] R. Pässler, J. Appl. Phys. **96**, 715 (2004).

Chapter 7

Depth Profiles of Density of Deep Levels Induced by Device Processes in SiC

7.1 Introduction

Reactive ion etching (RIE) is an essential process for fabrication of SiC and GaN devices to form mesa and trench structures. However, lattice damage produced by ion bombardment is a concern for the development of the devices. For example, a reduction of barrier height and degradation in the forward characteristics due to RIE damage in 4H-SiC SBDs have been reported [1]. Carrier traps generated during the RIE process, unlike those created during ion implantation processes [2–4], are localized near the etched surface (< 1 μm) and may have steep depth profiles.

In the DLTS [5] and ICTS [6] techniques, which are generally employed to characterize deep levels that act as carrier traps, it is typically assumed that the carrier trap density in a detection region is constant [7, 8]. In contrast, the double-correlation method [9] has been employed [4, 10–14] when a carrier trap density shows a spatial distribution in the depth direction. However, the double-correlation method has a trade-off relationship between the depth resolution and the resolution in the carrier trap density due to the measurement principle Therefore, it is difficult to investigate a steep depth profile, such as in the case of carrier traps induced during RIE processes. Reports on detailed depth profiles of carrier traps generated during RIE processes in SiC and GaN have been limited [14, 15].

In this chapter, the author proposes a method to measure depth profiles of carrier trap density with both the high depth resolution and the high resolution in the carrier trap density, i.e., the proposed method enables to measure steep depth profiles. In the proposed method, ICTS measurement with various measurement bias voltages for RIE-etched samples are performed and the ICTS data are analyzed assuming appropriate shapes of the depth profiles. Using the method, the depth profiles of the electron traps generated during the

RIE process in n-type SiC are extracted and the generation mechanisms of the electron traps are discussed. The method are applied for also RIE-induced defects in n-type GaN.

7.2 Theoretical and Experimental Approaches

When an n-type SBD is used to investigate electron traps with DLTS or ICTS measurements, the electron trap density calculated from the DLTS or ICTS peak height ($\tilde{N}_{\mathrm{T}}$) has the following relationship with the depth profile of the actual trap density $\tilde{N}_{\mathrm{T}}(x)$, where x is the distance from the Schottky junction [16, 17]:

$$\begin{aligned} \tilde{N}_{\mathrm{T}} &= 2\frac{\Delta C}{C_{\mathrm{R}}} N_{\mathrm{d,net}} \\ &= \frac{2}{w_{\mathrm{R}}^2} \int_{x_{\mathrm{start}}}^{x_{\mathrm{end}}} x N_{\mathrm{T}}(x) \left[f(x,0) - f(x,\infty) \right] \mathrm{d}x, \end{aligned} \tag{7.1}$$

where ΔC and C_{R} are the DLTS or ICTS peak intensity of the electron trap and the steady-state capacitance, respectively. In this study, the capacitance transient Fourier spectroscopy technique was employed [18] and the b_1 coefficient was used as ΔC. $N_{\mathrm{d,net}}$ is the net donor density, and w_{R} is the depletion layer width when a measurement bias voltage (U_{R}) is applied for the Schottky junction. x_{start} denotes the start depth of the detection region, which is determined from the condition of the filling pulse in capacitance transient spectroscopy. x_{end} denotes the end depth of the detection region, which is determined from the U_{R} in capacitance transient spectroscopy. $f(x,t)$, where t is time from application of the measurement bias voltage, is the time evolution of the depth profile of the electron occupancy ratio of the electron traps. The electron traps in $x_{\mathrm{start}} < x \leq x_{\mathrm{end}}$ can be detected. In Eq. (7.1), the following assumptions are typically made: (1) ΔC is small compared with C_{R} and (2) $N_{\mathrm{d,net}}$ is a function that varies slowly in the range of $x_{\mathrm{start}} < x \leq x_{\mathrm{end}}$. In this study, the following assumption is also made: (3) each electron trap in $x_{\mathrm{start}} < x \leq x_{\mathrm{end}}$ emits one electron during the measurement period, which is sufficiently longer than the time constant of electron thermal emission from the electron trap to the conduction band (τ_{n}), i.e., $f(x,0) = 1$ and $f(x,\infty) = 0$ in $x_{\mathrm{start}} < x \leq x_{\mathrm{end}}$. $\tilde{N}_{\mathrm{T}}$ obtained from Eq. (7.1) is not equal to the actual trap density N_{T} and is the averaged trap density in the entire depletion layer when the measurement bias voltage is applied. Considering that electrons in the conduction band are captured by electron traps in the depletion layer under application of the measurement bias voltage, $f(x,t)$ can be approximated as follows [16, 17]:

$$\begin{aligned} f(x,t) &= f(x,0) - \left[f(x,0) - \frac{n(x,w)\sigma_{\mathrm{n}} v_{\mathrm{th,n}}}{e_{\mathrm{n}} + n(x,w)\sigma_{\mathrm{n}} v_{\mathrm{th,n}}} \right] \left(1 - \exp\left[-\frac{t}{1/(e_{\mathrm{n}} + n(x,w)\sigma_{\mathrm{n}} v_{\mathrm{th,n}})} \right] \right) \\ &\simeq \begin{cases} \exp\left(-\frac{t}{1/e_{\mathrm{n}}} \right) & , x_{\mathrm{start}} < x \leq w - \lambda \\ 1 & , w - \lambda < x \leq w. \end{cases} \end{aligned} \tag{7.2}$$

Here, $e_{\mathrm{n}} = 1/\tau_{\mathrm{n}}$ is the thermal emission rate of electrons from the electron traps to the conduction band, w is the depletion layer width, and $v_{\mathrm{th,n}}$ is the electron thermal velocity.

$n(x, w)$ is the free carrier concentration, assuming that [17, 19]:

$$n = \begin{cases} N_{\mathrm{d,net}}(w)\exp\left[-\frac{(w-x)^2}{2L_{\mathrm{D}}(w)^2}\right] & , 0\ \mathrm{nm} < x < w \\ N_{\mathrm{d,net}}(x) & , w \leq x, \end{cases} \tag{7.3}$$

where, $L_{\mathrm{D}}(w) = \sqrt{\varepsilon_{\mathrm{s}} k_{\mathrm{B}} T / n(w,w) e^2}$ is the Debye length, ε_{s} is the static permittivity and the static permittivity of 4H-SiC in the direction parallel to the c axis $\varepsilon_{\mathrm{s}}^{||} = 10.3\varepsilon_0$, where ε_0 is the vacuum permittivity. $\varepsilon_{\mathrm{s}}^{||}$ is obtained using the Lyddane-Sachs-Teller relation [20], where the optical permittivity of 4H-SiC in the direction parallel to the c axis ($varepsilon_{\infty}^{||}$) is 6.78 ε_0 [21], and the optical-phonon angular frequencies of the $A_{1\mathrm{T}}$ mode and the $A_{1\mathrm{L}}$ mode ($\omega_{T,L}^{||}$) are 783 cm^{-1} and 964.2 cm^{-1}, respectively [21]. k_{B} is the Boltzmann constant. In Eq. (7.3), it is assumed that the donor is completely ionized. In Eq. (7.2), $w - \lambda$ is the depth where the trap energy level crosses the bulk Fermi level, i.e., the trap energy level in the depletion layer of $w - \lambda < x \leq w$ is below the Fermi level in the neutral region, and $f(w - \lambda, \infty) = 0.5$. λ is given as [19]:

$$\lambda(w) = L_{\mathrm{D}} \sqrt{2\ln\left(\frac{N_{\mathrm{d,net}}(w)\sigma_{\mathrm{n}} v_{\mathrm{th,n}}}{e_{\mathrm{n}}}\right)}. \tag{7.4}$$

In $w_{\mathrm{R}} - \lambda(w_{\mathrm{R}}) < x \leq w_{\mathrm{R}}$, the electron traps emit very few electrons because the trap energy level is located below the quasi-Fermi level. This phenomenon is called the lambda effect [7, 10, 17, 19, 22]. It is noted that the magnitude of the lambda effect depends on $e_{\mathrm{n}}^{\mathrm{t}}$ and σ_{n} of the electron trap and n, which is assumed to be equal to $N_{\mathrm{d,net}}$ in this study. In this study, $\lambda(w_{\mathrm{P}})$ and $\lambda(w_{\mathrm{R}})$ are considered to be equal [$\lambda = \lambda(w_{\mathrm{P}}) = \lambda(w_{\mathrm{R}})$]. Here, w_{P} is the depletion layer width when the filing pulse bias voltage (U_{P}) is applied to the Schottky junction. x_{end} is given as $x_{\mathrm{end}} = w_{\mathrm{R}} - \lambda$. Considering the lambda effect, Eq. (7.1) can be approximated as:

$$\begin{aligned} \tilde{N}_{\mathrm{T}} &= 2\frac{\Delta C}{C_{\mathrm{R}}} N_{\mathrm{d,net}} \\ &= \frac{2}{w_{\mathrm{R}}^2} \int_{x_{\mathrm{start}}}^{w_{\mathrm{R}}-\lambda} x N_{\mathrm{T}}(x) \mathrm{d}x. \end{aligned} \tag{7.5}$$

In $0 < x \leq x_{\mathrm{start}}$, the electron traps do not capture electrons during the filling pulse period and the electron traps can not be detected during the measurement period. When the lambda effect during the filling pulse period is considered, x_{start} is given as:

$$x_{\mathrm{start}} = \begin{cases} 0 & , w_{\mathrm{P}} \leq \lambda \\ w_{\mathrm{P}} - \lambda & , \lambda < w_{\mathrm{P}}. \end{cases} \tag{7.6}$$

Assuming that the depth profile of an electron trap density generated during an RIE process has a distribution that decays exponentially from the etched surface in the depth direction [15], $N_{\mathrm{T}}(x)$ can be described as an equation based on:

$$N_{\mathrm{T}}(x) = N_{\mathrm{T}}(0)\exp\left(-\frac{x}{L}\right). \tag{7.7}$$

Here, L is defined as the depth of carrier trap generation, and $N_\mathrm{T}(0)$ is the carrier trap density at the etched surface. The depth profile of an electron trap density is shown as a black solid line in Fig. 7.1(a). The dependence of the averaged trap density on the depletion layer width calculated from Eqs. (7.5) and (7.7) is also shown as a black broken line in Fig. 7.1(a). Figure 7.1(b) and Fig. 7.1(c) show band diagrams of an SBD with an assumed depth profile of trap density during the filling pulse period (upper side) and the measurement period (lower side) with U_R of U_R1 and U_R2 ($U_\mathrm{P} > U_\mathrm{R1} > U_\mathrm{R2}$), respectively. The depletion layer widths during the measurement period with U_R1 and U_R2 are set to w_R1 and w_R2, respectively. For simplicity, x_start is set to $w_\mathrm{P} - \lambda$ in Fig. 7.1.

In the case of a carrier trap generated during an RIE process, not only the lambda effect but also the steep depth profile localized near the etched surface should be considered with respect to the dependence of the averaged trap density on the depletion layer width. When $x_\mathrm{end} - x_\mathrm{start} = (w_\mathrm{R} - \lambda) - (w_\mathrm{P} - \lambda)$, which is the width of the detection region, is smaller than or approximately the same length as λ [e.g. $w_\mathrm{R} = w_\mathrm{R1}$ in Fig. 7.1(b)], $\tilde{N}_\mathrm{T}(w_\mathrm{R})$ is strongly affected by the lambda effect. The electron traps in the depletion layer during the measurement period are then localized near the etched surface. Therefore, $\tilde{N}_\mathrm{T}(w_\mathrm{R})$ is also strongly affected by the steep depth profile of the electron trap density. When $(w_\mathrm{R} - \lambda) - (w_\mathrm{P} - \lambda)$ is much larger than λ [e.g. $w_\mathrm{R} = w_\mathrm{R2}$ in Fig. 7.1(c)], the lambda effect on $\tilde{N}_\mathrm{T}(w_\mathrm{R})$ becomes small because the number of electron trap in the no-electron-emission region, which is far from the etched surface as shown in Fig. 7.1(c), is negligible with respect to that in the detection region. As a consequence of $N_\mathrm{T}(x)$, the averaged trap density $\tilde{N}_\mathrm{T}(w_\mathrm{R})$ then decreases with increasing w_R.

$\tilde{N}_\mathrm{T}(w_\mathrm{R})$ is determined in the competition between the lambda effect and the depth profile of the electron tarp density. Figure 7.1(a) shows that in this case with the surface-localized $N_\mathrm{T}(x)$, $\tilde{N}_\mathrm{T}(w_\mathrm{R})$ has a maximum value at $w_\mathrm{R} = 1.8$ μm. It is crucial to appropriately determine the conditions for the filling pulse and the measurement pulse by considering the shape of the depth profile, the properties of the electron traps to be evaluated, and the structure of the SBD, such as the doping concentration of the epilayer and the Schottky barrier height.

7.3 Experiments

N-doped n-type 4H-SiC (0001) epilayers were used as a starting material for defect characterization. Inductively coupled plasma (ICP)-RIE was performed for 5 min under a typical condition [SF_6: 10 sccm, O_2: 20 sccm, Ar: 100 sccm, ICP power: 900 W, bias power: 100 W, pressure: 2 Pa, etching rate: 0.6 *umu*m/min], which resulted in the removal of a 3.0 *umu*m thick layer. After the RIE process, all samples were cleaned in the RCA cleaning process [23]. To detect carrier traps generated during the RIE process with the capacitance transient spectroscopy technique, Ni was deposited on the etched surfaces as Schottky con-

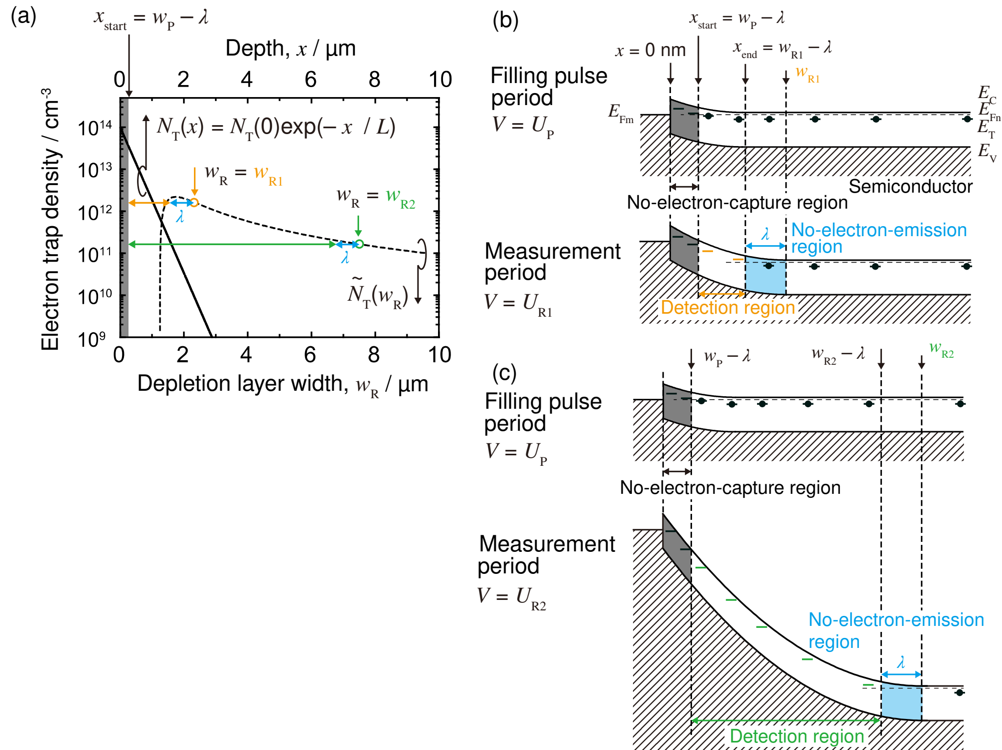

Figure 7.1: Representative example for the approach of the proposed method. (a) Exponential depth profile of an electron trap density [$N_T(x) = N_T(0)\exp(-x/L)$; black solid line] and the dependence of the averaged trap density on the depletion layer width calculated from Eq. (7.5) [$\tilde{N}_T(w_R)$; black broken line]. Band diagrams of an SBD during the filling pulse period (upper side) and the measurement period (lower side) with measurement bias voltages of (b) U_{R1} and (c) U_{R2} ($U_{R1} > U_{R2}$).

tacts by using vacuum evaporation. The diameters of the Schottky electrodes were 1.5 mm. Aluminum was employed for backside ohmic contacts. The $N_{\mathrm{d,net}}$ of $1{\times}10^{15}$ cm^{-3} was determined from capacitance-voltage ($C-V$) measurements of the SBD using the epilayer.

For the RIE-etched sample, ICTS measurement was performed at 300 K to investigate electron traps. In the ICTS measurement, a typical filling pulse bias voltage U_{P} and filling pulse width (t_{P}) were 1.5 V and 200 ms, respectively. The ICTS measurement was performed with various measurement bias voltages from 0 V to −50 V. The detection limit of $\tilde{N}_{\mathrm{T}}$ in the samples was $2{\times}10^{11}$ cm^{-3} using $\Delta C/C_{\mathrm{R}} = 10^{-4}$ [24]. To determine the energy positions of electron traps ($\Delta E_{\mathrm{T}} = E_{\mathrm{C}} - E_{\mathrm{T}}$), DLTS measurements were performed in the temperature (T) range from 200 K to 380 K with $U_{\mathrm{P}} = 1.5$ V and $t_{\mathrm{P}} = 200$ ms. The measurement period widths were set to 20.5 ms, 205 ms and 2.05 s, and a measurement bias voltage of −5 V was used in the DLTS measurement. To investigate electron traps that exist before the RIE process, ICTS and DLTS measurements were also performed for a Ni/n-type SiC SBD using the as-grown sample. Considering low electric field strength at the Schottky interface (< 1 MV/cm), interface states do not affect DLTS and ICTS measurements in this study.

In the measurement principle, depth profiles can be extracted from either the DLTS or ICTS measurement with the proposed method. Here, the ICTS technique was selected because of the following two perspectives. From an experimental point of view, measurement with various bias voltages is required with this method. Therefore, it is difficult to apply the DLTS technique for this method. From an analytical point of view, to eliminate the impact of the lambda effect dependence on the temperature [7, 10, 17, 19, 22] and the steady-state capacitance C_{R} from the obtained trap density, the ICTS technique is more suitable for this method. In this study, constant-voltage ICTS mode was used. On the other hand, when the measured carrier trap density $\tilde{N}_{\mathrm{T}}$ is as high as the net donor density $N_{\mathrm{d,net}}$, constant-capacitance ICTS mode is useful to extract depth profiles of carrier trap density with the proposed method.

7.4 Result and Discussion

7.4.1 Deep Levels Detected in RIE-etched SiC

Figure 7.2 shows ICTS spectra of (a) the as-grown sample and (b) the RIE-etched sample. In the as-grown sample, the $Z_{1/2}$ center ($E_{\mathrm{C}} - 0.64$ eV) [2, 25, 26] was detected and the $Z_{1/2}$ center density of $4.3{\times}10^{11}$ cm^{-3} was obtained from the ICTS data with consideration of the lambda effect. After the RIE process, the EH_3 center ($E_{\mathrm{C}} - 0.74$ eV) [12, 27–29] emerged while the $Z_{1/2}$ center was also observed. Figure 7.3 shows Arrhenius plots of $\ln(\tau_{\mathrm{n}}T^2)$ versus the reciprocal temperature with the assumption that the electron capture cross-section (σ_{n}) is independent of temperature, where τ_{n} is the time constant for electron emission from an electron trap to the conduction band. The energy positions and electron capture cross-sections of the electron traps are summarized in Table I. The $Z_{1/2}$ center,

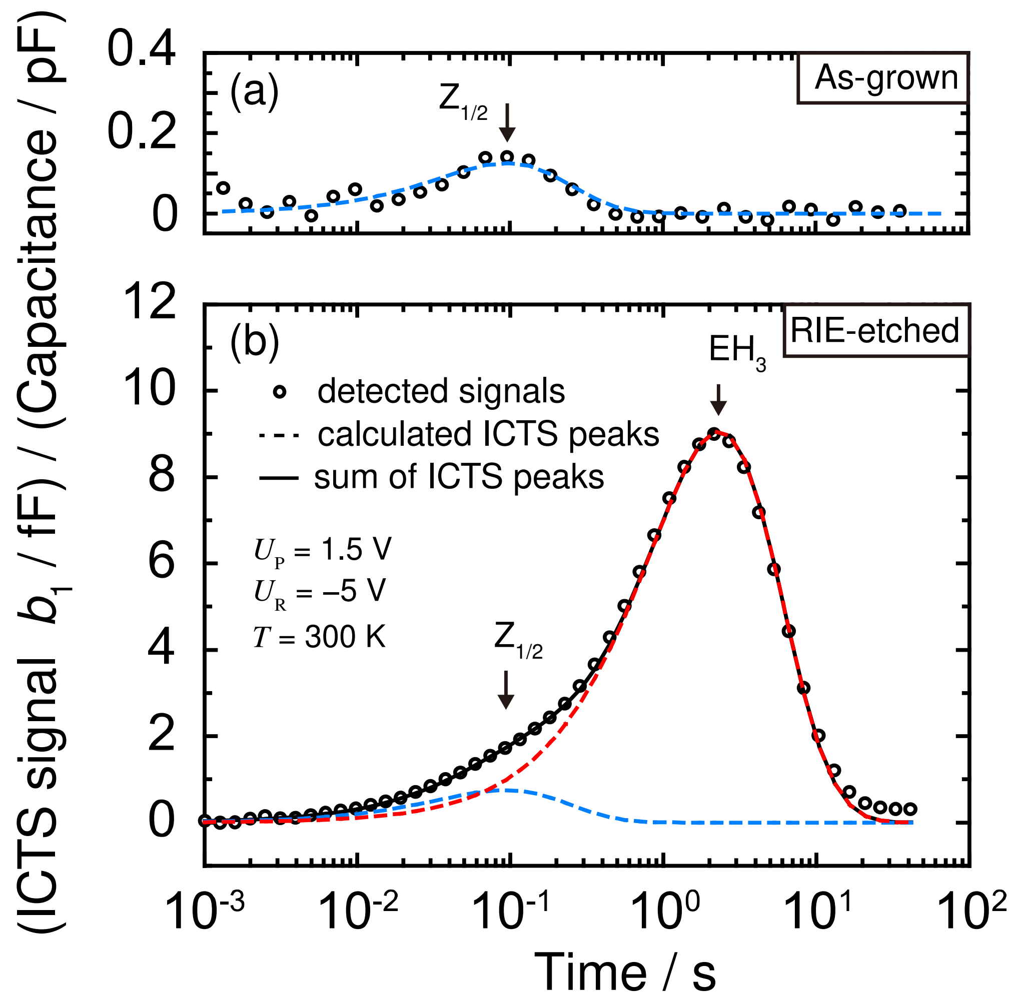

Figure 7.2: ICTS spectra obtained at 300 K from (a) as-grown n-type 4H-SiC and (b) RIE-etched n-type 4H-SiC. The experimental ICTS spectra are indicated with open circles. The blue and red broken lines show calculated ICTS peaks for the $Z_{1/2}$ and EH_3 centers, respectively. The black solid line shows the sum of the calculated ICTS peaks.

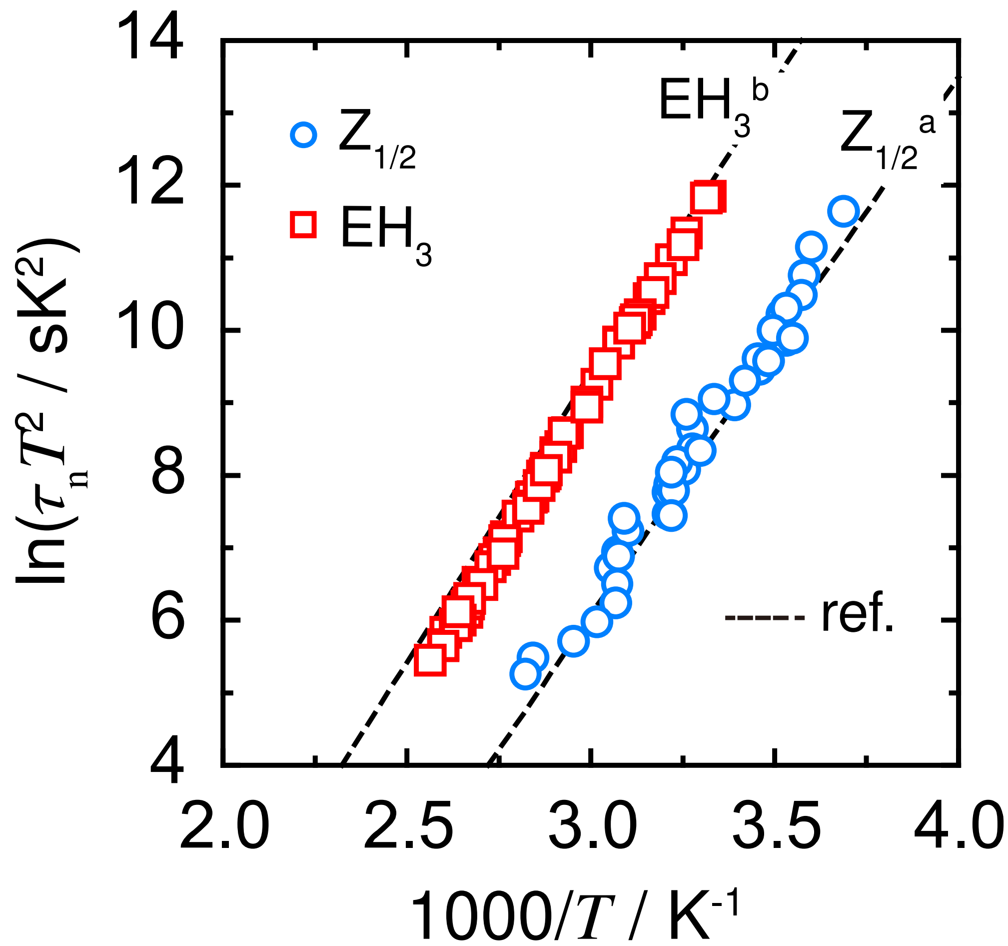

Figure 7.3: Arrhenius plots of $\ln(\tau_n T^2)$ versus reciprocal temperature obtained from DLTS measurements for the $Z_{1/2}$ center (blue circles) and the EH_3 center (red squares). Reported Arrhenius plots of $\ln(\tau_n T^2)$ versus the reciprocal temperature for each electron trap are also shown as black broken lines. [a]Reference [26], [b]Reference [28].

which originates from carbon vacancies (V_C), has been observed in as-grown 4H-SiC layers [13, 25, 26, 30, 31]. The EH_3 center has been reported to be generated by electron or proton irradiation [12, 27–29, 32], ion implantation [4], or the RIE process [14]. The origin of the EH_3 center is considered to be carbon interstitial (C_i)-related defects because the EH_3 center was generated after irradiation with low energy electron (116 keV) [12, 29], by which only carbon atoms may be displaced [33]. The analysis based on the diffusion-limited theory for the annealing behavior of EH_3 center also suggested that the EH_3 center is C_i-related [30]. In this study, the author focused on these two contrasting electron traps.

7.4.2 Condition of Filling Pulse Bias Voltage

To investigate the depth profiles of the electron traps generated during the RIE process, x_{start} in Eq. (7.5), which is the start depth of the detection region as shown in Fig. 7.1, must be sufficiently small because the etching damage should be localized near the etched surface. ICTS measurement was thus performed at 300 K and at $U_{\mathrm{R}} = -5\ V$ with various filling pulse bias voltages to select an appropriate filling pulse condition.

Figure 7.4(a) shows the dependence of $w_{\mathrm{P}} - \lambda$ on the filling pulse bias voltage for the $Z_{1/2}$ (blue circles) and EH_3 (red squares) centers in the RIE-etched sample. An electron trap with small ΔE_{T} shows a tendency to have a small lambda length due to its high thermal emission rate of electrons from the electron traps to the conduction band at a certain temperature. The filling pulse bias voltage that satisfies the condition of $w_{\mathrm{P}} - \lambda = 0$ nm is higher in the case of the $Z_{1/2}$ center than the EH_3 center, which is consistent with λ of the $Z_{1/2}$ center being shorter, e.g., λ is 6.7×10^2 nm for the $Z_{1/2}$ center and 7.5×10^2 nm for the EH_3 center with $U_{\mathrm{P}} = 0$ V. Figure 7.4(b) shows the dependence of $\tilde{N}_{\mathrm{T}}$ on the filling pulse bias voltage. The vertical axis in Fig. 7.4(b) is normalized with respect to $\tilde{N}_{\mathrm{T}}$ obtained with $U_{\mathrm{P}} = 2$ V. The start depth of the detection region x_{start} decreases with increasing filling pulse bias voltage. Therefore, the detection region width $[x_{\mathrm{end}} - x_{\mathrm{start}} = (w_{\mathrm{R}} - \lambda) - x_{\mathrm{start}}]$ increases with increasing the filling pulse bias voltage. $\tilde{N}_{\mathrm{T}}$ also increases because the electron traps localized near the etched surface, which have a high density, become detectable. It should be noted that the dependence of the normalized $\tilde{N}_{\mathrm{T}}$ on the filling pulse bias voltage reflects the actual depth profiles of each electron trap density. In Fig. 7.4(b), the normalized $\tilde{N}_{\mathrm{T}}$ becomes saturated at unity when the filling pulse bias voltage is higher than the filling pulse bias voltage that satisfies the condition of $w_{\mathrm{P}} - \lambda = 0$ nm. This result suggests that the trap energy level becomes lower than the quasi-Fermi level within the entire depletion layer during the filling pulse period. Therefore, electrons can be captured by the electron traps even near the Schottky interface during the filling pulse period.

On the other hand, an electron trap with an energy level located above the quasi-Fermi level in the depletion layer can be observed during the measurement period [34]. The barrier height of the SBD on the RIE-etched sample obtained from the $C-V$ measurement is 1.5 eV, which is larger than the trap energy depth for the electron traps detected in

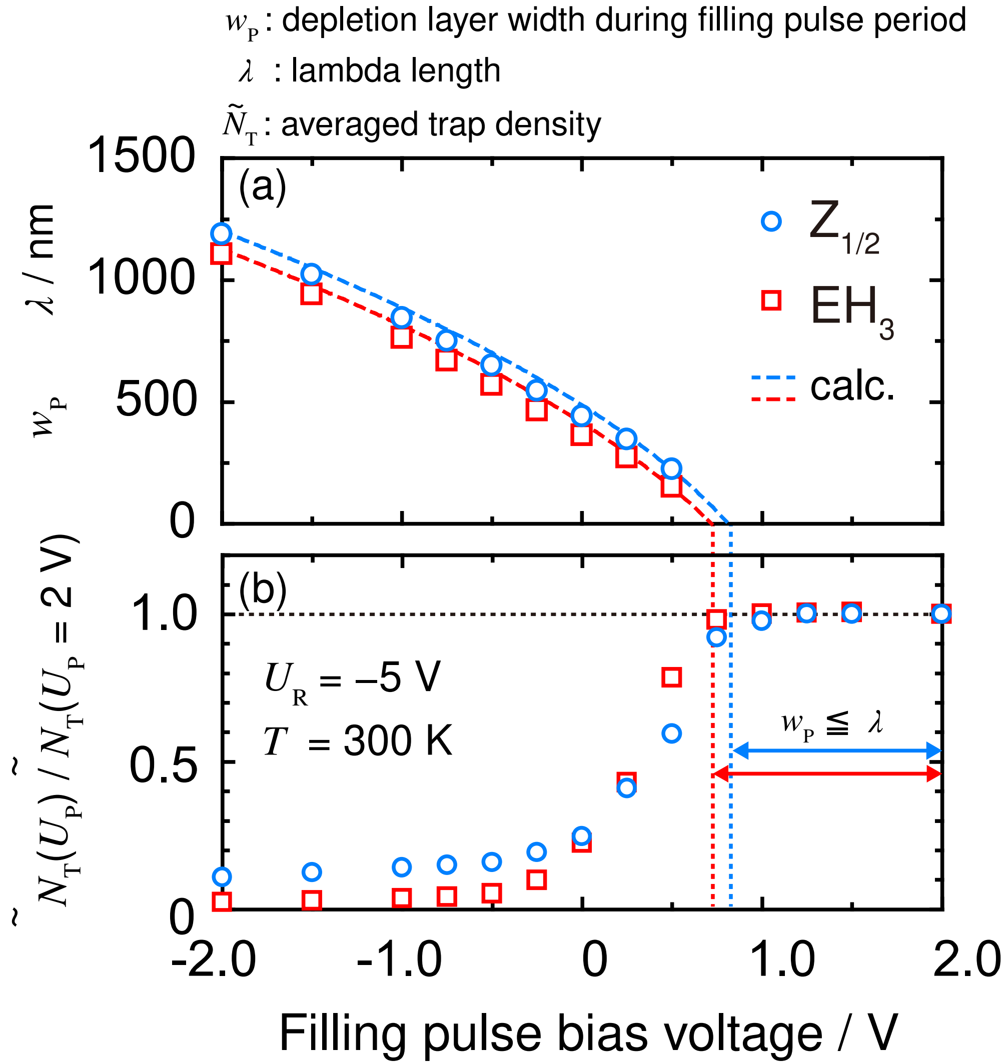

Figure 7.4: (a) Difference between the depletion layer width and the lambda length ($w_P - \lambda$) for each defect center in the RIE-etched sample during the filling pulse period. The blue circles and the red squares indicate the $Z_{1/2}$ and EH_3 centers, respectively. The broken lines show the calculated dependence of ($w_P - \lambda$) on the filling pulse bias voltage for each electron trap using a Schottky barrier height of 1.5 eV. (b) Filling pulse bias voltage dependence of the averaged trap density obtained from the ICTS peak at a measurement bias voltage of −5 V. The blue circles and red squares indicate the $Z_{1/2}$ and EH_3 centers, respectively. The vertical axis is normalized with respect to the averaged trap density when the filling pulse bias voltage is 2 V. The color dotted lines denote the filling pulse bias voltage with $w_P - \lambda$ of 0 nm for each electron trap.

this study, and these trap energy levels are located above the quasi-Fermi level, except for the no-electron-emission region during the measurement period. Analysis was performed assuming that x_{start} is 0 nm when a filling pulse bias voltage of 1.5 V was employed and each electron trap in 0 nm $< x \leq w_{\mathrm{R}} - \lambda$ emits one electron during the measurement period.

7.4.3 Depth Profiles of Density of Deep Levels

It is preferable to satisfy the condition of $x_{\mathrm{start}} = 0$ nm for obtaining the depth profile of the electron trap density near the etched surface. On the other hand, an increase in $x_{\mathrm{start}} = w_{\mathrm{P}} - \lambda$ allows only the depth profile of the electron trap density in the deeper region to be extracted. Extraction of a common depth profile of the electron trap density from the dependency of several averaged trap densities in the depletion layer width with various x_{start} can yield a depth profile with both a high-density distribution near the etched surface and a low-density distribution in the deeper region.

Figure 7.5 (red open squares) shows the dependence of the averaged EH_3 center density on the depletion layer width in the RIE-etched sample obtained from ICTS measurement at 300 K with (a) $U_{\mathrm{P}} = 1.5$ V, (b) $U_{\mathrm{P}} = 0$ V, and (c) $U_{\mathrm{P}} = -4$ V with various U_{R} from 0 V to –50 V. Schematic cross-sections of the SBD during the filling pulse period (upper side) and the measurement period (lower side) with filling pulse voltages of (d) 1.5 V, (e) 0 V, and (f) −4 V are also shown. When $U_{\mathrm{P}} = 1.5$ V is applied for the Schottky junction [Fig. 7.5(a)], the EH_3 center in 0 nm $< x \leq w_{\mathrm{R}} - \lambda$ is detected in the ICTS measurement. For $U_{\mathrm{P}} = 0$ V [Fig. 7.5(b)] and −4 V [Fig. 7.5(c)], $x_{\mathrm{start}} = w_{\mathrm{P}} - \lambda$ for the EH_3 center is $3.6{\times}10^2$ nm and 1.6 μm, respectively. When $\tilde{N}_{\mathrm{T}}$ is compared at the same w_{R}, the averaged EH_3 center density decreases with decreasing the filling pulse bias voltage because 1) the ratio of the detection region to the lambda length becomes small [Figs. 5(d)-(f)] and the impact of the lambda effect becomes large and 2) the EH_3 center is localized near the etched surface.

The detected EH_3 center in Fig. 7.5(c) is located in the deeper region ($x > 1.6$ μm). The depth profile of the EH_3 center density in the deeper region can not be described from the depth profile of the single exponential in Eq. (2), which corresponds to that near the etched surface. In this study, the depth profile of the EH_3 center density is assumed to be a double exponential with a small generation depth L_1 and a large generation depth L_2:

$$N_{\mathrm{T}}(x) = N_{\mathrm{T1}}(0)\exp\left(-\frac{x}{L_1}\right) + N_{\mathrm{T2}}(0)\exp\left(-\frac{x}{L_2}\right). \tag{7.8}$$

The exponential term with L_1 corresponds to the depth profile of the EH_3 center density near the etched surface, which indicates a non-channeling component. The exponential term with L_2 corresponds to the depth profile of the EH_3 center density in the deeper region, which indicates a channeling component. It is noted that the depth profiles can be reproduced to some extent by assuming the dual Pearson distribution function [35], which is often used in the case of ion implantation (not shown). However, the dual Pearson

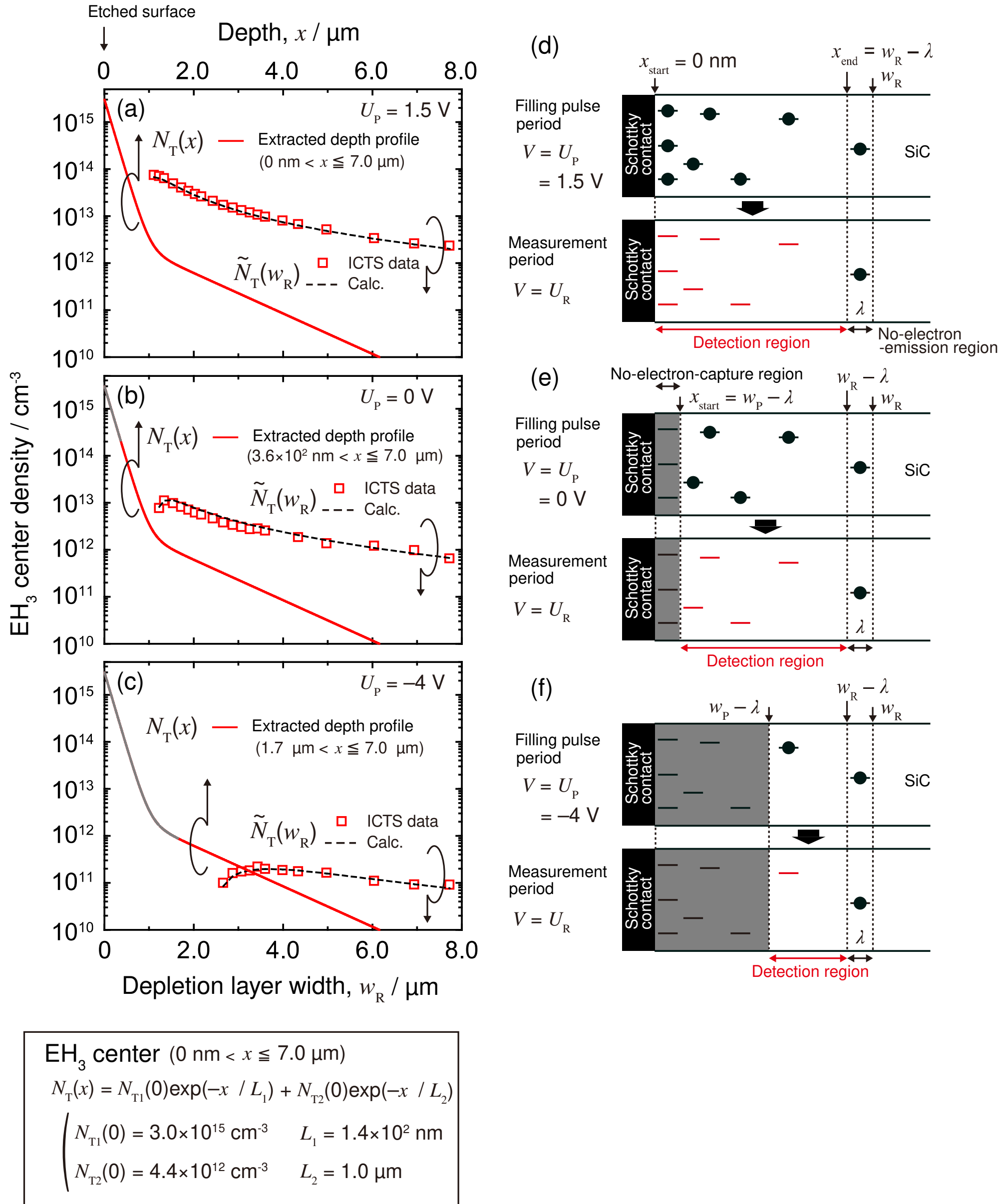

Figure 7.5: Dependence of the averaged trap density obtained from ICTS measurements at 300 K for the EH3 center in the RIE-etched sample on the depletion layer width with filling pulse voltages of (a) 1.5 V, (b) 0 V, and (c) –4 V. The open squares denote the averaged EH_3 center densities calculated from the ICTS peaks. The black broken lines are fitting curves based on Eq. (7.8). The extracted depth profiles are shown as red solid lines. The depth profiles in undetectable regions are shown by gray solid lines. Schematic cross-sections of an SBD during the filling pulse period (upper side) and the measurement period (lower side) with filling pulse bias voltages of (d) 1.5 V, (e) 0 V, and (f) –4 V.

distribution function needs much more parameters. Thus, the authors considered that the present double exponential function is a reasonable approximation.

The common depth profile of the EH_3 center density was extracted from the three different dependencies of the averaged EH_3 center density on the depletion layer width with different x_{start} shown in Figs. 5(a), 5(b), and 5(c), where x_{start} is 0 nm, 3.6×10^2 nm, and 1.6 *umu*m, respectively. In the ICTS measurement, the maximum value of x_{end} is 7.0 *umu*m for the EH_3 center when $U_{\mathrm{R}} = -50$ V. Each $\tilde{N}_{\mathrm{T}}(w_{\mathrm{R}})$ was calculated using the common $N_{\mathrm{T}}(x)$ in Eq. (3), i.e., the parameters $N_{\mathrm{T1}}(0)$, $N_{\mathrm{T2}}(0)$, L_1, and L_2 are the same each other in Figs. 5(a), 5(b), and 5(c). Curve fitting with the calculated $\tilde{N}_{\mathrm{T}}(w_{\mathrm{R}})$ [black broken lines in Figs. 5(a)-(c)] to the measured $\tilde{N}_{\mathrm{T}}(w_{\mathrm{R}})$ [red squares in Figs. 5(a)-(c)] was performed with the common fitting parameters, which are $N_{\mathrm{T1}}(0)$, $N_{\mathrm{T2}}(0)$, L_1, and L_2 in Eq. (3). The fitting parameters for the calculation are shown in Fig. 7.5. The extracted depth profile of the EH_3 center density is plotted in Figs. 5(a)-(c) as red solid lines. When $U_{\mathrm{P}} = 0$ V and $U_{\mathrm{P}} = -4$ V are respectively applied, the EH_3 center for $0\ \mathrm{nm} < x \leq 3.6\times10^2$ nm and $0\ \mathrm{nm} < x \leq 1.6$ μm can not be detected. The extracted depth profile of the EH_3 center density in the no-electron-capture region is shown as gray solid lines in Figs. 5(b) and 5(c). Although the EH_3 center generated during the RIE process is localized near the etched surface ($x < 1$ μm), the EH_3 center also exists in the deeper region ($x > 2$ μm), where the density is low [$N_{\mathrm{T}}(x) < 10^{12}\ \mathrm{cm}^{-3}$]. The existence of the EH_3 center in the deeper region is confirmed to be valid from the ICTS measurement at $U_{\mathrm{P}} = -4$ V [Fig. 7.5(c)], in which the EH_3 center is not detected near the etched surface ($0\ \mathrm{nm} < x \leq 1.6$ μm). The EH_3 center may be carbon-interstitial (C_i) atoms [12, 29]. It is considered that the EH_3 centers generated during the RIE process originate from carbon atoms ejected from the etched region and accumulated in the SiC epilayer.

Figure 7.6 (blue open circles) shows the dependence of the averaged $Z_{1/2}$ center density on the depletion layer width in the RIE-etched sample obtained from ICTS measurement at 300 K with (a) $U_{\mathrm{P}} = 1.5$ V, (b) $U_{\mathrm{P}} = 0$ V, and (c) $U_{\mathrm{P}} = -4$ V. In the same way as that for the EH_3 center in Fig. 7.5, the depth profile of the $Z_{1/2}$ center density in the RIE-etched sample was extracted and is shown as blue solid lines in Fig. 7.6. x_{start} in Eq. (1) for the $Z_{1/2}$ center is 0 nm, 4.4×10^2 nm, and 1.7 μm with U_{P} of 1.5 V [Fig. 7.6(a)], 0 V [Fig. 7.6(b)], and −4 V [Fig. 7.6(c)], respectively. The maximum value of x_{end} is 7.1 μm for the $Z_{1/2}$ center when U_{R} of −50 V was used in the ICTS measurement. As the depth profile of the $Z_{1/2}$ center density, a double exponential with a constant term is assumed.

$$N_{\mathrm{T}}(x) = N_{\mathrm{T1}}(0)\exp\left(-\frac{x}{L_1}\right) - N_{\mathrm{T2}}(0)\exp\left(-\frac{x}{L_2}\right) + N_{\mathrm{T,as-grown}}. \tag{7.9}$$

The two exponential terms and the constant term correspond to the $Z_{1/2}$ center generated during the RIE process and that existing before the RIE process, respectively, the fitting parameters of which are shown in Fig. 7.6. In the RIE-etched sample, a constant term $N_{\mathrm{T,as-grown}}$ of $5.6\times10^{11}\ \mathrm{cm}^{-3}$ is obtained and is almost identical to the $Z_{1/2}$ center density in the as-grown sample of $4.3\times10^{11}\ \mathrm{cm}^{-3}$.

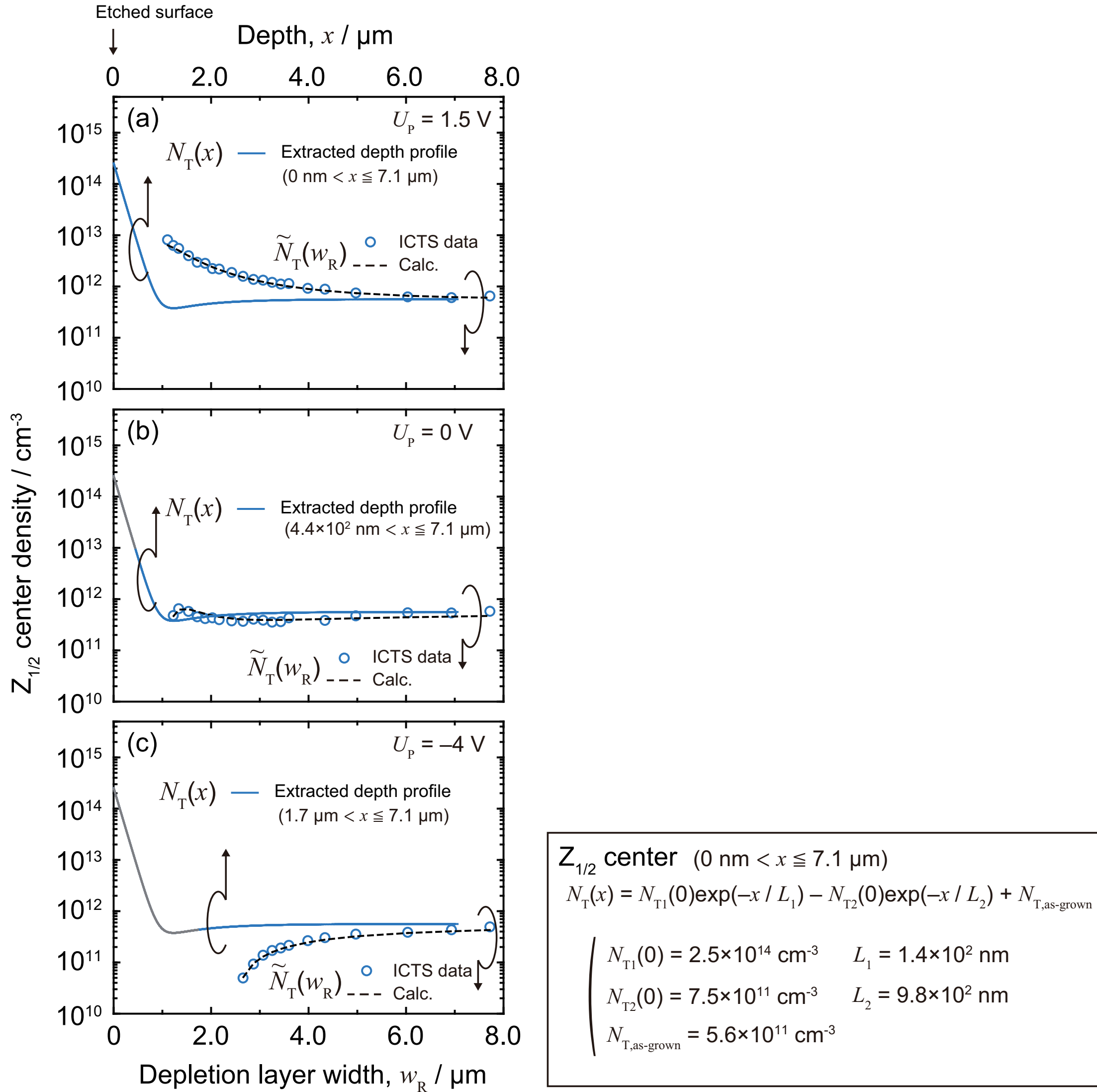

Figure 7.6: Dependence of the averaged trap density obtained from ICTS measurements at 300 K for the $Z_{1/2}$ center in the RIE-etched sample on the depletion layer width with filling pulse voltages of (a) 1.5 V, (b) 0 V, and (c) –4 V. The open circles denote the averaged $Z_{1/2}$ center densities calculated from the ICTS peaks. The black broken lines are the fitting curves based on Eq. (7.9). The extracted depth profiles are shown as blue solid lines. The depth profiles in undetectable regions are shown by gray solid lines.

7.4.4 Discussion

The extracted depth profiles of the $Z_{1/2}$ center density (blue solid line) and the EH_3 center density (red solid line) are shown in Fig. 7.7. The blue and black broken lines denote the second exponential term, which has a larger generation depth L_2, and $N_{T,as-grown}$ in the depth profile of the $Z_{1/2}$ center density, respectively. Near the etched surface ($x < 800$ nm), the first exponential term, which has a smaller generation depth L_1, is dominant in the depth profiles of both the $Z_{1/2}$ center density and the EH_3 center density. L_1 of the $Z_{1/2}$ center (1.4×10^2 nm) is almost identical to that of the EH_3 center (1.4×10^2 nm), which suggests that the $Z_{1/2}$ center (V_C) is generated near the surface by high-energy ion bombardment during the RIE process and the EH_3 center (C_i) is generated by the carbon atoms ejected to the deeper region by the ion bombardment. In the deeper region ($x \approx 1$ μm), the $Z_{1/2}$ center density is lower than $N_{T,as-grown}$. On the other hand, consideration of the EH_3 center in the deeper region ($x > 1$ μm) reveals that the second exponential term, which has a larger generation depth L_2, becomes dominant in the depth profile of the EH_3 center density. L_2 of the EH_3 center (1.0 μm) is very similar to that of the $Z_{1/2}$ center (9.8×10^2 nm). This result suggests that in the deeper region ($x > 1$ μm), 1) few V_C defects (the $Z_{1/2}$ center) are generated by ion bombardment during the RIE process and 2) pair annihilation of V_C defects, that are present before the RIE process, and ejected carbon atoms, of which the depth profile is similar to that of the EH_3 center (Ci) density, occurs.

Depth profiles of (a) the $Z_{1/2}$ and (b) EH_3 center densities extracted by the proposed method (color solid lines) and obtained using the double-correlation method (black solid lines) [9, 11] are shown in Fig. 7.8. In the double-correlation method, a depth profile of the electron trap density can be obtained without assuming a shape of the depth profile using the following steps: (1) the detection region ($w_P - \lambda < x \leq w_R - \lambda$) is adjusted to be small using an appropriate filling pulse bias voltage and an appropriate measurement bias voltage, (2) it is assumed that the trap density in the small detection region is constant, and (3) the averaged trap density obtained from the ICTS peak is corrected with respect to the lambda effect during both the filling pulse period and the measurement period. In the double-correlation method, when the depletion layer width is small and the detection region is close to the etched surface, where the depth profile shows a sharp drop, the difference of filling pulse bias voltages was chosen to be small so that a high spatial resolution is held. On the other hand, when the depletion layer width is large and the detection region is deeper, where the trap density is low, the difference of filling pulse bias voltages was chosen to be large so that a high density resolution is achieved. Figure 8 shows that the depth profiles of the $Z_{1/2}$ and EH_3 center densities extracted from the dependence of $\tilde{N}_T$ on the depletion layer width are consistent with those determined by the double-correlation method in the density range larger than 10^{11} cm^{-3}. The double-correlation method has a trade-off relationship between the depth resolution and resolution in the trap density due to the measurement principle. However, with the proposed method, the trade-off relationship

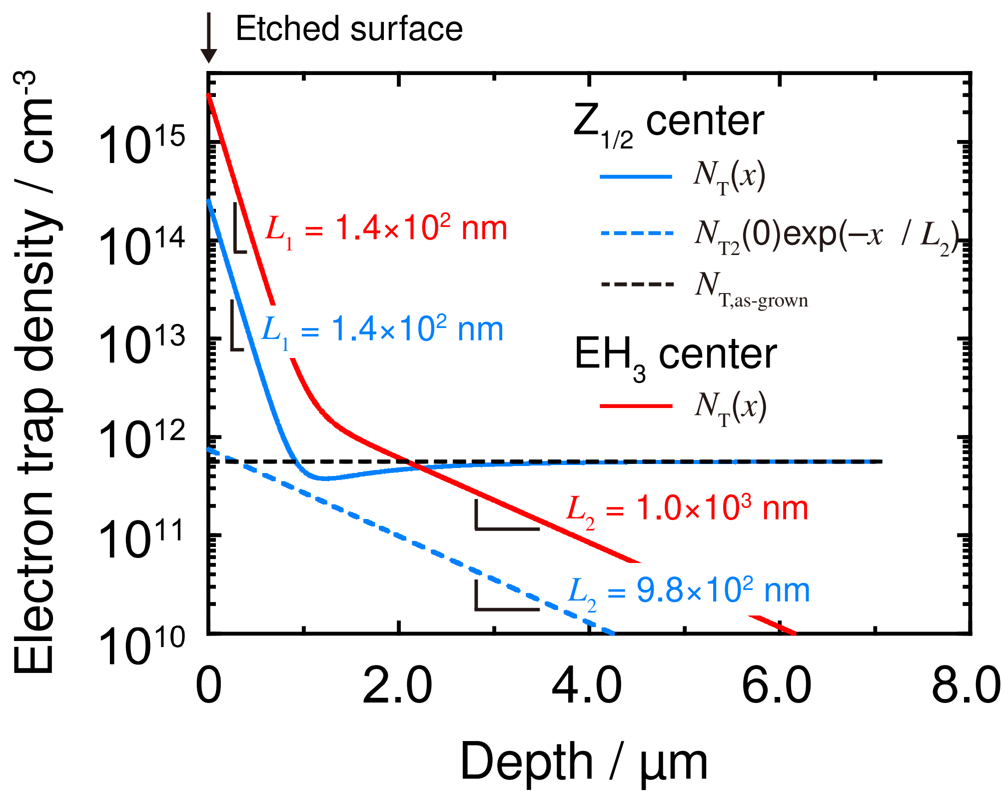

Figure 7.7: Extracted depth profiles of the $Z_{1/2}$ center density (blue solid line) and the EH_3 center density (red solid line). The blue and black broken lines are the second exponential term and the constant term of the depth profile of the $Z_{1/2}$ center density, respectively.

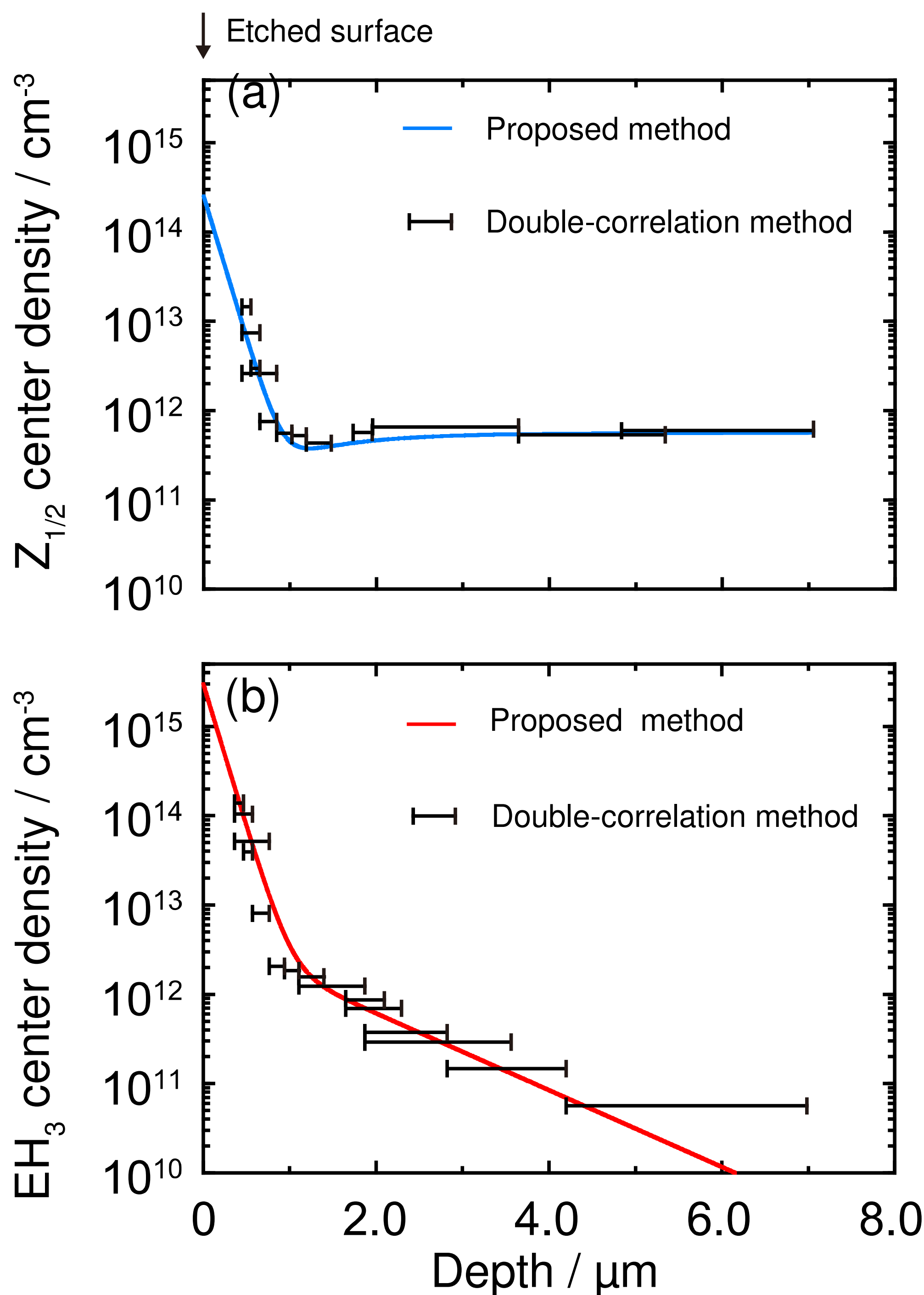

Figure 7.8: Depth profiles of (a) the $Z_{1/2}$ center and (b) the EH_3 center. The color solid lines show the depth profiles extracted from the dependence of the averaged defect density on the depletion layer width. The black solid lines are depth profiles obtained with the double-correlation method.

is relieved and a reasonable depth profile of trap density can be extracted by measurement and analysis of the dependence of $\tilde{N}_{\mathrm{T}}$ on the depletion layer width when an appropriate function shape for the depth profile is assumed.

7.5 Application for RIE-induced defects in n-type GaN

The proposed method was applied to RIE-induces defects in n-type GaN. Si-doped n-type GaN epilayers on n^+-type GaN substrate were used as a starting material. [Si] is 7×10^{15} cm^{-3}. ICP-RIE was performed under a typical condition [ICP power: 200 W, bias power: 40 W], which resulted in the removal of a 200 nm thick layer. Ni was deposited on the etched surfaces as Schottky contacts by using vacuum evaporation. Aluminum was employed for backside ohmic contacts. For the RIE-etched sample and as-grown sample, DLTS measurements were performed in the temperature range from 75 K to 350 K with $U_{\mathrm{P}} = 1.5$ V and $t_{\mathrm{P}} = 20.5$ ms, and various measurement bias voltages from 0 V to -10 V.

Figure 7.9 shows the DLTS spectra at $U_{\mathrm{R}} = -2$ V of as-grown GaN (blue solid line) and RIE-etched GaN (red solid line). In as-grown GaN, the electron traps E1 ($E_{\mathrm{T}} = E_{\mathrm{C}} - 0.26$ eV, $\sigma_{\mathrm{n}} = 2 \times 10^{-15}$ cm^2) and E3 ($E_{\mathrm{T}} = E_{\mathrm{C}} - 0.59$ eV, $\sigma_{\mathrm{n}} = 5 \times 10^{-15}$ cm^2) are detected. In RIE-etched GaN, in addition to the electron traps E1 and E3, electron traps E_{R1} ($E_{\mathrm{T}} = E_{\mathrm{C}} - 0.59$ eV, $\sigma_{\mathrm{n}} = 1 \times 10^{-13}$ cm^2) and E_{R2} ($E_{\mathrm{T}} = E_{\mathrm{C}} - 0.14$ eV, $\sigma_{\mathrm{n}} = 1 \times 10^{-17}$ cm^2) are detected.

In Fig. 7.10, dependences of detected density of the electron traps in the DLTS measurements on the depletion layer width are shown as the blue open for as-grown GaN circles and red closed circles for RIE-etched GaN. In the same way as the RIE-induced defects in SiC, depth profiles of defect density are extracted from the analysis of $\tilde{N}_{\mathrm{T}}(w_{\mathrm{R}})$. In the analysis, a constant depth profile [$N_{\mathrm{T}}(x) = N_{\mathrm{T}}$] and an exponential depth profile [$N_{\mathrm{T}}(x) = N_{\mathrm{T}}(0)\exp(-x/L)$] are assumed for defects in as-grown GaN and defects induced during the RIE process, respectively. The calculated dependences of detected density of electron traps $\tilde{N}_{\mathrm{T}}$ on the depletion layer width w_{R} and extracted depth profiles of defect density are shown in Fig. 7.10 as the color solid lines and the color broken lines, respectively. As shown in Fig. 7.10, the electron traps E_{R1} and E_{R2}, which are detected in only RIE-etched GaN [Fig. 7.9], have a single exponential depth profile[E_{R1}: $N_{\mathrm{T}}(0) = 4.6 \times 10^{15}$ cm^{-3} and $L = 14$ nm, E_{R2}: $N_{\mathrm{T}}(0) = 3.9 \times 10^{14}$ cm^{-3} and $L = 13$ nm] and localized near the etched surface (< 500 nm). The electron traps E_{R1} and E_{R2} may be assigned to the electron trap EE3 ($E_{\mathrm{T}} = E_{\mathrm{C}} - 0.59$ eV, $\sigma_{\mathrm{n}} = 1 \times 10^{-13}$ cm^2) and EE1 ($E_{\mathrm{T}} = E_{\mathrm{C}} - 0.59$ eV, $\sigma_{\mathrm{n}} = 1 \times 10^{-13}$ cm^2), which are detected in GaN after 2 MeV electron beam irradiation [36],respectively. The electron trap E_{R1} may correspond to the electron trap E_{DL1} ($E_{\mathrm{T}} = E_{\mathrm{C}} - 0.60$ eV, $L = 8$ nm), which is detected GaN after RIE process [15]. In the as-grown GaN, the electron trap E1 has a constant depth profile ($N_{\mathrm{T}} = 1.4 \times 10^{12}$ cm^{-3}). The

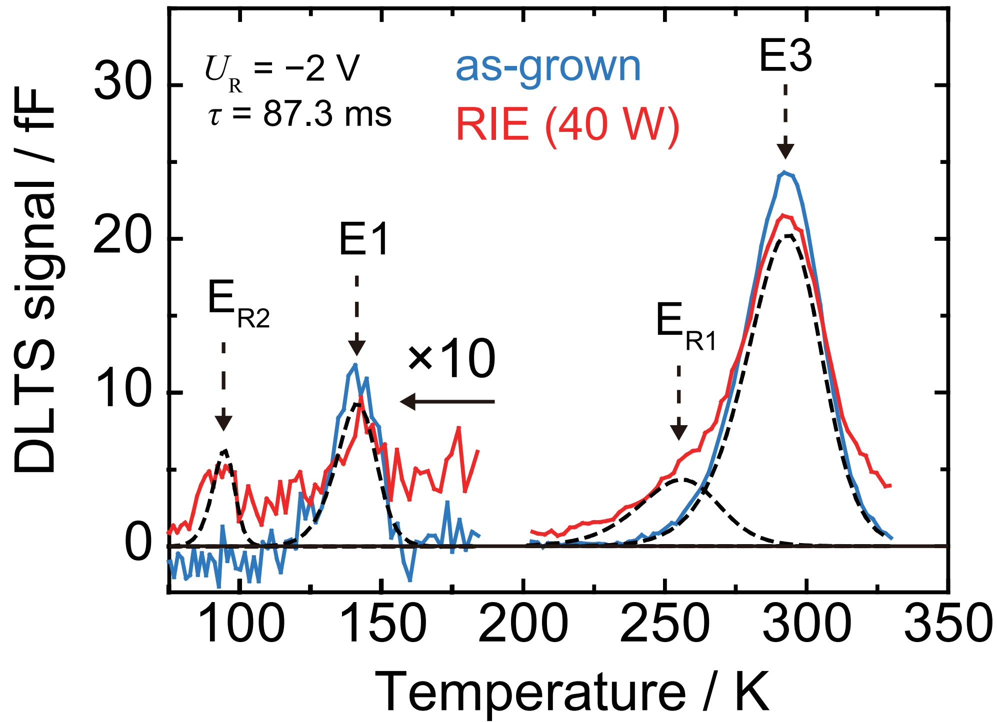

Figure 7.9: DLTS spectra for the as-grown sample (blue solid line) and the RIE sample (red solid line).

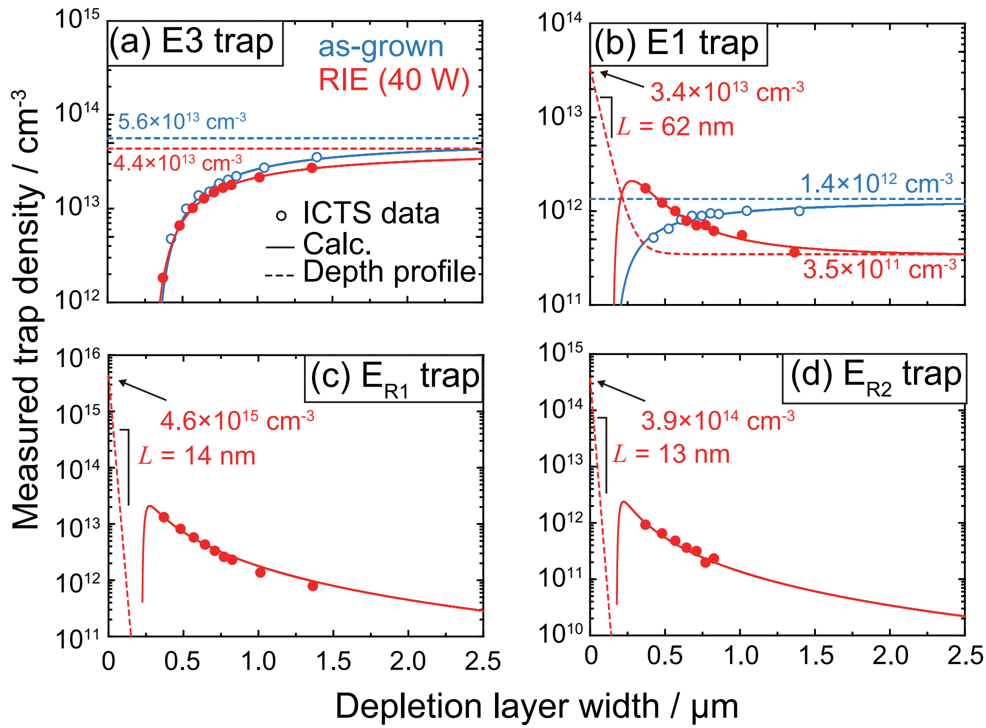

Figure 7.10: Depletion layer width dependence of the measured trap density. Solid lines are calculation results and broken lines are extracted depth profiles. In the analyses, a spatially uniform or exponential distribution is assumed as the depth profile.

extracted depth profile of density of electron trap E1 in the RIE-etched GaN has a constant component ($N_T = 3.5 \times 10^{11}$ cm^{-3}) and an exponential component [$N_T(0) = 3.4 \times 10^{13}$ cm^{-3} and $L = 62$ nm]. Therefore, it is seemed that the electron trap E1 is a point defect generated during both crystal growth process and RIE process. On the other hand, the electron trap E3 has a constant depth profile in both the as-grown GaN ($N_T = 5.6 \times 10^{13}$ cm^{-3}) and RIE-etched GaN ($N_T = 4.4 \times 10^{13}$ cm^{-3}). This result is reasonable because the electron trap E3 in MOVPE-grown GaN originates from the substitution of Fe atoms at Ga sites [37]. The electron trap E3 detected in this study corresponds to Fe_{Ga} induced during the crystal growth. For detail discussion, more detailed experimentation and analysis are required as in the case of RIE-induced defects in SiC described above (Sec. 7.4).

7.6 Summary

In this chapter, the depth profiles of electron traps generated in n-type 4H-SiC during the RIE process were investigated. In the RIE-etched samples, two electron traps, the $Z_{1/2}$ and EH_3 centers, were detected in ICTS measurements at 300 K. Depth profiles of trap density can be extracted with the proposed method from the dependence of the averaged trap density on the depletion layer width. When a function based on an exponential is assumed as the depth profile, electron trap densities near the etched surface of 10^{14} to 10^{15} cm^{-3} and the depth of electron trap generation at 140 nm were obtained with the proposed method using the ICTS technique for the RIE-etched sample. The electron traps generated during the RIE process were confirmed to be localized near the etched surface ($x \leq 1$ μm). A comparison of the extracted depth profile of the $Z_{1/2}$ center density to that of the EH_3 center density in the deeper region ($x > 1$ μm) suggested that the pair annihilation of carbon vacancy defects and carbon atoms ejected by ion bombardment during the RIE process occurs. The proposed method is useful to investigate the depth profile of carrier trap density when the carrier trap has a large depth direction distribution.

References

[1] V. Khemka, T. P. Chow, and R. J. Gutmann, J. Electronic Materials **27**, 1128 (1998).

[2] T. Dalibor, G. Pensl, H. Matsunami, T. Kimoto, W. J. Choyke, A. Schöner, and N. Nordell, Phys. St. Solidi A **162**, 199 (1997).

[3] T. Troffer, M. Schadt, T. Frank, H. Itho, G. Pensl, J. Heindl, H. P. Strunk, and M. Maier, Phys. St. Solidi A **162**, 277 (1997).

[4] K. Kawahara, G. Alfieri, and T. Kimoto, J. Appl. Phys. **106**, 013719 (2009).

[5] D. V. Lang, J. Appl. Phys. **45**, 3023 (1974).

[6] H. Okushi and Y. Tokumaru, Jpn. J. Appl. Phys. **20**, 261 (1981).

[7] R. R. Senechal and J. Basinski, J. Appl. Phys. **39**, 4581 (1968).

[8] K. Kanegae, M. Horita, T. Kimoto, and J. Suda, Appl. Phys. Express **11**, 071002 (2018).

[9] H. Lefèvre and M. Schulz, Appl. Phys. **12**, 45 (1977).

[10] Y. Zohta and M. O. Watanabe, J. Appl. Phys. **53**, 1809 (1982).

[11] A. Usami, Y. Tokuda, M. Katayama, S. Kaneshima, and T. Wada, J. Phys. D: Appl. Phys. **19**, 1079 (1986).

[12] K. Danno and T. Kimoto, J. Appl. Phys. **100**, 113728 (2006).

[13] L. Storasta, H. Tsuchida, T. Miyazawa, and T. Ohshima, J. Appl. Phys. **103**, 013705 (2008).

[14] K. Kawahara, M. Krieger, J. Suda, and T. Kimoto, J. Appl. Phys. **108**, 023706 (2010).

[15] S. Yamada, M. Omori, H. Sakurai, O. Y, R. Kamimura, T. Hashizume, J. Suda, and T. Kachi, Appl. Phys. Express **13**, 016505 (2020).

[16] D. Pons and S. Makram-Ebeid, J. de Physique **40**, 1161 (1979).

[17] G. M. Martin, A. Mitonneau, D. Pons, A. Mircea, and D. W. Woodard, J. Phys. C: Solid St. Physics **13**, 3855 (1980).

[18] S. Weiss and R. Kassing, Solid-State Electronics **31**, 1733 (1988).

[19] S. D. Brotherton, Solid-State Electronics **26**, 987 (1983).

[20] R. H. Lyddane, R. G. Sachs, and E. Teller, Phys. Rev. **59**, 673 (1941).

[21] H. Harima, S. Nakamura, and T. Uemura, J. Appl. Phys. **78**, 1996 (1995).

[22] C. T. Sah and V. G. K. Reddi, IEEE Trans. Electron Device **11**, 345 (1964).

[23] W. Kern, J. The Electrochemical Society **137**, 1887 (1990).

[24] P. Blood and J. W. Orton, The Electrical Characterization of Semiconductors: Majority Carriers and Electron States.

[25] T. Kimoto, A. Itoh, H. Matsunami, S. Sridhara, L. L. Clemen, R. P. Devaty, W. J. Choyke, T. Dalibor, C. Peppermüller, and G. Pensl, Appl. Phys. Lett. **67**, 2833 (1995).

[26] J. Zhang, L. Storasta, J. P. Bergman, N. T. Son, and E. Janzén, J. Appl. Phys. **93**, 4708 (2003).

[27] C. Hemmingsson, N. T. Son, O. Kordina, J. P. Bergman, E. Janzén, J. L. Lindström, S. Savage, and N. Nordell, J. Appl. Phys. **81**, 6155 (1997).

[28] G. Alfieri, E. V. Monakhov, B. G. Svensson, and A. Hallén, J. Appl. Phys. **98**, 113524 (2005).

[29] G. Alfieri and A. Mihaila, J. Phys.: Condensed Matter **32**, 465703 (2020).

[30] N. T. Son, X. T. Trinh, L. S. Løvlie, B. G. Svensson, K. Kawahara, J. Suda, T. Kimoto, T. Umeda, J. Isoya, T. Makino, T. Thshima, and E. Janzén, Phys. Rev. Lett. **109**, 187603 (2012).

[31] K. Kawahara, X. T. Trinh, N. T. Son, E. Janzén, J. Suda, and T. Kimoto, Appl. Phys. Lett. **102**, 112106 (2013).

[32] L. Storasta, J. P. Bergman, E. Janzén, A. Henry, and J. Lu, J. Appl. Phys. **96**, 4909 (2004).

[33] H. J. v. Bardeleben, J. L. Cantin, L. Henry, and M. F. Barthe, Phys. Rev. B **62**, 10841 (2000).

[34] S. A. Reshanov, G. Pensl, K. Danno, T. Kimoto, S. Hishiki, T. Oshima, H. Itoh, F. Yan, R. P. Devaty, and W. J. Choyke, J. Appl. Phys. **102**, 113702 (2007).

[35] A. F. Tasch, H. Shin, C. Park, J. Alvis, and S. Novak, J. The Electrochemical Society **136**, 810 (1989).

[36] M. Horita, T. Narita, T. Kachi, and J. Suda, Appl. Phys. Express **118**, 012106 (2021).

[37] M. Horita, T. Narita, T. Kachi, and J. Suda, Appl. Phys. Express **13**, 071007 (2020).

Chapter 8

Conclusions

8.1 Conclusions

In this thesis, the author aim to control the deep level in wide bandgap semiconductor GaN and SiC for improving the performance of power devices, and the deep level in the GaN layer introduced during crystal growth and the SiC layer introduced by the device process. The author established a precise quantification method for the deep level inside and clarified the physical properties of the deep level. The major conclusions obtained in this study are summarized as follows.

In Chapter 3, a method to measure the density of hole trap H1 in n-type GaN with p^+-n junction was proposed. In the proposed method, it is considerd both the spatial distribution of the injected holes and the quick carrier recombination via the hole traps near the depletion layer edge immediately after a reverse bias is applied. The reverse bias voltage dependence of the current-injection ICTS spectrum indicates that an accurate hole trap density, as well as the hole diffusion length and electron capture cross-section of the hole trap, can be determined.

In Chapter 4, the ratio of photoionization cross-sections of the hole trap H1 under sub-E_g-light illumination (390 nm) was determined.Current-injection ICTS and sub-E_g-light-excited ICTS were performed for a PND and hole occupancy ratio f_T under 390 nm light illumination was investigated. From the analysis of f_T based on the rate equation of hole trap H1 during light illumination, the ratio σ_n^o/σ_p^o of 3.0 was extracted for 390 nm light illumination.

In Chapter 5, three methods to quantify the density of hole trap H1 in n-type GaN layers with Schottky junction were proposed. To quantify the density of hole trap H1 in n-type GaN layers, hole occupancy ratio f_T has to be corrected on the measured density in sub-E_g-light-excited ICTS. The hole occupancy ratio under 390 nm light illumination was determined using the ratio of photoexcitation rates, which was determined in Chapter 4, and the sum of photoexcitation rates. To obtain the sum, measurement conditions during optical filling pulse (UV light illumination) period were modulated: temperature, optical

intensity, or optical-filling-pulse-width. Moreover, the three methods can be combined with the dual-color method, in which the capacitance transient due to not only hole thermal excitation but also photoexcitation from the hole-occupied H1 trap to the V.B. by a long-wavelength light illumination is measured and it makes shortened the measurement time. Easy, accurate, and quick methods to quantify the density of hole trap H1 in n-type GaN layers were demonstrated.

In Chapter 6, nature of the hole trap H1 in n-type GaN layers was investigated: quantitative relationship between carbon concentration and density of hole trap H1, electron capture cross-section of the hole trap H1, and dependence of the photoionization cross-section ratio σ_n^o/σ_p^o of the hole trap H1 on photon energy $h\nu$. In the density range from 10^{14} cm^{-3} to 10^{17} cm^{-3}, the density of hole trap H1 [$C_N(0/-)$] was almost equal to the carbon concentration in n-type GaN layers regardless growth methods and conditions. This result suggests that almost all incorporated carbon atoms substitutes at N sites in n-type GaN layers. The electron capture cross-section of the hole trap H1 σ_n of 3×10^{-21} cm^2 was obtained. The investigated $\sigma_n^o/\sigma_p^o(h\nu)$ in the photon energy range from 2.6 eV to 3.2 eV was reasonably explained from the theoretical model of the photoionization cross-section calculated with reported CC diagram of $C_N(0/-)$.

In Chapter 7, a method to investigate depth profiles of defects was proposed. The method has the high depth resolution and the high resolution in the carrier trap density. Extraction of steep depth profiles of defects induced during RIE processes in SiC and GaN layers was demonstrated with the proposed method. From the analysis of extracted depth profiles, generation mechanism of the RIE-induced defects was discussed. In RIE-etched SiC, the $Z_{1/2}$ center ($E_C - 0.64$ eV) and EH_3 center ($E_C - 0.74$ eV), which originate from $V_C(0/2-)$ and C_i-related defect, respectively, were localized near the etched surface ($<$ 1 μm) due to ion bombardment. In the deeper region ($\sim$ 3 μm), annihilation of V_C defects generated during crystal growth and carbon atoms kicked-out from the etched region and/or etched surface was investigated.

8.2 Future Work

The author studied quantitative methods and nature of deep levels in GaN and SiC from various aspects in this thesis. However, there remain several issues to be solved, and there have emerged several goals to be accomplished in the future.

- **Methods to measure depth profiles of the density of hole trap H1 in n-type GaN:** The devised method for quantifying the density of hole trap H1 in the n-type GaN layer assumes that the density is uniform in the depth direction. It is necessary to devise and demonstrate a general case where the density (carbon concentration) of the hole trap H1 has a distribution in the depth direction in combination with a method for quantifying the density of deep level having a distribution in the depth

direction.

- **C_N donor in n-type GaN:** Nitrogen site carbon in GaN is predicted from first-principles calculations to form donor level $C_N(0/+)$ ($E_V + 0.3$ eV) [1] near the valence band and is detected by capacitive transient spectroscopy [2, 3]. It is believed to be the origin of the hole trap H3 [3]. It is necessary to apply the method of quantifying the density of hole trap H1 to determine the density of hole trap H3, and compare it with the carbon concentration, for example, to clarify its origin.

- **Ga vacancy-related defect in n-type GaN:** It is suggested that there are relatively high density deep acceptor levels in the n-type GaN layer with an effective donor density of 5×10^{16} cm^{-3} or more, in addition to nitrogen site carbon [4]. Its origin is thought to be a Ga vacancy-related defect that forms a deep level on the valence band side. It is necessary to apply the hole trap density quantification method devised in this study to detect and quantitatively study it.

- **Measuring depth profiles of other device process-induced defects in SiC:** In this study, the author quantified the density distribution and considered the generation mechanism of reactive ion etching-induced defects in SiC. The method for quantifying the density of deep level with a steep depth direction distribution proposed in this study is also effective for quantifying the density distribution of other device process-induced defects, and quantitative study is required.

References

[1] J. L. Lyons, A. Janotti, and C. G. V. d. Walle, Phys. Rev. B **89**, 035204 (2014).

[2] Y. Tokuda, ECS Trans. **75**, 39 (2016).

[3] T. Narita, K. Tomita, Y. Tokuda, T. Kogiso, M. Horita, and T. Kach, J. Appl. Phys. **124**, 215701 (2018).

[4] N. Sawada, T. Narita, M. Kanechika, T. Uesugi, T. Kachi, M. Horita, T. Kimoto, and J. Suda, Appl. Phys. Express **11**, 041001 (2018).

List of Publications

A. Full Length Papers and Letters

1. K. Kanegae, M. Horita, T. Kimoto, and J. Suda
   "Accurate method for estimating hole trap concentration in n-type GaN via minority carrier transient spectroscopy,"
   Applied Physics Express **11**, 071002 (2018).

2. K. Kanegae, M. Kaneko, T. Kimoto, M. Horita, and J. Suda
   "Characterization of carrier concentration and mobility of GaN bulk substrates by Raman scattering and infrared reflectance spectroscopies,"
   Japanese Journal of Applied Physics **57**, 070309 (2018).

3. K. Kanegae, H. Fujikura, Y. Otoki, T. Konno, T. Yoshida, M. Horita, T. Kimoto, and J. Suda
   "Deep-level transient spectroscopy studies of electron and hole traps in n-type GaN homoepitaxial layers grown by quartz-free hydride-vapor-phase epitaxy,"
   Applied Physics Letters **115**, 012103 (2019).

4. K. Kanegae, T. Narita, K. Tomita, T. Kachi, M. Horita, T. Kimoto, and J. Suda
   "Dual-color-sub-bandgap-light-excited isothermal capacitance transient spectroscopy for quick measurement of carbon-related hole trap density in n-type GaN,"
   Japanese Journal of Applied Physics **59**, SGGD05 (2020).

5. K. Aoshima, K. Kanegae, M. Horita, T. Kimoto, and J. Suda
   "Electron traps formed by gamma-ray irradiation in homoepitaxial n-type GaN and their annealing behavior,"
   AIP Advances **10**, 045023 (2020).

6. K. Kanegae, T. Narita, K. Tomita, T. Kachi, M. Horita, T. Kimoto, and J. Suda
   "Photoionization cross section ratio of nitrogen-site carbon in GaN under sub-bandgap-light irradiation determined by isothermal capacitance transient spectroscopy,"
   Applied Physics Express **14**, 091004 (2021).

7. K. Kanegae, T. Okuda, M. Horita, J. Suda, and T. Kimoto
"Depth profiles of electron traps generated during reactive ion etching in n-type 4H-SiC characterized by using isothermal capacitance transient spectroscopy,"
Journal of Applied Physics **130**, 105703 (2021).

B. International Conferences

1. K. Kanegae, M. Horita, T. Kimoto, and J. Suda
"Investigation of hole traps in n-type homoepitaxial GaN by ODLTS focusing on sub-bandgap-light optical excitation process,"
12th International Conference on Nitride Semiconductors, Strasbourg, France, July. (2017), C02.24, poster.

2. K. Kanegae, M. Horita, T. Kimoto, and J. Suda
"Measurement of H1 trap concentration in MOVPE-grown homoepitaxial n-type GaN by optical isothermal capacitance transient spectroscopy using sub-bandgap photoexcitation,"
Asia-Pacific Workshop on Fundamentals and Applications of Advanced Semiconductor Devices 2018, Kitakyusyu, Japan, July. (2018), A7-4, oral.

3. K. Kanegae, M. Horita, T. Kimoto, and J. Suda
"Accurate estimation of H1 trap concentration in n-type GaN layers,"
International Symposium on Growth of III-Nitrides, Warsaw, Poland, August. (2018), Tu4.4, oral.

4. K. Kanegae, H. Fujikura, Y. Otoki, T. Konno, T. Yoshida, M. Horita, T. Kimoto, and J. Suda
"DLTS studies of quartz-free-HVPE-grown homoepitaxial n-type GaN,"
International Workshop on Nitride Semiconductors, Kanazawa, Japan, November. (2018), CR11-2, oral.

5. K. Kanegae, T. Narita, K. Tomita, T. Kachi, M. Horita, T. Kimoto, and J. Suda
"Hole occupancy ratio of H1 trap in homoepitaxial n-type GaN under sub-bandgap light irradiation,"
International Workshop on Nitride Semiconductors, Kanazawa, Japan, November. (2018), CR16-1, oral.

6. K. Kanegae, T. Narita, K. Tomita, T. Kachi, M. Horita, T. Kimoto, and J. Suda
"Determination Methods of H1 Trap Concentration in N-Type GaN Schottky Barriers via Sub-Bandgap-Light Isothermal Capacitance Transient Spectroscopy,"
13th International Conference on Nitride Semiconductors, Bellevue, Washington, USA, July. (2019), J01.03, oral.

7. K. Kanegae, T. Narita, K. Tomita, T. Kachi, M. Horita, T. Kimoto, and J. Suda
"Photon energy dependence of photoionization cross-section ratio of electron to hole for the carbon-related hole trap in n-type GaN,"
30th International Conference on Defects in Semiconductors, Seattle, Washington, USA, July. (2019), Poster Session Ⅱ 2, poster.

8. K. Kanegae, T. Narita, K. Tomita, T. Kachi, M. Horita, T. Kimoto, and J. Suda
"Quick measurement method of carbon-related defect concentration in n-type GaN by dual-color-sub-bandgap -light-excited isothermal capacitance transient spectroscopy,"
2019 International Conference on Solid-State Devices and Materials, Nagoya, Japan, September. (2019), K-7-04, oral.

9. K. Kanegae, T. Okuda, M. Horita, J. Suda, and T. Kimoto
"Depth Profiles of Deep Levels Generated by ICP-RIE in 4H-SiC,"
International Conference on Silicon Carbide and Related Materials 2019, Kyoto, Japan, October. (2019), We-3B-05, oral.

10. K. Kanegae, T. Okuda, M. Horita, J. Suda, and T. Kimoto
"Depth Profiles of Defects Generated by RIE in 4H-SiC Characterized by Deep-level Transient Spectroscopy,"
9th Asia-Pacific Workshop on Widegap Semiconductors, Okinawa, Japan, November. (2019), ED4-5, oral.